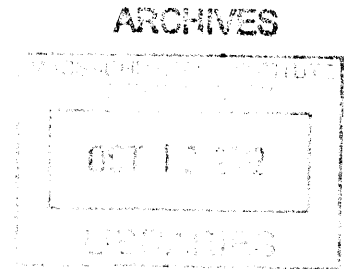# Nanomechanical Coupling of Mechanomutable Polyelectrolytes

by

Steven W. Cranford

B.Eng., Civil Engineering
Memorial University (2006)
M. Sci., Civil and Environmental Engineering
Stanford University (2008)

Submitted to the Department of Civil and Environmental Engineering
in partial fulfillment of the requirements for the degree of

Doctor of Philosophy

at the

MASSACHUSETTS INSTITUTE OF TECHNOLOGY

September 2012

Author . . . .
Department of Civil and Environmental Engineering
July 15, 2012

Certified by . . . .
Markus J. Buehler
Associate Professor of Civil and Environmental Engineering
Thesis Supervisor

Accepted by . . . .
Heidi M. Nepf
Chair, Departmental Committee for Graduate Students

Nanomechanical Coupling of Mechanomutable Polyelectrolytes

by

Steven W. Cranford

Abstract

Nanotechnology has advanced to the point where almost any molecular functional group can be introduced into a composite material system. However, emergent properties attained *via* the combination of arbitrary components - *e.g.*, the complexation of two weak polyelectrolytes - is not yet predictive, and thus cannot be rationally engineered. Predictive and reliable quantification of material properties across scales is necessary to enable the design and development of advanced functional (and complex) materials. There is a vast amount of experimental study which characterize the strength of electrostatic interactions, topology, and viscoelastic properties of polyelectrolyte multilayers (PEMs), but very little is known about the fundamental molecular interactions that drive system behavior.

Here, we focus on two specific weak polyelectrolytes - poly(acrylic acid) (PAA) and poly(allylamine hydrochloride) (PAH) - that undergo electrostatic complexation, and can be manipulated as function of pH. While the driving mechanism investigated here is ionic interactions, the findings and atomistic approaches are applicable to a variety of systems such as hydrogen bonded polypeptides (*e.g.*, protein structures), as well as similar polyelectrolyte systems (*e.g.*, PSS, PDMA, etc.). Specifically, in this dissertation, the coupling of electrostatic cross-links and weak interactions, polyelectrolyte persistence length and molecular rigidity of PAA and PAH is investigated with full atomistic precision. Large-scale molecular dynamics (MD) simulations indicate the stiffening of PEMs cannot be explained by increased electrostatic cross-linking alone, but rather the effect is amplified by the increase in molecular rigidity due to self-repulsion. Based on MD simulations, a general theoretical model for effective electrostatic persistence length is proposed for highly flexible polyelectrolytes and charged macromolecules through the introduction of an electrostatic contour length which can applied to other chemical species. A focus on adhesion reveals the effective cross-linking strength exceeds the strength of ionic interaction alone, due to secondary effects (*e.g.*, H-bonding, steric effects, etc.) Moreover, a derived elastic model for complexation reveals a critical bound for cross-link density and stiffness, indicating the required conditions to induce cooperative mechanical behavior. The

.

key insight is that these critical conditions can be further extended for the coupling of flexible molecules in general, such as proteins or flexible nanoribbons. The results demonstrate how nanoscale control can lead to uniquely tunable mechanomutable materials from designed functional building blocks.

While PEM systems are currently being developed for biosensor, membrane, and tissue engineering technologies, the results presented herein provide a basis to tune the properties of such systems at the nanoscale, thereby engineering system behavior and performance across scales. Understanding the bounds of mechanical performance of two specific polyelectrolyte species, and their joint interaction through complexation, provides a basis for coupling molecules with various functionalities. Similar to complete understanding the limitations of a steel beam in construction of a bridge, the systematic delineation of polyelectrolyte complexation allows quantitative prediction of larger-scale systems.

Thesis Supervisor: Markus J. Buehler
Title: Associate Professor of Civil and Environmental Engineering

Acknowledgments

First and foremost, I will take the opportunity to thank my wife, Deborah, partner in crime and LOML. I am forever indebted to her for her support and patience. As she constantly reminds me, my education has been a long journey through three institutions of higher learning. We have jointly gone through the trials and tribulations of grad school and my success is forever shared with her. ·

One cannot progress to this point as an individual, and there are many people I would like take the opportunity to thank. At a personal level, it is an honor for me to thank my parents for their unconditional support and guidance. In particular, I thank my father, Wayne, whom I always wished to emulate, for his understanding of my desire to excel. Entrepreneurial spirit can be applied to academics as in business. I equally thank my mother, Judy, for her motivation and strength. As she commonly jokes, "he may have gotten his good looks from his father, but his brains are from me". I also thank my sister, Vanessa, who set the bar high with her own professional success and provided an example I wished to follow.

I would like to express my gratitude for many who have supported me during my studies at Memorial, Stanford, and MIT. I will always ensure to thank Prof. Amgad Hussein in the Department of Civil and Environmental Engineering at Memorial University, who directed me towards scientific research, and saw the potential (and reward) of graduate study. Additionally, I thank my colleagues from undergrad, Colleen MacNeil (nee McDonald), Tim Matthews, and Michael Colbert, otherwise known as *Team Rebar*. Memorial provided my academic foundation and confidence on par with any I have encountered. I thank all the professors and peers at Stanford University, especially Prof. Greg Deierlein who showed us how to simplify even the most complex problems, and Prof. Sarah Billington, for her advice and guidance. For their friendship and excellent discussions, I am also in debt to all my peers at the Blume Center, especially Abbie Liel for showing me what can be expected of a graduate student, and Amy Askin for sharing my somewhat cynical views on education.

I could not have made it to this point without my extraordinary collaborators within the LAMM at MIT, with special thanks to Zhao Qin who shared this entire doctoral journey with me. My officemates, Graham, Andre, Shu-Wei, Chia-Ching, Max, Tristan, Greta, Leon, C.T. and Anna, as well as undergrads involved in our group, all contributed to my work in some way. Further, I would like to particularly acknowledge LAMM alumni and postdocs, Dr. Dipanjan Sen, Prof. Sinan Keten, Dr. Raffaella Paparcone, Dr. Melis Arslan, Dr. Alfonso Gautieri, and Dr. Arun Nair for their friendship, support, and motivation. I reserve special thanks for Sébastien Uzel at MIT, always available for interoffice lunches at the student center.

I owe my deepest gratitude to my advisor Professor Markus J. Buehler, who has introduced me to the atomistic and nano-scale mechanics, as well as the idiosyncrasies of academia. I would not have arrived at this point if not for his excellent mentorship and support. I have learned a great deal beyond my "civil" background, and have become a much better scientist and writer by being a part of the Buehler group. Markus has been a great source of motivation and inspiration for me and I am forever

grateful. Regarding academic guidance, I would like to thank my thesis committee of Professor Christine Ortiz, Professor Mary Boyce, and Professor John Williams for fruitful suggestions and valuable time.

Finally, I am grateful to my extended family and friends for their never-ending support, encouragement and faith in my academic endeavors (and Ruby, for her silent support).

Make everything as simple as possible, but not simpler.

Albert Einstein (1879 − 1955)

For my wife, Deborah, who was there for all the ups and downs.

Contents

List of publications

Portions of work presented throughout this thesis has been previously published in texts and peer reviewed journals. Relevant articles are cited throughout. However, in some cases, technical details and less relevant results were omitted for clarity and/or brevity. For more information, the reader is referred to the following publications (listed in reverse chronological order).

Manuscripts in submission and/or under review:

- **S. Cranford**, J. de Boer, C.A. van Blitterswijk, M.J. Buehler, "*Materiomics: an −omics approach to biomaterials research,*" Advanced Materials, *in submission.*

- **S. Cranford**, M.J. Buehler, "*Variation of weak polyelectrolyte persistence length through an electrostatic contour length,*" Macromolecules, *under revision.*

- **S. Cranford**, D. Brommer, M.J. Buehler, "*Extended graphynes: simple scaling laws for stiffness, strength and fracture,*" Nanoscale, *in submission.*

- N. Pugno, **S. Cranford**, M.J. Buehler, "*Simultaneous material and structural optimization in the spider web attachment disk,*" Small, *in submission.*

- **S. Cranford**, L. Han, C. Ortiz, M.J. Buehler, "*Nanoscale shear of PEM nanotube arrays: mesocale modeling and lateral force microscopy,*" *in preparation.*

- **S. Cranford**, M.J. Buehler, "*Critical cross-Links to couple polyelectrolytes,*" *in preparation.*

Articles accepted in peer-reviewed journals:

- **S. Cranford**, M.J. Buehler, "*Selective hydrogen purification through graphdiyne under ambient temperature and pressure,*" Nanoscale, Vol. 4, pp. 4587-4593, 2012.

- **S. Cranford**, A. Tarakanova, N. Pugno, M.J. Buehler, "*Nonlinear material behavior of spider silk yields robust webs,*" Nature, Vol. 482, pp. 72-76, 2012.

- O. Compton, **S. Cranford**, K. Putz, C. Brinson, S.T. Nguyen, M.J. Buehler, "*Tuning the mechanical properties of graphene oxide paper and its associated polymer nanocomposites by controlling cooperative intersheet hydrogen bonding,*" ACS Nano, Vol 6(3), pp 2008-2019, 2012.

- **S. Cranford**, M.J. Buehler, "*Packing efficiency and accessible surface area of crumpled graphene,*" Physical Review B, Vol. 84, 205451, 2011.

- **S. Cranford**, M.J. Buehler, "*Shaky foundations of hierarchical biological materials,*" Nano Today, Vol. 6(4), pp. 332-338, 2011.

- **S. Cranford**, M.J. Buehler, "*Twisted and coiled ultralong multilayer graphene ribbons,*" Modelling and Simulation in Materials Science and Engineering, Vol. 19, 054003 (20 pp), 2011.

- **S. Cranford**, M.J. Buehler, "*Mechanical properties of graphyne,*" Carbon, Vol. 49(13), pp. 4111-4121, 2011.

- A. Nair, **S. Cranford**, M.J. Buehler, "*The minimal nanowire: mechanical properties of carbyne,*" European Physics Letters, Vol. 95, 16002, 2011.

- R. Paparcone, **S. Cranford**, and M.J. Buehler "*Self-folding and aggregation of amyloid nanofibrils,*" Nanoscale, Vol. 3(4), pp. 1748-1755, 2011.

- R. Paparcone, **S. Cranford**, and M.J. Buehler "*Compressive deformation of ultralong amyloid fibrils,*" Acta Mechanica Sinica, Vol. 26(6), pp. 977-986, 2010.

- **S. Cranford**, M.J. Buehler, "*Materiomics: biological protein materials, from nano to macro,*" Nanotechnology, Science and Applications, Vol. 3, pp. 127-148, 2010.

- G.H. Bratzel, **S. Cranford**, H. Espinosa, M.J. Buehler, "*Bioinspired noncovalently crosslinked "fuzzy" carbon nanotube bundles with superior toughness and strength,*" Journal of Materials Chemistry, Vol. 20, pp. 10465-10474, 2010.

- **S. Cranford**, C. Ortiz, M.J. Buehler, "*Nanomechanics of PAA/PAH polyelectrolyte complex: rate dependence and ionization effects on adhesion strength,*" Soft Matter, Vol. 6, pp. 4175-4188, 2010.

- **S. Cranford**, M.J. Buehler, "*In silico assembly and nanomechanical characterization of carbon nanotube Buckypaper,*" Nanotechnology, Vol. 21, 265706, 2010.

- **S. Cranford**, H. Yao, C. Ortiz, M.J. Buehler, "*A single degree of freedom 'lollipop' model for carbon nanotube bundle formation,*" Journal of the Mechanics and Physics of Solids, Vol. 58(3), pp. 409-427, 2010.

- **S. Cranford**, D. Sen, M.J. Buehler, "*Meso-origami: folding multilayer graphene sheets,*" Applied Physics Letters, Vol. 95, 123121, 2009.

- Q. Zhao, **S. Cranford**, T. Ackbarow, M.J. Buehler, "*Robustness-strength performance of hierarchical alpha-helical protein filaments,*" International Journal of Applied Mechanics, Vol. 1(1), pp. 85-112, 2009. ***selected best paper IJAM 2009-2010***

- **S. Cranford**, M.J. Buehler, "*Mechanomutable carbon nanotube arrays,*" International Journal of Material and Structural Integrity, Vol. 3(2-3), pp. 161-178, 2009.

Published book chapters and monographs:

- N. Groen, **S. Cranford**, M.J. Buehler, C.A. van Blitterswijk, *"Introduction to Materiomics,"* *Materiomics: High Throughput Screening of Biomaterial Properties*, editors: J. de Boer and C.A. van Blitterswijk, Cambridge University Press, 2012.

- **S. Cranford** and M.J. Buehler, *"Biomateriomics,"* Springer, 2012.

- **S. Cranford**, M.J. Buehler, *"Coarse-Graining Parameterization and Multiscale Simulation of Hierarchical Systems Part I: Theory and Model Formulation,"* *Multiscale Modeling: From Atoms to Devices*, editors: Pedro Derosa and Tahir Cagin, Taylor and Francis, 2011.

- **S. Cranford** and M.J. Buehler, *"Coarse-Graining Parameterization and Multiscale Simulation of Hierarchical Systems Part II: Case Studies,"* *Multiscale Modeling: From Atoms to Devices*, editors: Pedro Derosa and Tahir Cagin, Taylor and Francis, 2011.

List of Figures

17

18

List of Tables

Chapter 1

Introduction and Background

There is a emerging paradigm that - perceived across scales - the concepts of *material* and *structure* become interwoven and inseparable. One cannot consider a complex material system without full understanding of the structural hierarchies that compose it. Likewise, traditional material properties such as strength and toughness can be manipulated based on the structure of the components (*e.g.*, how components are assembled together). Opportunity lies in the seamless merger of each perspective. While materials scientists have recently shouldered this challenge, structural engineers can contribute a mechanistic perspective. Experts in structural analysis and design can provide new insight on material structure, behavior, and failure, from *nanoscale* to *macroscale, molecules* to *materials.*

1.1 From Molecules to Materials

Advances in nanoscale processing and simulation have led to the capability to directly control the mechanical properties of a material through change of its structural makeup at the atomistic scale. With the advent of "nanotechnology", within the past few decades, many key technological advancements have been pioneered using new materials and material design strategies from the "molecules up". Composites have revolutionized aviation and space exploration, polymers have prolonged life expectancy through their use in armor technology and medicine, and silicon has trans-

formed our world by facilitating the information technology revolution. In almost all fields, *materials* define the vanguard of technology and innovation.

In concord, we have now entered the era of nanoscience and nanotechnology where materials are made with atomistic precision - enabling advances in the design and synthesis of molecular building blocks that we can (theoretically) design and exploit. This bottom-up approach - designing a material/system through the behavior and combination of each constituent element and atom - was envisioned in the 1960's by Richard Feynman, the popular physicist and pioneer of nanotechnology. Feynman hypothesized the direct manipulation of individual atoms as the most powerful form of synthetic chemistry - unlocking the blueprints for atomistic construction. The challenge posed by Feynman was simple [114]:

> *What would happen if we could arrange the atoms one by one the way we want them?*

Following Feynman's famous address, referring to intriguing physical phenomena at the nanoscale, current trends in developing new materials rely heavily on fabricating systems at exceedingly smaller length scales through nanotechnology - the piece-wise combination of molecular building blocks (so-called "Feynman paradigm" [71]; see Figure 1-1) - reaching the limit of what can even be detected or observed with the most sophisticated characterization tools available. Controlling matter at the nanoscale in a bottom-up scheme (further advocated by Drexler in the 1990's [100]) has many advantages compared with classical top-down approaches. Key phenomena that cannot be anticipated through continuum predictions can be investigated and exploited at the atomic scale with nanoscale engineering. Currently, we are at the convergence of both bottom-up and top-down routes, closing the gap between material, structure, and function. Being said, a key issue that needs to be resolved for truly mastering molecular engineering is understanding the role of hierarchies that extend from "nano" to "macro" in complex materials, and how this translates into enhanced system behavior and performance.

Understanding what a material is composed of and how a material behaves has
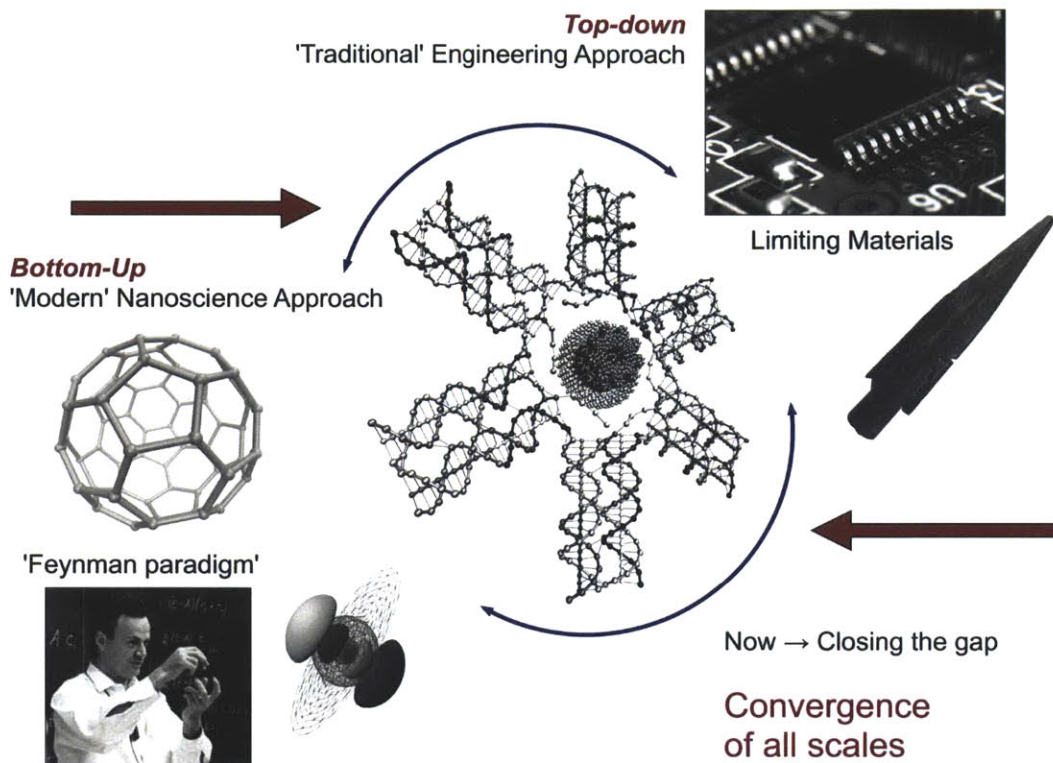
Figure 1-1: Juxtaposition of the "Feynman" paradigm with "traditional" engineering approaches. Current top-down methodologies have advanced from simple manipulation of available materials (*e.g.*, crude stone age weaponry) to sophisticated exploitation of material properties (*e.g.*, semiconductors in integrated circuits). Nanotechnology has also developed the ability to investigate and manipulate materials on the atomistic and molecular scale from a bottom-up perspective. Currently, we are at the convergence of both bottom-up and top-down routes, closing the gap between material, structure, and function. As Feynman suggested [114], precise engineering and control at the nanoscale may dictate the future of material design, but we must also fully understand how nanoscale properties are expressed at the macroscale. Are nanoscale "designer" materials the future? From Cranford and Buehler, *Biomateriomics*, Springer 2012 [71].

always been of great importance to enable and advance technologies [12, 121]. The key to molecular material design, like any efficient structural design, is the exploitation of universal, interchangeable and predictable building components (a molecular "ASTM standards", so-to-speak). For example, most of the structural materials in biology employ proteins as a key building block, and most proteins are made from only a handful of twenty common amino acids. The genius of Nature is attaining diverse functionality with such a small set of universal building blocks. Examples for such

ingenuity include protein materials such as spider silk, hair, connective tissue (skin, cartilage, tendon) and cells [122, 46]. Can we mimic such an approach, perhaps exploiting the entire periodic table? Unfortunately, we cannot.

For biological materials, if we consider a single scale, one phase, with perfect knowledge of composition and sequence, in controlled conditions, we can make predictions - *e.g.*, with knowledge of constitutive amino acids (*i.e.*, sequence), we may predict an α-helical structure for short polypeptide [344, 324], and its corresponding properties (such as strength [2, 3]). Similarly, synthetic efforts such as "click" chemistry [183, 32] and recombinant DNA approaches [144, 307, 278, 139] can produce materials with desired (and engineered) properties and behaviors at a single scale, or assembled into simple hierarchies (*e.g.*, fibers [286, 101, 181, 316] or films [182, 313], or tubes [59]). Advancements in materials synthesis has undoubtedly introduced complexity to non-biological materials (as depicted in Figure 1-2). Yet while great strides have been made in fabrication, we cannot, at this time, accurately predict the behavior of larger molecular assemblies and networks, such as the role specific proteins play in a cellular structure (*e.g.*, the nuclear envelope), nor can we exploit building components across scales (for example, the difficulty in achieving the intrinsic molecular strength of carbon nanotubes at the macroscale [261, 262]). There is an inherent disconnect between complex material systems and traditional engineered structures.

We have copious amounts data and resources, but are unable (at this point) to fully use it. We utterly fail in real-world applications - the exact opposite of the goals of engineering! For engineering, we can design the components of a system or structure with reliable and repeatable accuracy - the performance of a fabricated steel member can be utilized in the design of a truss, for example, which is subsequently implemented in a bridge design. The critical roadblock is that complex materials are universally hierarchical - there is underlying structure and function at a multitude of diverse scales [122, 46]. This introduces a level of system complexity - piecewise understanding of individual parts (by scale or by function) cannot simply be superimposed and assembled [82, 334]. Unlike in engineered structures, at the molecular level, the difference between material properties and structural function is not clear

26
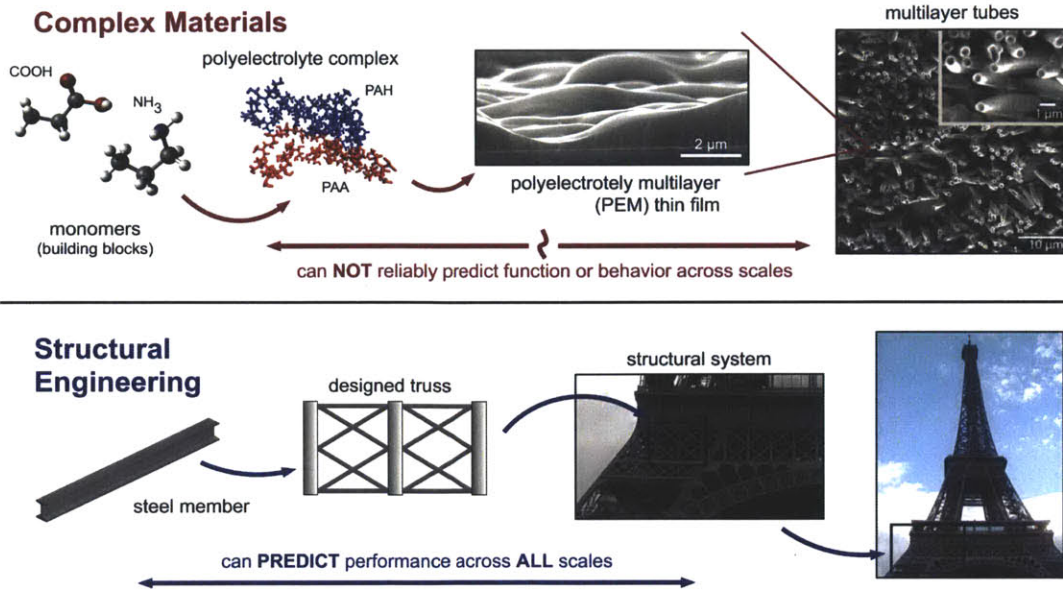
Figure 1-2: Example of the inherent disconnect between complex material systems and traditional structures. If we consider a single scale, one phase, with perfect knowledge of chemical composition, in controlled conditions (pH, temperature, pressure, etc.), we can make predictions. Here, with knowledge of the constitutive monomers (COOH and NH_3, for example), we can predict complexation for short polyelectrolyte segments, and exploit such known interactions for higher order structures (such as films and tubes). We cannot, however, accurately predict large scale behavior of these larger composites/assemblies directly from the molecular scale. We utterly fail in predicting performance - the exact opposite of the goals of engineering! For engineering, we can design the components of a structure with reliable and repeatable accuracy - the performance of a fabricated steel member can be utilized in the design of a truss, which is subsequently implemented in a structural system. (Insets: SEM of film from Guo *et al.* [135], *Langmuir*, 2009, used with permission, copyright © 2009 American Chemical Society; SEM of tubes from Chia *et al.* [59], *Langmuir*, 2009, used with permission, copyright © 2009 American Chemical Society.)

- as a direct result, the previously disparate concepts of "material" and "structure" are undergoing a implicit convergence, and cannot be separated. The intellectual challenge resides in reconciling material and structure across scales.

1.2   The Multiscale Challenge and Functional Building Blocks

While some materials, such as metals, maintain long-range order across scales (*e.g.*, crystallinity, grain boundaries), interesting behaviors arise from soft matter (*e.g.*,

polymer systems) in ways that cannot be predicted, or are difficult to predict, directly from the atomistic or molecular constituents. This discrepancy can be captured by the concept of *material behavior scaling*, one possible measure of the complexity inherent in a material system (see Cranford and Buehler [71] for more discussion). Commonly, the limit of material scaling is a function of multiple scales of order (*e.g.*, hierarchies) - often because soft matter self-organizes into mesoscopic physical structures that are much larger than the microscopic scale (the arrangement of atoms and molecules), and yet are much smaller than the macroscopic (overall) scale of the material. This can be considered analogous to biological tissues, where hierarchies are typically grown by physiological processes. Regardless, the properties and interactions of these mesoscopic structures may govern the macroscopic behavior of the material.

The consequence, of course, is that we must consider intended functionality in the investigation and design of novel materials. While easy to say, this task is complicated by the complex, hierarchical nature of such materials [122]. Functionality is ultimately rooted at the molecular scale [46, 45]. Through recent advancements in single-molecular assays, analytical chemistry, and computational approaches, we have made great strides in probing material systems from the molecular level. In particular, modeling and simulation have evolved into predictive tools that complement experimental analysis at comparable length- and time-scales. Whereas many questions regarding material systems can be studied with a single-scale approach at a single level of resolution, the use of theoretical and computational multiscale approaches enables critical progress in linking the chemical or molecular, and mesoscopic structures of these materials to macroscopic properties, across disparate scales (see Figure 1-3). The work of this thesis is primarily based on full atomistic molecular dynamics (MD), the necessary cornerstone to build a multiscale foundation.

Atomistic simulations have proved to be a unique and powerful way to investigate the complex behavior of phenomena such as dislocations, cracks, and grain boundary processes at a very fundamental level. Material system characterization founded at the molecular scale is motivated by three fundamental factors: (1) providing a common, universal basis for all materials; (2) reflecting fundamental functional behaviors

28
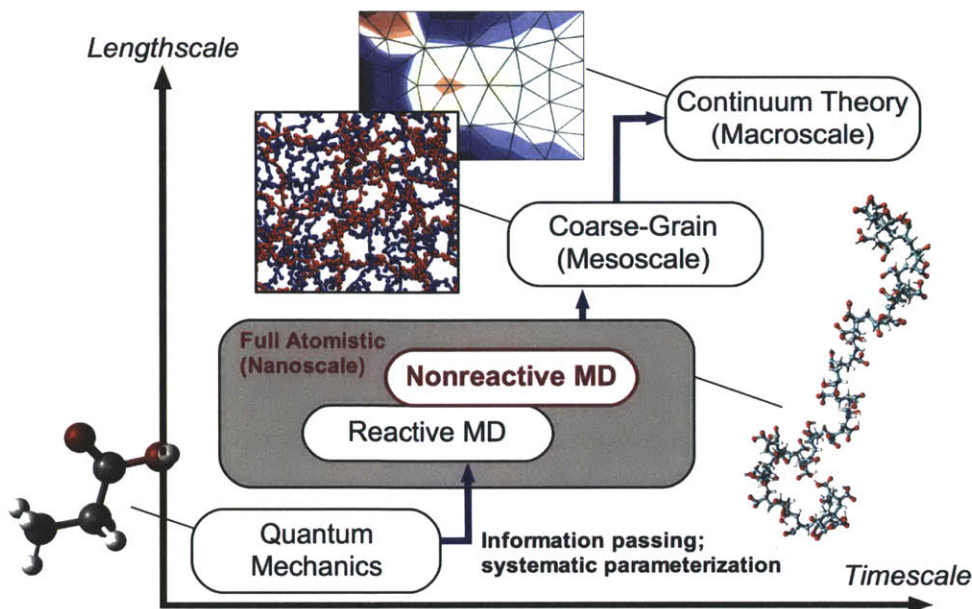
Figure 1-3: Hierarchy of characteristic/accessible time and length scales for computational materials science. The analytical, computational, and/or experimental approach to a complex material system is dependent on the particular scale of interest. To illustrate, while quantum mechanics (*e.g.*, density functional theory) may be suitable to describe the interaction of a few atoms and elements and their resulting band gaps, for example, continuum methods are more apt for the description of macroscale deformation, such as plastic yield. The complication which emerges is that one scale may influence others in unpredictable ways. Single scale perspectives are thus incomplete, requiring a holistic, multi-scale understanding of material systems. There exist numerous approaches in achieving this connection, notably hierarchical (*i.e.*, information-passing) and concurrent (*i.e.*, simultaneous) methods. The mechanistic foundation taken here is at the atomistic or molecular scale, enabling the treatment of molecular species.

and properties without any *a priori* assumptions, and; (3) capturing even the weakest contributions to functionality (which may be expressed at large scales). It can indeed be argued that the common, universal basis is rooted in the quantum behavior of materials, providing a mathematical description of the waveparticle duality of matter and energy. This is undoubtedly the case. Atomistic simulation must develop along with such *ab initio* information, and, ideally, each molecular force and bond explained *via* subatomic interactions. However, the quantum realm is a tricky scale, full of uncertainty and probabilities. Characterizing a complex material system, however, is inherently multiscale, requiring the description of material interactions from

the Ångstrom to the meter. If a common language is to be used for such a description (and seamlessly bridge scales), classical (or Newtonian) physics provides the fundamental basis and a common, mechanistic foothold, proven to be theoretically sound. If we are to consider full atomistic behavior the cornerstone in which to build our multiscale perspective, quantum mechanics provides the foundation of that stone, but they both support the same structure.

The linking of mechanisms across multiple scales by using a materials science approach to provide structure-process-property links characterizes the emerging field of *materiomics*. Materiomics - a transparent portmanteau of "material" with the suffix "omics" - can be simply defined as the holistic study of material systems. While typically applied to complex biological systems and biomaterials, materiomics is equally applicable to non-biological systems. Complementary to the field of biomaterials, materiomics represents a necessary holistic approach to the investigation of biological material systems, through the integration of natural functions and processes (biological, or "living" interactions) with traditional materials science perspectives (physical properties, chemical components, hierarchical structures, mechanical behavior, etc.). The addition of −omics adds a subtle layer of complexity to the material systems we are interested in. The term omics generally refers to *"all constituents considered collectively"*. For instance, genomics and the study of the human genome refer to all of our genes, not just a single subset that determines if you have your Mother's hair or your Father's stubbornness. Similarly, materiomics encompasses much more than a piecewise cataloging of the properties and behavior of a material - it encompasses all possible functionalities and material interactions, from nano to macro, in an abstract holistic sense.

It is the contention of materiomics that complex hierarchical material systems, by definition, prohibit such "separation of scales" − they are intrinsically woven. A continuum model cannot be accurately developed without consideration of molecular phenomena, and molecular phenomena can be highly dependent on atomistic and quantum level effects. A complete description of the material system is required incorporating all scaleswhat we have labeled as the materiome. Thus, from a materiomic

perspective, an integrative multiscale approach is not only desired but necessary, to not only describe material properties but to understand the structural organization, physical mechanisms throughout scales that contribute to material function. *But what means can we begin to construct such a perspective?*

Due to the inherent complexity of biological tissues (*e.g.*, as functional material systems) there is an intrinsic motivation to simplify the characterization in a holistic sense. One such approach is the definition, characterization, and categorization of material structures and components by their function - abstract functional building blocks - delineating the functional behaviors rather than detailing the material specific properties, so-to-speak. The definition of these "fundamental building blocks, however, is a matter of (changing) perspective. For example, in terms biological systems, the primary building blocks of proteins are commonly considered the amino acids (which constitute a unique sequence). However, these acids are also composed of side-chains (*e.g.*, amino acid = amine + carboxylic acid + side-chain), which can also be deconstructed to a few elements and atoms (illustrated by Figure 1-4). Even the atoms themselves can be considered "hierarchies" of protons, neutrons, and electrons. Practical application requires a "truncation of decomposition", which is dictated by a system under analysis. For certain systems, the behavior of neutrinos and other elementary subatomic particles may be required.

To fully exploit the "pliability" of proteins as structural building blocks, we must fully understand their potential interactions. Normal biological function requires that a systemss biochemical network be highly interconnected and interactive [22]. The reductionist approach employed by recent biologists is effective in defining the molecular structure and organization of DNA and proteins, but less effective at delineating function, because most biological molecules do not operate independently [148] they must be considered in the context of all of the other proteins in the cell and their organization [147]. Certain properties of biological systems are recognizable by engineers, such as positive and negative feedback loops, and parallel (redundant) circuits [148]. To exploit a modular building block understanding of cellular function it will be necessary for biologists to understand design principles more familiar to engineers

31
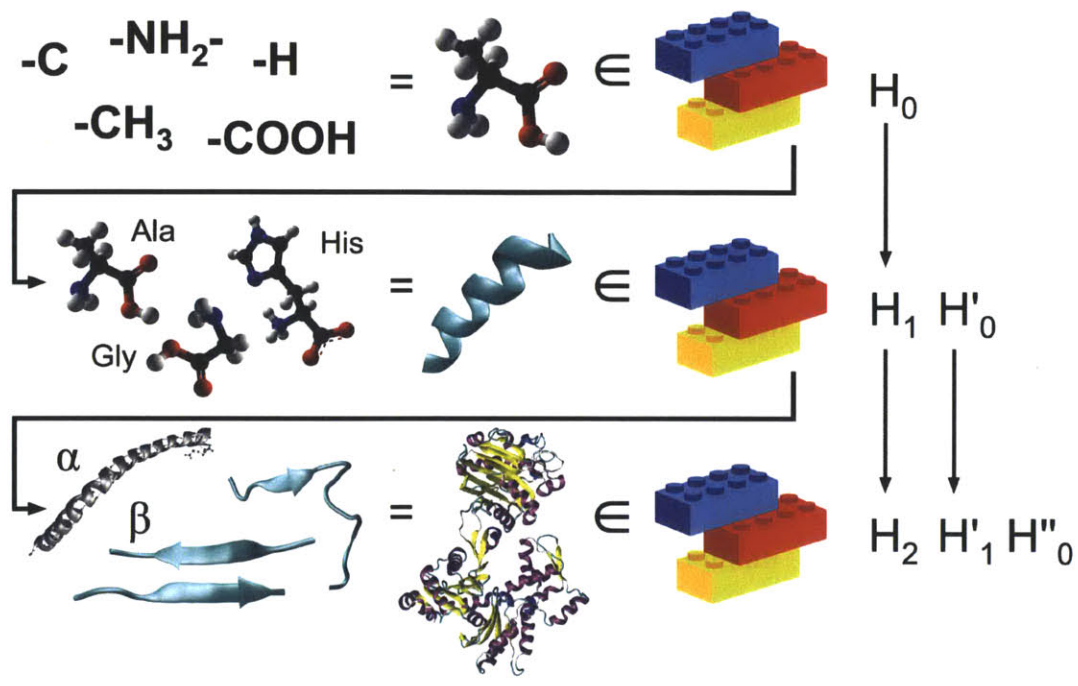
Figure 1-4: Building blocks built by building blocks? Hierarchical systems composed of structural units are subject to functional perspective. Here, we consider basic molecular groups (amine, carboxylic acid, and a side chain, such as the a methyl group depicted) as the fundamental irreducible building blocks of amino acids (such as alanine), and the set of amino acids provide the building blocks at the primary hierarchy (H_0), defined as the first structural unit. The set of amino acids (glycine, alanine, histidine, etc.) can form sequences with characteristic structures (such as α-helix), which compose the next hierarchy (H_1). Finally, many secondary structures (α-helices, β-sheets, etc.) can form a folded protein (here, actin) at the highest hierarchy considered (H_3). At higher scales, proteins themselves form the set of building blocks (actin is one of the three major components of the cytoskeleton). Depending on application, amino acids can be considered irreducible building blocks, and thus the secondary structures provide the primary hierarchy (H_0) followed by the protein structures (H_1). Similarly, from a cellular sense, the secondary structures may be considered irreducible, and thus the proteins provide the first structural unit (H_0). Definition of hierarchies and building blocks, therefore, is dependent on application and the function of each block. Note too that the characterization of secondary structures is a choice - as the amino acid sequence can be considered the building blocks of entire proteins, without the intermediate definition of secondary structures. From Cranford and Buehler, *Biomateriomics* [71].

32

and computer scientists, such as amplifiers, oscillators, and logic circuits [94]. Instead of having to include many of the molecular details of protein-protein or cellular interactions, the functional behavior each module (or system "motif") can be described using mathematical models that have a certain degree of universality. In many cases the models do not require plunging into the details of how every protein works they only need to include information on whether X activates or inhibits Y, and at what concentration (and perhaps a few additional parameters). Such models seem to capture the essential dynamics of protein "circuits", while being, in a sense, insulated from most of the complexity of the materials themselves [8].

Thereby, delineated levels of resolution (*e.g.*, network module or material building block) provides access to specific functional properties, which can be achieved by defining a particular material structure at each hierarchical scale. This paradigm, the formation of distinct structures at multiple length scales, also enables biological materials to overcome the intrinsic weaknesses of the building blocks [47]. This can be illustrated in the use of *nanoconfinement* that often results in enhanced strength and ductility despite the intrinsic brittleness of the same material in bulk form [126]. In an example relevant for sea creatures such as diatom algae and sponges, while silicon and silica is extremely brittle in bulk, the formation of nanostructures results in great ductility and extensibility, where the specific geometry used allows for a continuum of mechanical signatures. Thus, the realization of distinct structural designs provides a means to tune the material to achieve a great diversity of functional properties despite the use of the same building blocks. More generally, if it is possible to alter the materials structure at specific hierarchy levels, independently and during operation of a material, there exists the potential to realize varied material properties depending on functional needs.

The definition of functional building blocks becomes attractive if general material interactions can be identified across a range conditions (or constraints) - *e.g.*, they are transferable. Such efforts lie at the root of *biomimetics* [334, 4], to exploit the principles of Nature for technological means beyond the evolved functionalities of a biological system. Indeed, spider silk is not a focus of intense research to allow us to

swing from the skies like Spiderman, but rather the attraction of high performance, lightweight fibers. Required is the definition and categorization of key structures, relationships, and interactions between system components, beyond the current standard set of material properties. It is thought that if we can then procure equivalent building blocks (in terms of functions and interactions, but not necessarily in terms of materials and structures) we can develop similar system behavior. Indeed, if such definitions are robust and theoretically sound, it has been proposed one could draw insight from fields as diverse as *art* and *music* and apply general relationships to biology and material science [47, 70, 309, 129, 71]. Such efforts, however, are still in their infancy.

The keystone to the bottom-up design of such materials is a synergistic multiscale theoretical foundation from atomistic scales to the mesoscale to macroscale continuum-level constitutive modeling. Hierarchical "handshaking" at each scale is crucial to predict structure-mechanical property relationships, to provide fundamental mechanistic understanding of behavior, and to enable predictive material design optimization to guide synthetic design efforts.

Here, we apply this approach to a system of weak polyelectrolytes at the atomistic level, the primary component of an assembled multilayer system, and potential stimuli-responsive composites. The rationale of the current investigation is to quantify the complete range of atomistic-level nanomechanical properties as a function of polymer ionization experienced during the assembly process. Such information can then be utilized in future larger-scale modeling techniques (*i.e.*, continuum studies) and as a guide for synthetic efforts grounded in fundamental molecular behavior rather than empirical results. An understanding of the molecular origin of the behavior of polyelectrolyte properties can provide new insights into the basic polymer physics as well as provide new possibilities for their application.

1.3 Responsive Materials and Tunable Polyelectrolyte Multilayers

The ability to directly manipulate material properties and parameters at multiple levels significantly expands the design space available to a material system, facilitating new functionalities and applications despite having the same material components. Mutable (or tunable) materials are a class of materials that exhibit a variation in behavior either while undergoing assembly (*e.g.*, electrospun composites, shape memory allows), or under external stimuli *in situ* (*e.g.*, hydrogels, magnetorheological elastomers, and piezoelectrics). Mechanomutable materials, in particular, are material systems with variations in mechanical properties such as strength, stiffness, and toughness *via* external stimuli such as stress, temperature, moisture, pH, electric or magnetic fields; function can thus be both *tunable* and *reversible*. It is emphasized that mechanomutable materials differentiate themselves from simple responsive materials in the sense that mechanical properties do not react to external phenomena in an *ad hoc* manner based on chemical behavior, but can be controlled *via* tunable stimuli with designed intent. The desire for tunable mechanical properties, rather than a simple responsive multi-phase system requires the known behavior at the atomistic level, including full chemical details, macromolecular structure, and inter-macromolecular interactions, requiring a holistic materiomic framework.

The basis of these mechanical changes can typically be attributed to *in situ* modifications in the material structure (such as mutable nanotube arrays [75, 142, 143, 74]) or changes in the molecular interactions of the material components (*e.g.*, reversibly swellable polymers [152, 162, 59]). The trigger typically resides in spatially localized and controlled nanoscale units of varying components - the desired "functional building block". To unlock the potential of candidate mechanomutable systems, a complete understanding of the mechanisms responsible for a change in material properties is required - quantification and delineation of the property range is necessary to determine potential applications and functions. In particular, for most polymer

systems, the controllable property is the extent of intermolecular cross-links[1].

Cross-linking endows polymer-based composites with desirable properties such as resistance to solvents and flow, high softening temperatures, and excellent dimensional stability [237]. The classic example of cross-linking technology is the vulcanization of rubber [207], where polymer chains are linked *via* sulfur bridges to form a resilient network [118]. A more recent example is the material Kevlar® - a fibrous polyamide attaining strength from a combination of hydrogen bonding and aromatic stacking [323]. Most cross-linking strategies currently applied to materials employ irreversible chemical cross-links, which results in desired, yet permanent properties. Precise control of irreversible (and energetically expensive) cross-link formation and density has found success in achieving tunable mechanical properties, but lack the reversibility desired by mechanomutable materials. Materials that straddle this broad distinction of tunable and mutable include shape memory polymers and thermo-responsive polymers, which demonstrate reversible mechanical transitions, but are typically limited to discrete behaviors (*i.e.*, two-phase materials) triggered by external stimuli. However, methods of forming reversible physical cross-links are also known. Examples include hydrogen-bonded networks [10, 177, 67] and thermally reversible cross-links [58, 256].

Electrostatic, or ion-pairing, interactions between polyelectrolytes of opposite charge also yield cross-linked structures with reversible physical junctions [163, 59]. The driving force in the formation of these polyelectrolyte complexes is ion pairing between polyelectrolyte segments. Polyelectrolyte complexes are formed at surfaces by a sequential adsorption process involving dilute solutions of a polycation (+) and polyanion (−) and are known to exhibit a unique combination of properties due to their ionically cross-linked nature [255]. As a result there has been much experimental study on the interactions between polyelectrolytes and their respective functional groups [303, 166, 193, 65, 216, 162, 62, 163]. Polylectrolytes undergo a balance of

---

[1]We note that, for weak polyelectrolytes considered herein, cross-linking is dominated by electrostatic, or ionic, interactions. However, other systems, such as PEO films [177] or PVA/graphene oxide papers [67], exploit similar reversible and weak hydrogen bonding (H-bonding), and the arguments presented can be held equivalently for such systems.

electrostatics (as well as hydrogen bonding and other weak interactions) that facilitate the development of novel composites [255, 89]. As a result, a designed composite can take advantage of this trigger to achieve tunable mechanical properties *in situ* by adjusting the external environment [59].

Under an entropically driven regime, the counterions (I^+, I^-) that are lost during complex formation may be reintroduced by exposing the complex to a solution of controlled ion content (*i.e.*, pH). For example [102, 103, 113]:

$$(PE^+PE^-)_c + I^+ + I^- \rightleftharpoons (PE^+I^-)_c + (PE^-I^+)_c \tag{1.1}$$
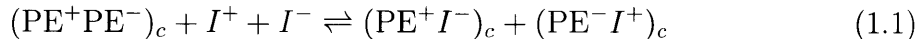
where PE^+ and PE^- are respective positive and negative polyelectrolyte repeat units. The subscript "c" refers to components in the complex phase. When complexes are exposed to ions according to Eq. 1.1, they can potentially break ion-pairing cross-links (note it is possible to decompose the complexations fully at sufficiently high salt concentrations [288]). A polyelectrolyte complex immersed in a solution of salt therefore represents an intriguing and complex system: an amorphous composite, blended at the molecular level (due to the attractive segment/segment interactions), with cross-linking density under *reversible thermodynamic control*. In addition, polyelectrolyte multilayers made from *weak* polyelectrolytes (*e.g.*, large changes in ionization at near-neutral pH) have the advantage that their properties can be tuned by simple pH adjustments. For this reason, the pH of weak polyelectrolyte solutions is an extremely important parameter when assembling higher order structures such as thin films or tubes. Unlike strong polyelectrolytes, which remain charged over the entire pH range, the degree of ionization of weak polyelectrolytes depends greatly on solution pH.

Polyelectrolyte multilayers are typically assembled in a layer-by-layer (LbL) approach, wherein the self-assembly of regular film-like layers is achieved through alternating deposition/adsorption of oppositely charged polyelectrolytes onto a charged solid substrate [88, 87, 89]. Each polyelectrolyte deposition actually overcompensates for the surface charge resulting in a reversal of ionic charge [288], thereby attracting

37
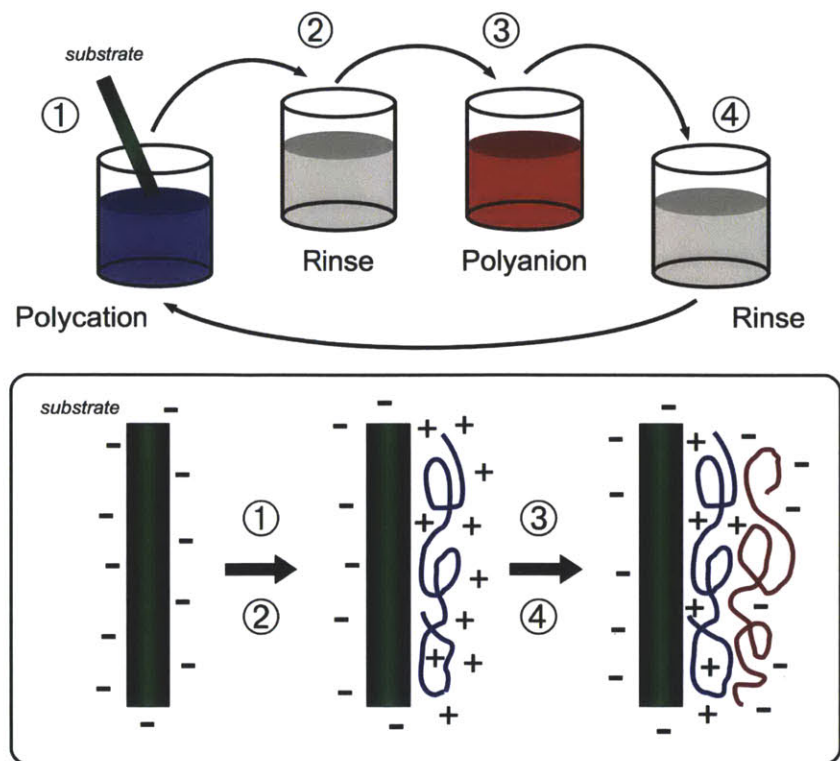
Figure 1-5: Schematic of layer-by-layer assembly by dip-coating. Assembly of regular film-like layers is achieved through alternating deposition/adsorption of oppositely charged polyelectrolytes onto a charged solid substrate [88, 87, 89]. (1) A charged (-) bare substrate is exposed to a polycation (+) solution at pH "n" and the polyelectrolyte is adsorbed. (2) The system is rinsed to remove excess polymer. (3) The new system (+ surface charge) is exposed to a polyanion (-) at pH "m", and the polyelectrolyte is adsorbed. Each polyelectrolyte deposition overcompensates for the surface charge resulting in a reversal of ionic charge [288], thereby attracting the subsequent layer. The process, (1) → (4) is repeated until the desired number of layers is deposited. The resulting film is dense, uniform, and of highly defined stoichiometry (*i.e.*, 1:1 matching of positive and negative polyelectrolyte segments), with very little residual counterion content [289].

the subsequent layer. The process is repeated until the desired number of layers is deposited (see Figure 1-5). The multilayers can be applied using any method that allows the polyelectrolyte solution to come into contact with the substrate, with the most common methods including dip-coating [88], deposition on colloids [98], or spin-coating [60, 249]. The resulting film is dense, uniform, and of highly defined stoichiometry (*i.e.*, 1:1 matching of positive and negative polyelectrolyte segments), with very little residual counterion content [289]. The approach has been the focus of significant interest due to the ease of processing, lack of specialty equipment, variety

of materials which can be incorporated into their assembly, and the versatility of the technique [287].

One of the immediate emerging (and controllable effects) is that the incremental thickness of adsorbed weak polyelectrolyte layers changes greatly with the degree of ionization [350, 303]. It is also well known that pH responsive polymers *geometrically* respond to the changes in the surrounding medium, swelling or collapsing depending on the pH (*e.g.*, ionization) of their environment (see Figure 1-6). This behavior is exhibited due to the presence of certain functional groups in the polymer chain. In general, there are two kinds of pH sensitive materials: one which have acidic group ($-COOH$, $-SO_3H$) and swell in basic pH, and others which have basic groups ($-NH_2$) and swell in acidic pH. Poly(acrylic acid) is an example of the former and chitosan is an example of the latter. The response is triggered due to the presence of ionizable functional groups (like $-COOH$, $-NH_2$) which acquire a charge ($+/-$) in a certain pH. The polymer chains now have many similarly charged groups which causes repulsion and hence the material expands in dimensions. The opposite happens when pH changes and the functional groups lose their charge hence the repulsion is gone and the material collapses back. These thickness differences subsequently affect the bulk and surface characteristics of the film. While the swelling of PEMs by pH control has been known for many decades, the critical missing insight is linking the geometric effects of swelling to mechanical properties. While swelling may be assessed directly by volume changes, very little quantitative work has been reported on the mechanical properties of PEMs as a function of their counterion content (*e.g.*, pH), although trends have been measured. Variation of morphology has stimulated much recent work on the mechanical properties of PEMs, employing experimental probes such as nanoindentation [275, 252], atomic force microscopy [335], and strain-induced elastic buckling [238]. These studies revealed a material with an elastic modulus in the range of 0.001 to 5 GPa [252].

Our intent here is to focus on a single PEM system, and determine the effect of ionization from the primary cause - the full atomistic molecular interactions. Specifically, we exploit the developed system of Rubner *et al.*, a matrix of polyelectrolyte mul-
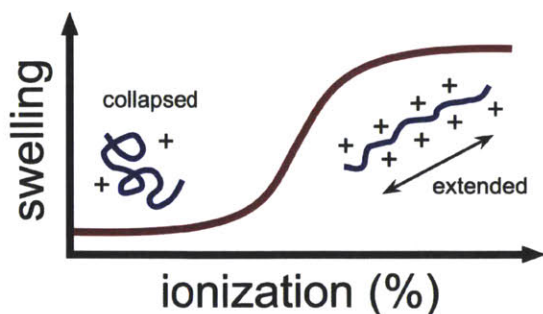
Figure 1-6: A well-known behavior of PEMs is the tunability of layer thickness and controlled swelling as a function of pH [350, 303]. The response is triggered due to the presence of ionizable functional groups which acquire a charge $(+/-)$ in a certain pH. The polymer chains now have many similarly charged groups which causes repulsion and hence the material expands in dimensions. The opposite happens when pH changes and the functional groups lose their charge hence the repulsion is gone and the material collapses back. It is generally inferred that collapsed polymers (with an increase in loops and tails) result in a less dense, more compliant structure, while extended polymers result in a higher cross-linked, compact, and stiff network. The quantification of this effect is one goal of this dissertation.

tilayer films using two model weak polyelectrolytes, poly(allylamine hydrochloride) (PAH) and polyacrylic acid (PAA), depicted in Figure 1-7. Exploiting the protonation and deprotonation in PEMs has successfully been achieved for PAA/PAH systems. The pH-to-ionization relationship of weak polyelectrolyte solutions is extremely important when assembling the films. For example, in isolation, the solution pKa (pH where 50% of polyelectrolyte's repeat units are charged) of PAH is approximately 8.8 [351, 62], and the solution pKa for PAA is approximately 6.5 [254, 62], suggesting an approximate regime of pH-tunability (*e.g.*, about 6.0 to 9.0). We note that the exact pKa's of both PAA and PAH is not constant, can change when incorporated into polyelectrolyte multilayers [62], and is further addressed in subsequent chapters.

Regardless, basic knowledge of pH/ionization can be used to assemble LbL films with a variety of morphologies [303]. Consider three multilayer systems with different pH values, or 6.5/6.5 PAH/PAA, 7.5/3.5 PAH/PAA, and 2.5/2.5 PAH/PAA films (where n/m indicates the PAH was deposited at pH $= n$ and PAA at pH $= m$). In the 6.5/6.5 PAH/PAA system, both polymers are highly charged and form thin layers (< 1 nm); *e.g.* a collapsed film that is tightly electrostatically stitched together with

a. Poly(acrylic acid)
$(C_3H_4O_2)_n$

b. Poly(allylamine hydrochloride)
$(C_3H_7N)_n$
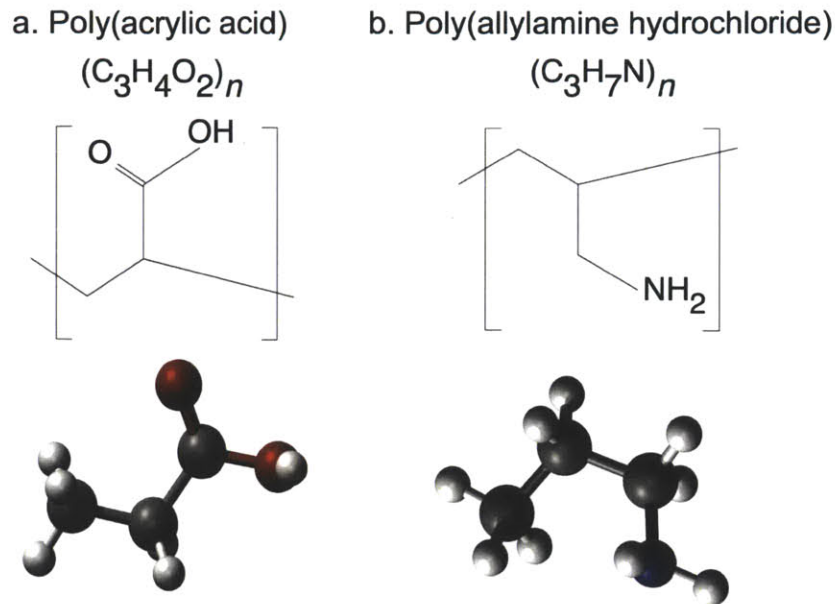
Figure 1-7: Chemical formula, structure, and monomer models for the weak polyelectrolytes, (a) poly(acrylic acid) (PAA) and (b) poly(allylamine hydrochloride) (PAH). To extend polymer chains, hydrogen atoms are removed to allow bonding between adjacent backbone carbon atoms. PAA is a weak polyanion in which charge density increases (COOH $\rightarrow$ COO$^-$) as the solution pH increases. PAH, a weak polycation, decreases in charge density ($NH_3^+ \rightarrow NH_2$) as the solution pH increases.

very few free acid or amine groups. In contrast, the 7.5/3.5 PAH/PAA, each species have less charge, and the resultant films are thick; *e.g.*, swollen with a great deal of polymer loops and tails. However, due the high pH of the PAH solution, the PAA charges up in the next layering step, facilitating PAH adsorption. Finally, the 2.5/2.5 PAH/PAA multilayer contains a thick layer of PAA (low ionization leading to loops and tails) but a smaller amount PAH is attracted to the film surface during assembly, and there is an abundance of free (unmatched) acid groups throughout the film. See Shiratori *et al.* for a complete discussion [303]. Various PAA/PAH multilayers have been implemented in a variety of applications, including to selectively adsorb block copolymers [61], create porous films [215, 151], plate nickel and metal inclusion [340, 338, 339], deliver drugs [29], resist cell adhesion [216], and superhydrophobic surfaces [353]. As an example, Figure 1-8 depicts PAA/PAH multilayers with porosity ranging from the nano to the microscale, assembled to mimic the pore sizes of corneal membranes *in vivo* [137]. The porosity was controlled by controlled exposure to acidic

solutions with low pH, inducing a phase separation resulting from the protonation of carboxylic acid moieties ($COO^- \rightarrow COOH$) in acidic solutions [215, 151].

Being said, while these systems are continuously refined, they are not yet fully understood quantitatively in terms of molecular structures, strength of electrostatic cross-linking, charge distribution, and deformation modes under load. This need not be the case for such a simple system at the molecular level. In other words, while the behavior of PAA/PAH multilayers have been quantified, there is a lack of deterministic models transferable to similar systems (such as PAH/PSS, PDADMA/PSS, PLL/HA systems [218], as examples), which exploit equivalent interactions.

The vast array of potential constituent polymers (*e.g.*, the "library" of available functional groups) allow for application specific mechanical properties or molecular structures [255], requiring a systematic and rational approach to characterization. It is known that weak polyelectrolytes can be manipulated to control complexation that results in a variation of mechanical strength as a function of pH and ionic strength. Indeed, by exploiting a propensity for dissociation, it is possible to tune the adhesion strength of polyelectrolytes - the remaining challenge is to quantify such changes. The resulting composites can utilize this potential mutability for changes in mechanical properties, controlled swelling, porosity, and diffusion applications [294, 59]. For example, in biomaterial applications, polyelectrolyte multilayer films are being implemented in attempts to actively control the surface properties of biomaterial scaffolds utilized for cell adhesion/proliferation and tissue engineering [133], as well as to direct key cellular processes [38], a possible route to counter the variation in cellular needs (the so-called "shaky" foundations of tissue engineering; see Cranford and Buehler [80]).

In effect, PEMs offer a highly complex system wherein even the most fundamental interactions - the complexation and coupled nanomechanical behavior of a single polyanion and polycation - remain unknown and unpredictive. It is proposed that the resulting mechanical properties of an electrostatically cross-linked polyelectrolyte complex are amplified beyond the simple summation of the constituent polymers, due to cooperativity at the molecular scale. Here, we attempt to characterize the
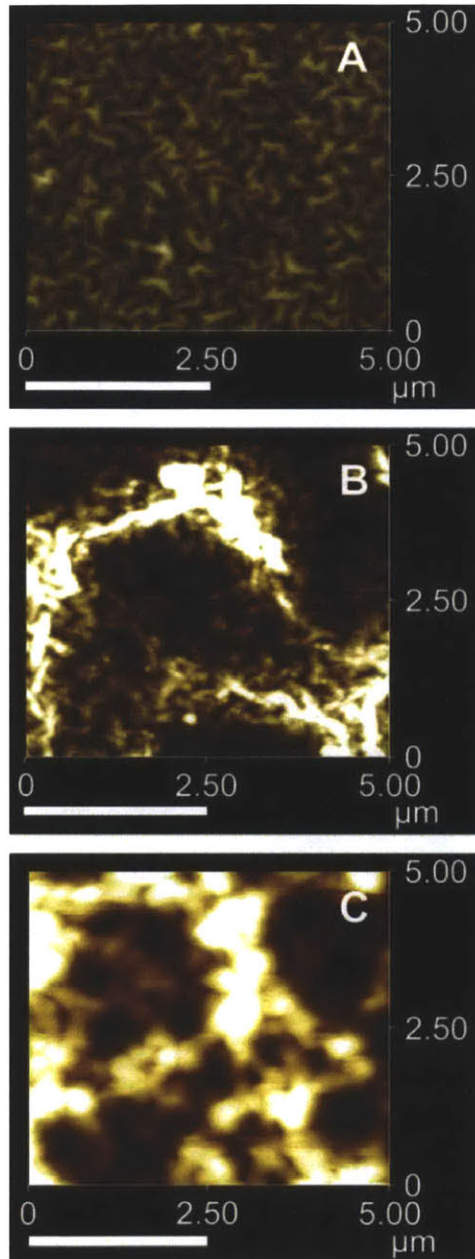
Figure 1-8: PAA/PAH polyelectrolyte multilayers with tunable porosity ranging from the nano to the microscale, assembled to mimic the pore sizes of corneal membranes *in vivo*. AFM images depict **A**. Non-porous, **B**. Nanoporous, and **C**. Sub-micron PEM substrates. The porosity was controlled *via* exposure to acidic solutions (pH ranged from 2.0 to 2.3), inducing a pH-controlled phase separation, resulting from the protonation of carboxylic acid moieties ($COO^- \rightarrow COOH$) in acidic solutions [215, 151]. In this study, a purely physical feature, specifically, porosity, provided cues to human corneal epithelial cells. While all porous surfaces supported corneal cell adhesion, nanoscale porosity significantly enhanced cellular response. The mechanical properties were not characterized. From Hajicharalambous *et al.* [137], *Biomaterials*, 2009, used with permission, copyright © 2009 Elsevier Ltd.

properties of this fundamental "building block" to serve as a cornerstone for larger-scale performance. Advances in material synthesis, combined with robust theoretical techniques in material modeling and simulation at the nanoscale, facilitate a new paradigm of material design. Multi-scale modeling and simulation approaches can play an important role in the bottom-up design of purpose-specific materials from the atomistic to the continuum levels by elucidating both structure-property relations at all levels of hierarchy and integrating the effects of cross-scale interactions from nano to macro [46, 45, 71], making polyelectrolytes and their associated composites ideal candidates for materiomic investigation.

1.4   Outline

The scope of this thesis is the prediction of the nanomechanical properties of coupled polyelectrolytes, focusing on the final application in multilayer systems. While the manipulation of electrostatic cross-linking has been exploited at the micro- and macroscopic scales, no systematic study has focused on delineating the mechanical properties of the simplest molecular construct (or building block) with full atomistic precision and fidelity. Addressing this issue by laying out a theoretical and computational framework for studying polyelectrolyte interaction is the fundamental goal of this thesis. While the studies herein involve two specific polyelectrolytes - namely PAA and PAH - the analytical methods employed can be equally applied to variegated molecule types (*e.g.*, PAH/PSS, PDADMA/PSS, PLL/HA systems) under variegated interactions (*e.g.*, H-bonding, electrostatic, π-stacking, etc.). Being said, the atomistic precision afforded by full atomistic approaches requires the focus on a particular chemical structure, acting as a quantitative and definitive case study for similar complex systems. The results presented in this thesis are based entirely on computational and theoretical approaches, and all findings are extensively compared with experimental data available to provide validation and support to the hypotheses presented in this work. The content is arranged as follows:

Chapter 2: Computational Methods Outlines full atomistic molecular dynam-

ics (MD) and coarse-graining methods used for studying complex hierarchical materials, focusing mostly on the approaches used and uniquely developed in this thesis. Full atomistic approaches include a description of the CVFF potential implemented for the polyelectrolytes, technical issues regarding solvation and ionization, as well as a developed method for unbiased statistical sampling (temperature assisted sampling).

Chapter 3: Variation of Molecular Rigidity Prior to the investigation of a polyelectrolyte complex, focus is given to the behavior of single molecules. This chapter investigates and quantifies (both computationally and theoretically) the variation in molecular rigidity of PAA and PAH as a function of ionization. Simple mechanical and energetic arguments are presented to separate the polymer contour length from an abstract "electrostatic contour" that is able to capture the effect of electrostatic persistence at small length scales *ex post*. Variation of rigidity with ionization is determined, to be used in the elastic complexation model.

Chapter 4: Rate Dependence and Ionization Effects on Adhesion Reports an atomistic-level MD study, used to investigate the tunable adhesion properties of a polyelectrolyte complex to elucidate the complexation and electrostatic cross-linking. To accommodate a link between experimental and simulation results, a rate dependence investigation of the adhesion strength is undertaken to reconcile the time-scale limitations of atomistic simulations.

Chapter 5: Critical Ionization to Couple Polyelectrolytes Using the properties obtained from full atomistic studies of previous chapters, a general elastic model is developed to capture the cooperative deformation of cross-linked polyelectrolytes. Representative behavior (and effective rigidity) is extracted from the classical eigenvalue problem of vibrational mode superposition, wherein the induced flexural modes can be compared to isolated polymers. A critical range of ionization in which cooperative deformation is preferred is used to define mechanical complexation, and the associated cross-link density is related to the

persistence length of the constituent polymers.

Chapter 6: Beyond Full Atomistic Characterization To illustrate control of material systems beyond the atomistic scale, as well as the emerging effects of molecular phenomena (such as complexation), a coarse-grain investigation is undertaken to investigate microscale arrays of vertically aligned PEM tubes. Here, rather than ionization and complexation, change in pH results in variation in stiffness and volume (*e.g.*, swelling). Effective mechanistic response (*e.g.*, lateral resistance) is shown to be controlled *via* small scale molecular behavior (*e.g.*, intrinsic response) and large scale geometric design (*e.g.*, extrinsic control).

Chapter 7: Conclusion Provides a summary of previous chapters, caveats and self-criticism of the approaches implemented, and an outlook for anticipated applications of PEM based systems.

Developed nanoscale components, once attained, must demonstrate the reproducibility needed to build functional materials and systems, and do so at a size and complexity difficult to achieve by traditional top-down approaches. Complementary multi-scale theoretical approaches can lead to the bottom-up design of purpose-specific materials from the atomistic to the continuum levels. The keystone to the bottom-up design of nanomaterials - demonstrated throughout this dissertation - is a synergistic multiscale theoretical foundation from atomistic scales to the mesoscale to macroscale continuum-level constitutive modeling.

Chapter 2

Computational Methods

While the toolset for materials exploration is vast, the use of computation and simulation has recently emerged as a critical and necessary counterpart to empirical measures. In this chapter, a brief review of the methods used in analyzing the nanomechanics of polymers is provided, both full atomistic and coarse-grain. Along with theoretical methods, atomistic and molecular simulation approaches are reviewed, focusing on molecular dynamics (MD) simulation, atomistic force fields, treatment of pH and ionization, and enhanced sampling techniques. Focus is given to the novel methods developed for full atomistic investigation of charged polyelectrolytes. Mesoscale coarse-grain methods are presented, focusing on developed methods implemented in subsequent chapters.

2.1   Full Atomistic Molecular Dynamics

This section overviews atomistic and molecular modeling approaches used in this thesis. Particular emphasis is given to molecular dynamics (MD) method and its variants. Molecular dynamics is a tool for elucidating motion (*i.e.*, trajectories) of atoms and molecules at the nanoscale. The MD method is capable of describing atomistic mechanisms that control many physical phenomena, in particular those related to the mechanics of materials.

As discussed in **Chapter 1: Introduction and Background**, a cursory inven-

tory of polymer materials (or, more specifically, polyelectrolytes) uncovers the basic building block at the atomistic scale, the specific functional groups. It is through these components and at this scale that polymers are differentiated - the carboxyl groups ($-COOH$) of PAA, the amine groups ($-NH_2$) of PAH. This is one of the reasons we can root computation and simulation at the atomistic scale, and by-pass fundamental quantum-level approaches. Moreover, we wish to focus on the scale at which the mechanics of the macroscale system arises (*e.g.*, the deterministic basis of the (potential) variable properties of PEMs). Monomers and short polymer chains do not exhibit extraordinary behavior in isolation, but only through molecular complexation at the scale of thousands of atoms. As such, a powerful tool in the investigation of any polyelectrolyte is MD. While continual computational advances have made MD approaches more accessible (and powerful) than ever before, the theoretical foundations can be traced to the mid-20th century. While full atomistic Monte Carlo methods can be attributed slightly earlier to the work of Metropolis, Ulam, Teller and co-workers [222, 221], the MD method was first introduced by Alder and Wainwright in the late 1950's [5, 6, 7] to study the interactions of hard spheres (*i.e.*, hypothetical and ideal "atoms"). Even with such an "engineering approximation", many important insights concerning the behavior of simple liquids emerged from their studies. In 1964 the first MD simulations using a realistic potential for liquid argon [267] were undertaken, followed shortly by simulation of liquid water in 1971 [268]. The first polymer simulations - with a focus on macromolecular instead of bulk atomistic behavior - appeared in 1970's [64, 192, 127, 212].

Molecular dynamics has evolved as a suitable method for elucidating the atomistic mechanisms that control deformation at the nanoscale, and for relating this information to macroscopic material properties. Mechanistic behavior, function, and failure are directly linked to distinct atomistic mechanics and require atomistic and molecular level modeling as an indispensable tool for studying complex materials. Unlike a bulk metal (such as gold, for example), knowledge of a specific functional group that defines a specific polymer (such as polyethylene or polyvinyl alcohol, for example) begets new responsibility (nay, liability) on the researcher to both understand each

group interaction, and the resulting affect on structural and system-level behavior. Other methods commonly associated with polymers - such as idealized statistical chains - can delineate behaviors qualitatively, but lack the precision and specificity necessary to quantify mechanical phenomena.

The sole objective of MD techniques is to accurately simulate the motion of a group of atoms, generally representing the fraction of a larger system, to observe a critical phenomenon of interest, and/or to get an estimate of the global system properties. This is similar to *statistical mechanics*, wherein the microscopic properties of individual atoms and molecules are related to the macroscopic bulk properties of a system *via* thermodynamic metrics. Rather than dealing with statistical ensembles, MD considers the evolution of a system over time, and the results of MD simulations may be used to determine macroscopic thermodynamic properties of the system.

The basic computational instrument behind MD is to calculate the dynamical trajectory (the spatial movement over time) of each atom in the material using atomic interaction potentials that describe attractive and repulsive forces in between pairs or larger groups of atoms. Thereby, the complex 3D structure of an atom (composed of electrons and a core of neutrons and protons) is approximated by a point particle (or point mass). The interaction potentials are generally based on a mix of empirical data and first-principles (or *ab initio*) based information such as quantum mechanics calculations (see Figure 2-1(a)). Solving each atom's equation of motion according to Newton's Law $F = ma$, enables the calculation of positions $\bar{r}_i(t)$, velocities $\bar{v}_i(t)$, and accelerations $\bar{a}_i(t)$ at each step in time, leading to atom trajectories that can reveal overall dynamics of the system as well as properties such as viscosity, bulk modulus, or fracture toughness. It can be considered an alternative approach to methods like Monte Carlo (repeated random sampling of atomistic systems), with the difference that MD actually provides full dynamical information (*i.e.*, material behavior "timelines") and deterministic trajectories[1].

Formally, the total energy of the system can be written as the sum of kinetic

---

[1]It should be emphasized that Monte Carlo schemes provide certain advantages, such as the nonrequirement of physical timesteps; however, such approaches will not be discussed further as all simulation studies presented here are carried out with a MD methodology.
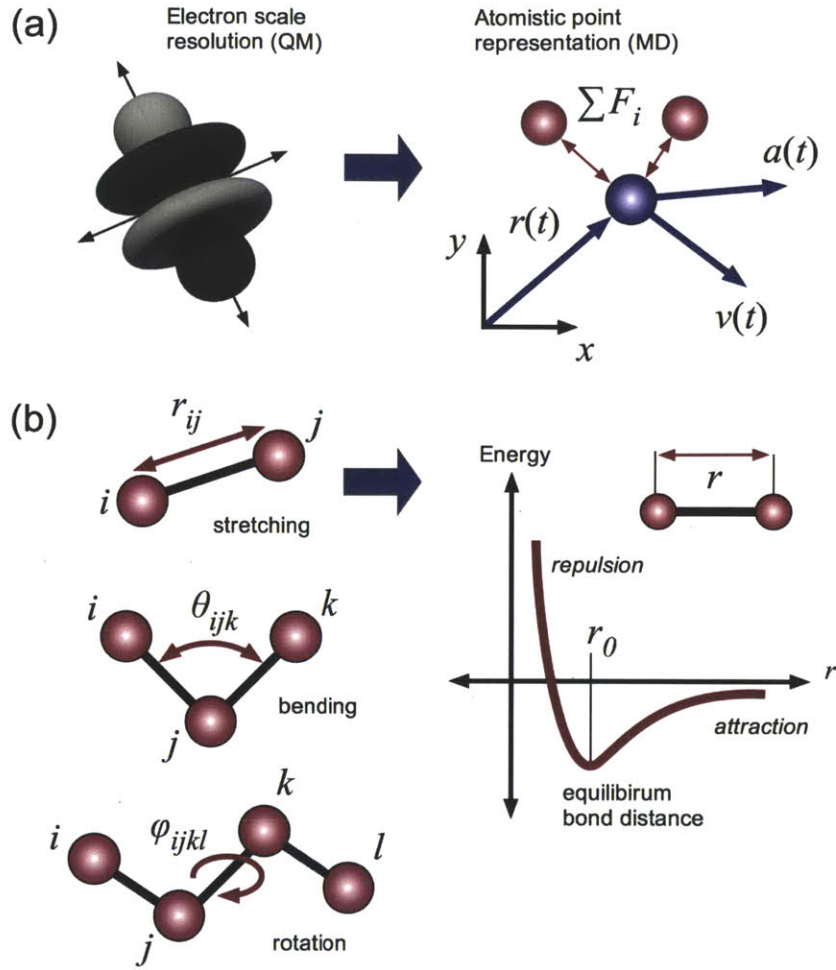
Figure 2-1: Basic approach of the molecular dynamics (MD) simulation method. (a) Atomistic structure (neutrons, electrons, and protons) replaced by a point representation in the MD approach. (b) Illustration of the energy decomposition in classical MD force fields, along with a representation of a simple potential function between pairs of atoms.

energy (K) and potential energy (U):

$$E = K + U \tag{2.1}$$

where the kinetic energy is given by

$$K = \frac{1}{2} \sum_{j=1}^{N} m_j \bar{v}_j^2 \tag{2.2}$$

and the potential energy is an effective function of the atomic coordinates, $\bar{r}_i(t)$, such

that:

$$U = \sum_{j=1}^{N} U_j(\overline{r}_j) \qquad (2.3)$$

with a properly defined potential energy surface, $U(\overline{r})$. Here, we emphasize the *effective* potential energy as a function of coordinates (or position), because more sophisticated atomistic force fields take into account not only position, but also environmental effects (such as atomic neighbors and local charge). In general, the potential, U can be formulated as a function of multiple geometric constraints (summed for each atom), including bond stretching, $U(r_{ij})$, bending, $U(\theta_{ijk})$, and rotation or torsion, $U(\phi_{ijkl})$ (See Figure 2-1(b)). Regardless of form, the forces are obtained from the potential energy surface (sometimes also called force field or potential) as $\overline{F} = -\nabla_{\overline{r}_j} U(\overline{r}_j)$. Simplification of atomic interactions by a closed-form potential significantly increases the computational efficiency of MD simulation. Thus, through Newton's Second Law, MD is reduced:

$$\overline{F}_j = m_j \frac{d^2 \overline{r}_j}{dt^2} = -\nabla_{\overline{r}_j} U(\overline{r}_j) \qquad (2.4)$$

For $j = 1 \ldots N$. The numerical problem to be solved is thus a system of coupled second-order nonlinear differential equations that can only be solved numerically given more than two particles (*i.e.*, the classical n-body problem). Thus, the basic idea behind atomistic simulation using MD is to compute the dynamical trajectory of each atom in the material, by considering their atomic interaction potentials, by solving each atom's equation of motion according to $\overline{F} = m\overline{a}$, or, more specifically in vector quantities $a_i = F_i/m$, for $i = 1, 2, 3$. The numerical integration of Newton's law by considering proper interatomic potentials to obtain interatomic forces enables one to simulate a large ensemble of atoms that represents a larger material volume, albeit typically limited to several nanoseconds of time scale. Typically, MD is based on updating schemes that yield new positions from the old positions, velocities, and the current accelerations of particles, as well as any imposed boundary conditions, forces, of constrains. For instance, in the commonly used Verlet scheme, this can be

51

mathematically formulated as:

$$r_i \left(t_0 + \Delta t \right) = -r_i \left(t_0 - \Delta t \right) + 2r_i \left(t_0 \right) \Delta t + a_i \left(t_0 \right) \left(\Delta t \right)^2 + O \left(\Delta t^4 \right) \qquad (2.5)$$

This technique - the time integration of particle positions based on applied potentials - cannot only be used for particles that are atoms, it can also be applied for particles that represent groups of atoms, such as in molecules or in coarse-grain models. Various fast numerical integration schemes are employed to solve the equations of motion and simulate a large ensemble of atoms representing a larger material volume; however, in particular for all-atom simulations, high-frequency vibrations of light atoms (such as hydrogen atoms) requires a time step in the order of femtoseconds (10^{-15} seconds) for accurate and numerically stable calculations. This limits the application of full-atomistic MD methods to nanometer size systems, at submicrosecond time scales.

Unlike many continuum mechanics approaches, atomistic techniques require no *a priori* assumption on the defect dynamics or elastic properties, such as isotropy, for example. Once the atomic interactions are chosen, the complete material behavior is determined. Further discussion of the advantages and disadvantages of molecular simulation can be found in Cranford and Buehler [71]. The availability of interatomic potentials for a specific material (based on the characteristic type of chemical bonding) is often a limiting factor for the applicability of the MD method. Provided interatomic potentials are available, MD is capable of directly simulating a variety of very complex physical phenomena, including self-assembly of polymers, diffusion, fracture, as well as protein folding, unfolding and aggregation. For polymers, a commonly used potential is the *consistent valence force field,* or CVFF [68].

2.1.1 Consistent Valence Force Field

To model polymers we utilize the CVFF, originally parameterized for peptide and protein structures, and also applicable to polymers in similar, aqueous environments [31]. This all-atom potential is considered to be highly accurate and an increasingly computationally efficient way of studying dynamics of macromolecules. Parameters

for CVFF were obtained from *ab initio* quantum calculations with additional optimization based on available experimental data. The CVFF force field belongs to a class of models with similar descriptions of the interatomic forces; other models include the CHARMM force field [200, 201], DREIDING force field [210], UFF [270] or the AMBER [253, 340] models.

Such classical - or *nonreactive* - force fields are based on bonded terms which are modeled with harmonic springs (or variations thereof), and therefore can't be modified or broken once defined by the connectivity input obtain from the topology of the molecule. Further, atom charges are fixed and cannot change during simulation. These simplifications improve the simulation speed drastically and are not a major issue for most simulations studying polymers under ambient physiological conditions. On the other hand, simulations in extreme conditions such as mechanical perturbations (*e.g.*, molecular fracture or chemical reactivity) or harsh chemical environments require reactive force fields that can take into account changes in fixed charges of the molecules, formation and breaking of bonds, as well as variations in bond order (for example, ReaxFF or AIREBO potentials). While such *reactive* force fields show promise for capturing intricate chemical details of materials at extreme conditions [51], they are also more expensive computationally, and are excessive for the current application.

While various software packages can be used implemented MD algorithms and potentials, here we use the open-source code LAMMPS [257] (**L**arge-scale **A**tomic/**M**olecular **M**assively **P**arallel **S**imulator[2]) which can carry out computations using CVFF (among other force fields). The main aspects of the CVFF force field and its implementation in LAMMPS will be discussed here.

The CVFF potential includes bonding and non-bonding (interaction) terms to describe short and long-range forces between particles. It is assumed that, even highly charged, the inter-polymer interactions are significantly weaker then the covalent bonds between monomers, thus maintaining small deformation of covalent bonds. The total empirical energy function of the polymers is represented as a sum of valence

---

[2]http://lammps.sandia.gov/

53

(*i.e.*, bond, angle, dihedral, and improper), and non-bonded (*i.e.*, van der Waals, Coulombic) interactions, or:

$$E = \sum_{bonds} E_b + \sum_{angles} E_\theta + \sum_{dihedrals} E_\phi + \sum_{impropers} E_\omega + \sum_{pairs} E_{vdW} + \sum_{ions} E_q \qquad (2.6)$$

Covalent interactions (nonreactive throughout the simulation) are represented by a harmonic potentials, wherein the force-displacement (or, equivalently, the stress-strain or *stretching*) relationship is *linear*, or:

$$E_b\left(r\right) = \frac{1}{2}k_b\left(r - r_0\right)^2 \qquad (2.7)$$

where k_b is the force constant, and r_0 the equilibrium bond distance assigned for each bond type. For example, a single carbon-carbon bond (*e.g.*, the carbon backbone of PAA, for example) has $k_b = 645.4$ kcal/mol/Å and $r_0 = 1.526$ Å. Molecular angles require the a triplet of atoms, defined by θ_{ijk}. Again, within the elastic (or small strain) regime, a harmonic potential is sufficient to represent the rotational stiffness (or, equivalently, the *bending* rigidity), or:

$$E_\theta\left(\theta\right) = \frac{1}{2}k_\theta\left(\theta - \theta_0\right)^2 \qquad (2.8)$$

where k_θ is again the rotational force constant, and θ_0 the equilibrium angle for each angle type. For example, the angle formed by carbon backbone of PAA is defined by the constant $k_\theta = 93.2$ kcal/mol/rad and an equilibrium angle of $\theta_{CCC} = \theta_0 = 110.5°$.

We note that if four atoms are joined by consecutive bonds and defined by consecutive angles, then rotation about the central bond is possible since it maintains all equilibrium states. The ability of an atom to rotate this way relative to the atoms which it joins is known as an adjustment of the torsional angle. However, if the two atoms have other atoms or groups attached to them then configurations which vary in torsional angle exhibit stable conformations. Dihedral angles - defined by the angle between two planes of atoms - can be considered a torsional stiffness, limiting the

rotation of the NH_3 functional group about the backbone, for example. Typically neglected in generalized bead-spring representations, the dihedral term plays a crucial role in local structure and steric effects of finite functional groups (*e.g.*, without a dihedral constraint, the side chains are free to rotate about the carbon backbone). Considered harmonic (for small perturbations), the dihedral potential is defined as:

$$E_\phi\left(\phi\right) = k_\phi\left[1 + d\cos\left(n\phi\right)\right] \tag{2.9}$$

where the dihedral angle, ϕ, is defined by the two planes of four atoms, ϕ_{ijkl}. Again, k_ϕ denotes the relative torsional stiffness (in kcal/mol, for example), and d and n define relative stable configurations. Note that n defines the periodicity of stable rotations, and thus, unlike bond and angle potentials, the dihedral term introduces multiple possible equilibrium states.

The final valence term accounts for so-called improper interactions between quadruplets of atoms - used to assert the correct geometry or chirality of atoms. Whereas the four atoms in a dihedral are typically linear (and thus defining a torsional relation), the bonded terms involved in an improper share a common atom, angularly constrained to a defined plane. Similar to the dihedral term, the improper potential is defined as:

$$E_\omega\left(\omega\right) = k_\omega\left[1 - d\cos\left(n\omega\right)\right] \tag{2.10}$$

where the improper angle, ω, is defined by the two planes of four atoms, ω_{ijkl}, k_ω denotes the relative stiffness, and d and n define stable configurations.

Nonvalence (*e.g.*, nonbonded) interactions differ from valance, as there is no assigned configuration (*e.g.*, topology of what atom is bonded to what atom). Instead, nonvalance interactions take into account the local neighbors of each atom, and are pairwise (*e.g.*, a function of interatomic spacing, r_{ij}, between two atoms) within the CVFF formulation (reactive potentials, such as ReaxFF, consider multiple atoms simultaneously). In CVFF, the nonvalence are separated into a traditional Lennard-Jones (LJ) interaction (encompassing van der Waals interactions and hydro-

gen bonding) as well as electrostatic interactions. The Lennard-Jones 12:6 potential is expressed as:

$$E_{vdW}(r) = 4\varepsilon \left[\left(\frac{\sigma}{r} \right)^{12} - \left(\frac{\sigma}{r} \right)^{6} \right] \tag{2.11}$$

where ε is the depth of the potential well, σ defines the finite distance at which the inter-particle potential is zero, where $\sigma = r_0/\sqrt[6]{2}$, and r is the distance between the particles. Repulsion at small separations between atoms is associated with the Pauli exclusion principle, while weak attraction at larger distances is due to London dispersion interactions. The important feature of E_{vdW} is its fast decay as $r \to \infty$ (due to the r^{-6} term). For this reason LJ interactions are considered short-ranged, and a cutoff implemented to reduce the computational cost of pairwise interactions. The pair potential parameters for the van der Waals interactions between different atom types (e.g., types "a" and "b") are mixed according to geometric mean and arithmetic mean for the energy and distance terms respectively (i.e., Lorentz-Berthelot mixing rules), where $\sigma_{ab} = (1/2)(\sigma_a + \sigma_b)$ and $\varepsilon_{ab} = \sqrt{\varepsilon_a \varepsilon_b}$.

Finally we consider the electrostatic interactions between electrostatically charged atoms. The Coulomb potential describes the interactions between pairs of partial charges. Its functional form is:

$$E_q(r) = \frac{Cq_iq_j}{\bar{\epsilon}} \frac{1}{r} \tag{2.12}$$

where C is an energy-conversion constant, q_i and q_j are the charges on the two atoms, and $\bar{\epsilon}$ is the solution-dependent constant (e.g., dielectric permittivity). Due to the importance of this interaction to the behavior of polyelectrolytes, it is further discussed in following sections. We note here that because E_q decays according to $1/r$, the electrostatic interactions are considered as long-ranged. As the effects of electrostatics can reach beyond the periodic boundaries of simulation arrangements, a long-range electrostatic solver, such as Ewald or particle-particle particle-mesh (PPPM) [198], is typically implemented to homogenize the effect of periodic images of a charged system. Unless otherwise noted, the PPPM method has been implemented for all
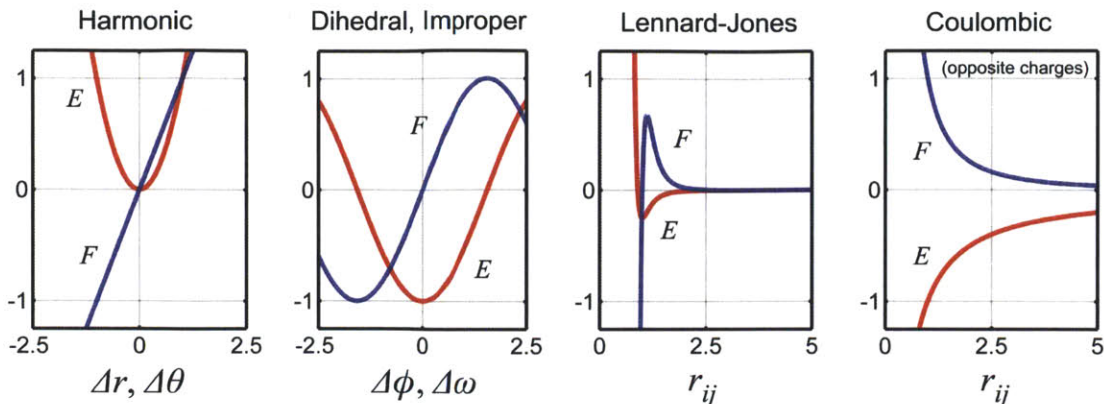
Figure 2-2: Functional form of CVFF potentials (E) and forces (F), representing linear bond (harmonic potential; $f(\Delta r)$) and angular (harmonic potential; $f(\Delta\theta)$) interactions, periodic functions for dihedrals ($f(\Delta\phi)$) and impropers ($f(\Delta\omega)$), a classical Lennard-Jones 12:6 function for pairwise interactions (*e.g.*, van der Waals; $f(r_{ij})$), and a Coulombic potential for electrostatic interactions (here, attractive for opposite charges; $f(r_{jj})$). All functions are plotted according to Equations 2.7, 2.8, 2.9, 2.10, 2.11, and 2.12 with all constants set to unity.

simulations. Finally, we note that in CVFF no additional terms are used for hydrogen bonds (similar to CHARMM potential [200, 201]), as the nonvalence parameters were verified to be adequate for describing polymer, solvent and interface hydrogen bonding. The functional forms of the described CVFF potentials (and corresponding force relationships) are depicted in Figure 2-2.

2.1.2 Explicit Solvent

One of the primary differences between full atomistic polymer simulation and generalized models is the treatment of solvation, critical to polyelectrolyte interaction. In all-atom force fields, water molecules (*i.e.*, bonded H_2O) are generally also treated explicitly. Parameters of the force field generally are specified considering a specific water model (such as the TIP3P dimer model for CHARMM [200, 201]).

Historically, there has been two main directions of thought in modeling solvent in polymers. We note that most of the comparative work has considered polypeptide protein systems [169, 260]. Most molecular simulations have either an *explicit* or *implicit* treatment of solvent around the molecules, as performing simulations in vacuum

generally leads to inaccurate results, since the molecular friction, hydrophobic effects and dielectric screening properties of the solvent are not captured. It is also noted that sufficient solvation serves to homogenize ensemble properties such as temperature (*e.g.*, damping) providing a sufficient number of molecules for statistical distribution. In the explicit solvent approach, each water molecule is treated individually in the simulation, and all molecular forces and solvent dynamics are computed on each of these molecules as they are done on the polymer. As a result of including most of the details of water in the simulation, explicit solvent approaches are considered to be the most truthful to experimental data. In the implicit solvent approach, the combined effect of water with respect to the conformation of the molecule is assumed. Instead of extensive dynamics calculations on the solute, these models carry out theoretical calculations on the behavior of solvent around the solute as a continuum (*e.g.*, distributed charge and effective dielectric screening), and compute forces and energies accordingly. Viscosity of water molecules can be approximated by using Langevin dynamics with a friction coefficient, for example. Implicit models attempt to reduce the effect of water molecules to a few parameters[3].

Several molecular models have been developed for explicit water. Most approaches take the molecule as rigid, and consider only non-bonded interactions such as electrostatics (Coulomb's law), dispersion and repulsion forces, typically described with a 12:6 Lennard-Jones potential (see Equation 2.11). Three-site models such as SPC and TIP3P, with interactions on the two H and O atoms of the molecule, are the most commonly used approaches. Models such as TIP3P have been implemented with small modifications for their use with empirical force fields such as CVFF [68]. Higher accuracy models, based on a larger number of interactions sites (*e.g.*, TIP4P, TIP5P) have also been proposed [170, 202]. The explicit solvent model implemented in this thesis is the TIP3P model, 3-site rigid water molecule with partial charges and Lennard-Jones parameters assigned to each of the 3 atoms, harmonic bonding (O-H) and bending rigidity (H-O-H), with CVFF potentials described as per the previous

---

[3]For more information on mathematical basis and details of different implicit solvent models, see comprehensive reviews in this field [279, 322, 56, 57].

section [200].

Despite the increase in accuracy, explicit treatment of water brings significant computational challenge. Explicit treatment of water is a severe obstacle against scaling up full atomistic simulations, since a large water box needs to be used to keep the desired molecule within a periodic boundary - especially when the conformations of the molecule (such as a flexible polyelectrolyte) are unknown and extremely variable. In many cases, majority of the computational effort goes into simulating motion of the solvent - for example, the simulations described in the subsequent chapter consist of approximately 500 polyelectrolyte atoms, compared to approximately 10,000 water atoms (a ratio of 20-to-1). In addition, to the shear number of atoms required, the use of explicit water (by design) increases the number of atomistic neighbors for each molecule, further handicapping computational efficiency.

While undoubtedly, at this time, implicit methods are necessary to investigate large polyelectrolyte systems (*e.g.*, chains with hundreds of monomers extending hundreds of nanometers in extension), the atomistic investigations described herein rely on explicit solvation for two reasons. Primarily, there are few (if any) full atomistic studies of such polyelectrolyte systems, and thus the work herein can be considered a basis of future implicit works. Secondly, implicit methods homogenize the effect of electrostatics *a posteriori*, commonly through mean-field approximations determined by the Poisson-Boltzmann equation [107, 106]. Although ingenious efforts have been made to allow for local effects (*e.g.*, variation of the electrostatic free energy with respect to the location change of solute-solvent interfaces and point charges [56]), assumptions are still made regarding system behavior. As electrostatic interaction between charged particles gives rise to one of the strongest intermolecular forces that determine the structure and dynamics of an underlying molecular system, and is the driving mechanism of the polyelectrolyte system under investigation, further discussion of the modeled electrostatics is warranted.

2.1.3 Electrostatic Interactions

Atomistic electrostatic interactions are determined *via* the well-known Coulomb's law, as described by Equation 2.12. Like a harmonic potential, this is a simplified representation of a more complex interaction. The classical inverse-square relation for electrostatic force is extended by the introduction of the dielectric constant, $\bar{\epsilon}$, where:

$$\bar{\epsilon} = 4\pi\epsilon_0\epsilon_r \tag{2.13}$$

where ϵ_0 describes the permittivity of a vacuum and ϵ_r is the relative permittivity of the medium, accounting for the permittivity of the solution (*e.g.*, the dielectric constant of water is $\simeq 80$). In terms of electrostatic interactions in solution, Equation 2.12 is commonly referred to as the Debye−Hückel potential. This formulation, however, is only sufficient for two point charges in isolation - complicating the theoretical treatment of fluids is the damping or *screening* effect of additional (surrounding) local charges. As each atom of the system consists of at least a partial charge, this screening is critical to assumptions about system behavior[4].

The effective screening of electrostatic interactions due to polar/charged solvent (such as water) requires that E_q decays faster than r^{-1}. To account for the effect of screening, an exponential decay term is introduced to the Debye−Hückel potential. Polyelectrolyte theory [146] uses the Debye-Hückel screening radius κ^{-1} as the measure of effective screening length. It is defined as the distance by which the action of an electric field of a separate charge placed in the medium containing other charges is spread, where:

$$\kappa^{-1} = (8\pi l_B \mu)^{-1/2} \tag{2.14}$$

where $l_B = e^2/(4\pi e_0\bar{\epsilon}k_B T)$ defines the *Bjerrum length* characterizing the screening

---

[4]Screening, however, is a necessary phenomena. Consider the fact that the Coulomb *force* diminishes with r^{-2}, but the average number of particles at each distance r is proportional to r^2, assuming a fluid is fairly isotropic. As a result, a charge fluctuation at any one point has non-negligible effects at large distances. In reality, these long-range effects are suppressed by the electrostatic screening.

$$Q(r) = \frac{q^2}{\epsilon r}\left[e^{-\kappa r}\right]$$
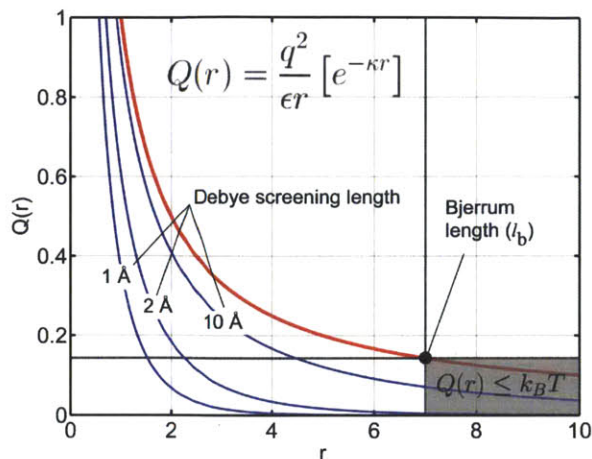
Figure 2-3: Plot of the Debye–Hückel interaction (as described by Equation 2.15; here denoted $Q(r)$) for various screening lengths, κ^{-1}. Also indicated is the *Bjerrum length*, at which the thermal kinetic energy, $k_B T$, is equivalent to the electrostatic interaction.

action of the solvent (e is the elementary charge, e_0 is the electrical energy constant, $\bar{\epsilon}$ is the dielectric permittivity of the medium, k_B is the Boltzmann constant and T the temperature), and $\mu = (1/2)\sum n_i Z_i^2$ is the ionic strength of solution, n_i is the number of ith ions per unit volume, and Z_i is the charge of the ith ion (in e units). The screening length is then introduced the typical formulation of the charge-charge interaction for a screened Coulombic potential energy:

$$E_q(r_{ij}) = \frac{C q_i q_j}{\bar{\epsilon}}\frac{e^{-\kappa r_{ij}}}{r_{ij}} \tag{2.15}$$

Where again, r_{ij} is a measure of absolute distance from the charge q_i form charge q_j. This relation is commonly referred to as the *screened* Debye-Hückel potential. The effect of varying screening length is depicted in Figure 2-3.

Being said, if solvent is treated explicitly in simulations (as it is here), the dielectric properties of the medium is taken into account automatically by explicitly computing all electrostatic interactions (*e.g.*, the pairwise interactions of the H_2O molecules), and Equation 2.12 is sufficient to capture electrostatic interactions. The need for κ-dependence arises for implicit solvent models or the analytical treatment of the electrostatic charges. Thus, when we refer to the electrostatic potential for CVFF, we rely on equation 2.12, whereas analytical treatment of the electrostatic interactions

(used for derivations in **Chapter 3** and **Chapter 5**) considers Equation 2.15.

Despite the numerous approximations inherent in the Debye-Hückel potential (see [26], for example), it has been successful in the modeling of polyelectrolytes, capturing the essential physics to first order, specifically screened electrostatic interactions between polyelectrolyte charge groups, while being relatively simple in form (few parameters) and computational implementation. The screening length, κ^{-1}, for example, can be calculated *via* known simulation volume, charged monomers, and number of counterions. Alternative electrostatic energy models include the Generalized-Born model or tabulated solutions to the continuum Poisson-Boltzmann equation for pairwise interacting monomers [311, 285, 266]. Such methods are considerably more complex and computationally expensive than the potential given in Equation 2.15, however, and are not warranted for the current atomistic investigations.

2.1.4 Ionization and pH

Unlike strong polyelectrolytes, which remain charged over the entire pH range, the degree of ionization of weak polyelectrolytes depends greatly on solution pH. Indeed, while several solution processing variables play important roles in molecular organization for strong (pH-independent) polyelectrolyte systems [102, 49], pH becomes a key factor in the case of weak polyelectrolytes such as PAA and PAH. As discussed in **Chapter 1**, in the LbL assembly of PEM materials, control of the layer thickness and molecular organization of an adsorbed polymer chain is achieved by adjustments of the pH of the solutions [303, 248]. A change in pH controls the linear charge density of an adsorbing polymer as well as the charge density of the previously adsorbed polymer layer. One of the benefits of a full atomistic representation is the ability to directly manipulate the protonation/deprotonation of desired functional groups, yet, empirically, this is indirectly controlled by by simple pH adjustments. For this reason, the pH of weak polyelectrolyte solutions is an extremely important parameter when assembling the films.

To account for the effect of changes in pH in our current atomistic model, the number of protonated/deprotonated monomers is explicitly defined in the simulation

model, either *via* random distribution or uniform distribution:

- **Random distribution**: for each simulation, charges are assigned to the functional groups randomly implementing a continuous uniform distribution. For a known ionization density, $\rho_{ion} = [0, 1]$, a random variable is generated, $u \in [0, 1]$, and the particle is charged if $u < \rho_{ion}$. The resulting charge distribution is asymmetric, resulting in a charge sequence effect, approximating the physical protonating/deprotonating effects of local charge through changes in pH. This method is used to assign charges to the oligomers simulated in **Chapter 4: Rate Dependence and Ionization Effects on Adhesion**, eliminating artificial dependency of charge distribution as related to adhesion strength.

- **Uniform distribution**: for a given ionization percentage, charges are assigned to the functional groups at random intervals (*e.g.*, every fifth function group results in ionization of 20%). As a result, average charge spacing is also a known (set) parameter. This method is implemented in **Chapter 3: Variation of Molecular Rigidity**, wherein individual polyelectrolytes are considered. Without effects of other polymers, it is presumed that a statistical averaging of random distributions would converge to the behavior of a uniform, homogeneous distribution.

Regardless of method, distributed charges are set, and constant throughout the MD simulations. This method of explicit ionization can allow the exploration of charged polymer combinations not possible in experimental systems (*i.e.*, combinations of ionizations without a physical pH correspondence). At this point, it behooves us to address the relatively uncertain charged state of the polyelectrolytes in solution as a function of pH.

Traditionally, the relation between pH and ionization is described by the pK_a value of the a polyelectrolyte (defining the extent of dissociation). Using pK_a values and degree of ionization from literature, a qualitative correlation of pH and ionization can be established. For example, the degree of ionization of poly(acrylic acid) (PAA) (using a pK_a of approximately 6.5 [62]) is approximately 70% at pH 7.0 (note a range of 55%-70% given in reference [66]). Similarly, at pH 7.0, the degree of ionization of poly(allylamine hydrochloride) (PAH) (a pK_a of 8.5 [62]) is approximately 95% (compared to 85% reported in reference [66]). An inherent complication with such weak polyelectrolyte systems is in their propensity to adjust their local charge density (or
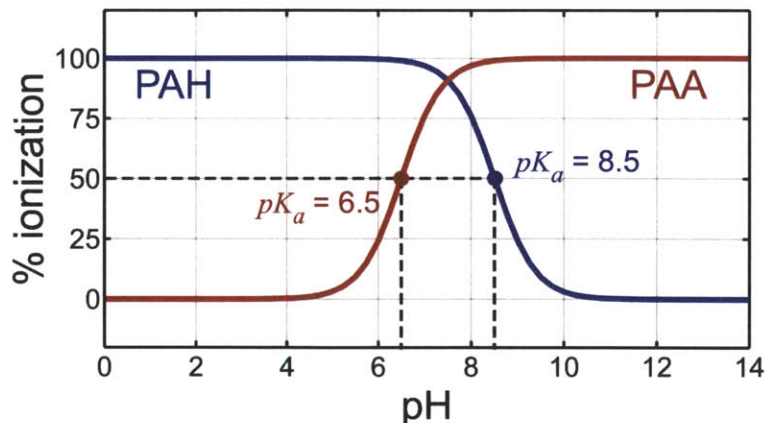
Figure 2-4: Plot ionization (%) as a function of pH for PAA (**red**) and PAH (**blue**), assuming constant pK_a values as an approximation. The solution pK_a of PAH is approximately 8.5 [351, 62], and the solution pK_a for PAA is approximately 6.5 [254, 62]. Although a one-to-one correspondence between ionization and pH is not possible, one can infer relatively accurate pH for a given range of ionization. Varying the relative pK_a values merely infers a change in interpreted represented pH value, and does not affect simulation results.

ionization) to accommodate different molecular environments (such as in a multilayer system). In general, the pH level and level of ionization (or protonation/deprotonation) can be accounted for *via* pK_a values (see Figure 2-4), where in the simplest form:

$$pK_a = \text{pH} + \log\left(\frac{\text{protonated}}{\text{unprotonated}}\right) \qquad (2.16)$$

It is noted that since the pK_a of a weak polyelectrolyte can be a complex function of degree of ionization [206], we use the term "pK_a" to indicate the pH at which exactly 50% of the polymer's functional groups are ionized. However, from experimental observations of various PEM systems, it is noted that, at a given pH, both the charge density and the effective pK_a of an adsorbing weak polyelectrolyte can *shift* dramatically from its single-polymer-type solution value when it is incorporated into a multi-layer system [277, 346, 254, 315, 62]. As a consequence, the pK_a of a weak polyelectrolyte can only be associated with specific environmental and solution conditions.

With this consideration, it has been demonstrated that changes in the local electric field of a weak functional group induced by the surrounding media can inhibit or

enhance the ability of both acid and base groups to achieve an ionized state [41]. For example, it is has been proposed that the pK_a of polyamines is generally a decreasing function of degree of ionization [284]. Although there are reports of the pK_a values of ≈ 9.0 for PAH, degrees of ionization for PAH have been reported as low as 70% at pH levels of 7.0 to 7.5 [351]. The variation of pK_a with degree of ionization in polyelectrolytes can be attributed to the difficulty of adding charge incrementally to an already ionized polymer backbone due to effects of charge repulsion [284]. Conversely, in a multilayer system, the effect can be the opposite. Indeed, the degree of ionization of the carboxylic acid groups of PAA can be more favorable in an oppositely charged environment, and thus exceed its expected solution value [346, 48, 254, 178] resulting in a shift of the apparent pK_a value of PAA to a lower pH. Further, the effect is most dramatic in multilayer systems consisting of two weak polyelectrolytes [62]. At the very least, howefver, using the pK_a values and degree of ionization from literature, a *qualitative* correlation of pH and ionization can be established. For example, from the work of Clark and Hammond [66] the degree of ionization of poly(acrylic acid) (PAA) (using a pK_a of approximately 4.3) is approximately 35% at pH 4.0. Similarly, at pH 4.0, the degree of ionization of poly(allylamine hydrochloride) (PAH) (pK_a of 7.0) is approximately 99%-100%.

We consider here the work of Rubner *et al.* [303, 61, 62], considering the pK_a values for the respective polyelectrolytes in solution with no added salt, corresponding closest to the explicit solvent conditions of simulation. The solution pK_a of PAH is approximately 8.5 [351, 62], and the solution pK_a for PAA is approximately 6.5 [254, 62]. Using LbL deposition of both PAA and PAH over a pH range of 2.5 to 9.0, Shiratori and Rubner [303] found the degree of ionization of an adsorbed PAA chain to be about 20%-30% at a pH of 2.5 and reaches close to 100% at a pH of 6.5, supporting a complex relation between ionization and pH rather than a constant pK_a. In the same study, the PAH chains remain fully ionized over the same range, but become deprotonated above a pH of about 10.0. Consequently, although a one-to-one correspondence between ionization and pH is not possible, one can *infer* relatively accurate pH for a range of ionization levels.

In effect, varying the relative pK_a values merely requires a change in corresponding represented pH value. The selected ionization distribution combinations remain unaffected. It is specifically for these reasons that we systematically vary ionization rather than pH, and results should be considered only in terms of such.

2.2 Temperature Assisted Sampling

One issue with dealing with the simulation of polyelectrolytes, unlike metals or crystalline structures, is that they lack any definitive structure. Indeed, polymers have many accessible configurations, resulting in many analytical techniques grounded in statistical approaches. Statistical mechanics approaches and polymer field theory can successfully describe the statistical behavior large polymer systems, such as polymer solutions [15, 290], polymer melts [290, 209, 123] and thermoplastics [16], and are an integral component of a complete (*i.e.*, holistic) and multiscale understanding of polymer composites and systems. Such statistical approaches complement continuum mechanics based formulations, and provide greater molecular details to constitutive material laws (*e.g.*, the effect of functional group size, chain length, mass density, crystallization, inclusions, cross-linking, temperature effects, etc.). Typically, statistical methods are derived by formulating partition functions (*i.e.*, a many-dimensional integral representation over the particle degrees of freedom), based on the statistical mechanics of continuous Gaussian chains (discrete) or threads (continuous) to represent the polymers, where the solvent is taken into account implicitly [15, 14]. In effect, the partition functions describe the statistical properties of a system in *thermodynamic equilibrium*. The tradeoff, of course, is removing chemical details in exchange for universal properties. Here, out goal is defining the mechanics of a polyelectrolyte complex at the molecular scale, and thus such mean field approaches are inapplicable. That, however, does not completely remove the need for *statistical sampling*.

Due to the short time scale of MD simulations and the challenges in observing rare events (*e.g.*, molecular folding, unfolding, structural transitions), many different methods have been developed to speed up the sampling rate of MD simulations. For

example, atomic-level structures of major ampullate silk proteins were obtained using *replica exchange molecular dynamics* (REMD), enabling robust nanomechanical analysis [174]. The challenges of reaching native (*e.g.*, equilibrium) structures within the time scales accessible to conventional MD simulation require enhanced sampling methods such as REMD [314]. REMD is considered to be an effective tool for investigating folding and aggregation of macomolecules, as it reduces the likelihood of kinetic trapping at non-native states through temperature assisted conformational sampling [283, 274, 269, 226, 174]. One presumption of the replica exchange method, however, is the existence of an optimal or preferred structure. Energetic metrics are utilized to cluster replicas into "most likely" configurations, thereby attaining an accurate representation of a protein, for example. Other sampling techniques, such as meta-dynamics [328, 36] (*e.g.*, PLUMED), rely on energetic biasing through the (clever) definition of collective variables to explore the molecular phase space. Again, there is an assumption of a preferred configuration or reaction pathway, or, at the very least, a well-defined collective variable. Such metadynamic (and similar umbrella sampling) approaches have been successful in exploring protein fibril nucleation [17], redox chemical reactions [175], and molecular interface characterization [310].

Unlike protein folding prediction in which there is one energetically optimal structure, only a sample of random but likely equilibrated polymer conformations is required for analysis (for example, to obtain a mean square end-to-end distance, $\langle R^2 \rangle$, as in **Chapter 3: Variation of Molecular Rigidity**). Thus, we desire a means to attain a *nonbias* statistical ensemble of likely polymer conformations. If we consider the *ergodic hypothesis*, all accessible microstates are *equiprobable* over a long period of time, and thus a sampling over random time intervals would be sufficient (see Figure 2-5(a)). However, such a method would be computationally unfeasible.

Due to the limitations in timestep (and thus physical sampling time), we exploit *temperature* to accelerate the kinetics of the molecular system by implementing cyclical temperature fluctuations ($T_{low} \rightleftharpoons T_{high}$) to achieve "likely states". This has two direct effects: (1) it allows the sampling of a larger temporal space (similar to the principle of time-temperature equivalence in viscoelastic solids [197, 199]) and; (2)
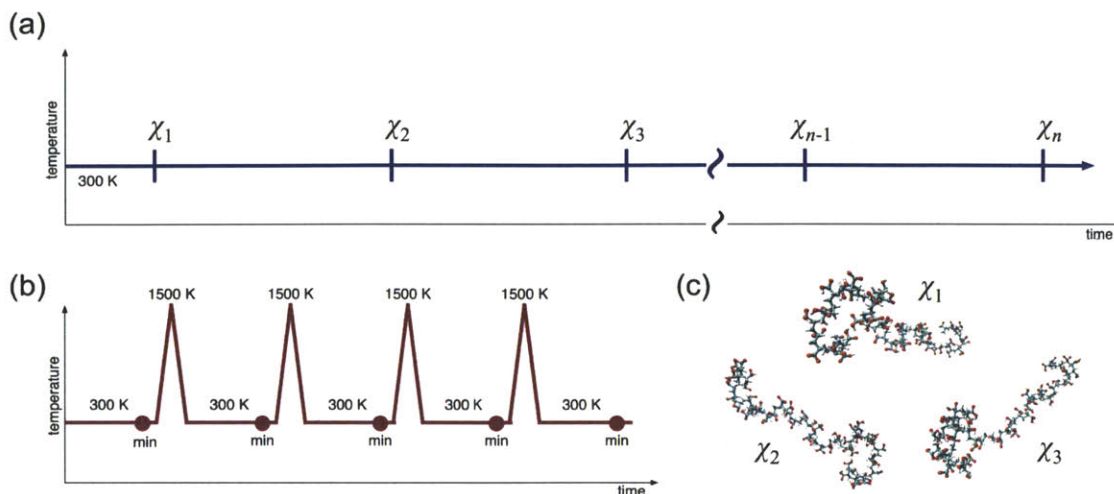
Figure 2-5: Using temperature fluctuations ($T_{low} \rightleftharpoons T_{high}$) to attain a nonbias statistical ensemble of a likely polymer conformations. (a) If we consider the *ergodic hypothesis*, all accessible microstates, *e.g.*, χ_1, χ_2, ..., χ_n, are *equiprobable* over a long period of time at finite temperature (here, 300K). (b) Regular increases in cyclic temperature (temperature increase followed by an equilibration/minimization) can attain a similar sampling of χ_i's. (c) Procedure assumes that each state is *equiprobable*, and thus $E(\chi_1) \equiv E(\chi_2) \equiv E(\chi_3)$.

enables escape for potential energetic (or kinetic) trapping in local minima (similar in effect to REMD [314] or PLUMED). We refer to this technique as *temperature assisted sampling* (TAS).

Temperature assisted sampling is only beneficial for systems that express many equiprobable conformations (see Figure 2-6). Metrics to ensure applicability of TAS include root-mean-square displacement (RMSD), which should show variation between cycles, as well as system energy for each sampled state, which should be approximately equal (a sign of equiprobability). Such results are discussed further in **Chapter 3**.

Admittedly, pure Monte Carlo (MC) approaches could draw samples from all possible statistical conformations, and are frequently used in polyelectrolyte simulations. However, most implementations utilize a idealized chain (*i.e.*, bead-spring) representation of the molecule, significantly reducing the number of degrees of freedom required to be sampled. As such, MC can be efficiently employed (using random perturbations of the $x-$, $y-$,and $z-$coordinates of the beads, for example) and equilibrium states easily attained. For example, a recent study of glycosaminoglycans

68
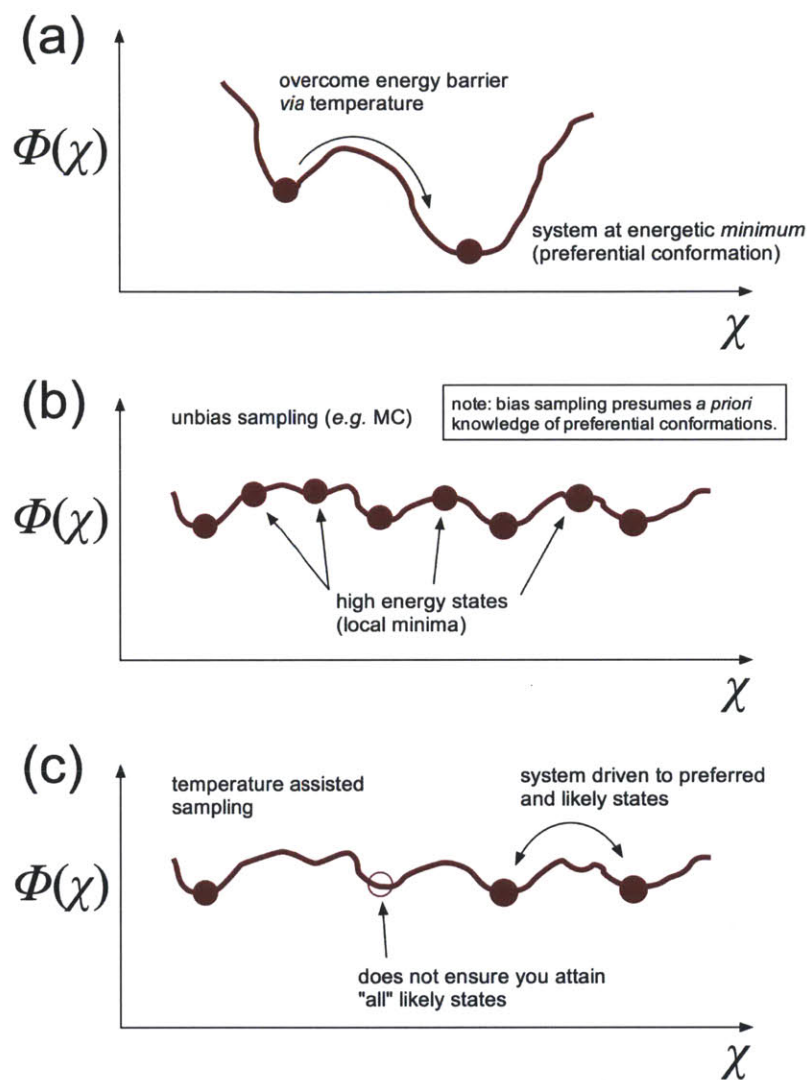
Figure 2-6: Appropriate energy landscapes, $\Phi(\chi)$, for temperature assisted sampling (TAS). (a) Inappropriate energy landscape, which has a absolute energy minima or preferential conformation. While high temperatures can assist in overcoming local energy barriers (*e.g.*, kinetic traps), other sampling methods such as REMD [314] and PLUMED are more adequate to explore such a bias phase space. (b) Unbias sampling (*e.g.*, MC) of appropriate landscape, with many equivalent minima. Full MC approaches would sample high energy states within a complete sample set, necessitating equilibration and minimization. This can be overcome by bias (*a priori*) knowledge of preferred states (*e.g.*, preferential torsional angles, for example). (c) TAS sampling of appropriate landscape. Temperature fluctuations drive system to local minima, resulting in efficient equilibration and minimization per cycle. It is noted however, states can be re-visited, and not all states may be attained. However, if many states are presumed equiprobable, such effects are reduced *via* repeated sampling.

implemented a Monte Carlo algorithm to generate thousands of equilibrium states in conformation-protonation space [26]. The move set consisted of torsion angles, Cartesian displacements, and protonation. Such an approach is unsuitable for the current system for two reasons: Primarily, it is difficult to select a set of "good" sampling variables. While backbone coordinates may seem a promising candidate, they are coupled to the function groups, and there may be dependencies on the orientation with protonated/deprotonated groups. Likewise for any angular or dihedral variables. No such assumptions are to be made, and no free parameters or degrees of freedom are needed to be selected *a priori* to explore the possible conformation space, allowing physically accessible conformations to be attained *via* the MD trajectory. Secondly, the full atomistic resolution (especially explicit solvation) result in a computationally expensive cost of equilibration and minimization. As a direct result, attempting to sample thousands (or even hundreds) of equilibrium states is computationally untractable. Indeed, if "good" control parameters were known, they could be randomly varied to attain a statistical sample, but in absence of such knowledge, the system should be left to evolve on its own accord (in terms of the MD protocol).

The process is technically implemented (within LAMMPS) as follows:

1. The constructed polymer(s) are surrounded by an explicit solvent box to ensure sufficient screening and isolation of the macromolecule.

2. To ensure the initial configuration is not unique, the system is minimized (using a conjugate gradient algorithm with an energy-convergence criterion as implemented in LAMMPS) and then subject to 1.5 ns of equilibration at $T_{low} = 300K$ using an NVT ensemble (approx. 300,000 time integration steps). This equilibration time was determined by trial and error by tracking trajectory RMSD and energy quantities.

3. The system undergoes a steady increase in temperature to T_{high}, in the range of 1000K to 1500K over 0.5 ns to 1.0 ns, followed by an steady decrease in temperature to $T_{low} = 300K$ over 0.5 ns (approx. 100,000 time integration steps total).

4. The system is again subject to 0.5 ns of equilibration at $T_{low} = 300K$. A stable equilibrated structure is confirmed by RMSD calculations.

5. System is subject to minimization after temperature cycles to ensure preferential (energetically) conformation attained. Random velocities are assigned after minimization to ensure the polymer has no memory of current state.

6. Steps (3) to (5) are repeated multiple times within the same MD run to obtain a statistical ensemble of states.

We note that initial equilibrate structure obtained after minimization (*i.e.*, step (2)) is not considered to eliminate any unnatural residual effects in the random ionization process and construction of the initial polymer geometry. Using this method, high temperature can be used to drive the polymer to a new, equilibrated state, overcoming possible kinetic trapping and ensuring each attained conformation is physically accessible, requiring less simulated equilibration time per conformation. In effect, TAS provides a means to attain multiple, independent and nonbias samples of polymer conformations from one initial state.

2.3   Coarse-Grain Methods

The study of complex multi-scale hierarchical systems as found in biological and synthetic materials require a new approach of analysis to elucidate the inherent structure-property relationships that transcend atomistic, mesoscopic to macroscopic scales[5]. Commonly, a system-dependent "finer-trains-coarser" paradigm is applied for coarse-grain model development that aims to maintain relevant mechanics and accurate interactions, focused on behaviors at the mesoscale (*e.g.*, subsequently higher structural scales). Ideally, parameterization of such models is achieved through full atomistic results, thereby providing a sound theoretical basis for coarse-grain potentials and a significant reduction of computational expense. The system simplification can be efficiently implemented to reconcile the differences between empirical and simulation results by bridging the time- and length-scale limitations of classical MD into physically relevant and experimentally accessible regimes. Being said, vast the number of potential system variations and combinations of constituent materials requires different model formulations depending on the intended application. Such a system-dependent restriction contradicts the formulation of a universal stepwise coarse-graining procedure. Here, we present a generalized framework elucidates the fundamental principles

---

[5]For a thorough discussion of such coarse-graining methods, refer to Cranford and Buehler [78, 79]

necessary for coarse-grain model formulation, as applied to polyelectrolyte complexes and PEM microtubes.

A developed coarse-grain model can only reflect the behavior included in their governing potentials and associated parameters, and consequently, the source of such parameters typically determines the accuracy and utility of the coarse-grain model. A complete theoretical foundation for any system requires synergistic multiscale transitions from atomistic to mesoscale to macroscale descriptions, providing consistency between "building blocks constructed of building blocks". Indeed, a finer-trains-coarser approach is not limited to bridge atomistic to mesoscopic scales (which is the focus of the current discussion), but can also refer to hierarchical parameterization transcending any scale, such as mesoscopic to continuum levels, or structural steel members to the Eiffel tower. For the current discussion, the term "hierarchical" is used loosely to indicate a material system with at least a single distinct differentiation between constituent material components and global system structure. For example, previous studies have developed coarse-grain representations of amyloid fibrils [246, 247]. For the amyloids, the components are defined as cross-beta molecular structure [245], while the system of interest is the entire fibril. It is noted that cross-beta structures are themselves composed of a hierarchical arrangement of polypeptide chains, which are also composed of constituent amino acids [245]. Thus, the defined components need not be the *fundamental* building blocks of the system, only a component able to be *parameterized.*

A commonly stated motivation and presumed primary benefit for the development of coarse-grain potentials and models is to allow the simulation of larger systems at longer timescales. Indeed, the reduction of system degrees-of-freedom and the smoother potentials implemented allow larger timestep increments (and thus timescales) and each element is typically an order of magnitude or more larger in length scale. Additionally, cheaper potential calculations (in terms of computational efficiency) can be exploited to either increase the number of coarse-grain elements (thus representing even larger systems) or simulate a relatively small system over more integration steps (further extending accessible timescales). Such benefits are

inherent to any coarse-grain representation, and can serve as a *de facto* definition of the coarse-graining approach. Nevertheless, a pragmatic approach of system simplification is found in many engineering disciplines. Complex electronic components are designed based on simplified models of circuits, with element behavior defined by such general properties as current, voltage, and resistance. Robust building structures are analyzed *via* notions of beam deflections and beam-column joint rotations, among other simplifying assumptions. In both cases, more detailed system representations are known and can be implemented (*e.g.*, implementation of temperature and material effects in a transistor, or a detailed frame analysis including stress concentrations in bolts or welds). It is apparent that such additions result in a more accurate representation of the modeled system, but also serve to increase the computational expense of analysis as well as introduce a more sophisticated theoretical framework (which subsequently requires a more detailed set of material and model parameters). Rarely, however, is the use of simplified and computationally efficient models justified by inaccessible time- and length-scales of the more detailed description. Such models are applied for analysis *in lieu* of a more detailed description because they provide an accurate representation of the system level behavior and response with confidence in the properties of the model components. It is stressed that even if full atomistic representations are computationally possible, a coarse-grain description can be still be suitable for systematic analysis of variable system configurations - taking a broader perspective to discover critical behaviors.

2.3.1 Examples of Coarse-Graining Methods

In the last decade, various simple models have been used to describe the large-scale motions of complex molecular structures where more detailed classical phenomenological potentials [42, 253] involving all atoms cannot be used because of the restrictions on the amount of time that can be covered in computer simulations. The reader is referred to recent reviews for a more thorough discussion of techniques and applications [20, 327, 301]. Single-bead models are the most direct approach taken for coarse-graining macromolecules. The term "single bead" derives from the idea of us-

ing single point masses for describing a functional group, such as single amino acids or monomers, in a macromolecular structure. The Elastic Network Model (ENM) [326], Gaussian Network Model [138], and Gō-models [149] are well-known examples that are based on such bead approximations. These models treat each monomer as a single bead located at the C_α position, with mass equal to the mass of the monomer. The beads are connected *via* harmonic bonding potentials, which represent the covalently bonded backbone. Elastic network models have been used to study the properties of coarse-grained models of proteins and larger biomolecular complexes, focusing on the structural fluctuations about a prescribed equilibrium configuration, such as normal vibrational modes. A variation of elastic network models is developed for polyelectrolytes, and are therefor discussed further in the following section. Despite their simplicity, these models have been extremely successful in explaining thermal fluctuations of proteins [327] and have also been implemented to model the unfolding problem to elucidate atomic-level details of deformation and rupture that complement experimental results [343, 92]. A more recent direction is coupling of ENM models with a finite element-type framework for mechanistic studies of protein structures and assemblies [25].

The lack of intermolecular interaction characterization in the simple coarse-graining approaches required a more complex formulation - one that maintains a definitive structure of the macromolecule, as well as integrate particular interactions between macromolecules. Using more than one bead per monomer provides a more sophisticated description of molecules. In the simplest case, the addition of another bead can be used to describe specific side-chain interactions in proteins [19]. Higher-level models, for instance, four- to six-bead descriptions, capture more details by explicit or united atom description for backbone carbon atoms, side chains, and carboxyl and amino groups of amino acids [235, 236]. The recent development of the MARTINI force field, for example, attempted to provide a general coarse-grain model that could be efficiently adapted for a multitude of biological systems by taking advantage of the fact that the majority of biological molecules (such as protein structures and lipids) are composed of the same categories of functional groups at the atomistic level. Such

approaches were previously implemented with various degrees of complexity for application to specific systems, integrating multiple beads per functional group, or more complex parameter formulations [299, 300, 208, 230]. Even coarser-level multiscale modeling methods have been reported more recently, applied to model molecular systems at larger time- and length scales [75, 69, 77, 72, 246, 247]. These models typically employ super-atom descriptions that treat geometric clusters of atoms as beads and are computationally quite efficient.

We proceed to introduce a general framework through a finer-trains-coarser multiscale paradigm, which effectively defines coarse-grain potentials *via* a known (finer) component response, while introducing relevant mechanical properties at the mesoscopic scale. The approach is unique in its ability to transcend multiple scales enabling the investigation of a broad regime of systems from protein-based materials to synthetic composite structures, while emphasizing a theoretical foundation on full atomistic investigations and asserting energetic equivalence and consistent mechanical behavior between all levels of modeling. The result is a set of problem-specific coarse-grain representations with diverse applications. The ensuing discussion presents guiding principles behind model formulation.

2.3.2 General Model Formulation

From the previous discussion, it is apparent that a universal, stepwise procedure for coarse-graining a system is limited by the inherent simplifications and intent of the coarse-grain representation. A model developed to investigate arrays of carbon nanotubes [69, 77] will differ from a model developed for the simulation of amyloid fibrils [246, 247], even though the coarse-grain elements and potentials are similar (see Figure 2-7). The coarse-graining of a particular system can be characterized by trial-and-error and subjective omissions or inclusions of pertinent behaviors, and as such considered just as much an *art* as a *science* [40].

The first step in the development of a coarse-grain model is to determine the necessary potentials to characterize the system. In general, we define the total energy of a coarse-grain system as the sum of these potentials:
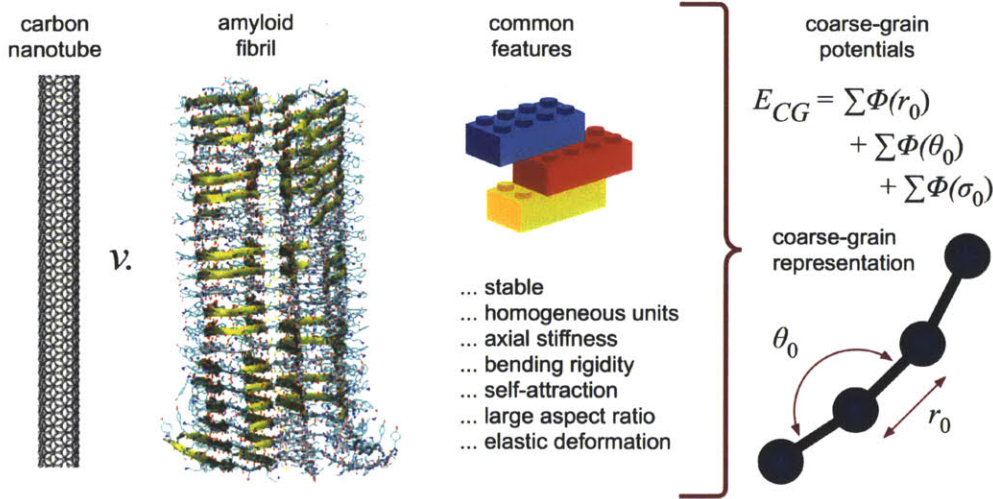
Figure 2-7: While a general procedure for coarse-graining a system is limited by the intent of the model, universal or common features (*e.g.*, sufficient and necessary "building block" characteristics/properties) can be exploited and similar models developed for diverse materials. For example, here we show two distinct fibrillar structures - a carbon nanotube and an amyloid fibril. While the parameters differ by orders of magnitude, both structures can be represented by a simple coarse-grain representation considering stretching, bending, and self-adhesion (see [69, 77, 246, 247] for applications of such models).

$$E_{system} = E_{CG} = \sum \phi_{CG} \qquad (2.17)$$

where ϕ_{CG} are the defined coarse-grain potentials. Although a simple statement, it is nontrivial in implementation. Indeed, the type of developed potentials can serve to both broaden and restrict the applications of the model. Specifically, the coarse-grain potentials must be complex enough to represent the finer system in the intended mesoscopic simulation. One must consider whether provisions are necessary for fracture, intermolecular interactions, plasticity, formation of secondary structures, or a host of other behaviors depending on the intent of the investigation. The goal is to utilize the fewest and simplest potentials as possible that represent the system structure(s), mechanical properties, and interactions. Such an approach can be facilitated by the utilization of harmonic spring potentials to reflect mechanical response, where:

$$\phi_i(\psi) = \frac{1}{2}k_i(\psi - \psi_0)^2 \qquad (2.18)$$

Here, k_i refers to a harmonic spring stiffness while ψ typically refers to either an interatomic distance, r, or an angle, θ, for stretching and bending deformations, respectively (the subscript "0" indicating equilibrium value). The harmonic spring potential results in a linear relationship between force and deformation, allowing efficient computation of interactions. Indeed, more complex nonlinear behavior can be approximated by combinations of linear functions (such as bilinear or trilinear formulations) to maintain computational efficiency *in lieu* of the introduction of more complex potentials. A possible deficiency, however, of harmonic potentials is the continuous increase in force with deformation. Systems subject to large deformations will subsequently deviate from true behavior, and thus, without provisions such as a potential cutoff, the use of the harmonic potential should be limited to small deformation (*e.g.*, a linear elastic assumption).

The finer-trains-coarser approach necessitates the parameterization of coarse-grain potentials from other methods - either higher resolution atomistic or empirical results. A "test suite" is thus developed (directly or indirectly) to obtain the necessary mechanical response and interactions to be integrated into coarse-grain potentials. Typically, a relatively simple assay is applied to isolate a single mechanical behavior. For example, uniaxial stretching can be applied to obtain the force-displacement $(F - \Delta)$ or stress-strain $(\sigma - \epsilon)$ response of a macromolecule or material component, allowing the calculation of Young's modulus, and the parameterization of coarse-grain "bond strength". Further, a three-point bending test can be utilized to determine the bending stiffness of a molecule, thereby allowing the parameterization of the coarse-grain rigidity. In essence, a single result is used to characterize a single coarse-grain potential, ensuring accurate representation of each behavior. The number of required "tests" depends on the number of coarse-grain potentials (and associated parameters) implemented to describe the system.

The fundamental principle underlying the parameterization of coarse-grain potentials is the assertion of *energy conservation*. Energy equivalence is imposed between potential energy functions and relevant atomistic energy results. The basis of the formulation of the energy functions, either through elastic strain energy, deformation

energy, adhesion energy, or other techniques, essentially defines the accuracy and be-havior of the representative coarse-grain system. Coarse-grain interactions can be thought of as the summation of finer interactions, expressed as:

$$\phi_{CG}(R) = \sum_{ij} \omega_{ij} \phi_{ij}(r_{ij}) \qquad (2.19)$$

where ϕ_{CG} is the coarse-grain potential, R is grouped independent variable, and ω_{ij} is a weight associated with the finer potentials, ϕ_{ij}. This is essentially how coarse-grain potentials are developed for a small number of atoms per superatom (such as MARTINI-type force fields [208]), where the superposition of multi-body effects is apparent in the mapping. The relation becomes more complex as the number of incor-porated/mapped atoms increase, required explicit atomistic simulation of the desired macromolecules. It is further stressed that the the coarse-grain potential incorpo-rates effects of the entire represented system (such as hydrophobic and other solvent effects, electrostatic interactions, hydrogen bonding between molecules, and/or en-tropic effects), requiring the introduction of unknown weighting coefficients, ω in the summation (*e.g.*, there is no analytical or closed-form solution). As there can be many contributions to even simple mechanical process (such as breaking of hydrogen bonds or solvent friction during molecular stretching or bending), we introduce conservation of energy for the relevant mechanical response (as opposed to the potential energy of direct energy equivalence) resulting in consistent mechanical behavior between full atomistic and coarse-grain representations. The approach is to apply energy equiv-alence between the coarse-grain potential and the observed strain or deformation energy of the full atomistic system:

$$\phi_{CG}(\psi) = U(\psi) \qquad (2.20)$$

where ϕ_{CG} is again the coarse-grain potential, and U is the representative energy func-tion for a given mechanical response, ψ. It is an underlying assumption of the model that the response of the finer system is accurately described by the energy function, $U(\psi)$. The choice of the strain or deformation energy function is dependent on the

system to be coarse-grained, and assumptions of elastic/plastic behavior, material isotropy, system failure such as yielding or fracture, etc., affect the definition (and interpretation) of atomistic results. As an example, for an elastic-isotropic material, we can define strain energy as:

$$U\left(\epsilon\right) = \frac{1}{2} \int_{\overline{V}} \sigma \epsilon d\overline{V} \tag{2.21}$$

To equate with $\phi_{CG}(\psi)$, we must formulate U as a function of ψ. For axial stretching, this requires the formulation of strain as a function of bond length, $\epsilon(r)$, while for shearing, this may require the formulation of strain as a function of shearing angle, $\epsilon(\theta)$, for example.

Once the coarse-grain potentials are developed validation of the coarse-grain model is a necessary step to assure an accurate representation. Experimental techniques such as nanoindentation or atomic or chemical force microscopy (AFM/CFM) can directly probe materials at the mesoscale and determine system level characteristics and mechanical properties. The development of coarse-grain models is intended to elucidate such system-level behavior and thus correlation with experimental results is essential. Reciprocally, an accurate coarse-grain model can serve to validate and support experimental results (further explored in **Chapter 6**). It is noted that advances in experimental techniques are continually probing smaller scales, reaching atomistic precision and allowing single molecule investigations (such as optical tweezer methods, atomic force microscopy (AFM), etc.). Such data can serve to reinforce full atomistic representations and any developed coarse-grain models, thereby increasing confidence in both representations and supporting the finer-trains-coarser approach.

Using these principles, we now describe the specific coarse-grain representations applied to (a) normal mode analysis of a polyelectrolyte complex and (b) large scale model of PEM microtube array.

2.3.3 Elastic Network Models and Normal Mode Analysis

At the atomistic scale, in the simplest form, a coarse-grain model can be defined by a single potential for all atoms (see Figure 2-8). For example, the aforementioned elastic network models (ENMs) can be thought of as a single pair potential between neighbor atoms, such that:

$$E_{CG} = E_{ENM} = \sum \phi_{ENM}(r) \tag{2.22}$$

where

$$\phi_{ENM}(r) = \frac{1}{2}K_r(r - r_0)^2 \tag{2.23}$$

Here, each pair of atoms is assigned a harmonic spring bond potential with stiffness, K_r, about an initial equilibrium spacing, r_0. The elastic constant, K_r, can be defined a constant or, as another example, a function of r_0, where:

$$K_r(r_0) = \overline{K}\frac{\overline{r}}{r_0} \tag{2.24}$$

or

$$K_r(r_0) = \overline{K}\exp\left[-\frac{\overline{r}}{r_0}\right] \tag{2.25}$$

The first scales the mean value of the elastic constant, $\overline{K}$, with the initial bond length, r_0, such that $K_r(\overline{r}) = \overline{K}$. If the ENM is representative of a solid or continuous media, this method treats each elastic elements as if they had the same cross sectional area, A, and a constant Young's modulus, E, such that the quantity (EA/r_0) is the same for all elements in the network [145]. The second method subjects the elastic constant to an exponentially decaying function with respect to a mean bond distance $(\overline{r})$. Such a formulation of K_r can represent weak interactions of atoms at a distance (such as van der Waals interactions) and provide a more complex description of interactions [153, 154]. In effect, presumed mechanical knowledge of the system (*e.g.*, constant and homogeneous stiffness) is introduced into the elastic network. Indeed,

(a) Full atomistic structure

(b) General elastic network model (ENM)

harmonic springs
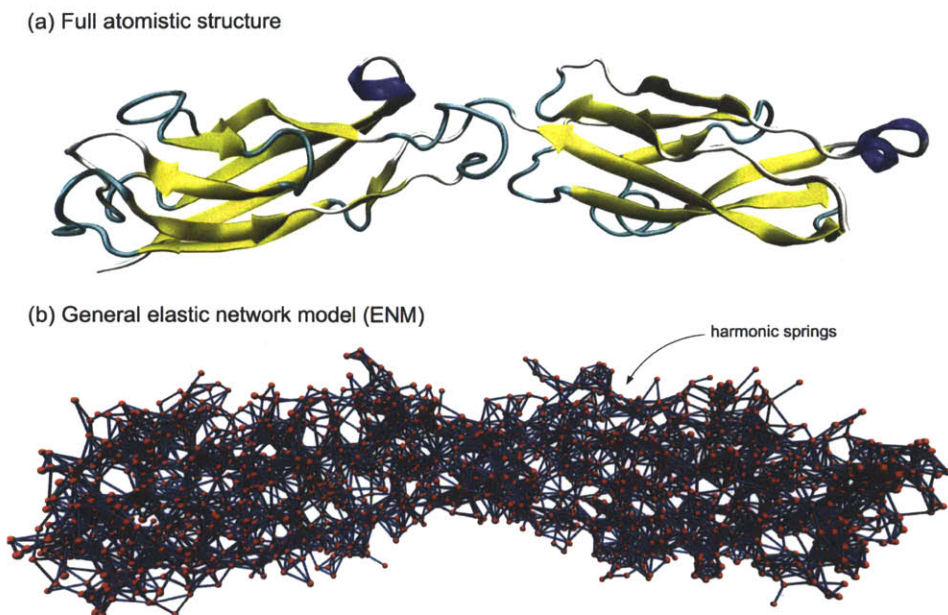
Figure 2-8: Example of general elastic network model (ENM) of human E-cadherin protein. Loss of E-cadherin function or expression has been implicated in cancer progression and metastasis. (a) Full atomistic representation, depicting secondary structure(s) of the protein; approximately 2000 atoms. (b) General elastic model, where harmonic springs are introduced between adjacent neighbors within a cut-off of approximately 10 Å, resulting in a a network of over 5000 elastic "elements".

if the interaction is known, such as the case for cross-linked polyelectrolytes, a more accurate potential can be introduced for stiffness, such as the screened Debye-Hückel potential. This is implemented in **Chapter 5**, such that the effective elastic stiffness is a function of distance, screening, and potential energy, or $K_r = f(r, \kappa^{-1}, \phi(r))$. More complex model representations introducing directionality and anisotropy can be formulated [13]. As such, even a single potential description can become increasingly sophisticated as applications attempt to probe complex molecular deformations such as protein residue fluctuations [99] and equilibrium state transitions [359, 233].

Recent works demonstrate that ENM modes can provide an efficient sampling of conformational space, such as that covered by available HIV-1 protease structures [348], in a manner similar to MD trajectory or NMR ensemble analysis. In consideration of a convoluted polymer system (biological or nonbiological), it is noted that an ENM has superficial similarities to the work of Flory [119], considering the statis-

tics associated with the end-to-end distance of a finite polymer chains in a random network [325], and thus the load path of a an elastic network - assigned along the polymer length - can likewise be considered as such. However, the random walk of a polymer chain and the vibrational states are distinct, where the vibration requires force constant matrices with (presumed) spring constants. Random walk distributions are associated entirely with entropy, whereas vibrations consider both enthalpic and entropic contributions associated with small amplitude fluctuations from equilibrium.

Existing elastic models can be extended *via* more sophisticated potentials to achieve an optimal description of both protein conformational motions and thermal fluctuations [360]. More complex ENM approaches to conformational change involve the introduction of multiple equilibrium states [30], for example to generate double-well models. A number of other models for conformational flexibility merit further exploration, including those which group rigid blocks within a protein with flexible connections [130]. *Can ENMs be useful beyond conformational investigations?*

Consider that elastic network models fall into two broad classes, those with Hookean springs which describe the *rigidity* of the macromolecule [326], and those describing the *connectivity* of the macromolecule [18]. Unlike folded protein structures wherein only structural information (*e.g.*, geometry/shape) is known *a priori*, the aim here is to model the effective behavior from known (ideal) mechanical components - the geometry of the polymer complex is secondary. As such, connectivity is only prescribed insofar as it dictates mechanical function, *e.g.*, through definition of chain extension and sites of potential ionic cross-links. Rather than an atomistic geometry-dependent network (*e.g.*, connections between C_α carbons), we utilize understanding of the molecular system to develop a mechanical structure-dependent network (*e.g.*, equivalent mechanical components). The molecule to 2D structural analogue is depicted in Figure 2-9. Such approaches have been effective in reducing a system of hydrogen bonds to a simple 2D spring network [264], for example, substituting geometric complexity for mechanical function to isolate mechanical features.
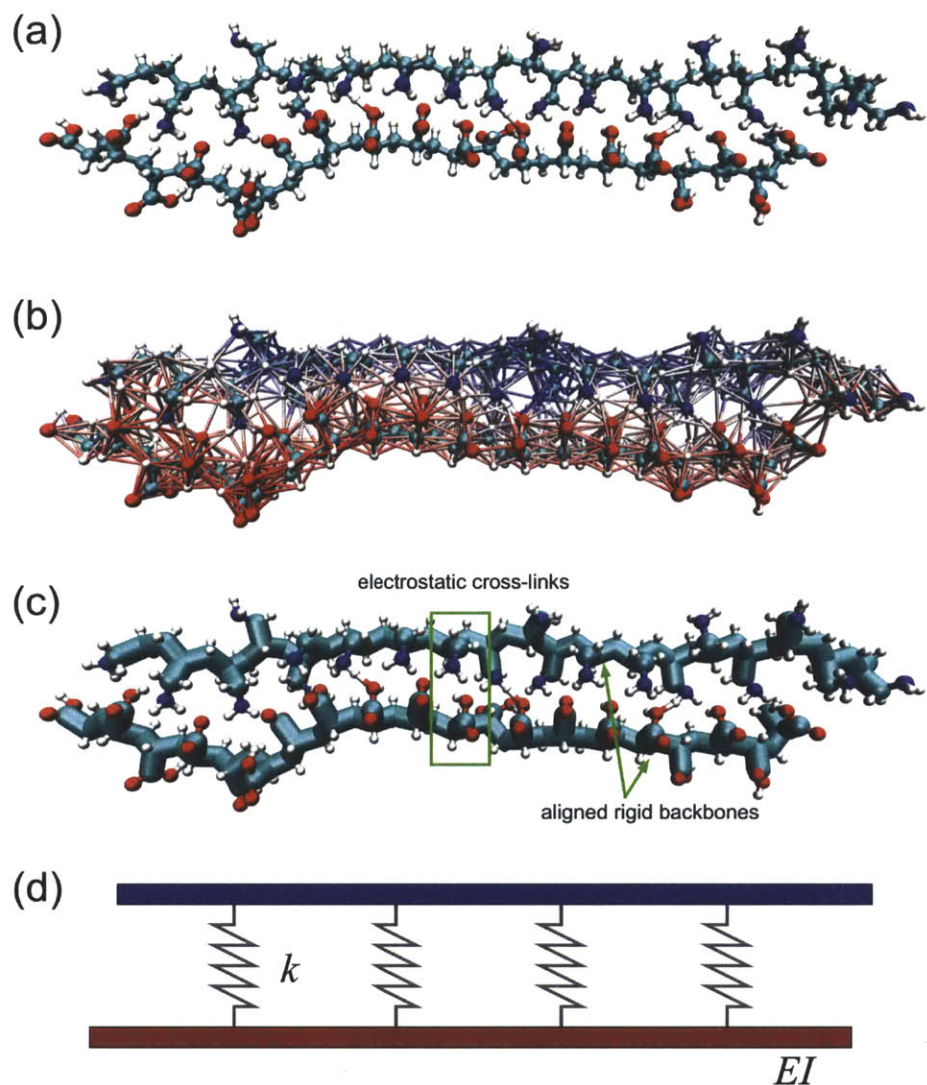
Figure 2-9: Uncovering an elastic model for a polyelectrolyte complex. (a) Full atomistic representation of a short complex (20 monomer chains of PAA and PAH for schematic purposes; explicit solvent hidden for clarity). (b) A general, uninformed elastic network, connecting adjacent atoms with harmonic springs. Note the extreme amount of harmonic "cross-links" introduced between the polyelectrolytes due to their alignment and proximity. If the polymer interaction was completely unknown (such as the case for many complex protein structures), this ENM could provide a first-order approximation of conformational and mechanical behavior. (c) Introduction of additional modeling information by recognizing (i) the main cross-links are electrostatic between known functional groups, and (ii) both polyelectrolytes are dominated (mechanically) by a rigid backbone chain (enlarged to highlight). Note that both of these features (cross-links and rigidity) are a function of ionization. Explicitly accounting for these components can significantly reduce the necessary elastic model elements. (d) General 2D elastic model of a polyelectrolyte complex, consisting of two rigid backbones and electrostatic cross-links in the form of beam (flexural member) and spring elements respectively. A 2D representation is formulated to avoid torsional deformations.

83

Comment on Elastic Model of Polyelectrolyte Complex

The basis of our elastic model of a polyelectrolyte complex is the assumption that is consists of two aligned cross-linked polymer chains with finite rigidity. The introduction of specific mechanical behavior - *e.g.*, bending stiffness - represents a deviation from the *geometric* accuracy of the elastic model, but reflects the general *mechanics*. This can be thought of as reducing a more general network to the effective stiffness (akin to the technique of *static condensation* in finite elements [345, 24, 63, 213]). Similarly, the bending rigidity can be thought of simply as a constraint, such that groups of atoms deform cooperatively, similar to other ENM implementations (*e.g.*, such as the rotation translational block method [320, 105], or restriction to torsional motions [333]). In the rotational block method, for example, physical insight is used to choose groups of atoms (*e.g.*, "blocks") which are assumed to be more rigid [320, 105]. Since these blocks are no longer nodal points, six degrees of freedom (three translational, three rotational) are introduced to the dynamical matrix. Similarly, for our 2D "flexural members", we introduce six degrees of freedom (four translational, two rotational).

Here, the introduction of bending rigidity, EI or D, reduces the size of the required dynamical matrix, with physical insight. While isolated polyelectrolytes can be considered to behave as a worm-like chain with little bending stiffness (*e.g.*, conformation dictated by a random walk), the mean-square end-to-end, $\langle R^2 \rangle$, distance reflects an intrinsic stiffness based on the Kratky-Porod model [185] where, in the limit, $\langle R^2 \rangle \to 2PL$, and P is the persistence length of the polymer chain. In terms of bending rigidity, the persistence length is related to stiffness by the thermal energy, or $Pk_BT = EI$ (where k_B is Boltzman constant and T the temperature). The Kratky-Porod model and its implications are further discussed in **Chapter 3: Variation of Molecular Rigidity**. Low persistence lengths (on the order of a nanometer, as the case here for PAA and PAH) give rise to entropically dominated molecules, and the value of an elastic formulation for *predicting* mechanical response is uncertain. Being said, the elastic model here is temperature independent (insofar as the de-

rived parameters) and presumes equilibrium conditions only (the resulting eigenvalue problem presumes steady-state conditions [24]), and used as a mechanical condition for complexation. Derived mechanical parameters - such as the effective rigidity of the complex - can be thought of as placeholders to introduce into entropically-based formulations.

Details of the formulation of the elastic model are given in **Chapter 5: Critical Ionization to Couple Polyelectrolytes**.

Normal Mode Analysis and Eigenvalue Problem

As precision and atomistic details are removed by design, *what advantage does the development of an elastic model add to the description of polyelectrolytes?* Consider that if it was possible to characterize a system solely based on structure, it would eliminate the need for any loading or deformation altogether - boundary conditions and the time scale limitations of full atomistic MD would then be eliminated. With a sufficient elastic model, *normal mode analysis* provides such an approach, only requiring a system's geometric and chemical conformation as an input. The structural stability and mechanical properties of complex molecular systems can be determined by analyzing the associated normal modes. While complex deformations can be described for protein structures (*e.g.*, the unique "open" and "closed" forms of binding proteins [321]), here, we focus on fundamental mechanical responses (*e.g.*, stretching, shear, bending, etc.). Specifically, for a *flexural member*, the vibrational equation for transverse bending motion of the Euler-Bernoulli beam model can be written as:

$$\rho A \frac{\partial^2 u}{\partial t^2} = -EI \frac{\partial^2 u}{\partial z^2} \qquad (2.26)$$

where A is the cross-sectional area of the molecule, ρ the density, EI is the bending rigidity, and u is the transverse displacement (along the z-axis at time t). Subsequently, the frequency, ω for n-th order flexural mode under free vibration can be formulated as:

$$\omega_n = (\frac{n\pi}{L})^2 \sqrt{\frac{EI}{\rho A}} \qquad (2.27)$$

where L is the length of the member, and n indicates one of the solved eigenvalues [341]. It should be noted that the expression given above does not take into account any rotational and shear contribution. To include such effects, more sophisticated models such as Timoshenko beam theory could be used [341]. Higher order eigenmodes can be used to account for both axial stretching and torsional deformation. If the eigenmode reflects a single (non-coupled) mechanical deformation, the associated frequency (ω_n) can be directly correlated with a mechanical response. Typically, the lowest frequency modes are related to rigid-body motions and continuum-like deformations, such as twisting, bending, and stretching. As a representative model for the determination of these vibrational frequencies (*i.e.*, eigenvalues), elastic network models (ENMs) provide an efficient means [326, 153, 154, 319, 347] to construct an effective stiffness matrix.

Most frequently, if the elastic network model is formulated by elastic potentials (*e.g.*, similar to Equation 2.23), the frequencies and mode shapes are evaluated by diagonalizing the second derivative of the potential energy (or Hessian matrix), defined by:

$$H_{ij} = \frac{\partial E}{\partial x_i \partial x_j} \qquad (2.28)$$

where E is the total potential energy of system, and x_i, x_j are perturbation of atomic position on atom i and j. The eigenvalues of mass-weighted Hessian matrix, **H'**, give the frequencies of corresponding modes, defined by:

$$\mathbf{H'} = \mathbf{M}^{-1/2}\mathbf{H}\mathbf{M}^{-1/2} \qquad (2.29)$$

where **M** is a diagonal matrix of atomistic masses. The corresponding eigenvectors of **H'** represent the mode shapes required to correlate to a mechanical response. Six rigid body modes are indicated by zero frequencies (including three translation and three

rotation modes). Most of the next-higher modes (modes are ranked by eigenvalues from low to high) with low frequencies are collective modes, typically corresponding to elastic deformations such as twisting, bending and stretching. In the elastic network model, the Hessian matrices are often very sparse after introducing a cutoff range for the interaction. Thus diagonalizing these matrices requires much less computational effort and memory storage in comparison with full atomistic force fields.

As an alternative, in continuum dynamics and structural analysis, the vibration of large macroscale structures can also be described by the equations of motion through eigenmode analysis - the classical eigenvalue problem. The governing matrices are developed using a stiffness-based approach (*i.e.*, also called the direct stiffness method [24, 213]), where:

$$\{F\} = \mathbf{K}\{\Delta\} \tag{2.30}$$

where $\{F\}$ corresponds to applied loads (per node), Δ the governing displacement field, and $\mathbf{K}$ the stiffness matrix. The associated eigenvalue problem takes the general form for vibrational mode superposition [24, 63]:

$$[\mathbf{K} - \lambda\mathbf{M}]\eta = 0 \tag{2.31}$$

where $\mathbf{K}$ is the previously described global stiffness matrix, λ the set of eigenvalues, and η the corresponding eigenvectors. The final component, $\mathbf{M}$, is the consistent mass matrix. The direct stiffness method presumes the equivalence of molecular rigidity with a classical flexural member, facilitating the formulation of $\mathbf{K}$. In effect, we reduce the cross-linked polyelectrolytes to beams connected *via* springs, and impose ideal flexural modes, used to characterize the complex as a single mechanical unit/element (see Figure 2-10).

Normal-mode-based approach makes it possible to analyze the intrinsic mechanical properties of a system without the need for applied loads, boundary conditions and removes the constraint of accessible timescales in direct MD simulations. In contrast to applying force or strain loads, the normal mode decomposition of macromolecular
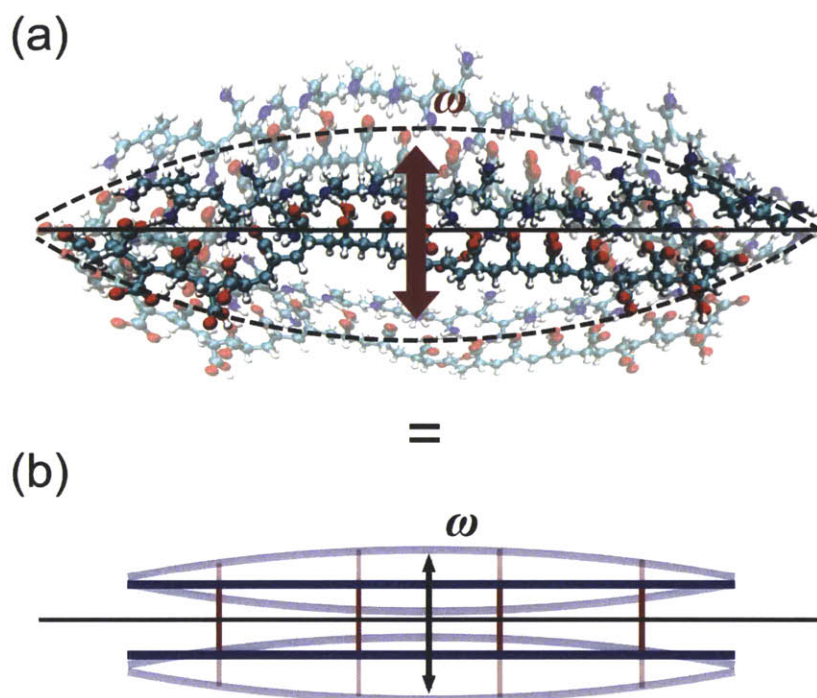
Figure 2-10: Atomistic and elastic model normal mode equivalency. The developed elastic model presumes equivalency between the flexural rigidity of (a) the molecular complex and (b) the structural model, determined by the free vibrational modes (*e.g.*, eigenvalue problem) and frequencies, ω_i. Properties determined from the idealized model can then associated with the polyelectrolyte complex as a single mechanical unit/element.

motions provides a specific frequency and stiffness for each mode, and thus offers direct information on the elastic constants of an equivalent continuum model. Provided that the collective motion of the molecular system corresponds directly (or closely) to the deformation modes assumed in a continuum model, the parameters extracted from a normal mode analysis are be related to the elastic constants in continuum models [321, 91, 319]. However, normal-mode analysis is also limited by the simplicity of the representative elastic network model. That is, if full-atomistic conventional force-field methods were to be used in the formulation of the Hessian or stiffness matrix, the resulting analysis would quickly become computationally intractable. Further, the predicted mechanical properties are restricted to elastic response, with no indication of potential failure mechanisms. While beneficial, the results of normal mode analysis
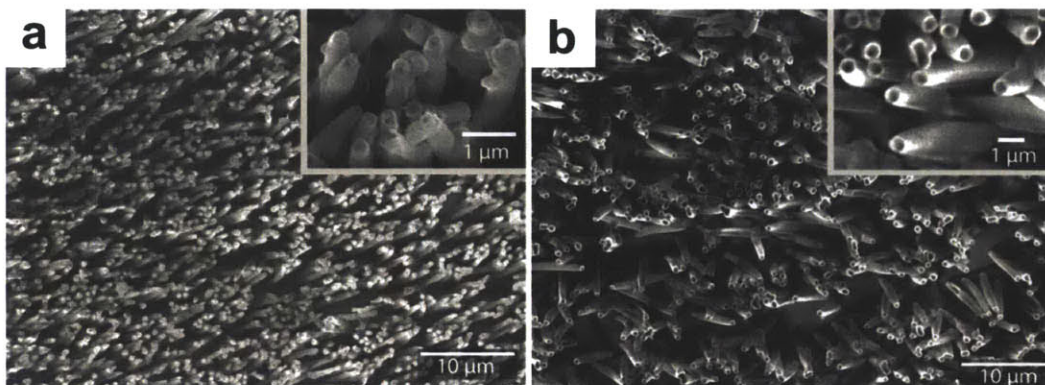
Figure 2-11: SEM images of (PAH7.5/PAA3.5)$_{20}$ PEM tube arrays synthesized with TEPC membranes with pore sizes of (a) 0.4 μm and (b) 0.8 μm. Inset: Higher magnification. From Chia et al. [59], used with permission, copyright © 2009 American Chemical Society.

can be complementary to properties extracted by other methods - *e.g.*, predicting critical modes of deformation to probe *via* full atomistic means [96].

2.3.4 Coarse-Graining PEM Microtubes

Due to the homogeneity of the structure, nanoscale and microscale tubes and fibrils are conducive for a coarse-graining approach. Simple bead-spring representations of the tube can be used to probe single filaments beyond atomistic length scales, or to develop and characterize large systems such as vertically aligned arrays [69], bundles [76, 39], random aggregates [77], and/or dense plaques [247]. For such structures, the developed coarse-grain model must capture two essential components: (1) the mechanical behavior of the fibrillar structure, for both stretching and bending, and; (2) the intra- and interfibrillar interactions between adjacent structures. We apply the approach here from PEM microtubes synthesized in vertically aligned arrays (see Figure 2-11), in order to characterize a range of mechanical responses (to be furhter discussed in **Chapter 6**).

As a reference for coarse-grain parameterization, AFM-based nanoindentation experiments were previous implemented to extract the mechanical properties of the PEM tubes and films [142]. Supported by previous continuum-level FE models of individual tubes and arrays [142, 143, 337], the mechanical behavior of the individ-

ual tubes can be captured by an "effective model" of a solid cylinder whereby the geometrical parameters and mechanical properties together provided the equivalent mechanical behavior and deformation mechanisms (*i.e.*, compression, bending, and buckling) of the hollow tubes.

The intent is to apply a coarse-graining approach to achieve a mechanical response while maintaining far-field and contact properties, an approach more *apropos* than equivalent continuum or elasticity techniques due to the system dependence on intermolecular interactions. To extend the capacity of particle interactions and exploit a MD computational framework, a novel coarse-grain representation is developed that can capture the deformation behavior of individual microtubes while reflecting random tube-tube interactions. Indeed, while coarse-grain models have successfully been developed for nanoscale fibrillar (*e.g.*, axial) structures such as carbon nanotubes [69, 77, 76, 39] and amyloid fibers [246, 247], the *micro*meter length scale of the PEM tubes requires modification to such particle-spring formulations. Previous "bead-spring" models typically employed Leonard-Jones-type interactions for fibrillar adhesion and friction, derived from molecular behavior (*i.e.*, the van der Walls interactions between adjacent carbon nanotubes, or weak hydrogen bonding between amyloid fibers). At the scale of PEM microtubes, there is little to no adhesion, and repulsion is more accurately captured by elastic deformation theory rather than molecular interpretations. We thus define the energy landscape as:

$$E_{tube} = E_{structure} + E_{contact} \tag{2.32}$$

where $E_{structure}$ captures the mechanical rigidity of the PEM tube, while $E_{contact}$ accounts for resistance due to contact and elastic hertzian deformation of the tubes. This decomposition of contributions is depicted schematically in Figure 2-12.

PEM Tube Coarse-Grain Representation (Structural Backbone)

For the polyelectrolyte multilayer tubes, an effective structural backbone is parameterized by known geometric and mechanical properties through a consistent energy
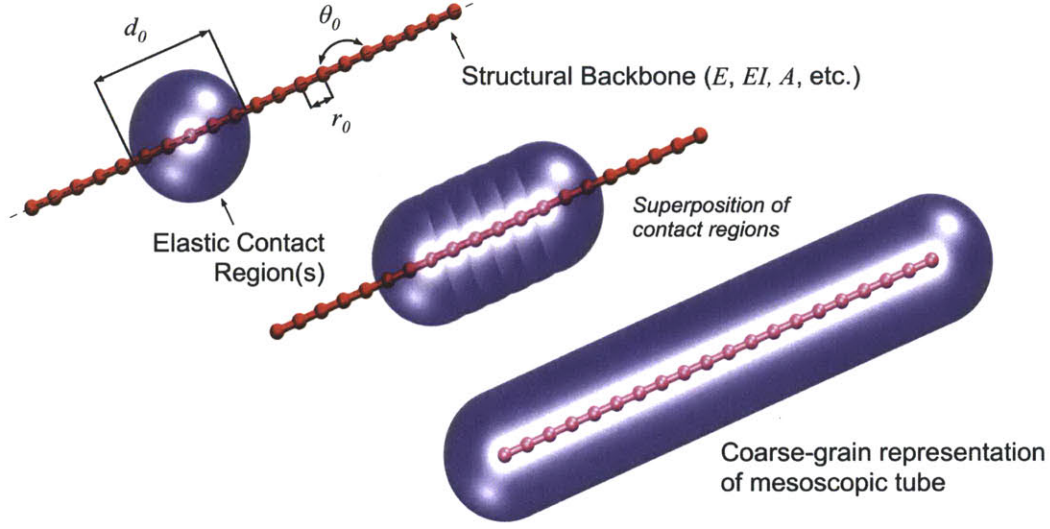
Figure 2-12: Representative coarse-grain PEM microtube model. The developed model can be formulated as two components - a structural backbone coupled with tube-tube contact regions (a mesoscopic pair potential), parameterized by known geometric and mechanical properties through a consistent energy approach. The structural backbone accounts for axial stiffness (*e.g.*, Δr_0) and bending rigidity (*e.g.*, $\Delta \theta_0$), whereas an elastic contact region accounts for spatial geometry and inter-tube contact (here assumed Hertzian). The model is parameterized only by the intrinsic stiffness of the PEM (defined by the modulus, E) and the geometric properties of the tubes (inner and outer diameter, A_c, I, etc.)

approach, based on a principle of energy conservation between elastic strain energy and coarse-grain potentials formulations. The structural model of each tube is represented by a function of the total energy of the system expressed as:

$$E_{structure} = E_T + E_B = \sum_{bonds} \phi_T + \sum_{angles} \phi_B \tag{2.33}$$

where E_T is the energy stored in the material bonds due to axial stretching, and E_B is the energy due to bending. The total energy contribution of each is calculated by a sum over all pair-wise (bonded) and triple (angular) interactions in for each nanotube. From the empirically determined Young's modulus (E) of the PEM composite, the axial stretching behavior of the representative particle-spring element is defined. Nonlinear behavior is neglected, as the coarse-grain simulations are intended for (and limited to) small deformation conditions. The total bond energy of the coarse-grain system is given by the sum over all bonded interactions (as expressed by Equation

2.33). For axial stretching a simple harmonic spring is used to determine the energy between all bonded pairs of particles in the system, given by:

$$\phi_T(r) = \frac{1}{2}k_T(r - r_0)^2 = \frac{1}{2}k_T\Delta r^2 = \phi_T(\Delta r) \tag{2.34}$$

with k_T as the spring constant relating distance, r, between two particles relative to the equilibrium distance, r_0. We assume each linear regime can be approximated using the equivalent elastic strain energy and utilize the determined Young's modulus to allow the formulation of strain energy and an equivalent k_T. The equivalent elastic strain energy is expressed as:

$$U(\epsilon) = \frac{1}{2}\int_{\overline{V}}\sigma\epsilon d\overline{V} = \frac{1}{2}\frac{A_c E\Delta r^2}{r_0} = U(\Delta r) \tag{2.35}$$

For the integration over the volume, $\overline{V}$, we assume a constant cross-section, A_c, such that $\overline{V} = A_c r_0$, define strain, $\epsilon = \Delta r/r_0$, and stress, $\sigma = E\epsilon$. Caution must be taken not to overextend the significance of the coarse-grain equivalence. Here, we only apply Young's modulus to characterize the work required to deform the PEM tube, and thus train the coarse-grain potential. It is not implied that PEMs can be completely described by elastic formulations, but such properties provide appropriate, conventional and convenient measures for behavior such as small deformation axial stretching. For equivalent energy and consistent mechanical behavior, we let $\phi_T(\Delta r) = U(\Delta r)$ and find:

$$k_T = \frac{A_c E}{r_0} \tag{2.36}$$

For the angle potential, E_B, the effective bending stiffness EI, of the PEM tube is required, calculated by the known modulus and measured geometry of the tubes. The bending energy is given by a sum over all triples in the system (Equation 2.33). For bending a rotational harmonic spring potential is used to determine the energy between all triples of particles in the system:

$$\phi_B(\theta) = \frac{1}{2}k_\theta(\theta - \theta_0)^2 = \frac{1}{2}k_T\Delta\theta^2 = \phi_B(\Delta\theta) \tag{2.37}$$

with k_θ as the spring constant relating bending angle, θ, between three particles relative to the equilibrium angle, $\theta_0 = 180°$. Again, using the equivalent elastic energy, we utilize the bending stiffness, EI, to allow the formulation of elastic energy and an equivalent k_θ. Since the bead-spring reflects three-point bending (simply supported member with central point load), we apply the equivalent load condition to approximate the elastic energy, $U(d)$, where:

$$U(d) = \frac{48EI}{L^3}d^2 = \frac{48EI}{(2r_0)^3}d^2 \tag{2.38}$$

where L is the bent length of the tube (note, by definition $L = 2r_0$) and d is the displacement at the load point. Again, application of beam-theory to PEMs is a matter of judgment, as considerations must be made for deformation mechanisms (*i.e.*, the presence of nonlinear plastic hinging or shear deformation). For small deformation, $\Delta\theta \approx 2d/r_0$, such that:

$$U(\Delta\theta) = \frac{3}{2}\frac{EI}{r_0}\Delta\theta^2 \tag{2.39}$$

Letting $\phi_B(\Delta\theta) = U(\Delta\theta)$:

$$k_\theta = \frac{3EI}{r_0} \tag{2.40}$$

Development of Mesoscale Pair Potential (Hertzian Contact)

We next characterize intertube interactions arising due to contact between pairs of non-bonded coarse-grain elements, $E_{pair} \equiv E_{contact}$, where:

$$E_{contact} = \sum_{pairs} \phi_{contact} \tag{2.41}$$

Pair potentials for molecular simulation typically account for the strong repulsive forces between atoms at close range (*i.e.*, Pauli repulsion at short ranges due to over-

lapping electron orbitals). Such repulsive forces are typically described by high-order polynomial or exponential terms in the pair potential formulation (*e.g.*, the commonly implemented Lennard-Jones 12:6 or Morse potential functions). At the mesoscale, however, such strong repulsion is unrealistic for coarse-grain body-to-body interactions such as contact between the current PEM nanotubes. Even within small deformation limitations, the interactions prescribed by traditional pair potentials result in "rigid" material interactions, limiting the effect of contact deformations critical to the nanotube system. The desire for a "soft" potential has been adopted for other computational techniques such as discrete element methods (DEM) [305] and discontinua approaches for microscopic granular systems [83, 355, 34]. Here, a similar accurate representation of contact deformation is desired, and as such we implement a coarse-grain pair potential developed from elastic theory. Previous indentation experiments on PAH/PAH PEM films, at both pH 2.0 and 5.5 indicate typical continuum multi-axial stress and strain field characteristics, of classical Hertzian contact, regardless of the indentation depth and physical state [142], suggesting such an approximation is valid for small-deformation applications.

The following aspects guide the formulation of such a simple contact potential for mesoscale: (i) a smooth and short-range potential, adequate for large integration steps used in the coarse-grain simulations; potential cutoff implemented to consider contact only (similar to truncated Lennard-Jones, or Weeks-Chandler-Anderson potentials [342, 150]); (ii) a sound theoretical basis in elastic theory, corresponding to the development of both bond (axial stretching) and angle (elastic bending) potentials through consistent elastic energy formulations (see [44] or [75] for examples); (iii) applicability and transferability to typical MD simulations, in terms of limited parameters required and simplicity of potential. Furthermore, the parameters are physically meaningful and used in a consistent manner.

The mathematical theory for the general three-dimensional contact problem was first given by Hertz in 1881, and there is extensive literature dealing with the contact problem [188, 125]. The solution to the normal contact between two elastic spheres can be analytically described according to Hertzian theory, with a few limiting as-
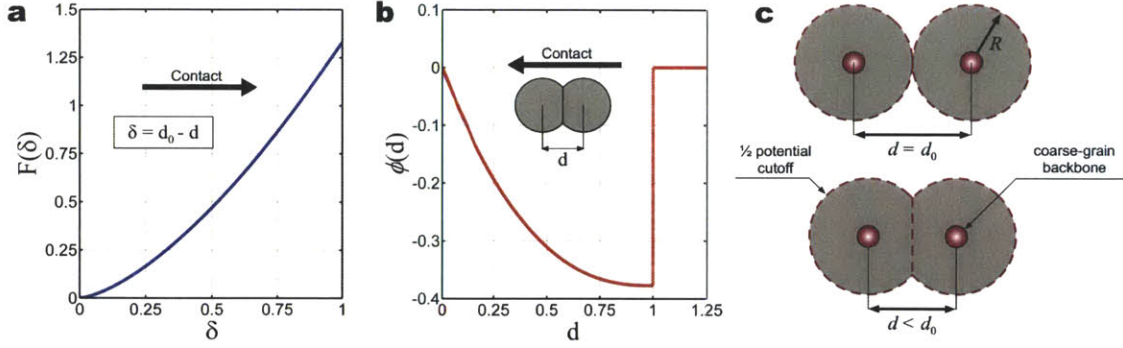
Figure 2-13: Governing Hertzian elastic contact mechanics. (a) Representation of Hertz's force-deflection relationship (Equation 2.42) for contact of two perfectly elastic spheres, where $K = 1.0$, and $R = 0.5$ such that $d_0 = 1.0$. (b) Derived contact pair potential (Equation 2.47), as a function of inter-particle spacing, d, applicable for $d < d_0$. (c) Range of coarse-grain contact potential. The contact pair potential is a function by the inter-particle spacing, d. Contact is defined by $d < d_0$ where $d_0 = 2R$, *i.e.*, equivalent to the diameter of the tubes.

sumptions[6]. Asserting these assumptions strictly on the current material system can be considered a first-order approximation of system behavior. We intentionally select the contact of two spheres to facilitate formulation as a molecular pair potential, typically described by a cutoff that defines a spherical region (*i.e.*, symmetrical potential field).

Hertz's force-deflection relationship (Figure 2-13a) for contact of two perfectly elastic spheres is [167]:

$$F(\delta) = \frac{4}{3}KR^{1/2}\delta^{3/2} \tag{2.42}$$

where K is the effective stiffness (N/m^2), and R is the radius of the sphere(s) in contact (m). In general, the effective stiffness between two bodies in contact, K_{ij}, is defined by:

$$\frac{1}{K_{ij}} = \frac{1 - \nu_i^2}{E_i} + \frac{1 - \nu_j^2}{E_j} \tag{2.43}$$

For the current investigation, only one material is being represented, thus:

---

[6]*e.g.*, that the surfaces in contact are perfectly smooth, that the bodies are isotropic and linearly elastic, that the elastic limits of the material are not exceeded, and that there are no frictional forces in action.

$$K_{PEM} = \frac{E_{PEM}}{2(1 - \nu^2_{PEM})} \tag{2.44}$$

where E_{PEM}, is the empirically determined elastic modulus of the nanotubes while ν_{PEM} is the Poisson's ratio (taken here as $\simeq 0.3$). It is again noted the above formulation is simplified by general assumptions, including: (i) the implied elasticity, isotropy, smoothness and homogeneity of the material; (ii) statically applied loading between the two spheres; (iii) small deformation and limitations in contact interface area and curvature; (iv) no friction at the contact surface. The validity of such simplifications has been investigated for specific systems, for example, and the reader is referred to Dintwa *et al.* [93] for a discussion on the accuracy of the Hertz model in terms of friction, contact surface, and small deformation strain assumptions. Here, we intentionally maintain a *minimalist* formulation to allow the transferability of such a "contact potential" to a wide array of systems. For the equivalent potential, we define the work of the contact force as:

$$\phi_{contact}(\delta) = \int F(\delta)d\delta = \frac{4}{3}KR^{1/2}\int \delta^{3/2}d\delta = \frac{8}{15}KR^{1/2}\delta^{5/2} + \phi_0 \tag{2.45}$$

Let $\delta = \Delta d = (d_0 - d)$ where $d_0 = 2R$ by geometry, and $\phi_0 = 0$, then (Figure 2-13(b)-(c)):

$$\phi_{contact}(\delta) = \begin{cases} \frac{8}{15}K\sqrt{\frac{d_0}{2}}(d_0 - d)^{5/2}, & d \leq d_0 \\ 0, & d > d_0 \end{cases} \tag{2.46}$$

For implementation into coarse-grain MD, we simplify the relation to two parameters, $\alpha_{contact}$ (in kcal/mol/3) and d_0 (Å), such that:

$$\phi_{contact}(\delta) = \alpha_{contact}\sqrt{d_0}(d_0 - d)^{5/2} \tag{2.47}$$

The above relation is plotted in Figure 2-13(b). Implementation was achieved by extending the LAMMPS source code to enable the treatment of the developed contact
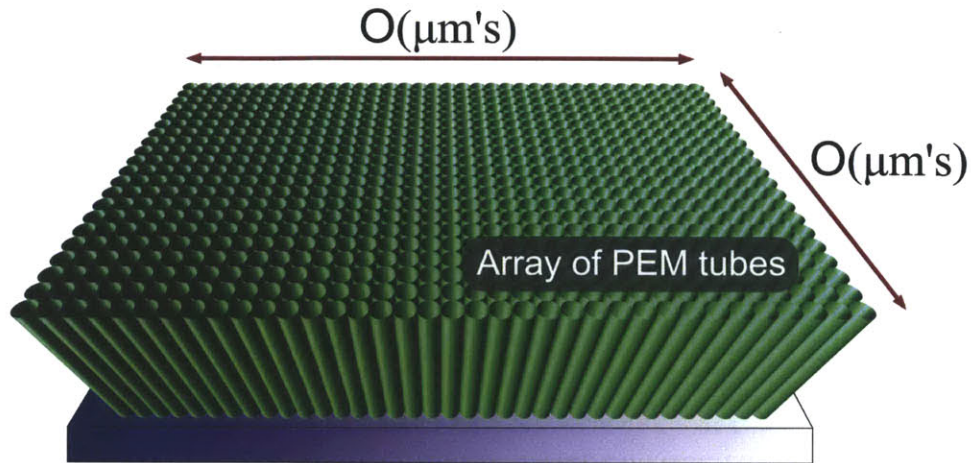
Figure 2-14: Constructed model of hundreds of PEM microtubes in a vertically aligned array, implementing the coarse-grain potentials for structural rigidity and contact stiffness described herein. Thousands of elements are implemented to extend the accessible length scale to the order of micrometers (μm).

potential, only requiring the parameterization of two variables ($\alpha_{contact}$ and d_0) to define the material interaction.

We assume this pair-wise interaction between different particles is sufficient to describe the contact between the coarse-grain elements under small deformation (*e.g.*, there are no multi-body considerations). As the coarse-grain particles are fundamentally point masses, it is also noted that a representative geometric "thickness" is a direct consequence of the pair potential.

The final consideration for the mesoscopic coarse-grain model is the assignment of mass to the particles. The mass of each bead is determined by assuming a homogeneous distribution of mass in the PEM tube. Note that the mass of each bead will scale with the selection of equilibrium bond distance, r_0. Being said, it behooves us to note that the full implication of this mass assignment approach to coarse-grain models on such thermodynamic properties as temperature effects has not been thoroughly investigated. However, the approach has proven adequate for investigations focusing on mechanical behavior at constant temperature conditions.

Finally, we can now define the mesoscopic model potentials by six parameters:

k_T; r_0; k_θ; θ_0; $\alpha_{contact}$, and; d_0. Empirical results and measurements are used to determine these six parameters *via* geometric conditions (r_0; θ_0; d_0) and mechanical behavior (k_T; k_θ; $\alpha_{contact}$) by imposing energy equivalence. It is noted such a PEM tube system is typically found in solution, and the influence of the solvent on the behavior of the material is captured in the aforementioned model constants, such that no explicit modeling of solvent is required. Typically, such models do not require an explicit solvent nor an implicit solvent force field - the effect of solvation is captured implicitly by the derived parameters and integrated into the coarse-grain potentials. Being said, an effective viscous damping parameter is introduced to reflect frictional drag on the system. Such a model can then be used to construct large arrays of identically parameterized tubes, as a basis for mechanical characterization. Such an array is depicted in Figure 2-14. This model is implemented in **Chapter 6: Beyond Full Atomistic Characterization.**

2.4   Summary

In the past, understanding of how materials mechanically behave was limited to phenomenological engineering theories that describe macroscale materials behavior, neglecting the underlying atomistic microstructure. Being said, deformation and failure of materials is ultimately governed by atomistic and chemical interactions. To include these effects, atomistic models and MD approaches were developed, capable of simulating the motion of all atoms in the material - yet limited in represented time (up to microseconds) and length (approaching micrometers). The goal of such atomistic models is to understand the macroscopic response of materials, for example, under mechanical stimulation, based on their fundamental, atomistic ultrastructure.

Along such lines of thought, computer simulations have sometimes been referred to as "computational experiments". Designing smart computer experiments is the key to successful simulation. Computational modeling allows a bottom-up approach in understanding the *materiome* of a system, focusing on the finest, atomistic scales of detail governed by quantum mechanics as a *de facto* starting point, reaching up

to large macroscopic scales described by continuum models, using hierarchical multiscale, or scale-bridging, modeling. Such approaches are complementary to many experimental efforts starting at the macroscopic level and reaching down to finer scales.

Modern multiscale modeling techniques use a sequence of overlapping hierarchies encompassing various simulation tools to bridge the scales from nano to macro. Book-ending these techniques are quantum mechanics, encapsulating the basic constituents of matter (electrons, protons, etc.), and continuum theory, which, by definition, has no limiting scale. These modeling techniques allow a rigorous linking of material properties. While bridging scales ultimately results in loss of "mechanical resolution", this does not prevent the utility of such approaches. The reduction of quantum-level interactions to bond potentials in atomistic force fields (in essence simple harmonic springs) does not limit the application of MD - the *necessary* behavior is maintained. This shares the same principle as coarse-graining a system of atoms into an effective "bond". Being said, defining the necessary behavior (and thus interaction parameters) is nontrivial. There is inherent value in the abstraction of defining a chemical bond as a spring - effectively a mechanical description relating load and deformation - as certain patterns of interactions lead to characteristic functional units.

Coarse-grain models provide an efficient means to simulate and investigate such systems in which the desired behavior, property or response is inherently at the mesoscale. The relatively few parameters and potentials that define a coarse-grain representation must accurately represent the full atomistic behavior of the structure in both mechanical response and intermolecular interactions. This simplification also allows a pragmatic approach to system analysis - similar to the simplification of macroscale systems - delineating global behavior from constituent element properties, thereby encompassing multiscale structure-property relations. Extension of accessible time- and length-scales can allow direct correlations with empirical investigations, providing a novel tool for experimental design and material characterization from the bottom-up and encompass the entire materiome.

Chapter 3

Variation of Molecular Rigidity

Prior to the investigation of a polyelectrolyte complex (*e.g.*, cross-linked molecules of different chemical species), full understanding of the behavior of a single molecule in isolation is a necessary intermediary. Indeed, how each molecular species behaves independently must be delineated in order to deduce any enhanced (or diminished) effects of complexation. This chapter investigates and quantifies (both computationally and theoretically) the variation of molecular rigidity for PAA and PAH as a function of ionization. It is well known that additional charge along a polymer chain induces self-repulsion, increasing persistence and thus rigidity, but a general method to quantify the change in highly flexible polyelectrolytes has not reached a consensus. Here, simple mechanical and energetic arguments are presented to separate the polymer contour length from an abstract "electrostatic contour" that is able to capture the effect of electrostatic persistence at small length scales *ex post*. Consequently, variation of rigidity with ionization is determined, to be used in the elastic complexation model (**Chapter 5**).

3.1   Electrostatic Persistence Length

Despite extensive work regarding polyelectrolytes, important aspects are still not well understood, even for the relatively simple case of single macromolecules in solutions of good solvent quality, disregarding the interesting interplay of chain stretching and col-

lapse that occurs in poor solvents. For example, there is currently no consensus that the classical perspective of electrostatic persistence length (so-called Odijk-Skolnick-Fixman, or OSF, formulation), derived by equating changes in electrostatic energy with bending rigidity, is applicable to weak (and highly flexible) polyelectrolytes. Characterizing the flexibility - or stiffness - of polymer chains is of basic importance for describing their structure and dynamics. To facilitate the use and design of such systems, simple yet theoretically sound design models are critical to capture the properties of synthetic polymers. Moderately stiff, or semiflexible, macromolecules behave like rods at the atomistic scale, and the stiffness can be captured by the concept of persistence length. It is well known that adding self-repulsive charges through ionization increases the persistence length (and thus effective rigidity) of polyelectrolytes.

In this chapter, we formulate a simple and general theoretical model featuring an electrostatic persistence length, P_e, through the introduction of an electrostatic contour length, L_e, such that the electrostatic energy balance is applicable to highly flexible charged polyelectrolytes. At the upper limit (rigid molecules), the new formulation converges to the classical OSF form, while the lower bound (flexible molecules) approaches proportionality to the Debye screening length, κ^{-1}. The theory is validated *via* full atomistic MD simulations of single, isolated model weak polyelectrolyte chains in explicit solvent - specifically poly(acrylic acid), PAA, and poly(allylamine hydrochloride), PAH, both of which undergo significant increases in persistence length under ionization. An ensemble of equilibrated polymer states is obtained *via* temperature assisted sampling, implementing MD to drive the polymers into physically accessible conformations *via* cyclical temperature fluctuations and equilibration.

Polyelectrolyte materials made from weak (and highly flexible) polyelectrolytes have the advantage that their *mechanical* properties can be tuned by pH-driven ionization. One well known behavior is the change of polymer rigidity and conformational changes with variation in electrostatic charges - at high levels of ionization, due to an increase repulsion of like charges, the polymer segments are more extended, whereas decreasing the ionization results in globular regions of aggregated segments [303, 166]. This behavior has been exploited to fine-tune the thickness of PEM systems during

102

the assembly process [303, 62]. A transition occurs when the charge density drops below a critical value to maintain a flattened conformation, resulting in clusters of loops and tails. At high levels of ionization, the entropic penalty for a flattened conformation is overcome by enthalpic gain of the PEM system, whereas a decrease in ionization results in insufficient energy to overcome the loss of configurational energy [303].

Being said, the theoretical understanding of macromolecules carrying ionizable groups remains challenging, particularly regarding the variation and effect of molecular rigidity. After several decades of investigation there is still no consensus on the behavior of the electrostatic persistence length of polyelectrolytes [111, 329, 26, 97]. Here, we reconcile the classical perspective of electrostatic persistence length (so-called Odijk-Skolnick-Fixman, or OSF, formulation [241, 306]) with previously introduced modifications (through empirical power-law dependences) *via* the introduction of an "*electrostatic contour length*".

3.2 Requisite Polymer Theory

The persistence length is a measure of how far a polymeric chain persists in a given direction, and therefore defines chain rigidity (critical to any cross-linked LbL polyelectrolyte system). From a mechanical perspective, the persistence length is defined as the molecular length at which entropic contributions to elasticity become important, as the molecular shows significant bending purely due to its thermal energy (*e.g.*, $k_B T$). A molecule with length far beyond the persistence length will bend, even without application of forces, and assume a conglomerated shape. With the bending stiffness of a polymer chain or polyelectrolyte complex denoted as D, the persistence length, P, is defined as:

$$P = \frac{D}{k_b T} \tag{3.1}$$

where, k_B is the Boltzmann constant and T the absolute temperature. Note that, from a structural perspective, $D \equiv EI$, for a traditional flexural member (such as a

Euler-Bernoulli beam). If we therefore quantify the persistence length of a polymer, P we indirectly determine the effective bending rigidity, D.

3.2.1 Mean Square End-to-End Distance

A rough measure of the average size of a polymer is given by the mean square end-to-end vector ($\langle R^2 \rangle$). The end-to-end vector, $\vec{R}$, is given by:

$$\vec{R} = \vec{R}_N - \vec{R}_0 = \sum_{i=1}^{N} \vec{r}_i \tag{3.2}$$

The mean square then reads:

$$\langle R^2 \rangle = \langle (\sum_i \vec{r}_i) \cdot (\sum_j \vec{r}_j) \rangle = \sum_i \sum_j \langle \vec{r}_i \cdot \vec{r}_j \rangle \tag{3.3}$$

3.2.2 Ideal Worm-Like Chain Behavior

The worm-like chain (WLC) model assumes an isotropic rod that is continuously flexible - while the current polyelectrolytes may be considered freely-jointed chains due to the flexibility only between discrete carbon backbone segments, the composite behavior of a complex of polyelectrolytes cannot be described as such, and thus the WLC model is implemented for consistency. The persistence length and the contour length comprise the adjustable parameters of the WLC model.

For a polymer of length L, the path of the polymer is parameterized as $s \in (0, L)$. Defining $\vec{t}(s)$ as the unit tangent vector along the chain at s, and $\vec{r}(s)$ to be the position along the chain. Then:

$$\vec{t}(s) = \frac{\partial \vec{r}(s)}{\partial s} \tag{3.4}$$

and the end-to-end distance

$$\vec{R} = \int_L \vec{t}(s) ds \tag{3.5}$$

The orientation correlation function for a WLC follows an exponential decay:

$$\langle \vec{t}(s) \cdot \vec{t}(0) \rangle = e^{-s/P} \tag{3.6}$$

where P is by definition the polymer's characteristic *persistence length*. The persistence length can then be related to mean square end-to-end distance of the polymer as described by Eq. 3.3:

$$
\begin{aligned}
\langle R^2 \rangle &= \langle \vec{R} \cdot \vec{R} \rangle \\
&= \langle \int_L \vec{t}(s) ds \cdot \int_L \vec{t}(\tilde{s}) d\tilde{s} \rangle = \int_L ds \int_L \langle \vec{t}(s) \cdot \vec{t}(\tilde{s}) \rangle d\tilde{s} \\
&= \int_L ds \int_L e^{-|s-\tilde{s}|/P} d\tilde{s} \\
&= 2PL[1 - \frac{P}{L}(1 - e^{-L/P})]
\end{aligned}
\tag{3.7}
$$

Note that in the limit of $L \gg P$, then $\langle R^2 \rangle \cong 2PL$.

3.2.3 Odijk-Skolnick-Fixman Electrostatic Persistence Length

The measurement and prediction of the persistence length, P, of polymers has been an important topic for the last few decades since the rigidity of a polymer is a crucial parameter for its conformation. In the particular case of polyelectrolytes, the persistence length, P, typically is considered a sum of two contributions, or:

$$P = P_0 + P_e \tag{3.8}$$

where P_0 is the intrinsic persistence length (attributable to the bonded chain structure and short-range nonelectrostatic interactions), due to the rigidity of the chain backbone and P_e is the electrostatic persistence length arising from the repulsion between neighboring ionic sites (largely dependent upon the ionic, or salt, concentration of the solution), resulting in additional effective stiffness. Odijk [241] and, independently, Skolnick and Fixman [306] were interested in bending fluctuations and considered the resulting increase of the electrostatic energy ($\Delta\phi_{electrostatic}$) relative to a ground state.
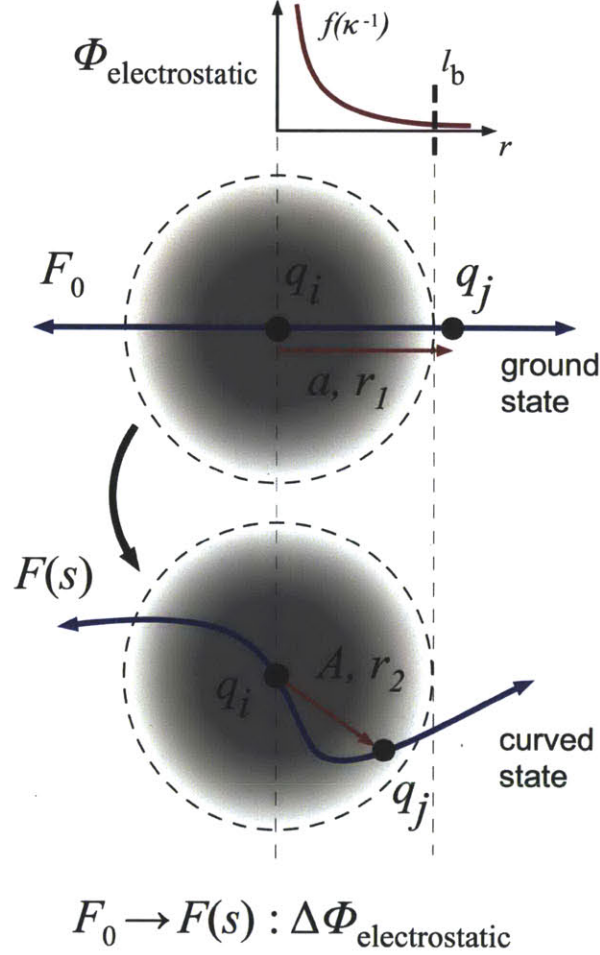
Figure 3-1: Energetic basis for electrostatic persistence length, P_e. A polymer with an extended ground state, F_0, has distributed charges, q_i, q_j, etc., separated by a distance a along the contour length (r_1), with an electrostatic interaction defined by $\phi_{electrostatic}$ (Equation 3.9). Upon transition to a curved state, $F_0 \to F(s)$, the charges are separated by a linear distance, A, or r_2 (where $r_2 < r_1$) such that the potential energy is increased by $\Delta\phi_{electrostatic} = \phi(r_2) - \phi(r_1)$.

In the low salt limit, the electrostatic screening length is considered much larger than the distance between charges on the polyelectrolyte chain, so a continuous charge distribution can be assumed along the polyelectrolyte length. The polymer therefore approaches an ideal structureless, charged space curve, *i.e.*, a worm-like polymer with a continuous charge distribution [306].

OSF theory [241, 306] considers a single chain characterized by its uncharged intrinsic persistence length, P_0, that carries uniform charges separated by a mean

distance, a, along its contour. The interaction between two charges, q, at a distance r is a screened Coulomb interaction, *i.e.*, $\phi_{electrostatic}$, described by the classical Debye-Hückel interaction:

$$\phi_{electrostatic} = \phi\left(r\right) = \frac{q_i q_j}{\epsilon r} \exp\left(-\kappa r\right) \tag{3.9}$$

dependent on l_B, the Bjerrum length (a measures of the strength of the interaction; *e.g.*, $l_B \cong 7\text{Å}$ in water at 300 K), the inverse screening length (or Debye length, κ^{-1}), related to the ionic strength of the electrolyte solution, and ϵ, the dielectric constant of the solution (note that here, for simplicity, q incorporates the energy conversion factor). For derivation of electrostatic persistence length, OSF computed the difference in electrostatic energy, $\phi_{electrostatic}$, between a strictly rod-like configuration ($\mathbf{F}_0$) and a slightly bent configuration of the chain ($\mathbf{F}\left(s\right)$). We consider here such a charged space curve (see Figure 3-1), from which we wish to calculate the persistence length due solely to the electrostatic interaction, P_e.

First, we assume $\Omega_{elastic}$ is the increase in elastic energy per unit length due to electrostatic repulsions relative to the reference configuration of a straight rod, given by:

$$\phi_{elastic} = \frac{1}{2}\frac{D}{R_c^2} \tag{3.10}$$

where D is the effective bending stiffness of the rod and R_c is the radius of curvature of the element of space curve at which ϕ is evaluated. It then follows that, for only electrostatic contributions:

$$P_e = \frac{D}{k_B T} \tag{3.11}$$

where k_B and T are again Boltzmanns constant and temperature. Thus, formulation of D can be exploited to derive P. Consider an arbitrary space curve parameterized by s, the contour length relative to the origin (see Figure 3-2). Let $\mathbf{F}(s)$ be a location of a point on the space curve, expressed as:

107
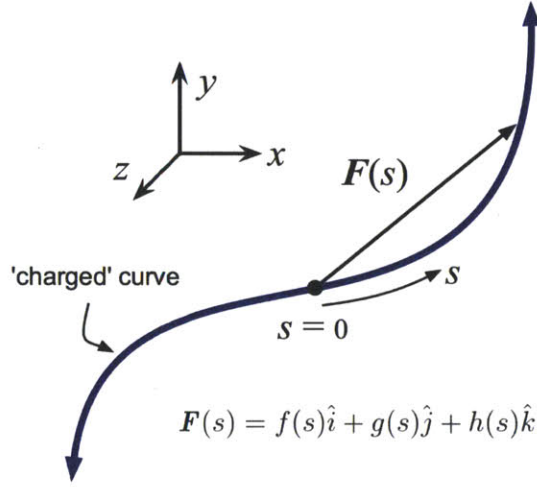
Figure 3-2: A general charged space curve, where $\mathbf{F}(s)$ is a defined arbitrary point along the curve (defined by Eq. 3.12), parameterized by s, the contour length relative to a prescribed origin.

$$\mathbf{F}(s) = f(s)\hat{i} + g(s)\hat{j} + h(s)\hat{k} \tag{3.12}$$

where $\hat{i}$, $\hat{j}$, $\hat{k}$ are the unit vectors in the x, y, and z directions respectively. We next introduce the formulation for the electrostatic energy of a single charge, q, as prescribed by Eq. 3.9. Defining the degree of ionization, α, and the distance between polyelectrolyte monomers, s_q, then the average charge per unit length of polymer is $\alpha q/s_q$. It follows that, for a given s along the curve from the origin, $r \equiv |\mathbf{F}(s)|$. Then, defining the difference in electrostatic potential at the origin relative to a straight rod configuration (where $|\mathbf{F}(s)| = s$):

$$\Delta\phi_{electrostatic} = 2\frac{\alpha q}{\epsilon s_q} \int_0^\infty \left[\frac{e^{-\kappa|\mathbf{F}(s)|}}{|\mathbf{F}(s)|} - \frac{e^{-\kappa s}}{s} \right] ds \tag{3.13}$$

From the derivation of Skolnick and Fixman [306]:

$$|\mathbf{F}(s)| = s\sqrt{1 - \frac{s^2}{12R_c^2}} \tag{3.14}$$

expanding $|\mathbf{F}(s)|$ and $e^{-\kappa|\mathbf{F}(s)|}$ in a Taylor series about $s = 0$ to terms of order $1/R_c^2$:

$$\frac{e^{-\kappa|\mathbf{F}(s)|}}{|\mathbf{F}(s)|} = e^{-\kappa s}\left[\frac{1}{s} + \frac{s}{24R_c^2} + \frac{\kappa s}{24R_c^2}\right] + \mathrm{O}\left(\frac{1}{R_c^3}\right) \tag{3.15}$$

Substituting the above expression into Equation 3.13 yields:

$$\Delta\phi_{electrostatic} = \frac{\alpha q}{\epsilon s_q}\frac{1}{4\kappa^2 R_c^2} \tag{3.16}$$

The potential of a segment of length dl is:

$$\phi_{electrostatic}dl = \frac{1}{2}\Delta\phi_{electrostatic}dq = \frac{1}{2}\Delta\phi_{electrostatic}\frac{\alpha q}{s_q}dl \tag{3.17}$$

From which it follows:

$$\phi_{electrostatic} = \frac{\alpha^2 q^2}{8\epsilon s_q^2\kappa^2 R_c^2} \tag{3.18}$$

Letting $\phi_{elastic} = \phi_{electrostatic}$, then:

$$D\left(\kappa\right) = \frac{\alpha^2 q^2}{4\epsilon s_q^2\kappa^2} \tag{3.19}$$

From which it follows:

$$P_e = \frac{D}{k_B T} = \frac{\alpha^2 q^2}{4\epsilon s_q^2\kappa^2 k_B T} \tag{3.20}$$

Noting the the Bjerrum length[1] is defined by:

$$l_b = \frac{q^2}{\epsilon k_B T} \tag{3.21}$$

Moreover, the spacing between charges can be expressed as $a = s_q/\alpha$. With these substitutions, Equation 3.20 can be simplified to:

$$P_e = P_{OSF} = \frac{l_b}{4\kappa^2 a^2} \tag{3.22}$$

Equation 3.22 is the classical OSF electrostatic persistence length for a continuous,

---

[1]Again, the Bjerrum length l_b characterizes the strength of the electrostatic interactions and is defined as the distance where the Coulomb energy of two unit charges q is equal to $k_B T$.

uniformly charged rod without charge rearrangements due to bending, and without fluctuations due to thermal motion (hence referred to as P_{OSF}). The elegance of the OSF formulation and simple energy balance has perhaps contributed to its use and longevity as the standard for defining the electrostatic persistence length. An attractive result is the appearance of a simple power law, where $P_{OSF} \propto \kappa^{-2}$. Being said, it is well-accepted that the OSF theory, although reasonably well verified for intrinsically rigid polyelectrolytes, is unsuitable for highly flexible chains [23, 97]. In such cases, the electrostatic persistence length has been reported to display no consistent power-law dependence at all [329], when the OSF assumptions breakdown (*e.g.*, WLC behavior, $P_0 \gg P_e$, $P_0 \gg \kappa^{-1}$, $a < \kappa^{-1}$, $a < l_B$). Indeed, for flexible polyelectrolytes, for which the intrinsic persistence length (P_0), electrostatic persistence length (P_e), and Debye screening length (κ^{-1}) are of the same order of magnitude, the relation is less clear.

Many studies have proposed to modify the OSF formulation beyond the so-called "OSF limit" [111]. Some simulations using large-scale Monte Carlo (MC) approaches have found no significant deviations from the prediction $P_e \propto \kappa^{-2}$ as described by Eq. 3.22 [111]. Other studies have reported the electrostatic persistence length to be $\propto \kappa^{-1.2}$ [330, 331, 329], or a linear dependence, $\propto \kappa^{-1}$ [271, 272, 23, 136, 97]. While there is consensus that the quadratic relation is a theoretical asymptotic value as P_0 approaches and exceeds P_e [194, 234, 111], multiple experiments and computational studies provide evidence for a comparatively weak κ-dependence [272, 168, 225, 27] (for extended discussions, see Everaers *et al.* [111], Ullner [329], or Dobrynin [97] and references therein). A modified OSF formulation can be re-written in general as:

$$P_e = \frac{C_0}{\kappa^{\alpha} a^2} \tag{3.23}$$

where the exponential parameter α allows for deviations from the OSF theory ($\alpha \in [1,2]$), while maintaining a power-law dependence with respect to κ (and C_0 is a empirical or theoretical fitted parameter). While theoretically supported by local increases in ionic concentration (*e.g.*, local fluctuations in κ), counterion condensation [9], or

short-range excluded-volume interactions [111, 232, 128], the initial elegance, simplicity, and rationale of balancing elastic strain energy with electrostatic contributions is lost.

3.3 Electrostatic Contour Length

Here, we take an alternative approach to the derivation and practical meaning of electrostatic persistence, while maintaining a theoretical foundation in the OSF assumptions while accounting for deviations beyond the OSF limit[2]. We consider that upon transition from a ground state to a curved state ($e.g.$, $\mathbf{F}_0 \rightarrow \mathbf{F}(s)$, the change in electrostatic energy, $\Delta\phi_{electrostatic}$, does not arise from the curvature of the polymer chain directly, but rather in the increased ionic interaction between adjacent charges (see Figure 3-3). The OSF formulation presumes an average distribution of charges along the contour length of the polymer chain, typically $a = L_0/n$, where L_0 is the total length of the polymer, and n is the number of charges ($e.g.$, electrostatic interactions are assumed to be smeared uniformly). Such an assumption is adequate for large charged macromolecules, when $P_0 \gg P_e$, such as DNA or aggrecan (20 to 60 nm contour length), as examples [26].

For weak polyelectrolytes, due to the finite length of the monomers, as well as the intrinsic flexibility ($e.g.$, as $P_0 \rightarrow P_e$), the actual charge-to-charge distance can deviate from a (depicted in Figure 3-3). However, only the linear distance between adjacent charges along the polymer length is critical to the screened Coulomb interaction, and thus affects the persistence length.

With this motivation, we impose an abstract "separation" of the electrostatic contribution from the intrinsic material behavior, through the introduction of an *electrostatic contour length*, L_e (see Figure 3-4). The electrostatic contour length defines a secondary chain length superimposed with the physical polymer. As electrostatic interactions and their effect are not bound to follow the contours of the polymer back-

---

[2]*i.e.*, our goal is to derive a simple OSF-like relation, applicable regardless of polyelectrolyte flexibility
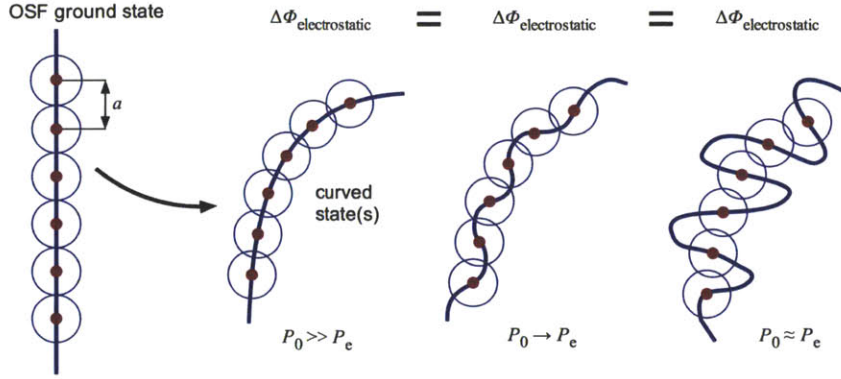
Figure 3-3: Change in energy from charge overlap. Upon transition from a ground state to a curved state (*e.g.*, $\mathbf{F}_0 \to \mathbf{F}(s)$, the change in electrostatic energy, $\Delta\phi_{electrostatic}$, does not arise from the curvature of the polymer chain directly, but rather in the increased ionic interaction between adjacent charges, regardless of charge separation along the contour (defined by a). For weak and flexible polyelectrolytes (as $P_0 \to P_e$), the actual charge-to-charge distance can deviate from a. However, only the linear distance between adjacent charges along the polymer length is critical to the screened Coulomb interaction, and thus affects the persistence length, equivalent in the cases depicted.

bone, the effective persistence length need not be a function of the actual contour length, L_0.

The electrostatic contour length is thus a loosely correlated "chain of charges", from which the OSF formulation can be applied (which only considers the energetic change from the Coulombic interactions), thereby independent of the specific charge distribution along the polyelectrolyte conformation. In that sense, we impose the same formulation as given in Equation 3.22, but implementing the spatial charge-to-charge distance, A (where $L_e = \sum A_i$), instead of the distance along the contour, a (where $L_0 = \sum a_i$), or:

$$P_e = \frac{l_B}{4\kappa^2 A^2} \tag{3.24}$$

Here, the primary difference is not in the energetic derivation, but rather the definition of contour charge spacing. By definition, $A < a$, and we anticipate an increase in the contribution of electrostatic persistence length for intrinsically flexible polyelectrolytes. As the definition of persistence length influences the calculated value [329], a review of the formulation and computational procedure used here is warranted. Here,
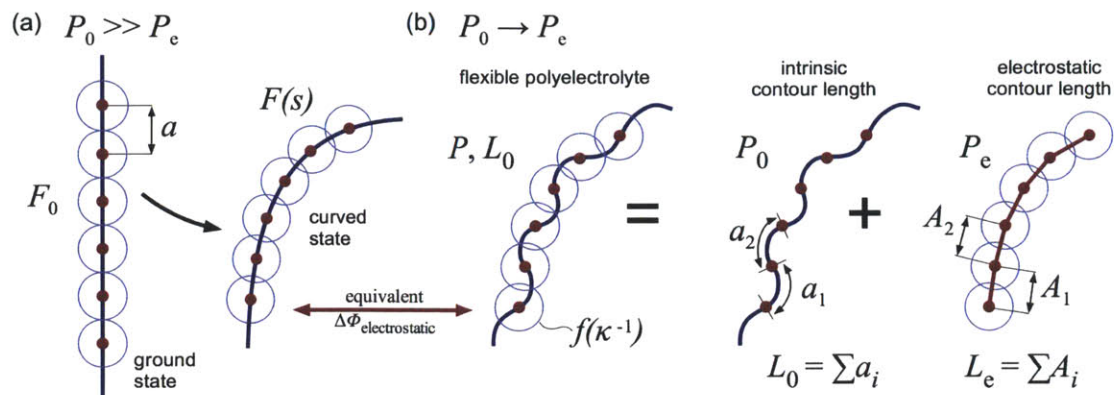
Figure 3-4: Separation of intrinsic and electrostatic contour lengths. (a) OSF conditions, where the intrinsic persistence length, P_0, is much larger than the electrostatic contribution, P_e. Electrostatic persistence length described by classical OSF formulation (Eq. 3.22) due to energetic changes displayed in Figure 3-1. However, upon transition from a ground state ($\mathbf{F}_0$) to an arbitrary curved state ($\mathbf{F}(s)$), the change in electrostatic energy, $\Delta\phi_{electrostatic}$, does not arise from the curvature of the polymer chain directly, but rather in the increased ionic interaction between adjacent charges. (b) For flexibility polyelectrolytes (as $P_0 \rightarrow P_e$), the screened Coulomb interaction is a function of the spatial charge-to-charge distance, defined as A, can deviate from a (along the contour). We separate the electrostatic contribution from the intrinsic material behavior (P_0, L_0), through the introduction of an electrostatic contour length, L_e, in addition to the electrostatic persistence length, P_e. The electrostatic contour length defines a secondary chain length superimposed with the physical polymer. The electrostatic contour length is thus a loosely correlated "chain of charges", from which the OSF formulation can be applied (which only considers the energetic change from the Coulombic interactions), thereby independent of the specific charge distribution along the polyelectrolyte conformation.

we determine persistence length as it relates to the mean-square end-to-end distance, $\langle R^2 \rangle$, as calculated by Eq. 3.3, according to the sequential vectors along the backbone of the polyelectrolyte (note that here, $|r_i| \approx a$). The common worm-like chain (WLC) formulation is used to determine the total persistence length, P, from the determined mean square end-to-end distance, according to Eq. 3.7. Again, we note that in the limit of $L \rightarrow P$, then $\langle R^2 \rangle \cong 2PL$. For simplicity, the following formulation applies this truncated version, but the argument remains the same.

The concept of electrostatic contour length effectively isolates the electrostatic persistence from the intrinsic persistence (that of a neutral polymer). As such, it serves as an abstract representation of the complex polymer interactions, which are effectively homogenized and indirectly quantified. From a mechanistic perspective,

similar to OSF equivalence between electrostatic and elastic contributions, the persistence length can be considered equivalent to the bending stiffness of a polymer chain or polyelectrolyte complex, and can be denoted by D, related to the persistence length by $Pk_BT = D$, or simply $P \sim D$, and thus $\langle R^2 \rangle \sim D$. In our separation of electrostatic contour length from the intrinsic material contour length, we effectively separate two distinct (but coupled) mechanical bending rigidities, which we can sum to attain the total (similar to a parallel spring system). It follows that:

$$\langle R^2 \rangle = \langle R^2 \rangle_e + \langle R^2 \rangle_0 = 2P_eL_e + 2P_0L_0 \qquad (3.25)$$

where $\langle R^2 \rangle_0$ is described by Eq. 3.3 and, considering vectors between adjacent charges:

$$\langle R^2 \rangle_e = \langle (\sum_i \vec{A}_i) \cdot (\sum_j \vec{A}_j) \rangle = \sum_i \sum_j \langle \vec{A}_i \cdot \vec{A}_j \rangle \qquad (3.26)$$

From Eq. 3.25, it follows:

$$\langle R^2 \rangle = 2 \left[P_e \frac{L_e}{L_0} + P_0 \right] L_0 \qquad (3.27)$$

By definition, $L_e = n\langle A \rangle$ and $L_0 = n\langle a \rangle$, such that $L_e/L_0 = \langle A \rangle / \langle a \rangle$, and is independent of the total length and number of charges, n, along the physical chain contour length, L_0 (note that here, the brackets "$\langle \rangle$" indicate the mean value). Then:

$$\langle R^2 \rangle = 2 \left[P_e \frac{\langle A \rangle}{\langle a \rangle} + P_0 \right] L_0 \qquad (3.28)$$

Substituting the modified OSF form of P_e (Eq. 3.24):

$$\langle R^2 \rangle = 2 \left[\frac{l_B}{4\kappa^2 \langle A \rangle^2} \frac{\langle A \rangle}{\langle a \rangle} + P_0 \right] L_0 = 2 \left[\frac{l_B}{4\kappa^2 \langle A \rangle \langle a \rangle} + P_0 \right] L_0 \qquad (3.29)$$

Thus the effective electrostatic persistence length can be written as:

$$P_e = \frac{l_B}{4\kappa^2 \langle A \rangle \langle a \rangle} \qquad (3.30)$$

Thus, the summation of the electrostatic and intrinsic contributions in terms of poly-

mer extension (*e.g.*, mean square end-to-end distance) results in a coupling of electrostatic contour, A, and intrinsic contour, a, within the electrostatic persistence, P_e.

Further consideration of the intrinsic rigidity, P_0, results in two limiting conditions:

1. $A \to a$ then $Aa \to a^2$ and Eq. 3.30 reverts to the OSF formulation of P_e, Eq. 3.22. This occurs as the intrinsic persistence length (P_0) is sufficient to maintain a near-rigid or extended conformation in spite of electrostatic contributions, *e.g.*, the OSF assumptions that $P_0 \gg P_e$ and $P_0 \gg \kappa^{-1}$.

2. $A \to \kappa^{-1}$ then $Aa \to a\kappa^{-1}$ and P_e approaches a linear dependence on the screening length, or $P_e \propto \kappa^{-1}$, *e.g.*, Eq. 3.23. This occurs when P_0 is sufficiently low within a flexible chain, such that the charges are only driven apart by electrostatic repulsion. In such cases, $P_e > P_0$, and electrostatic contour extension is dominate (*i.e.*, the intrinsic contour is reduced to an ideal random walk).

If $A < \kappa^{-1}$, then either P_0 is sufficient to resist extension (upper limit), extension will occur until $A \approx \kappa^{-1}$ (lower limit), or maximum extension has occurred and $A \approx a$, *e.g.*, for closely spaced charges (intermediate case). The introduction of electrostatic contour length is complementary to previous approaches to understand intrinsically flexible polyelectrolytes by considering a hierarchy of effects [111, 179], including the stretching between neighboring charged monomers into a "chain of blobs" (essentially $a \gg A$), and electrostatically excluded volume between segments [97, 242, 116].

One assumption of the OSF formulation is that $a < \kappa^{-1}$, but, for a flexible polyelectrolyte (of sufficient length) it is possible that $a > \kappa^{-1}$ while $A < \kappa^{-1}$, as by definition $A < a$. Comparing the classical OSF formulation (Eq. 3.22) to the current formulation (Eq. 3.30), we find a "crossover" from rigid to flexible polymer conditions is defined by the contour ratio, or:

$$P_{OSF} = P_e \frac{A}{a} \tag{3.31}$$

From an alternative perspective, the κ-dependence of the electrostatic persistence length is weaker than suggested by OSF formulation (by a factor of A/a), such that

the observed dependence can be expressed as $\kappa^{-\alpha}$ and $\alpha < 2.0$ for $A/a < 1$, as previously observed and expressed in Eq. 3.23. However, it is also noted that the adjustment is related to the employed definition of the persistence length (for further discussion, see Everaers *et al.* and citations within [111]).

Equation 3.30 will serve as the basis of our interpretation of polyelectrolyte persistence length in the following discussion, to reconcile the full atomistic MD results with theory. To test the prediction and the role of electrostatic contour length, we choose the same weak polyelectrolytes as model charged polymers: poly(acrylic acid) (PAA) and poly(allylamine hydrochloride) (PAH), as depicted in Figure 3-5. Such weak polyelectrolytes are a proven platform for layer-by-layer assembly [303]. Current full atomistic MD techniques limit such studies to length- and time-scales in which much of the multilayer assembly phenomena is inaccessible [81]. Full atomistic simulation, however, can serve to directly verify assumptions made in theoretical models describing PEM composites, which is inherently difficult solely by experimental means. We consider these two specific polyelectrolytes as recent experimental studies have exploited the changes in mechanical properties of PAA/PAH composites as a function of pH [59, 142, 143]. While orders of magnitude increases in material stiffness can be achieved at the microscale, the contribution of molecular mechanisms such as electrostatic persistence length is less clear.

For polymer brushes, for example, it has been shown that local intrinsic stiffness can be widely varied *via* changing the length of the side chains, and quantification is dependent on the formulation of "persistence length". Indeed, what is considered "intrinsic" persistence length is reflects global conformational properties, such as end-to-end distance, and is intimately coupled to system and environmental conditions. Hierarchical (multiscale) effects, including structural (*e.g.*, proteins and DNA), molecular (*e.g.*, polymer brushes and sidechains), and non-backbone interactions (*e.g.*, electrostatic, volume exclusion) complicate the separation of intrinsic and second-order contributions to molecular rigidity. Indeed, while we have derived expression for electrostatic persistence length (Eq. 3.30), this term is coupled to the intrinsic persistence length through the parameter A, the charge to charge spacing along the electrostatic

116
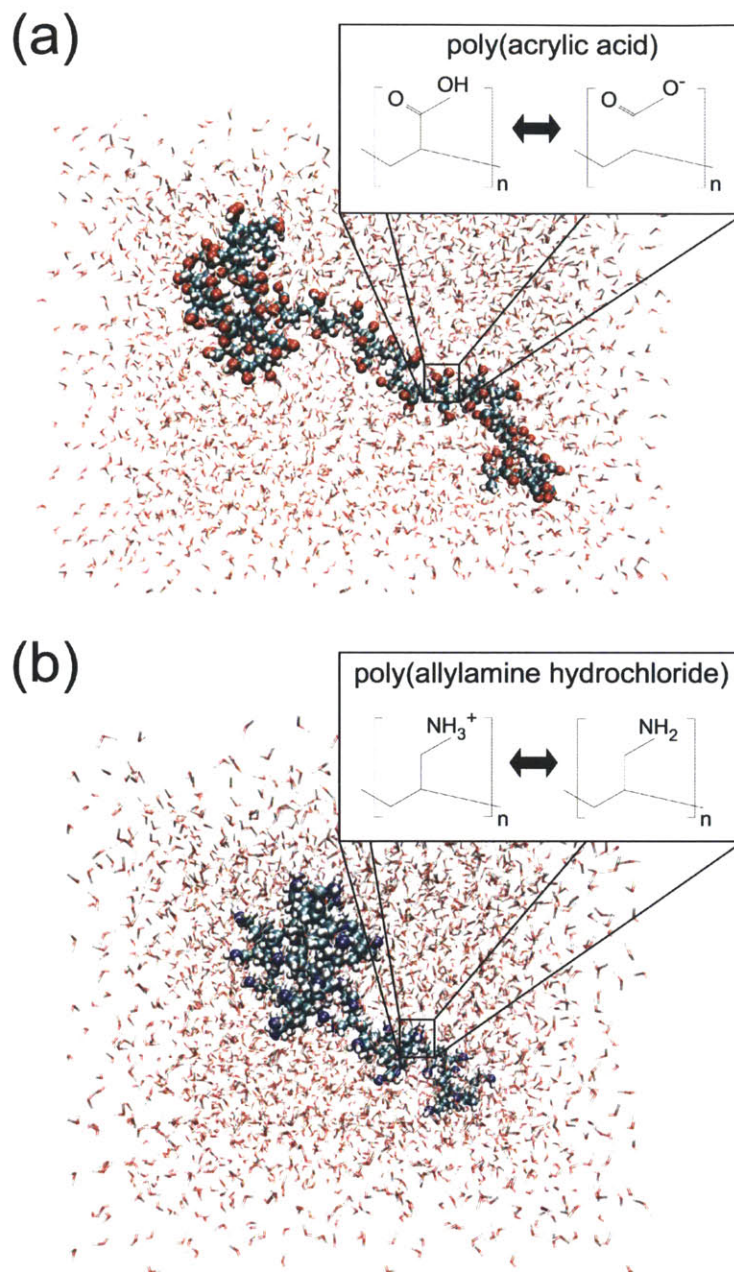
Figure 3-5: Simulation snapshots of model weak polyelectrolytes, poly(acrylic acid) (PAA) and poly(allylamine hydrochloride) (PAH). Full atomistic MD simulation requires no *a priori* assumptions regarding the intrinsic stiffness of the polymers or the effects of solvation screening. Both polymers consist of fifty repeated monomers ($L_0 \approx 150$Å), solvated in explicit water. (a) Poly(acrylic acid), or PAA; a polyanion with a carboxyl function group, with a COOH $\leftrightarrow$ COO$^-$ ionization. (b) Poly(allylamine hydrochloride), or PAH; a polycation with an amine function group, with a NH$_2$ $\leftrightarrow$ NH$_3^+$.

contour. This distance can only be quantified empirically - either through experimental or computational means. For example, one would expect A to increase with an increase in intrinsic persistence (assuming constant solvent conditions), even under constant ionization.

3.4 Full Atomistic Methodology

The rationale of the current MD investigation is to quantify the persistence length of individual polyelectrolytes (specifically PAA and PAH) as a function of polymer ionization[3], grounded in fundamental molecular behavior rather than empirical results. An understanding of the molecular origin of the behavior of polyelectrolyte properties can provide new insights into the basic polymer physics as well as provide new possibilities for their application. Molecular simulation can serve to directly verify assumptions made in theoretical models describing polyelectrolytes, which is inherently difficult solely by experimental means.

Previous simulation approaches to such polyelectrolyte systems include Monte Carlo [111, 329, 223, 220, 295] and idealized bead-spring molecular dynamic simulations [250, 165, 244, 51, 158], but typically focused on relatively small systems of short polymeric chains, the interaction between polyelectrolyte and substrate, or the rheology of assembly. Here, we implement full atomistic MD to avoid any *a priori* assumptions regarding the intrinsic stiffness of the polymers or the effects of solvation screening.

As described in the previous chapter, to model the polyelectrolytes, we utilize the consistent valence force field (CVFF) [68, 31, 81]. Model polymer segments were constructed consisting of fifty ($n = 50$) repeating monomers (see Figure 3-5). Again, full atomistic representation allows the direct manipulation of functional group protonation ($NH_2 \rightarrow NH_3^+$ for PAH) and deprotonation ($COOH \rightarrow COO^-$ for PAA).

---

[3]We note that we consider isolated, individual polyelectrolytes, as excluded volume theories assume that the unperturbed mean-square end-to-end distance $\langle R^2 \rangle$ is independent of the supporting electrolyte concentration [306]. For sufficient concentration, however, one would intuitively expect that local electrostatic forces exert a significant influence on $\langle R^2 \rangle$. Prior to consideration of such effects, the behavior of individual chains remains unresolved.

The polymers are solvated in a periodic water box with approximately 3,000 H_2O molecules using a TIP3P explicit water model [169, 200]. The dimension of the water box is sufficient to allow extension of the polymers during simulation (~ 150Å), while counterions are randomly distributed throughout the water box to ensure net charge neutrality. The particle-particle particle-mesh (PPPM) solver was implemented for long-range electrostatic interactions [155]. The simulations are implemented using the massively parallelized modeling code LAMMPS[4] [257].

For the atomistic models, desired ionization percentages were chosen, and a uniform selection of the ionized monomers is implemented to represent the approximate the desired pH level. The Debye-Hückel interaction potential is based on the (linearized) Poisson-Boltzmann equation and therefore implicitly assumes spatial uniformity of the electrochemical potentials of the electrolyte species, which in turn are assumed to be in osmotic equilibrium with a reservoir of fixed ionic strength.

A sample of random but likely equilibrated polymer conformations is required to obtain a mean square end-to-end distance, $\langle R^2 \rangle$, and a measure of total persistence length, P. For our formulation of electrostatic persistence length relying on the electrostatic contour length, we also require the average intercharge distance, $\langle A \rangle$, rather than presume a constant charge-to-charge distance, a.

Temperature accelerated sampling as described in **Chapter 2** was implemented to attain the necessary ensemble of polyelectrolyte states. The TAS process is as follows: (i) The constructed polymer(s) are surrounded by an explicit solvent box to ensure sufficient screening and isolation of the macromolecule. (ii) The system is minimized (using a conjugate gradient algorithm with an energy-convergence criterion as implemented in LAMMPS) and then subject to 0.15 ns of equilibration at 300K using an NVT ensemble (approx. 300,000 time integration steps). (iii) The system undergoes a steady increase in temperature to 1500K over 0.05 ns, followed by a steady decrease in temperature to 300K over 0.05 ns (approx. 100,000 time integration steps total). (iv) The system is again subject to 0.05 ns of equilibration at 300K. (v) The obtained conformation, χ_1, is then analyzed for square end-to-end

---

[4]http://lammps.sandia.gov/
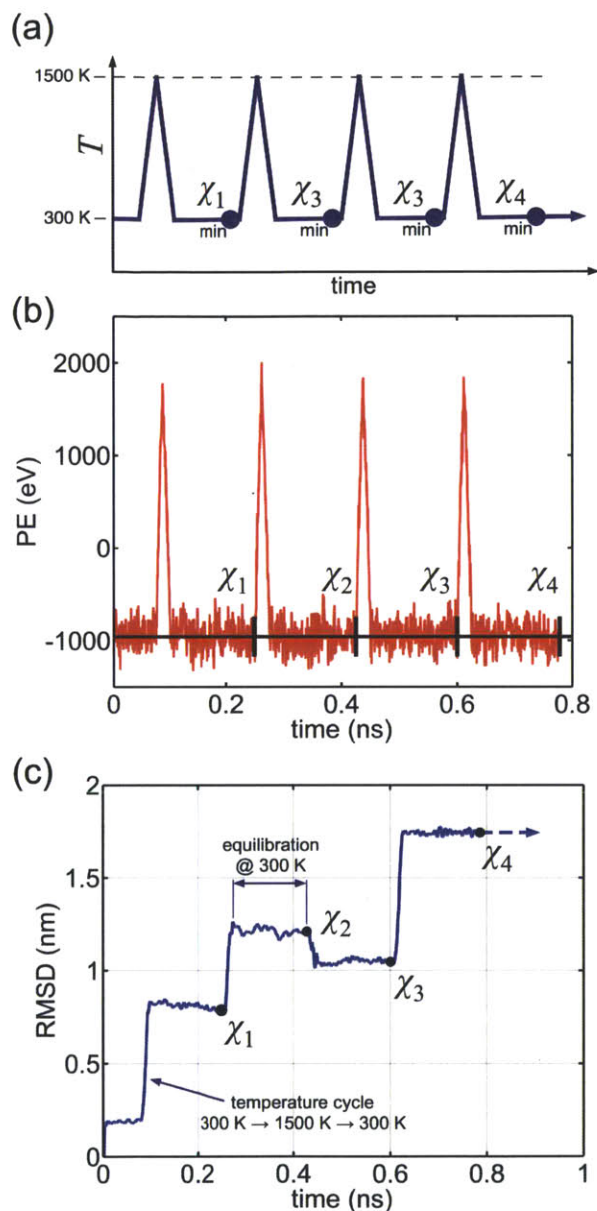
Figure 3-6: Ensemble of polymer conformations by temperature assisted sampling (TAS). (a) Molecular dynamics is implemented with periodic fluctuations in temperature, followed by periods of equilibration and system minimization to attain a set of states (χ_i). High temperature is used to overcoming possible kinetic trappings and ensuring each attained conformation is physically accessible, thereby requiring less simulated equilibration time per conformation. (b) Potential energy is checked to ensure no preferential conformation is attained, where $PE(\chi_1) \approx PE(\chi_2) \approx ... \approx PE(\chi_n)$. (c) The necessary equilibration period is determined by RMSD calculations at each state, depicting relatively stable polymer conformations at 300 K. Results (b) and (c) shown for PAA at 32% ionization; corresponding backbone conformations depicted in Figure 3-7.

distance, R^2 as well as interchange distance, A. (vi) Steps (iii) to (v) are repeated multiple times $(\chi_1, \chi_2, \ldots, \chi_n)$ within the same MD run to obtain a mean square end-to-end distance, $\langle R^2 \rangle$ and average charge separation, $\langle A \rangle$. To ensure there is no energetically "preferred" conformation, the potential energy is tracked for each temperature cycle (Figure 3-6(b)) and approximately equal for each attained state (e.g., $PE(\chi_i) \cong PE(\chi_{i+1})$). Moreover, an equilibration period of 0.05 ns is deemed sufficient as confirmed by RMSD calculations (Figure 3-6(c)). We note that initial equilibrate structure obtained after minimization (*i.e.*, step (ii)) is not considered to eliminate any unnatural residual effects in the random ionization process and construction of the initial polymer geometry.

3.5   Ionization Dependence of Rigidity

The TAS procedure was implemented to attain 10 conformation samples of PAA and PAH at ionizations of 0%, 20%, 32%, 50%, 68%, 80%, and 100% (see example Figure 3-7).

3.5.1   End-to-End Distance and Total Persistence Length

The square end-to-end distances, R^2, is calculated according to Eq. 3.3 and averaged over each ionization level for each polymer. The results for PAA and PAH are plotted in Figure 3-8. Due to the stochastic nature of the sampling technique as well as the length of the polymers (due to the limitations of full atomistic MD and the explicit solvation implemented), the standard deviation of $\langle R^2 \rangle$ is on the order of 10% to 30% (see Figure 3-8). However, in terms of end-to-end distance, R, this reflects an absolute deviation on the order of ± 3 to 8 Å, representing a relatively small change in possible polymer conformations.

The uncharged mean square distance, $\langle R^2 \rangle_0$ are on the order of 1300 Å^2 and 2200 Å^2 for PAA and PAH respectively, reflecting end-to-end distances on the order of 35 to 50 Å. Considering an intrinsic contour length, L_0, of approximately 150 Å, the values of R (and its variation) suggest a random sampling of a sufficiently convoluted
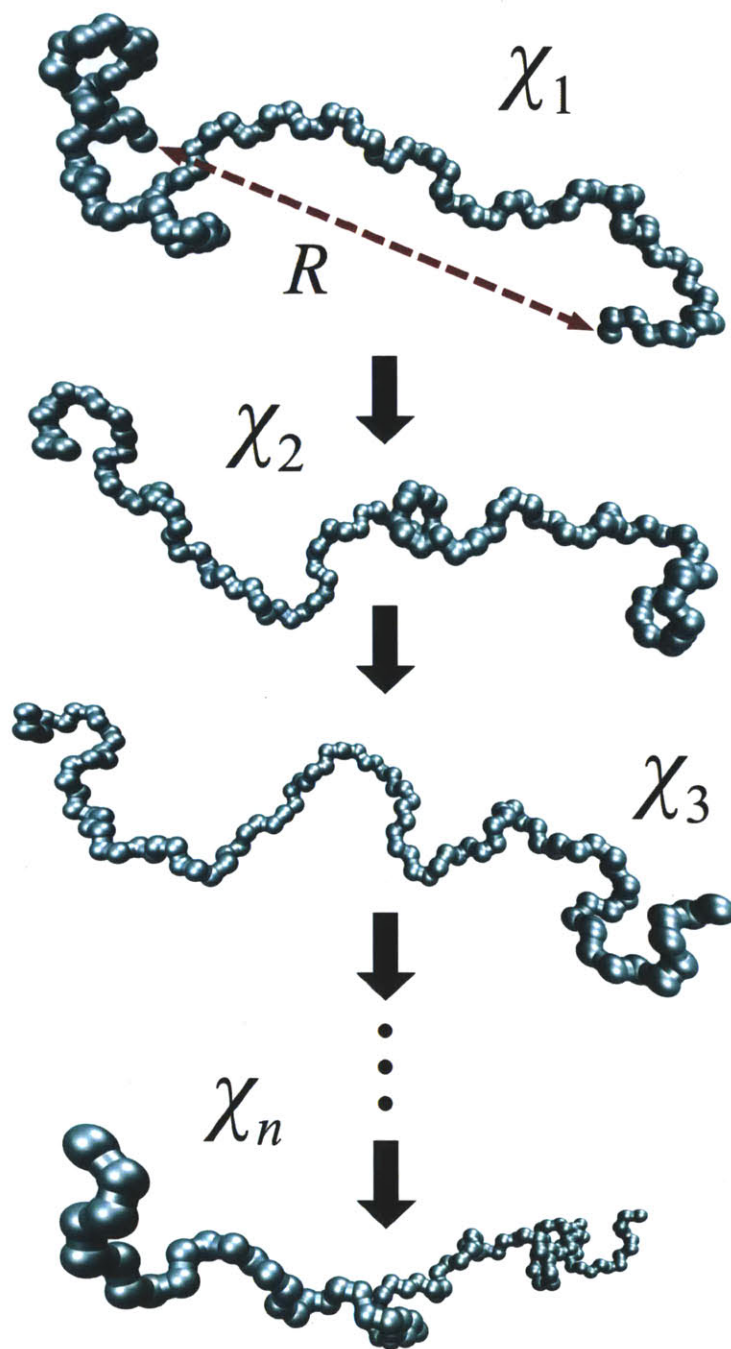
Figure 3-7: Representative states of polyelectrolyte backbone, PAA at 32% ionization. Only backbone carbon atoms depicted to indicate conformational shape/extension of polymer. Water and functional groups omitted for clarity. For each state, χ_i, the end-to-end distance, R, is determined, as well as the average charge-to-charge distance, A. Ten configurations are used to calculate statistical means, $\langle R^2 \rangle$ and $\langle A \rangle$, for each level of ionization of PAA and PAH.
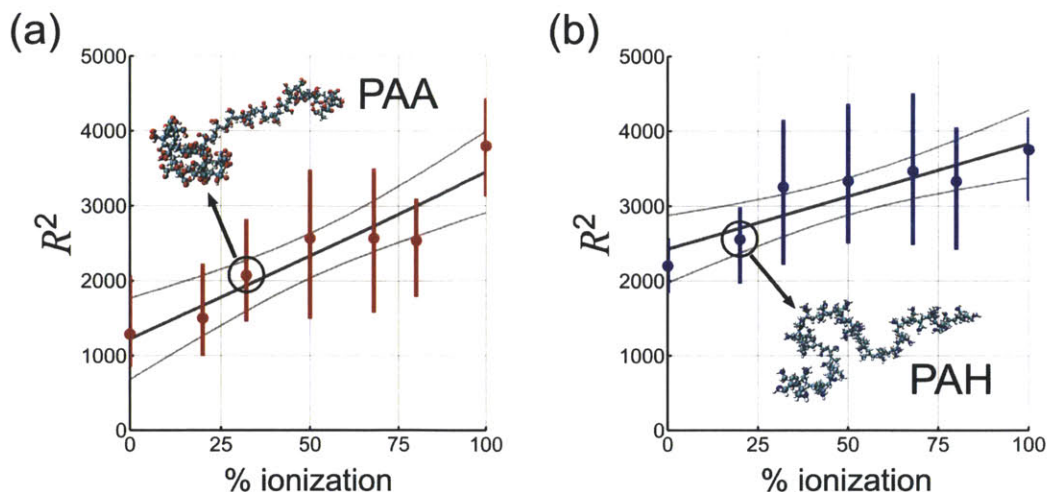
Figure 3-8: Calculated mean square end-to-end distances, $\langle R^2 \rangle$, for (a) PAA and (b) PAH. Insets depict sample conformations. The square end-to-end distances, R^2, was calculated (Eq. 3.3) and the mean of each ionization level plotted for each polymer (circles). Due to the stochastic nature of the sampling technique as well as the length of the polymers the standard deviation of $\langle R^2 \rangle$ is on the order of 10% to 28% (indicated by lines). Linear fits indicated a significant increase from 0% to 100% ionization (95% confidence intervals depicted by curved lines). Accounting for the inherent variation, there is a significant increase in $\langle R^2 \rangle$ as a function of ionization for both PAA and PAH, on the order of $3 \times \langle R^2 \rangle_0$ for PAA and $2 \times \langle R^2 \rangle_0$ for PAH, indicating $P_e \approx P_0$ (and thus beyond the suggested limits of the classical OSF formulation). The total persistence length, P, is calculated according to the WLC relation given by Equation 3.7, summarized in Table 3.1.

polymer. Accounting for the inherent variation, there is a significant increase in $\langle R^2 \rangle$ as a function of ionization for both PAA and PAH, on the order of $3 \times \langle R^2 \rangle_0$ for PAA and $2 \times \langle R^2 \rangle_0$ for PAH, indicating a substantial increase in persistence length driven by electrostatic interactions, where $P_e \approx P_0$, beyond the suggested limits of the classical OSF formulation.

From the mean square end-to-end distances, the total persistence length, P, is calculated according to the WLC relation given by Eq. 3.7. The intrinsic persistence length, P_0, is taken as the total persistence length at 0% ionization, resulting in approximately 4.3±1.1 Å for PAA and 7.3±0.8 Å for PAH, comparable in magnitude to previous experimental measurements ($\sim$3.2 Å for PAA [193] and $\sim$5.3 Å for PAH [352], both attained *via* non-equilibrium force-extension formulations). The mean intrinsic persistence length is then used to determine the effective electrostatic
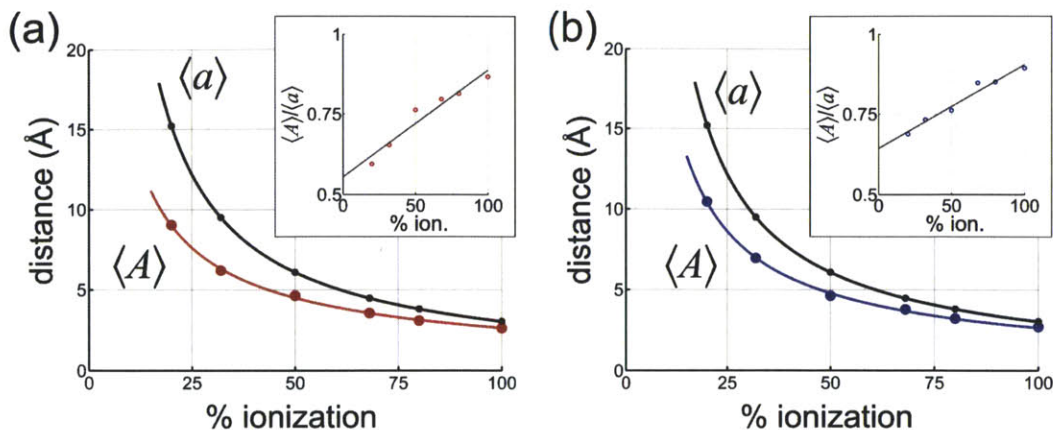
Figure 3-9: Average intrinsic contour length, $\langle a \rangle$, and electrostatic contour length, $\langle A \rangle$, as function of ionization for (a) PAA and (b) PAH. A critical component of the current formulation of electrostatic persistence length is that the electrostatic contour length, L_e, is, by definition, less than the intrinsic contour length, L_0, implying that $\langle A \rangle < \langle a \rangle$. Insets: For both PAA and PAH $\langle A \rangle / \langle a \rangle < 1$ for all levels of ionization. As ionization increases, $A \to a$. For both PAA and PAH, $\langle a \rangle \propto I^{-1}$ by definition and $\langle A \rangle \propto I^{-\beta}$ where $\beta < 1$ (I being the % ionization).

persistence length for ionizations greater than 0%, where $\langle P_e \rangle = \langle P \rangle - \langle P_0 \rangle$. The results are presented in Table 3.1.

3.5.2 Charge Separation and Screening Length

In addition to end-to-end distance, the charge-to-charge distances, A_i, along each polymer are averaged, $\langle A \rangle$, for each level of ionization. A critical component of the current formulation of electrostatic persistence length is that the electrostatic contour length, L_e, is, by definition, less than the intrinsic contour length, L_0, implying that $\sum A_i < \sum a_i$ and consequently $\langle A \rangle < \langle a \rangle$. We find that, for both PAA and PAH $\langle A \rangle / \langle a \rangle < 1$ for all levels of ionization (see Figure 3-9). Specifically, the ratio of $A : a$ can be used to quantify the deviation from the OSF formulation (see Eq. 3.31; Figure 3-9 insets). Note as ionization increases, $A \to a$ as: (i) the total persistence length increases, resulting in the polyelectrolyte becoming more extended and (ii) the charge-to-charge spacing is significantly reduced (less than $\sim 5\text{Å}$), allowing limited measurable difference between L_e and L_0.

If we consider the level of ionization, I, along the polyelectrolyte contour, then

124

$\langle a \rangle \propto I^{-1}$ by definition. We further find that, for both PAA and PAH, $\langle A \rangle \propto I^{-\beta}$ where $\beta < 1$ (see Figure 3-9) where, $\langle A \rangle_{PAA} \propto I^{-0.74}$ and $\langle A \rangle_{PAH} \propto I^{-0.85}$ (fitting a power law of the form $C_1 I^{-\beta} + C_2$). We see that the reduction in actual intercharge distance is less than the equivalent distribution along the contour for a given change in ionization, and is a function of the intrinsic persistence length. It would be expected that as P_0 increases, both $\langle A \rangle \propto I^{-1}$ and $\langle a \rangle \propto I^{-1}$ as $A \to a$. This indicates why the OSF assumption that charge distribution is proportional to a (and thus I) results in an underestimation of electrostatic persistence length for flexible polyelectrolytes - increasing ionization along the polyelectrolyte contour does not result in a proportional increase in charge density along the spatial extension of the polyelectrolyte.

In addition to charge-to-charge distance, we also explicitly consider screening length as a function of charge density (calculated as described in **Chapter 2**). The number of charged monomers and counterions, combined with the chosen volume of the solvation box result in screening lengths on the order of 5 Å to 12 Å, notably the same order of magnitude as the measured values of P, P_0, P_e, $\langle A \rangle$, and $\langle a \rangle$.

For extremely flexible polyelectrolytes of sufficient length, it is expected that if $A < \kappa^{-1}$, the polymer would extend until the charges are separated by the screening length (and thus have no direct effect). For such conditions, the Debye screening length sets the "lower limit" for intercharge spacing. Figure 3-10 depicts a plot of κ^{-1} versus $\langle A \rangle$ for both PAA and PAH across all levels of ionization. We see that for PAA, $\langle A \rangle \approx \kappa^{-1}$ for all ionization levels, while for PAH, $\langle A \rangle$ approaches, but is slightly larger than the screening length for all ionization levels. The different behavior can be attributed to the slightly larger intrinsic rigidity of PAH ($P_0 \approx 7.3\text{Å}$), such that the charged monomers are not as free to encounter adjacent charges (an interaction defined by the screening length) as those of PAA ($P_0 \approx 4.3\text{Å}$). *I.e.*, the polymer's orientational influence is sufficient to propagate beyond the Debye screening length.
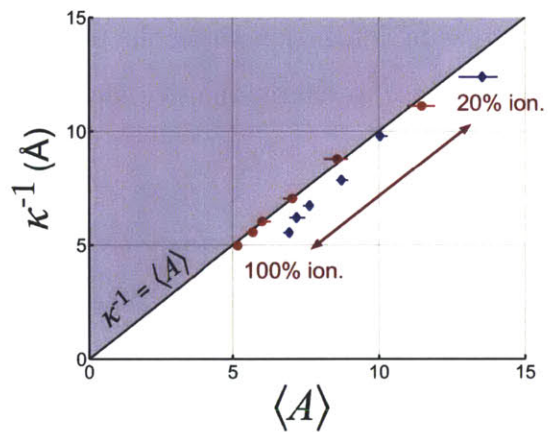
Figure 3-10: Relationship between screening length, κ^{-1}, and average intercharge distance, $\langle A \rangle$, for PAA and PAH. For the current simulation, the number of charged ions, combined with the chosen volume of the solvation box result in screening lengths on the order of 5 Å to 12 Å, the same order of magnitude of measured values of A. For extremely flexible polyelectrolytes of sufficient length, it is expected that if $A < \kappa^{-1}$, the polymer would extend until the charges are separated by the screening length (and thus κ^{-1} sets a lower bound for $\langle A \rangle$; *shaded region*) For PAA (**red**), $\langle A \rangle \approx \kappa^{-1}$ for all ionization levels, while for PAH (**blue**), $\langle A \rangle$ approaches, but is slightly larger than the screening length for all ionization levels. The two polyelectrolyte are close to the limiting condition where $A \to \kappa^{-1}$ then $Aa \to a\kappa^{-1}$ and P_e approaches a linear dependence on the screening length, or $P_e \propto \kappa^{-1}$.

126

Table 3.1: Summary of persistence lengths for the PAA and PAH, for varying ionization levels.

Ionization	PAA			PAH		
	P	P_e	P_e^{theory}	P	P_e	P_e^{theory}
0%	4.3±1.1	0.0	0.0	7.3±0.8	0.0	0.0
20%	5.0±1.3	0.7	1.6	8.5±1.1	1.2	1.7
32%	6.9±1.6	2.6	2.3	10.8±2.1	3.5	2.6
50%	8.5±2.5	4.3	3.1	11.1±2.4	3.8	3.9
68%	8.6±2.3	4.3	4.1	11.5±2.3	4.2	4.8
80%	8.4±1.5	4.2	4.7	11.1±1.9	3.7	5.6
100%	12.6±1.7	8.3	5.5	12.5±1.2	5.1	6.6

3.5.3 Electrostatic Persistence Length

The explicit calculation of $\langle A \rangle$ and κ^{-1} is used to compare the measured electrostatic persistence length (where $\langle P_e \rangle = \langle P \rangle - \langle P_0 \rangle$) with the theoretical prediction, P_e^{theory}, given by Eq. 3.30. The stochastic nature of the polyelectrolyte conformations restricts the prediction beyond a range of end-to-end distances (and thus persistence lengths) for a given level of ionization. As such, the simulation results for electrostatic persistence length are plotted along with the 95% confidence intervals for both PAA and PAH (Figure 3-11), along with the predicted values, P_e^{theory}. We find that, in both cases, the formulation given by Equation 3.30 falls within the confidence intervals, slightly underestimating the persistence length for PAA and overestimating for PAH (calculated coefficients of determination are $R_{PAA}^2 = 0.816$ and $R_{PAH}^2 = 0.692$). We note that the results are effectively "centered" to the average intrinsic persistence length, $\langle P_0 \rangle$, such that the largest discrepancy occurs at 100% ionization for both PAA and PAH. Again, the measured and predicted results are summarized in Table 3.1.

3.5.4 Rigidity and pH

Similar to the adhesion study of **Chapter 3**, for the current molecular model, a constant ionization distribution is used to account for the effect of changes in pH, where the number of protonated/deprotonated monomers is explicitly defined prior
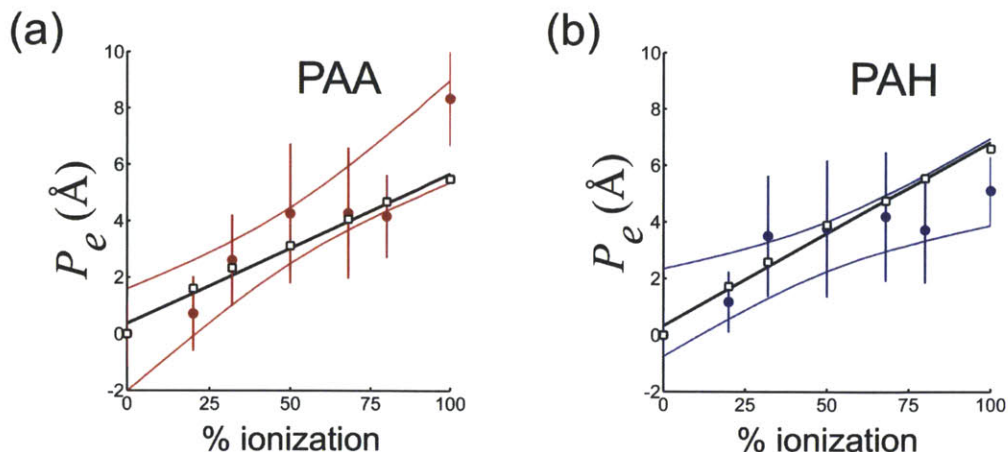
Figure 3-11: Electrostatic persistence length, P_e; simulation results and theoretical prediction for (a) PAA and (b) PAH. Prediction of electrostatic persistence length, P_e^{theory} (Eq. 3.30), is compared to measured simulation results of total persistence length; see Table 3.1 for summary of values. The stochastic nature of the polyelectrolyte conformations restricts the prediction beyond a range of measured persistence lengths for a given level of ionization. The results are plotted with the 95% confidence intervals (curved lines) for both PAA and PAH, along with the predicted values, P_e^{theory} (plotted squares). In both (a) and (b), the theoretical prediction falls within the confidence intervals (calculated coefficients of determination are $R_{PAA}^2 = 0.816$ and $R_{PAH}^2 = 0.692$). The results are effectively "centered" to the average intrinsic persistence length, $\langle P_0 \rangle$, such that the largest discrepancy occurs at 100% ionization for both polyelectrolytes.

to simulation. Here, the resulting charge distribution is symmetric, such that chain behavior can be considered homogenous - for the OSF energy equivalence (*e.g.*, elastic to electrostatic) the Debye-Hückel interaction implicitly assumes spatial uniformity of the electrochemical potentials of the electrolyte species, which in turn are assumed to be in osmotic equilibrium with a reservoir of fixed ionic strength (as is the modeled cases). For larger polyelectrolyte systems, it is presumed the effect of ionization would approach homogeneity at the global system level.

Once again, assuming constant pKa values and degree of ionization (Figure 3-12(a)), a qualitative correlation of pH and ionization can be established (as described in **Chapter 2**), and we can thereby predict the persistence length (and associated molecular rigidity) as a function of pH (see Figure 3-12(b)). Quantification of polymer rigidity coupled with electrostatic cross-linking can be useful in delineating the tunable mechanical properties of LbL composites as a function of pH [59, 142]. For
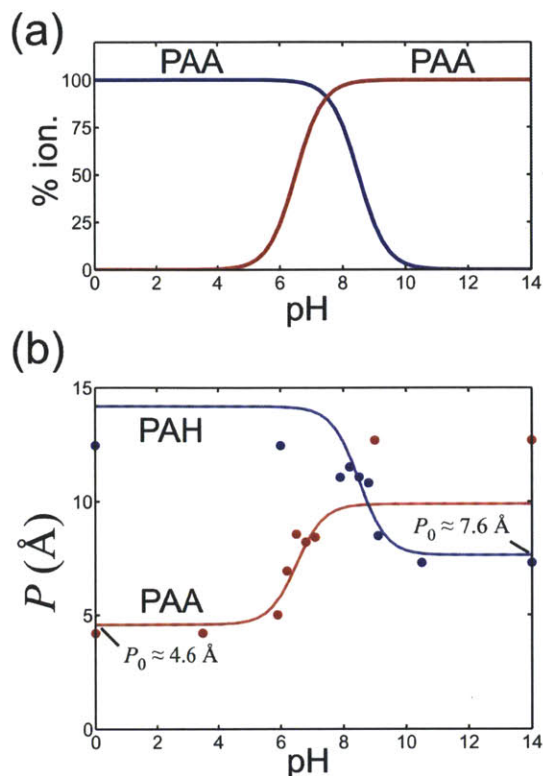
Figure 3-12: Ionization as a function of pH using pKa. While the pKa of a weak poly-electrolyte can be a complex function of degree of ionization and environmental conditions [206], in general, the pH level and level of ionization can be accounted for *via* pKa values; here pKa = 6.5 for PAA and pKa = 8.5 for PAH [62]. (b) Prediction of persistence length (and associated molecular rigidity) as a function of pH. Quantification of polymer rigidity can delineate the mechanical properties of polyelectrolyte materials and LbL composites as a function of pH [59, 142].

example, the current results suggest that maximum molecular rigidity would occur at a pH of approximately 6.5 to 8.0 (for a PAA/PAH composite) with potential "switching" of molecular rigidity between the polyelectrolyte species (flexible PAA at pH < 5; flexible PAH at pH > 10, etc.). Being said, the effect of polyelectrolyte complexation on molecular rigidity is not presently accounted for, and is to be further investigated.

3.6 Summary

While previous proposed extensions of OSF theory (accounting for scaling laws, local screening, etc.) define a crossover from rigid to flexible polyelectrolyte behavior,

the formulation developed here encompasses both regimes into a simplified framework capture by the simple concept of an electrostatic contour length, L_e, and a contour ratio, A/a. While more complex analysis can encompass the potential relation between intrinsic and electrostatic contours (in terms of variation theory, volume exclusion, monomer type, etc.), such is beyond the scope of the current investigation, where we aimed to provide a general and consistent basis to quantify the change in molecular rigidity of flexible polyelectrolytes.

The mechanical effect of adding charge, *via* an energy "penalty" for bending deformation, has been well accepted since the proposal of OSF decades ago. Indeed, the phenomena is similar to the addition of relatively large side chains to increase stiffness, such as in the case of molecular brushes, where, instead of steric interactions, the adding and removing of electrostatic interactions provide the structural "bulk" and a means to reversibly alter the effective rigidity of a polymer. This additional stiffness is well captured by the concept of electrostatic contours coupled with the polymer chain itself - a kind of electrostatic *reinforcement*.

The electrostatic contour length (and resulting coupling between, A, a, and κ^{-1}) proposed here provides a new perspective on the reported discrepancies between theory, computational, and experimental observations on the κ-dependence of electrostatic persistence length, P_e. This general form allows a single approach for both rigid and flexible macromolecules, based on a fundamental concept equating electrostatic energetics with bending rigidity. Being said, while the electrostatic contour length and intercharge distance can be theoretically introduced, both would be challenging to experimentally measure atomistically. New advances in molecular imaging, such as Kelvin probe force microscopy [228], may provide a means to directly quantify charge to charge spacing and investigate the complex nature of convoluted polyelectrolytes. We note that the specific polyelectrolyte cases considered here - PAA and PAH - consider isolated polyelectrolytes of like charges only, such that the electrostatic forces are purely repulsive. The effect of polyelectrolyte electrostatic cross-linking, complexation, and variable concentrations of salts must be considered to fully understanding the behavior of larger, multilayer systems, such as those attained by layer-by-layer

assembly.

Chapter 4

Rate Dependence and Ionization Effects on Adhesion

In this chapter, the adhesion properties of a PAA + PAH complex are determined. The primary goal is to determine the extent of *mutable* interactions between PAA and PAH *via* steered molecular dynamic (SMD) simulations and quantify the range of tunable adhesion strength and associated energy barriers, enabled by a systematic analysis of rate dependence and ionization. In addition, a subsidiary motivation is the adaptation of simulation and analysis techniques typically implemented on protein-based material systems to polymer systems (such as SMD and the Bell Model, to be discussed in detail). Finally, the results of the investigation are concurrently utilized in the development and formulation of a coarse-grain elastic model to further examine the PAA/PAH polyelectrolyte system under conditions not accessible to traditional molecular dynamics. The approach presented lays the groundwork for a combination of a multi-scale theoretical foundation with simultaneous experimental explorations. Such a finer-trains-coarser, hierarchical framework facilitate a new holistic basis of nanoscale material design, with behavior properties engineered at the molecular and mesoscale level.

4.1 Previous Experimental Investigations

The alternating, layer-by-layer (LbL) deposition of oppositely charged polyelectrolytes has been well-established for the preparation of composite materials such as polymer films [354] and nanotubes [211, 59], driven by the adhesion between oppositely charged molecules. Polyelectrolyte complexes are formed at surfaces by a sequential adsorption process involving dilute solutions of a polycation and polyanion and are known to exhibit a unique combination of properties due to their ionically cross-linked nature [255]. Here, we again focus on two specific polymers: (1) poly(acrylic acid) (PAA), and; (2) poly(allylamine hydrochloride) (PAH) and attempt to quantify the variation in adhesion with ionization. While there has been much experimental study on the interactions between these polymers and their respective functional groups [303, 65, 166, 62, 162, 354], there are few (if any) computational investigations with full atomistic resolution. Complicating matters, the exact mechanisms resulting in the formation of nanoscale films/composites is not yet clear, although a highly entangled and interpenetrated inner multilayer structure has been proposed and commonly accepted [293, 303].

The potential mutability of polyelectrolyte systems during assembly is well-known. With careful adjustment of solution pH during polymer deposition, it is possible to precisely tune at the molecular level the structure and properties of the resultant multilayer films [303]. Furthermore, one property of the resultant composite material is in its unique ability to reversibly and predictably swell in solution by alteration of pH values [186, 162]. Variations of the basic assembly process has led to the development of multitude of potential designed behaviors including nanoreactor schemes [338, 339], pH-gated micro- and nanoporosity transitions [215, 151], discontinuous reversible swelling transition [152], selectively responsive surfaces [61], and strategies for controlling the adhesion of cells [216]. Taking advantage of past experimental results, a full atomistic molecular model is easily constructed, based on the known chemical structure.

4.2 Full Atomistic Methodology

The particular choice of PAA and PAH for simulation is predicated by their propensity for the formation of stable complexes, widespread use in previous experimental investigations, and the extensive presence the carboxylic acid (COOH) and amine (NH_2) functional groups in both biological [54] and synthetic polyelectrolyte systems [89]. These functional groups undergo a balance of electrostatics and hydrogen bonding that can result in adhesion and complexation that varies in strength as a function of pH and ionic strength. The chemical structure implemented for atomistic modeling of poly(acrylic acid)(PAA) and poly(allylamine hydrochloride)(PAH) is depicted in Figure 1-7. Both polymers have chains approaching micrometers scale in length depending on intended use (*e.g.*, a representative molecular weight of approximately 50,000 amu for PAH [166] representing approximately 1,000 monomers, for a length on the order of 0.25 μm).

The layer-by-layer assembly of oppositely charged polyelectrolytes is facilitated by the formation of water-insoluble complexes of polycations and polyanions *via* the ionic attractions between the carboxylate (COO^-) and ammonium (NH_3^+) groups [205], thereby improving stability. Such a complexation interaction is well-established for the layer-by-layer process alternating oppositely charged polyelectrolytes [205], but little is known at the atomistic scale for monomer-monomer (*i.e.*, functional group) interactions. A full atomistic model is applied to describe the polymers, to elucidate both interactions at a fundamental level, serve as a cornerstone for the development of multiscale investigations, and to confirm the behavior observed in experimental studies.

The polymers are simulated within a solvation box, that is, surrounded by explicit water molecules, to ensure accurate representation of solution behavior and relevant hydrophobic interactions. It has been shown, both experimentally [35] and *via* simulation [229], that solutions of polyelectrolytes, such as PAA and PAH, exhibit complex phase behavior depending on the nature of the solvent and concentration of counterions. The intent of the current investigation is not to examine the behavior

of the electrolytes in solution, but rather the interactions *between* the polymers after complexation, thus the system is simplified to focus on the polymer complex and counterions are neglected for most simulated cases. It is the assumption of the current model that the ionization and complexation has occurred *a priori*, independent of counterion or environmental effects, and we proceed to characterize the adhesion strength in absence of such factors. While counterions would indeed serve to potentially screen and affect the bond/dissociation/association rates, we are attempting to delineate the upper and lower bounds of adhesion strength. As such, we reduce the polyelectrolyte model to a fundamental arrangement to allow quantification of the adhesion strength as a function of ionization alone.

Moreover, due to similar reasoning (*e.g.*, isolating the effect of polyelectrolyte interaction and not behavior in solution), no long-range electrostatic solver (such as Ewald or PPPM) is implemented. It has been shown that the use of long-range solvers do not necessarily result in more reliable trajectories (for example, see Fadrna *et al.* [112]) and it is assumed the contribution of long-range electrostatic interactions is negligible for the current dynamically driven system of highly ionized polymers.

The constructed polymer complex consists of 20 constituent monomers for each polymer aligned along a common axis. The physical layer-by-layer assembly of charged polyelectrolytes typically results in a disordered arrangement of polymers thousands of monomers long, due to the relatively short persistence length combined with the relatively long lengths of the constituent polymers (with a total length of hundreds of nanometers), and the stochastic nature of the layer-by-layer deposition. We assume a random "scrambled" model [224, 184, 281] with "ladder"-type aligned segments, of which a schematic is depicted in Figure 4-1. By limiting the polymer alignment to approximately 20 functional groups, a definitive macromolecular structure (*i.e.*, scrambled versus aligned loops, versus distinct layering of polyelectrolytes) is unnecessary.

We choose to model relatively short segments (approximately 5 nm) of aligned polymers (Figure 4-1, right). The purpose of such an alignment is fourfold:

1. To focus the simulations on the adhesion between the two polymers by eliminat-

136
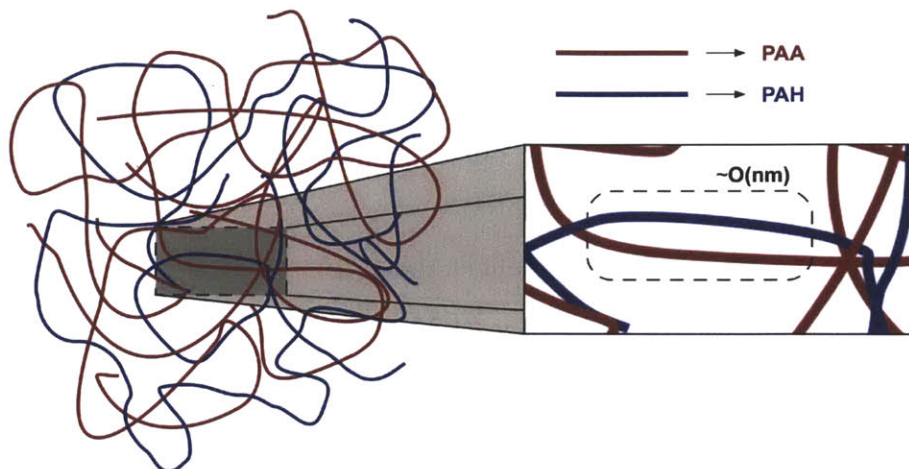
Figure 4-1: Schematic if polyelectrolyte composite of randomly oriented PAA and PAH polymers. Left: Typical constituent polymers consist of thousands of linked monomers, with a total length on the order of micrometers. Here, we focus on short aligned sections for inter-polymer adhesion and interactions, implemented in full atomistic modeling of oligomers approximately 5 nm in length. Right: We assume a random "scrambled" model with "ladder"-type aligned segments [224, 184, 281]. By limiting the polymer alignment to approximately twenty functional groups, a definitive macromolecular structure (*i.e.*, scrambled versus aligned loops versus distinct layering of polyelectrolytes) is unnecessary.

ing entropic effects (such as unfolding), as well as the possibility of intra-polymer interactions or self-adhesion (such as the formation of carboxylic acid dimers);

2. To allow direct manipulation of the ionization (*i.e.*, protonation/deprotonation) of each polymer to indirectly investigate the effect of pH levels as a triggering mechanism of adhesion strength;

3. To ensure functional group interaction and allow quantitative comparison between different simulations of varying loading rates and ionization (*i.e.*, a common, stable initial configuration). Possible configurations of a system allowing the free motion and potential misalignment of the polymers would relinquish any systematic analysis of the adhesion strength.

4. To concentrate on the interaction between individual polymer pairs, eliminating potential steric effects of long polymer chains or chain crossings of a larger multi-polymer system.

Overall, our goal is to construct a simplified base system to investigate the inter-

polymer adhesion strength, dismissing potential variations due to the complexity of a larger system. Notwithstanding, it behooves us to note that the aforementioned eliminated effects and interactions are nontrivial and play a critical role in the properties and behavior of such polyelectrolyte systems. While the current investigation is focused on the variation of a single effect (adhesion strength), it is not intended to represent a comprehensive model of the PEM system.

4.3   Steered Molecular Dynamics

Steered molecular dynamics (SMD) simulations [196], in which external forces are used to explore the response and function of macromolecules, have become a powerful tool complementing and guiding *in vitro* single-molecule experiments. Such simulations have increasingly been implemented to investigate complex biological phenomenon such as the unfolding behavior of protein materials [2, 3], ligand-receptor kinetics [336], and the unbinding trajectories of other biological matter [308].

Protein materials differ significantly from the synthetic, linear polyelectrolytes examined here, in that they exhibit uniquely folded, hierarchical secondary, tertiary, and quaternary structures, and even more complex conformations (as found in highly hierarchical biological materials such as nacre, bone or silks), and may undergo very specific interactions with other functional systems (*i.e.*, "lock-and-key" interactions). Nevertheless, the charged nature of the synthetic polyions, their dual hydrophobic and hydrophilic nature, and their macromolecular size are analogous to properties of proteins. The complexity of the present polyelectrolyte system, combined with a relatively robust atomistic representation and force field is conducive for the use of SMD to investigate the binding behavior between PAA and PAH.

SMD is based on the concept of adding a harmonic moving restraint to the center of mass of a group of atoms. In effect, the SMD approach applies a moving spring force (see Figure 4-2), such that the molecule can behave in a manner not captured by either force or displacement loading alone, allowing induced conformational changes in a system along a prescribed reaction vector. A driving force is applied to a selected
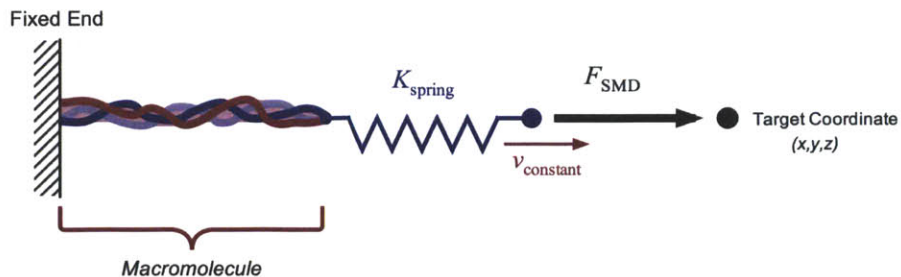
Figure 4-2: Schematic of constant velocity steered molecular dynamics (SMD), where macromolecule is subjected to a dynamic force, F_{SMD}, by harmonic spring with defined stiffness, K_{spring}, and a fixed velocity, v_{constant}, directed towards a defined target coordinate (x, y, z).

atom (or atom group) of magnitude:

$$F_{\text{SMD}} = K_{\text{spring}} \left[\left(\vec{R}(t) - \vec{R}_0 \right) \cdot \vec{n} \right] \tag{4.1}$$

where K_{spring} is the harmonic spring constant, $\vec{R}(t)$ is the position of restrained atoms at time t, $\vec{R}_0$ denotes original coordinates and $\vec{n}$ denote the pulling direction towards the tether point (*e.g.*, target coordinate). A constant velocity, v_{constant}, is prescribed which monotonously increments or decrements $\vec{R}(t)$ towards the tether point, as depicted in Figure 4-2. By monitoring the applied force (F_{SMD}) and the position of the atoms that are pulled over the simulation time, it is possible to obtain force-displacement data that can be used to derive the mechanical properties such as adhesion, unfolding pathway, bending stiffness, or effective modulus, as examples. The application of SMD simulations directly corroborates with atomic force microscopy (AFM) experiments at the atomic scale. Such AFM investigations have conjointly been used to probe the mechanical and kinetic properties of both PAA and PAH systems [193, 166]. We maintain a constant spring constant throughout the investigation and vary the loading rate, r_f, through assignment of pulling velocities only. It is noted that, in physical systems, the spring constant can influence the total energy landscape of the system [336, 203] however, the computational method utilized for SMD here prescribes point forces based on the loading rate only, in which the spring stiffness (K_{spring}) merely provides relation between prescribed velocity (v)

and loading rate, r_f (where $r_f = K_{\text{spring}} \times v_{\text{constant}}$). Being said, due to the time-scale limitations of MD to several nanoseconds, there is typically a large difference in the pulling rates and transducer stiffnesses in simulation and experiment. This requires additional consideration in order to interpret MD results in light of experimental findings.

We conduct SMD simulations of single PAA and PAH oligomers, consisting of twenty monomers each (as depicted in Figure 4-3(a)). The polymers are solvated in a water box with dimensions $30\text{Å} \times 30\text{Å} \times 160\text{Å}$ with approximately 4,500 water molecules using the TIP3P explicit water model [169], commonly implemented in CHARMM [200], specifying a three-site rigid molecule, previously discussed in **Chapter 2**. The relatively large length of the water box is constructed to ensure that the polymers remained solvated while being pulled from each other (Figure 4-3(b)). Conjugate gradient minimization of the system is utilized to attain a stable initial conformation. After minimization, unconstrained MD simulation over 100 ns at 300 K using and a NVT ensemble is performed to equilibrate the system prior to initiation of SMD.

A single backbone carbon atom at the end of the PAA oligomer is fixed to provide a reference point, while a single backbone carbon at the opposite end of the PAH oligomer is used to apply the SMD force. A tether point is fixed a distance of 100 Å from the PAH end, providing the direction of spring velocity (See Figure 4-4). A spring constant of 1.39 N/m is used with a timestep of 0.5 femtoseconds per iteration step (in the LAMMPS MD code, the units of force used for the simulation are kcal/mol/Å; the spring constant used is simply $K_{\text{spring}} = 2.0$ kcal/mol/Å^2, and thus the unseemly value of 1.39 N/m is a result of unit conversion). As a general rule, the spring stiffness should approximate that of the molecule(s) under load [336]. Variation of constant pulling velocities dictated the total length of the simulation, ranging from 10 ps to 200 ns. We obtain force-displacement data by monitoring the time-averaged applied force (F) and the position of the atom that is pulled at (x) over the simulation time.
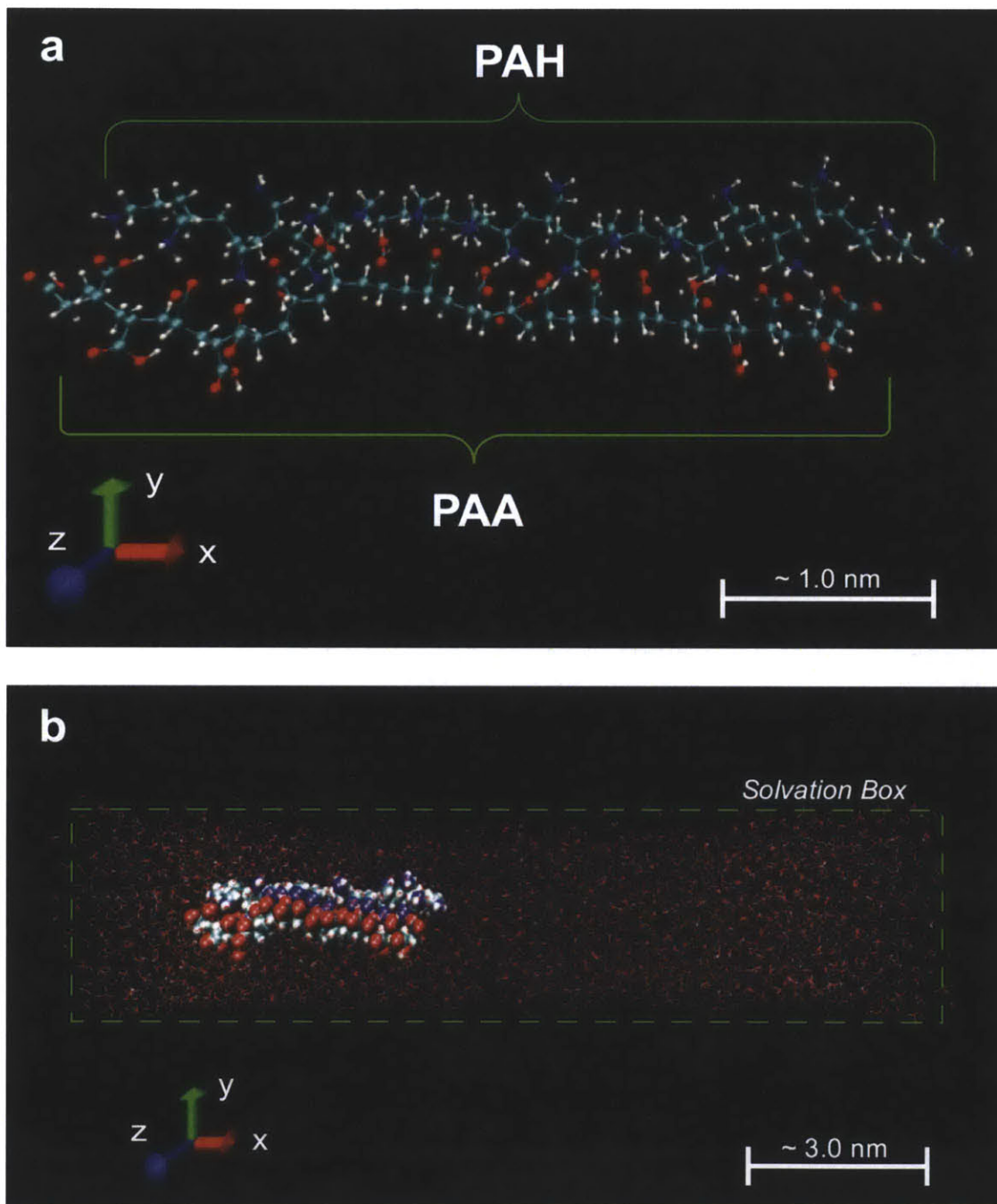
Figure 4-3: (a) Full atomistic model of PAA/PAH complex, consisting of 20 unit monomers each after system minimization. (b) Complete simulation system, with $30\text{Å} \times 30\text{Å} \times 160\text{Å}$ periodic water solvation box consisting of approximately 4,500 water molecules.
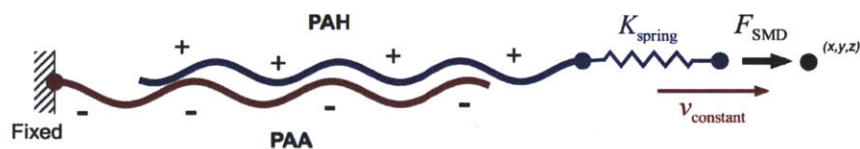
Figure 4-4: SMD arrangement for current investigation where a terminal carbon backbone atom of PAA is fixed while the opposite terminal carbon backbone atom of PAH is attached to the harmonic spring with stiffness, K_{spring}, and velocity, $v_{constant}$. The depicted charges are qualitative to illustrate the electrostatic interactions and not meant to represent a finite number of charged functional groups.

4.4 Rate Dependence of Adhesion Strength

We begin the analysis with a systematic investigation of the rate dependence on the adhesion force between polyelectrolytes. This study is motivated by the disparity between the timescales accessible to experimental and simulation results. As such, we carry out a series of classical MD simulations at varying loading rates, encompassing five orders of magnitude from approximately 0.14 N/s to 1400 N/s. To compare with experimental results, we choose a constant ionization of 95% for PAH and an ionization of 5% for PAA throughout the variable rate simulations, representing a pH environment of approximately 2.5 for the polymers in solution (see **Chapter 2** for further discussion on pH and ionization in multilayer systems).

For the PAA/PAH polyelectrolyte complex, two characteristic force-displacement curves are shown in Figure 4-5(a) for two pulling speeds (10 m/s and 2 m/s). The simulations reveal two distinctive regimes. The first regime consists of a linear increase in displacement until the force reached a critical level to initiate polymer detachment. During this elastic regime, it is observed that alignment of the functional groups occurs, as well as direct straining of the polymer backbone along the direction of pulling, resulting in extension of the polymer conformation from its initial state. Such a geometrical conformational evolution could possibly be acting as a trigger to induce rupture, as the load transfer transitions from polymer extension directly to the hydrogen and electrostatic bonding. The variation in aligned charged monomers

142
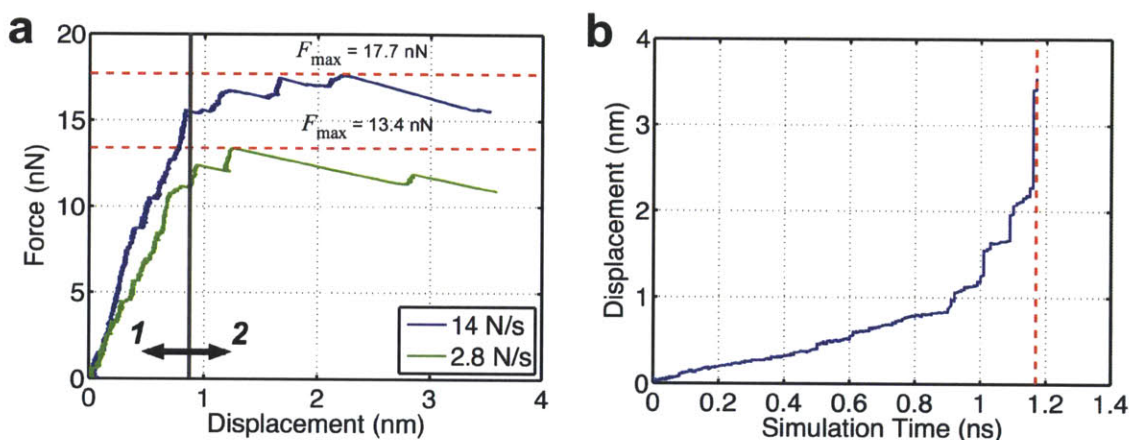
Figure 4-5: (a) Examples of force-displacement curves for end displacement of PAH polymer, depicting SMD pulling speeds of 10 m/s and 2 m/s for loading rates of approximately 14 N/s and 2.8 N/s, respectively. The force-displacement behavior consists of two regimes: (1) a linear increase in force until polymer detachment is initiated; (2) a plateau of approximately constant force, during which the PAH oligomer is pulled along the PAA oligomer. During the elastic regime, alignment of the functional groups occurs, as well as extension of the polymer conformation (also seen in Figure 4-6). Slight increases in force along the plateau region can be attributed to variable positioning of charged monomers (functional groups COO- and NH_3+) along the polymers, resulting in short periods of re-bonding and subsequent bond ruptures. (b) Example displacement-time curve for end of PAH polymer for SMD pulling speed of 10 m/s (14 N/s loading rate). The plot depicts a sudden increase in displacement at onset of maximum force (approximately 1.15 ns simulation time).

(*i.e.*, functional groups COO^- and NH_3^+) allow for slight deviations in the critical force and displacement. The second regime consists of a plateau of approximately constant force, during which the PAH oligomer is pulled along and detached from the PAA oligomer. Increases in force along the plateau region can be attributed to variable positioning of charged monomers along the polymers, as the functional groups effectively re-bond and rupture as they are pulled along the adjacent polyelectrolyte. A maximum force is reached *via* the applied spring force resulting in a sudden increase in displacement (Figure 4-5(b)), as the resistance provided by electrostatic bonding and van der Waals interactions is surpassed. Snapshots of the simulation process are shown in Figure 4-6. The maximum applied force is determined for each simulation, representing the maximum adhesion force between the two polymers.

4.4.1 Theoretical strength model

To quantify the relationship between energy barriers and applied force, *Bell's model* is a simple and commonly applied approach to extract kinetic and energetic binding constants. Bell's model is based on a energy landscape where rupture is induced by an external time-dependent force, surmounting the free-energy barrier (Figure 4-7). This method is often applied to the analysis of protein materials [2, 1, 3, 265]. However, Bell's model was initially developed as a more general theory, and is a simple phenomenological model that describes the frequency of failure of reversible bonds [28]. The concept of *reversibility* means that an individual bond can break under no force if one waits a sufficiently long time, and that it can reform spontaneously. Such bonds may be associated with electrostatic, van der Waals (vdW), or hydrogen-bond interactions. The frequency of failure, also called dissociation rate or off-rate, k, is defined as the inverse of the bond lifetime and is used as a concept to describe the dynamical behavior of such bonds. We apply the concept here to polymers primarily bonded by electrostatic interactions. Bell's model explains the force dependence of the off-rate and has shown a significant role of mechanical force in biological chemistry, such as the description of the forced unbinding of biological adhesive contacts such as adhesion of cells to cells [28].

144
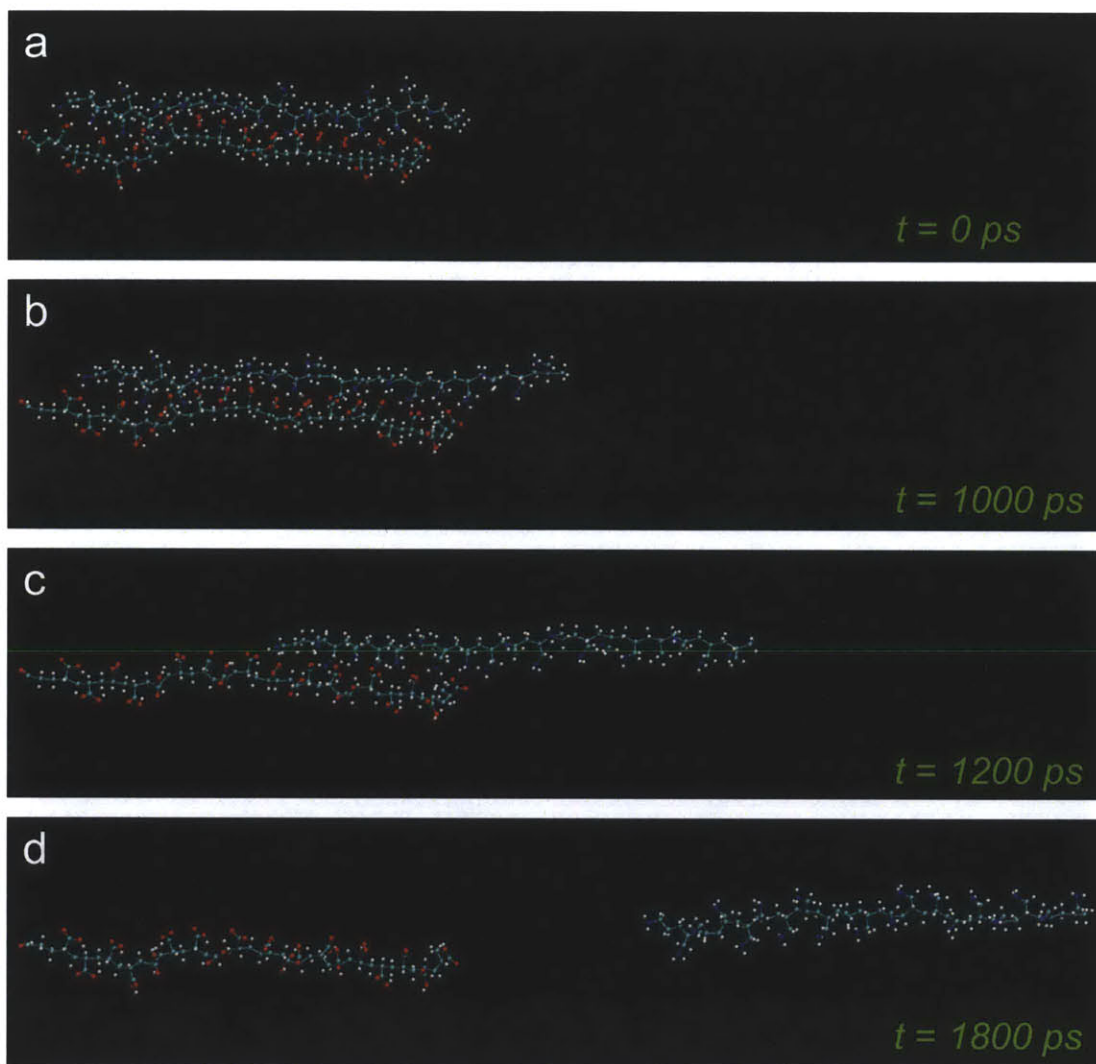
Figure 4-6: Representative simulation snapshots for SMD pulling speed of 10 m/s at: (a) 0 picosecond; (b) 1000 picoseconds; (c) 1200 picoseconds; and (d) 1800 picoseconds. For clarity, water molecules are removed and the hydrogen bonds are not shown. The plot confirms a relatively small displacement as the force increases linearly between snapshots (a) and (b). The maximum force occurs between snapshots (b) and (c) when PAH detaches from PAA oligomer, as indicated by Figure 4-5(b).
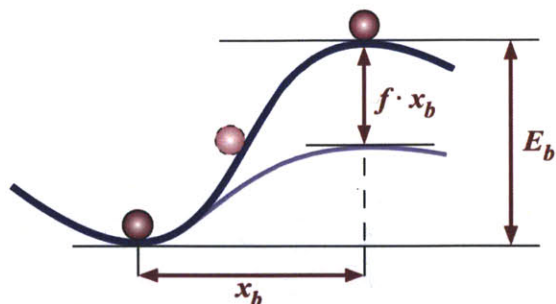
Figure 4-7: Evolution of the energy landscape of a bond subjected to a force according to Bell's model [28]. The graph depicts the energy as a function of deformation along a deformation variable, along a particular pathway that leads to bond rupture. The rupture of the bond occurs *via* thermally assisted crossing of an activation barrier E_b, which is reduced by $f \cdot x_b$ as the applied force f increases. Here, we apply this fundamental view of single bond behavior to the interactions of adjacent PAA/PAH polymers.

Bell predicted for the first time that the off rate of a reversible bond, which is the inverse of the bond lifetime, increases when subjected to an external force, f. Indeed, the rupture of bonds occurs *via* thermally assisted crossing of an activation barrier E_b which is reduced by energy equivalent to $f \cdot x_b$ as the applied force f increases, x_b being the distance between the bound state and the transition state (see Figure 4-7). Thus, the Bell off-rate, k, is given by [28]:

$$k = \omega_0 \cdot \exp\left[-\frac{E_b - f \cdot x_b}{k_B T}\right] \qquad (4.2)$$

where ω_0 is the natural vibration frequency of the bond and $k_B T$ the thermal energy (k_B being the Boltzmann constant, and T the temperature).

Although successful, the Bell model approach has some limitations that have led to several refinements. One such limitation is that the Bell's theory deals only with constant external force and does not explain the loading rate dependence of strength. Evans and Ritchie [110] extended the model by introducing the rate dependence of strength, demonstrating that the strength of bonds depends crucially on the loading rate. This dependence is critical, as experimental and simulation loading-rates typically differ by one or more orders of magnitude. They theoretically showed that, above a critical loading rate, the force of rupture increases logarithmically, reconciling differences between experimental and simulation results. For a monotonically

146

increasing applied force, an adaptation of this model relates the unbinding force to experimental, kinetic, and energetic parameters. Provided that x_b and E_b remain constant, a logarithmic dependence of strength on the loading rate is as follows:

$$f_r = \frac{k_B T}{x_b} \ln\left(\frac{r_f}{r_0}\right) \qquad (4.3)$$

where f_r is the required rupture force, r_f is the loading rate and r_0 is the dissociation load-rate (in N/s) in the absence of force, defined as:

$$r_0 = \omega_0 \cdot x_b \cdot K_{\text{spring}} \cdot \exp\left[-\frac{E_b}{k_B T}\right] \qquad (4.4)$$

as described by the Bell model, Equation 4.2 for $f = 0$; for further description, see reference [2]. For SMD with controlled increasing applied force, the loading spring is usually moved at constant speed relative to a fixed point. Again, the pulling speed, v, is linked to the loading rate, r_f, through the prescribed stiffness K_{spring} of the spring, $r_f = K_{\text{spring}} \cdot v$. Thus, this description of rate dependence is very significant for experimental and simulation studies because it enables one to get the bond constants r_0 and x_b from a regression on the force-log(r_f) curve. Moreover it rationalizes the variation among rupture force values obtained from different experimental and simulation techniques that implement different loading rates. Further, by accounting for the possible change in energy landscape as a function of force, the bond off-rate can subsequently be formulated as [110]:

$$k = k_0 \cdot g(f) \cdot \exp\left[\Delta E_b(f)\right] \qquad (4.5)$$

representing and extension to the Bell Model presented in Equation 4.2 where k_0 is a prefactor that contains the Arrhenius dependence on the barrier energy scaled by a characteristic time constant, $g(f)$ is a function which depends on deformation of energy landscape by external force, and $\Delta E_b(f)$ is the reduction in energy barrier height. This off-rate relation is more general compared with Bell's relation. Indeed, it does not use the simple linear approximation $\Delta E_b \propto E_b - f \cdot x_b$ for the reduction in energy barrier height. Thus it may be physically more relevant since it allows the

positions of transition state and bound state to change under external applied force. We propose the addition of a power-law decrement to the energy barrier height to account for the force-driven amplification of the kinetics, such that:

$$\Delta E_b\left(f\right) = \left[-\frac{E_b - f \cdot x_b}{k_B T}\right] - \left[\frac{x_b}{k_B T}\right] r_f^{\beta} \tag{4.6}$$

Here, the decrease in energy barrier is encompassed by the exponential term, r_f^{β}, where β is a statistically determined parameter. The addition of the power-law formulation has been a useful heuristic in previous studies to quantify rate dependence [171]. The intent is to maintain the logarithmic dependence as described by Bell's Model, while accounting for a potential decrease in energy barrier. A potential cause for the decrease of the energy barrier is the contribution of bond rebinding at slower loading regimes. Assuming $g\left(f\right) = 1$ (*i.e.*, the energy landscape is *independent* of external force) we can derive a relation between rupture force and loading rate, or:

$$f_r = \frac{k_B T}{x_b} \ln\left[\frac{r_f}{r_0}\right] + r_f^{\beta} = a \cdot \ln\left[r_f\right] + b + r_f^{\beta} \tag{4.7}$$

Thus, the parameters for the energy landscape, x_b, r_0, and E_b, can be extracted by a regression of the force-log(r_f) curve where $a = k_B T / x_b$, and $b = -a \cdot \ln\left[r_0\right]$, where β incorporates the rate-dependent effect on energy barrier. The model enables one to characterize the bonds, their ruptures and their energy landscape profiles from the fitting with experimental [336] or simulation results. As the above formulation is derived from the initial assumptions of the Bell Model (Equation 4.2), in subsequent sections, we refer to the relation presented in Equation 4.7 as the "extended" Bell model.

The Bell model and various extensions have been remarkably successful in fitting much of the data on forced unfolding of biological molecules, and we find it befitting to the application in the current polyelectrolyte system. It is noted that several other attempts have been made to extend and refine the simple "classical" Bell's model. For instance, it has been shown that rebinding can have a great impact on strength [296, 109, 297], as well as the energy landscape effect on the unfolding

148

pathway of convoluted protein structures [110, 2]. In non-equilibrium pulling regimes, other models attempt also to explain non-logarithmic and probabilistic loading-rate dependence [159, 104]. Moreover, other extensions try to implement the influence of the transducer stiffness in order to explain the disparities in measured unbinding force among different methods [336]. As a last example of extension, we can mention the existence of models which explicitly account for the energy landscape roughness of individual bonds [361, 160].

Here, we limit our discussion to the provided formulation (Equations 4.3 through 4.7). A more sophisticated analysis introducing further system parameters is not required to both justify the rate-dependent behavior of the current polymer system, as the intent is not to explicate the exact mechanism of adhesion and rupture, but rather to only investigate the rate-dependent *variation* of strength. Furthermore, although refinements of the model have been extensively implemented in the investigation of protein systems, the transferability to a polymer system is undetermined, with the current study providing initial corroborative results. The form of the "extended" Bell Model presented in Equation 4.7 is deemed appropriate to be applied to the polymer system at hand.

4.4.2   Analysis of simulation data

The adhesion strength is plotted as a function of the pulling speed in Figure 4-8, and an inspection of the simulation results indicate a dependence on adhesion strength and loading-rate (*via* pulling speed) for the polymer system, ranging from approximately 10 nN to 30 nN. For a direct application of the "classical" Bell Model (*i.e.*, Equation 4.3), we require a linear relation between adhesion force and the logarithm of loading-rate. However, linear-regression of the results indicates a deviation from this relation as pulling-speeds are decreased. As shown in Figure 4-8, the deviation from the linear relation occurs increasingly with an increase in loading rate.

We attribute this deviation from the Bell Model to the effect of rebinding of charged monomers at slower loading rates. It has been shown that rebinding can have a great impact on strength [296, 109, 297]. The argument can be summarized as

149
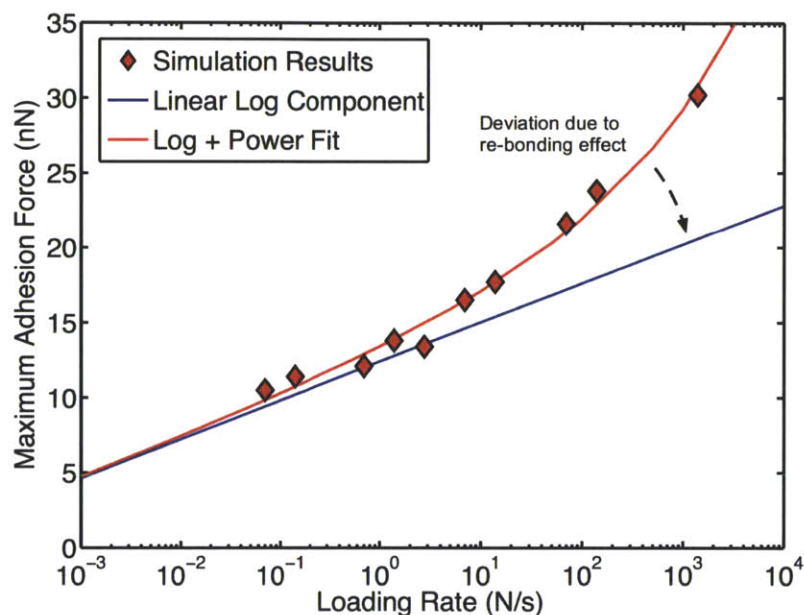
Figure 4-8: Maximum adhesion force dependence on loading rate, representing loading rates over five orders of magnitude from 0.07 N/s to 1400 N/s. Regression fit depicted for the linear force-$\log(r_f)$ relation representing the "classical" Bell Model (linear log component), illustrating deviation as loading rate varies. Mixed linear-log/power-law fit implemented to account for variation in energy barrier where, $\Delta E_b(f) \propto -E_b + f \cdot x_b - r_f^\beta$. Parameters result in a dissociation load-rate (r_0) of approximately $1.64 \times 10^{-5} N - s^{-1}$, with an energy transition distance parameter, x_b, of approximately 0.04 Å. The calculated zero-force dissociation load-rate results in an energy barrier, E_b, of approximately 8.96 kcal/mol. A regression coefficient of determination (R^2-value) of 0.993 is calculated for the "extended" Bell Model fitting indicative of a statistically significant correlation.

a balance between rupture (or dissociation) and rebinding events: at slower loading rates, the magnitude of rebinding rate approaches the rate of bond rupture, thereby requiring more energy to surmount [297]. For the current system, when the PAH polymer is pulled at a slower velocity, there is a higher probability of encountering another interaction site on the adjacent PAA polymer in which the energy barrier must be surpassed, developing a "catch" mechanism during the detachment process. At slower velocities, the effect of the "catch" mechanism increases, effectively creating more energetically favorable bonded configurations of the polymer system, resulting in cumulative increases maximum adhesion force and deviations from the extended Bell Model. At higher velocities, the effect of rebinding is negated, as the rebinding rate is irrelevant in comparison to the bond dissociation rate.

By fitting the results to the extended Bell Model (Equation 4.7), we obtain a zero-force dissociation load-rate, r_0, of approximately 1.64×10^{-5} N$-$s^{-1}, with an energy transition distance parameter, x_b, of approximately 0.04 Å. From Equation 4.4, the calculated zero-force ($f = 0$) dissociation load-rate results in an energy barrier, E_b, of approximately 8.96 kcal/mol. A regression coefficient of determination (R^2-value) of 0.993 is calculated for the "extended" Bell Model fitting indicative of a statistically significant correlation. We note the value of the energy barrier, E_b, is in the same order of magnitude for the breaking of groups of hydrogen bonds in alpha-helical and beta-sheet protein domains (approximately 11.1 kcal/mol [2]). This correspondence abets the application of the Bell Model for the current energy regime and adhesion strength of the polyelectrolyte system.

The inter-polymer interactions are presumed to arise from both electrostatic and hydrogen bonding (accounted for *via* pair interactions). We note that the bond breaking energy of a hydrogen bond in a peptide in water ranges typically from 3 to 6 kcal/mol [302]. We determine an energy barrier of approximately 9 kcal/mol, which supports the combination of dominant hydrogen bonding and partial electrostatic interactions (due to the limited ionization of PAA) between the functional groups of the weak polyelectrolytes. Additionally, we can obtain the potential energy evolution of the amine/amino functional groups (*i.e.*, both NH_2 and NH_3^+), assumed to account

151
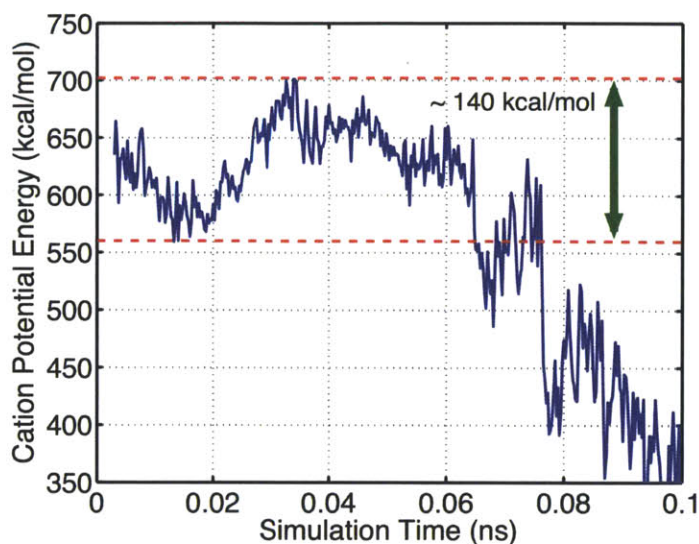
Figure 4-9: Potential energy evolution of polycation function groups of PAH oligomer. Initial decrease attributed to system finding energy minima. Increase equivalent to energy barrier of adhered functional groups (approximately 140 kcal/mol). Once surpassed, the oligomers separate, and potential energy further drops as the detached polymer is free to find a more energetically favorable conformation.

for the strongest bonding, directly from the simulation results (Figure 4-9). The initial potential energy decreases as the system finds an equilibrium configuration, followed by an explicit increase in energy as the spring force is applied to the PAH polymer. A maximum is reached, and the potential energy drops for the remainder of the simulation. Approximating the energy barrier results in a difference in potential energy of approximately 140 kcal/mol for the twenty monomers, or a per group energy barrier of approximately 7 kcal/mol. As the plotted potential energy only considers the functional groups (NH_2/ NH_3+ from the PAH oligomer), the calculated energy barrier is slightly lower then the Bell analysis, which accounts for interactions of the entirety of the polymers (such as interactions between the carbon backbones).

4.4.3 Comparison with experimental results

The results of the SMD simulations are correlated with previous chemical force microscopy (CFM) experimental results [166]. In this previous study, PAH molecules adhered to a colloid are implemented to probe the adhesion between the polyamine

152

and a carboxylic acid (COOH/COO-) self-assembled monolayer (SAM) at various pH levels. Although the molecular architecture of the system is quite different, the interaction between the COOH SAM and the amine groups of the PAH (NH_2/NH_3+) are identical in chemical composition to the functional groups of the modeled PAA/PAH system. The intent of the arrangement is to examine directly the intermolecular interactions between the polyamine PAH and a COOH-functionalized surface. Indeed, the use of a polyamine grafted colloidal sphere and a COOH-functionalized surface served to limit the free lengths of polymers, providing a closer correspondence to our relatively short oligomer molecular model.

The experimental results find at a low pH value of 2.5, strong adhesive interactions take place between the PAH and the COOH surface, reflecting ionic as well as hydrogen-bonding interactions. The PAH is highly protonated at pH of 2.5, but the acid surface is also in its protonated form (*i.e.*, a relatively small fraction of COO- groups present). Such conditions are similar to our molecular model. The ionized amino groups (NH_3+) of PAH act as strong hydrogen bond donors to the carboxylic acid groups, providing opportunity for increased adhesion. The result is an adhesion strength of 10.8 ± 0.88 nN (average of over 100 data points) [166]. The force value predicted by our simulations and the theoretical strength model at low loading rates (below 1.0 N/s), is in proximity to the adhesion strength determined by experimental CFM (10.8 ± 0.88 nN) at a pH of 2.5 [166]. The model indicates a decrease in adhesion strength at lower rates, however, discrepancy in experimental values can possibly be attributed to the adhesion of a PAH chain to multiple carboxylic acid segments, as opposed to a one-to-one alignment of the current atomistic simulations.

In addition, the electrostatic and hydrogen bonding between the present functional groups COOH-NH_2 and their respective charged (COO-, NH_3+) states have been experimentally studied in a range of solvents [240]. The adhesion strength is expected to vary depending on the details of the experimental conditions (*e.g.*, sample preparation and cleanliness, surface and CFM tip roughness, etc.). However, the magnitude adhesion force ranged from 4.5 nN to 14 nN [240], supporting the magnitude range of the findings reported here.

It is noted that a one-to-one correlation between these experimental values and the current simulation results is not intended. Indeed, it would be gratuitous to presume a single adhesion strength based on the stringent conditions of the simulation arrangement. It behooves us to note that there is inherent randomness in the rupture forces and times, predicated by system arrangement and conditions. The empirical values [166] contain substantial variability due to both experimental artifacts, system conformational heterogeneities, and entropic effects, eliminated by our simulation constraints. However, representing the experimental conditions exactly would be superfluous, as our aim is to determine the adhesion force for the current simulation conditions, to elucidate rate and ionization dependence specifically disassociated from such system variability. The correlation with experimental values is introduced as a means to: (1) justify the magnitude of the resulting adhesion strength, and; (2) provide a means to compare extrapolated simulation results (at limited time-scale regimes) with physical results.

We conclude the proposed method of systematically varying the loading-rate of a polymer system is applicable in determining the energy landscape and adhesion strength of a polyelectrolyte system. At high pulling speeds, the "extended" Bell Model provides an appropriate model to represent the dissociation rate of the weak polyelectrolyte interactions. For a modeled pH value of 2.5, we find an energy barrier, E_b, of approximately 8.96 kcal/mol, befitting the appropriate energy range of Bell Model analysis, as well as corresponding to known magnitudes of hydrogen bonding and electrostatic interactions. The energy barrier of approximately 9 kcal/mol is considered representative of a single "electrostatic cross-link". While higher than an isolated single charge-to-charge interaction, the energy accounts for the combined interactions induced, including hydrogen bonding, hydrophobic and/or steric effects. As such, it is used a a basis for electrostatic interactions in **Chapter 5: Critical Ionization to Couple Polyelectrolytes**. By extrapolation of the simulation results, the adhesion strengths are in good agreement with previous investigations of the polyelectrolyte functional groups. For further investigation on the adhesion strength of the system, we proceed to systematically vary the ionization of each polymer.

4.5 Ionization Dependence of Adhesion Strength

While several solution processing variables play important roles in molecular organization for strong (pH-independent) polyelectrolyte systems [102, 49], pH becomes a key factor in the case of weak polyelectrolytes (such as PAA and PAH). In the LbL assembly of PEM materials, control of the layer thickness and molecular organization of an adsorbed polymer chain is achieved by adjustments of the pH of the solutions [303, 248]. A change in pH controls the linear charge density of an adsorbing polymer as well as the charge density of the previously adsorbed polymer layer. To account for the effect of changes in pH in our current atomistic model, the number of protonated/deprotonated monomers is explicitly defined in the simulation model, using a random distribution as discussed in **Chapter 2**. For large polyelectrolyte systems, the effect of random ionization would vanish at the global system level. However, such fluctuations at the atomistic level can complicate the determination of rupture forces for varying heterogeneous conformations and initial states under fast non-equilibrium trajectories [120, 50]. As such, multiple simulations were run for chosen ionization groupings, with the relevant average behavior presented in the results (see Table 4.1, and Figure 4-10) to probe the relative consistency of adhesion strength for random initial ionization configurations[1].

4.5.1 Simulation results

To investigate the potential for tunable adhesion, a series of SMD simulations is undertaken at various combinations of PAA and PAH ionization levels. For efficient simulations, a relatively fast pulling speed of 10 m/s is implemented, limiting the simulation time to approximately 0.25 ns. Simulation conditions and boundary conditions are identical to those imposed by the rate dependence investigation. Force-displacement data is used to determine the maximum adhesion force between the two

---

[1]Before discussing simulation results, it is important to revisit the relatively uncertain charged state of the polyelectrolytes in solution as a function of pH. While, in general, the pH level and level of ionization can be linked *via* pKa values, characterizing a polymer by a single pKa value is unwarranted. As such, changes in adhesion should be assessed in terms of ionization, rather than pH.

Figure 4-10: Maximum adhesion force dependence on ionization (Table 2) from SMD simulations with a (loading rate of approximately 14 N/s. Subplot (a): Data points from simulations where fitted linear trend lines show increase in adhesion force with increase in net ionization. Minimum adhesion strength occurs at zero percent ionization (8.3 nN) while maximum adhesion strength occurs at complete (100%PAH, 100%PAA) ionization (41.2 nN). Mean values and error bars depicted for four groupings: 20% PAH with 20% PAA, 20% PAH with 50% PAA, 50% PAH with 20% PAA, and 50% PAH with 50% PAA representing standard deviation (refer Table 2). Highest variance associated with highest potential for electrostatic interactions (50%PAH, 50%PAA). Subplot (b): Shaded area represents region of attainable ionization levels as a function of pH. Data points removed from linear trend lines for clarity. Maximum adhesion strength on the order of $\sim$40 nN occurring at ionization levels of $\sim 95\% - 100\%$ and $90\% - 95\%$ for PAH and PAA respectively, corresponding to a pH of approximately 7.0.

bonds, depending on the distribution of the ionized functional groups (here, 50% ionization corresponds to ten ionized monomers). The other groups subject to multiple simulations were limited to a maximum of 20% ionization (four functional groups for either PAH or PAA), thus restricting the potential alignment and electrostatic interactions of functional groups, resulting in a decrease in variance of the resulting rupture forces.

We note that at zero percent ionization, there is minimum adhesion strength of 8.3 nN, reflecting a propensity for attraction regardless of electrostatic interactions *via* hydrogen bonding and van der Waals interactions. There is also a contribution of frictional forces due to the explicit water, which is presumed negligible for comparative purposes. As expected, maximum adhesion strength of 41.2 nN occurs when both oliogmers are completely ionized, where each COO- group is aligned with a corresponding NH3+ partner. Thus, manipulation of ionization can increase the adhesion of the polymer complex *fivefold*, with intermediate values possible *via* careful adjustment and control of ionization combinations. Both extrema (where both PAA and PAH are either 0% ionization or 100% ionization) are theoretical, as there is no corresponding pH value to completely protonate or deprontonate the respective oppositely charged weak polyelectrolytes, albeit values exceeding 90% ionization for both can be obtained (depending on pKa value; see Figure 2.2). If it were possible to explicitly control the ionization of each polyelectrolyte in solution, these forces represent the theoretical upper and lower bounds of potential adhesion strength.

Considering known levels of ionization at specific pH levels [66], and solution pK_a values ~6.5 and ~8.5 for PAA and PAH respectively, we can deduce a range of adhesion forces for a given system. For example, for a pH of approximately 2.0, PAH is approximately 95%-100% ionized, while PAA is less than 25% ionized. An approximate range can only be inferred due to the potential shift of pK_a values in a multilayer system [215, 303, 48, 62]. For example, the effective pK_a of PAA in the multilayer system with PAH is about 2.5, however, at a pH 2.0, the ionization is still below 25%. A more precise correspondence would require the specification of assembly conditions and solution treatments. From the results of the simulations,

this corresponds to an adhesion strength on the order of 15 to 20 nN. Similarly, a pH of 7.0, with approximately 95%-100% PAH ionization and 70%-90% PAA ionization can be limited a range of approximately 38-42 nN. Finally, at a pH of 10, the adhesion strength is on the order of 15 nN. As expected, the adhesion force reaches a maxima in the region in which the net ionization is greatest (between 70% and 90% PAA ionization and about 95%-100% PAH ionization).

Consequently, as the actual level of ionization is complex, precise determination of all possible ionization combinations is superfluous. However, determination of the relative magnitude and range of adhesion forces at different pH levels is critical for the development of potential mechanomutable systems. Using the known data for ionization levels and adhesion forces, we can develop an approximate regime of adhesion force as a function of pH (Figure 4-10). The exploration of possible ionization manipulation *via* environmental controls or assembly procedures can perhaps extend the accessible strength levels of the current or other polyelectrolyte systems.

4.5.2 Comparison with experimental results

We find that adhesion strength increases as the net level ionization increases. We would likewise expect the highest experimental values to occur at pH levels in which both polyelectrolytes are significantly ionized. At a pH range of approximately 4.0 to 7.0, there is a net increase in ionization of both the PAA and PAH. In contrast, experimental investigations have shown that the adhesion strength at these pH levels drops significantly to less than 1.0 nN [166]. The observation of this decrease in attractive forces is not intuitive.

The present study investigates the adhesion properties of polyelectrolytes after complexation, however, during assembly, the hydrophobic nature of long chains of PAH and PAA result in conformational changes as a function of ionization. It has been proposed that, at high levels of ionization, due to an increase in persistence length, the polymer segments are more extended[2], whereas decreasing the ionization results in globular regions of aggregated segments [303, 166]. It is partially for this

[2]We note that quantifying this change in persistence length is the focus of the preceding chapter.
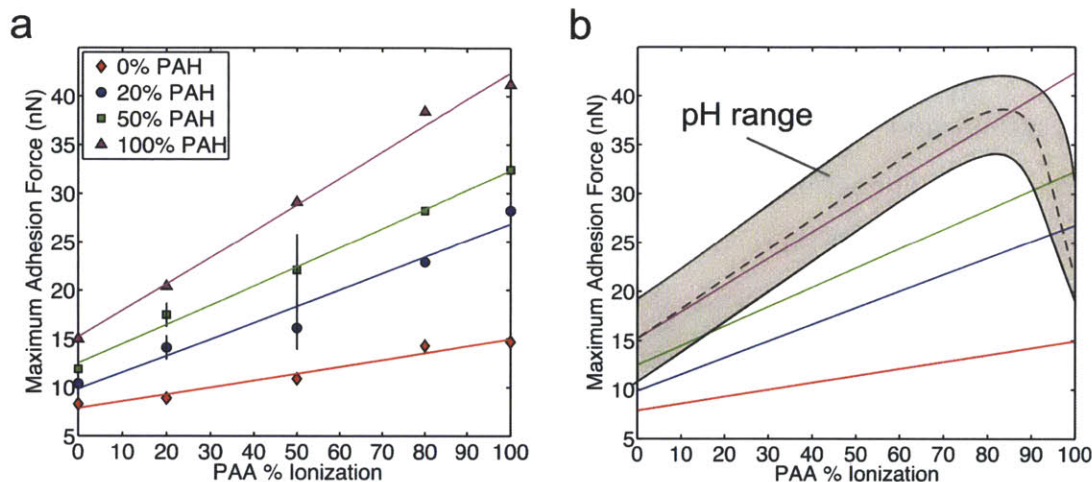
Figure 4-10: Maximum adhesion force dependence on ionization (Table 2) from SMD simulations with a (loading rate of approximately 14 N/s. Subplot (a): Data points from simulations where fitted linear trend lines show increase in adhesion force with increase in net ionization. Minimum adhesion strength occurs at zero percent ionization (8.3 nN) while maximum adhesion strength occurs at complete (100%PAH, 100%PAA) ionization (41.2 nN). Mean values and error bars depicted for four groupings: 20% PAH with 20% PAA, 20% PAH with 50% PAA, 50% PAH with 20% PAA, and 50% PAH with 50% PAA representing standard deviation (refer Table 2). Highest variance associated with highest potential for electrostatic interactions (50%PAH, 50%PAA). Subplot (b): Shaded area represents region of attainable ionization levels as a function of pH. Data points removed from linear trend lines for clarity. Maximum adhesion strength on the order of $\sim$40 nN occurring at ionization levels of $\sim$ 95% $-$ 100% and 90% $-$ 95% for PAH and PAA respectively, corresponding to a pH of approximately 7.0.

reason the thickness of PEM systems can be fine-tuned according to pH during the assembly process [303, 62]. Due to the initial extended configuration of our system (regardless of ionization), representing a preformed PEM, this effect is negated and any conformational changes are essentially eliminated. We emphasize that the objective of the present study is not to represent assembly conditions and, similarly, the simulations were not intended to replicate the entropic and hydrophobic behavior of larger systems. Rather, the focus is on the interaction between the functional groups of each polyelectrolyte. The results elucidate a single characteristic of the entire system and have a twofold purpose: (1) to contribute to a holistic view of polyelectrolyte interactions to dissociate distinct behaviors (such as electrostatic and hydrogen bonding with steric and entropic effects), and; (2) to provide the quantities required to parameterize multi-scale coarse-grain representations that will allow the efficient simulation of larger systems to investigate such effects.

In accordance, as the current simulation arrangement focuses on the functional groups, we can compare the effect of ionization and pH on the experimental adhesion strength of $COOH$-NH_2 pairings. Again, we revisit previous experimental investigations conducted using CFM *via* a COOH SAM colloidal probe and an NH_2 SAM surface [166]. The maximum adhesion strength values occurred in a pH range of approximate 5.0 to 7.0, when both functional groups were partially ionized (approximately 70%). As the pH is decreased from this range, the adhesion strength drops due to a decreased electrostatic contribution of the weakly ionized carboxylic acid group, while as pH was increased, low adhesion forces were subsequently attributed to the decrease in degree of ionization of the amino group. Although a quantitative comparison is not possible, the experimental isolation of the carboxylic acid and amino functional groups resulted in the same qualitative changes in adhesion strength in the same range of representative pH values. The effect of such isolation is in consensus with the separation of the functional groups from entropic effects in our simulations, by means of relatively short polyelectrolyte oligomers.

To conclude, the net ionization of oppositely charged polyelectrolytes serves to increase the adhesion strength when the polymers are in contact. At larger scales, it

is experimentally shown that there is competition between entropic and steric effects and adhesion strength, limiting the ability for the alignment of charged polyelectrolyte functional groups, which is further complicated by the complex nature of ionization of weak polyelectrolytes as a function of environmental conditions. We thus derive values of the theoretical adhesion strength as a function of ionization, and find a potential range of strengths that can be attributed to a pH level. Our SMD simulations at pulling speeds of 10 m/s have shown a twofold increase in adhesion strength (from approximately 15 nN to 40 nN) within attainable pH levels (approximately 2.5 and 7.0, respectively). To obtain the static adhesion strength, rate dependent investigations are required, captured by the "extended" Bell model. Such results serve to elucidate the upper- and lower-bounds of the potential adhesion strengths of tunable PEM system.

4.6   Summary

An advance in layer-by-layer assembly of polymers producing ultrathin films and nanocomposites, combined with implementing various constituent polymers and materials, has resulted in numerous experimental investigations to systematically probe the behavior and mechanical properties of such polyelectrolyte multilayer (PEM) systems. The current investigation focuses on two specific polymers: poly(acrylic acid) (PAA) and poly(allylamine hydrochloride) (PAH) due to extensive experimental study on the interactions between these polymers and their respective functional groups.

Simulations of such a system can provide an important complement to experimental techniques as they allow the isolation of relevant behavior at the atomistic scale. In the present investigation, we probe the chemical energy landscape that governs the physical strength and kinetics of the bonding of two polymers. Experimental requirements to isolate single molecule interactions of such a system complicates physical measurements, befitting simulation techniques such as steered molecular dynamics (SMD) that emulate laboratory processes (such as AFM). Due to the complexity

of the polymer system, we look to methods typically employed in protein-material investigations - specifically, SMD and Bell Model analysis.

An analysis of the rate dependence on the adhesion force between polyelectrolytes is motivated by the discrepancy between the timescales accessible to experimental and simulation results. The Bell Model is implemented to determine the energy barrier between two adhered polymers. Our findings of an energy barrier of approximately 9 kcal/mol is within the range for application of the Bell Model, as well as a reasonable magnitude for the combination of hydrogen and electrostatic bonding. Such findings provide support for the application of Bell Model analysis for other polyelectrolyte systems while contributing new insights into polymer complexation. We further extrapolate our rate dependence results to determine the static adhesion strength of PAA/PAH at a corresponding pH. Our value of 8.2 nN is within close proximity to experimentally determined values of a similar carboxyl-amine system.

Experimentally, it has also been shown that functional groups of the polymers under investigation undergo a balance of electrostatic and hydrogen bonding with each other that can result in adhesion and complexation that varies in strength as a function of pH. With careful judicious adjustment of the pH during assembly, the degree of ionization of these polymers can be altered substantially, thereby making it possible to tune at the molecular level the structure and properties of the resultant multilayer composite [62]. We simplify the complex nature of pH dependence on protonation/deprotonation of weak polyelectrolytes and isolate the effect of ionization on adhesion strength. We find that electrostatic interactions can serve to increase the theoretical adhesion strength fivefold (from approximately 8.0 nN to 40 nN), whereas physically attainable levels of ionization decrease this potential range. By theoretically determining the upper- and lower-bounds of adhesion strength, experimental investigations can be assisted in attempts to manipulate tunable properties (such as ionization) to attain precision engineered PEM systems. The desire for tunable mechanical properties requires the known behavior at the atomistic level, including full chemical details, macromolecular structure, and inter-macromolecular interactions. Experimental techniques cannot elucidate the mechanistic relation of hierarchical

multi-scale structures and their resulting properties. This limitation can be overcome by systematically studying polymer properties and interactions isolated at the atomistic level. These findings should be useful in steering experimental and simulation efforts in the characterization of polyelectrolyte multilayer composites, as well as provide a theoretical rate-dependence framework for other polymer systems. Such an approach is necessary for the fundamental understanding of the mechanics and mechanisms to be utilized in a new class of responsive, mechanomutable materials.

Chapter 5

Critical Ionization to Couple Polyelectrolytes

Previous chapters have investigated polyelectrolyte chains in isolation as well as their propensity for adhesion, but what can be said about complexation? It is well-known that that individual chains cross-link due to oppositely charged functional groups, but does such cross-linking induce mechanical cooperativity, or merely a random network of interconnected polymers? To shed insight on the potential mechanical coupling of polyelectrolyte complexation, a simple elastic model is developed representing two cross-linked molecules of finite rigidity. Parameterized by the previous full atomistic investigations, the elastic model can be considered a coarse-grain representation of the full atomistic system. Instead of grouping atoms to bridge length scales, the elastic model homogenizes atomistic interactions to known mechanical responses (*e.g.*, bending rigidity, cross-link stiffness). Solutions to the eigenvalue problem for the elastic model (*e.g.*, vibrational modes) is used to determine the critical ionization (and thus pH) to induce mechanical cooperativity.

5.1   Preamble and Motivation

As discussed, polyelectrolyte multilayers have been thoroughly investigated for their potential in a diverse array of applications, including biosensing and bioelectronics

[161], nanofiltration and fuel cell technology [358], as well as cell and tissue engineering [133, 80]. Being said, development of such applications tends to focus on the system level characteristics, without consideration of smaller-scale properties that may influence performance. For example, matching cells to multilayers requires intimate knowledge of hydrophobicity [216, 282], composition [276], and stiffness [294] of PEMs. But these system-level effects are not sufficient - what biological cells and tissues "see" is beyond a single scale interaction. Successful application requires full and predictive knowledge of mechanical behavior[1] *across* scales, from microscale interfacial properties to nanoscale molecular interactions. One does not engineer a complex machine (*e.g.*, functional material) without reliably knowing the properties and performance of each individual component.

While the experimental body of work on polyelectrolyte complexation is extensive, there are very few quantitative theoretical approaches. Moreover, most previous attempts have focused on bulk system behavior, mean field theory, and statistical measures [37, 52, 53], rather than explicit molecule-to-molecule interaction. Formulations based on the Debye-Hückel theory of electrolytes, for example, have been proposed, resulting in an effective phase-diagram for complexation and multilayers [52, 53]. Regardless of theoretical form, it is well known that electrostatic interaction drives the complexation of weak polyelectrolytes in multilayer systems [287], but less quantified is the subsequent mechanical effects. Complexation is indeed driven by entropic and enthalpic contributions [43], but such measures are not sufficient to completely describe the assembly and stability of PEMs in terms of *mechanical* properties.

In this chapter, the atomistic mechanism of cooperative deformation is investigated by means of an elastic structural model, derived to solve the representative vibrational modes, and used to extract the effective bending rigidity as a physical metric for complexation. The intent is to use the full atomistic mechanical properties derived in previous chapters to parameterize an idealized "truss" model of a

---

[1] As well as physiochemical, thermal, optical properties, etc. But here, we are primarily concerned with mechanical characteristics.

polyelectrolyte complex.

5.2 A "Truss" Analogy of Nanomechanical Coupling

The concept of *mechanical coupling* or *cooperativity* can be loosely defined as "equivalent mechanical behavior between components and complex" - here, when the effective rigidity of the complex is equivalent to that of each individual molecule (colloquially speaking, when "1+1=1"). For example, in terms of the end-to-end distances (and thus *effective* persistence length and rigidity) of each polyelectrolyte, they should converge as they become cross-linked (*i.e.*, each polyelectrolyte reciprocally "stretches" the other). While full atomistic approaches are accessible for two polyelectrolytes, quantifying the cooperativity of mechanical behavior is difficult from atomistic measures alone. Thus, a generalized model is desired, to capture the primary interactions and behaviors involved in complexation. If we assume two aligned polyelectrolytes of finite rigidity, with a known distribution of cross-links (of known stiffness), the mechanical system resembles a classical truss system - the polyelectrolytes representing the "flanges" while the ionic cross-links represent the "web" (see Figure 6-2).

To define the mechanical behavior of the truss, we turn to a modified version of elastic network models, a technique commonly implemented to attain normal modes of complex atomistic structures (such as proteins), and introduced in **Chapter 2: Computational Methods**. One of the key benefits of elastic networks is the insight attained on the relationship between *structure* and *function*. In contrast, here an elastic model is developed to determine the effective mechanics of a known molecular system. The structure and function (in terms of complexation in LbL systems) is known. Rather than uncover unsuspected behaviors of conformations, the alternative motivation is to reduce many degrees of freedom to a few simple mechanical parameters, describing molecular rigidity and degree of complexation of charged polyelectrolytes in an efficient manner.
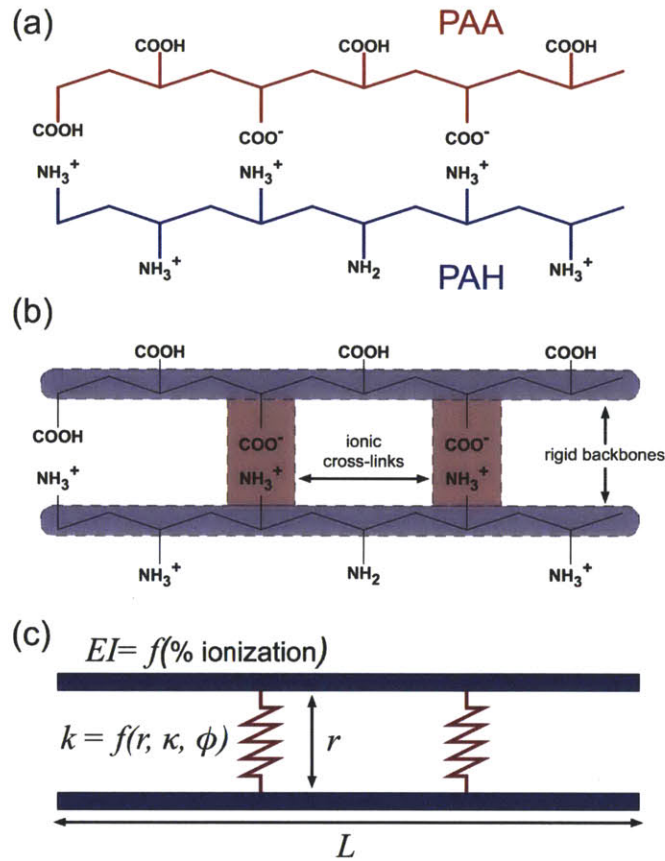
Figure 5-1: Polyelectrolyte complex to "truss" model representation. (a) General chemical structure of aligned polyelectrolytes, consisting a repeating carbon backbone with carboxyl ($COOH/COO^-$) and amine (NH_2/NH_3^+) functional groups for PAA and PAH respectively. (b) Recognition of primary structural components, including (i) the ionic cross-links (highlighted), and (ii) both polyelectrolytes are dominated (mechanically) by a rigid backbone chain (highlighted). Note that not all functional groups participated in cross-linking, and both cross-links and rigidity are a function of ionization. (c) General 2D elastic "truss" model of a polyelectrolyte complex, consisting of two rigid backbones and electrostatic cross-links in the form of beam (flexural members) and spring elements respectively. The model is parameterized by derived atomistic information (polymer length (L), effective backbone rigidity (EI) as a function of ionization, and cross-link stiffness (k) as a function of screening length (κ^{-1}), separation (r), and electrostatic energy (ϕ)).

Simple elastic network models have been proven to successfully model the large amplitude (*e.g.*, low frequency) vibrational models of a molecular structure [326], by means of phenomenological potentials that reflect geometric (*e.g.*, structural) connectivity rather than accurate molecular interactions (see Bahar and Rader [20] for a review). Indeed, ENMs could be considered equivalent to "truss" models, constructed

by linear-elastic truss elements ($e.g.$, $k_{\text{truss}} = EA/L$) in obscure and convoluted ($e.g.$, protein structure) architectures, capable of being analyzed by any standard finite element software package. Atoms are reduced to nodes, and potentials merely mechanical stiffness[2], and qualitative conformational changes ($e.g.$, low frequency modes) can be determined.

Beyond conformational metrics, modal frequencies also intrinsically contain relationships with mechanical properties. For example, the vibrational frequency of a flexural member is a function of bending rigidity (EI), mass ($m = \rho_L L$), and length (L) [341]. Regardless of atomistic geometry, we can effectively define the abstract "flexural member properties" of any molecule, if we consider the proper mode and frequency (it so happens that the shape structure of a polyelectrolyte complex is also befitting such a description, but it is not necessary). Beyond probing conformational fluctuations, such methods have been previously used to extract the mechanical characteristics from large but regular protein assemblies, such as amyloid fibrils [347]. One of the caveats of the approach is that the normal modes attained typically reflect $global$ motions, and omit any local mechanical idiosyncrasies ($e.g.$, hinging, occlusions, exposed functional groups, etc.) [349]. Being said, the system under investigation - a polyelectrolyte complex - is homogeneous in extent, and extraction of such global motions is the intent.

If an elastic model can be considered similar to a truss structure (in terms of mechanical elements), then the introduction of other simple structural members can serve to enrich the model, allowing efficient analysis of critical mechanisms, beyond the limitations of full atomistic MD. As such, we systematically investigate the mechanical properties of a simple polyelectrolyte complex (a system consisting of an electrostatically cross-linked polycation and polyanion; see Figure 6-2(a)) by using elastic model approaches, validated by simple full atomistic simulation. The elastic model of a polyelectrolyte complex can thus be used to extract low frequency flexural modes, reflective of bending rigidity. The rigidity of the complex is then compared

---

[2]It should come as no surprise that atomistic description of continuum mechanics benefits from Galerkin-$esque$ discretization.

to the constituent polyelectrolytes, to quantify potential mechanical cooperativity.

5.3 Development of Representative Elastic Model

We wish to formulate a general elastic model to represent an arbitrary molecular structure with (i) finite rigidity and (ii) variable cross-linking. In the simplest form, we derive a "cross-linked beam" system, consisting of two, parallel beam members, with elastic springs regular distributed along the length. As such, the macromolecular structure is reduced to connected nodes/elements with assigned boundary conditions and member properties (analogous to macroscale structural analysis [213]). We note that the elastic model by construction is an approximation, limited to small deformation about a presumed equilibrium.

5.3.1 General Elastic Model: Beam and Spring Elements

For consistency with the small-deformation assumption, we limit nonlinear effects to first-order geometric effects (*e.g.*, neglecting large deformation and potential material yield). Specifically, with a focus on bending rigidity (as opposed to failure) based on the developed idealized elastic model. Again, *via* the direct stiffness method [213], the global stiffness equation can be expressed as:

$$\{\mathbf{F}\} = \mathbf{K}\{\Delta\} \tag{5.1}$$

We assume that both the polyelectrolyte backbones as well as the complex itself can be effectively represented by a simple Euler-Bernoulli beam element. Note that this assumption is implemented to assess the change in system behavior as a function of electrostatic cross-linking, and is not intended to imply a one-to-one correspondence with beam-like behavior and entropic, polymer-like behavior. However, the mechanical effect - an increase in cooperativity (*e.g.*, coupled deformation) due to cross-links - is apparent, and an elastic approximation can be used about the small deformation regime. Note that this is similar to the normal mode analysis of complex protein

170
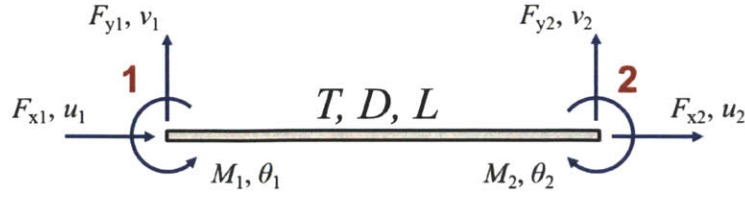
Figure 5-2: Local 2D beam element, assuming classical Euler-Bernoulli flexural behavior, defined by axial stiffness (T), bending stiffness (D), and length (L). Element consists of two nodes with three degrees of freedom (two translational, u_i, v_i; one rotational, θ_i) resulting in a 6×6 stiffness matrix, corresponding to the six components of the load vector, as described by Equation 5.2.

structures.

We consider a macromolecule with a known axial stiffness, T, and bending rigidity, D (assumed linear under near-equilibrium conditions). Note, in macroscale structures, $T = EA$ while $D = EI$. The elastic stiffness equation for a single beam element is expressed as (see Figure 5-2):

$$
\begin{bmatrix} F_{x1} \\ F_{y1} \\ M_1 \\ F_{x2} \\ F_{y2} \\ M_2 \end{bmatrix} =
\begin{bmatrix}
\frac{T}{L} & 0 & 0 & -\frac{T}{L} & 0 & 0 \\
0 & \frac{12D}{L^3} & \frac{6D}{L^2} & 0 & -\frac{12D}{L^3} & \frac{6D}{L^2} \\
0 & \frac{6D}{L^2} & \frac{4D}{L} & 0 & -\frac{6D}{L^2} & \frac{2D}{L} \\
-\frac{T}{L} & 0 & 0 & \frac{T}{L} & 0 & 0 \\
0 & -\frac{12D}{L^3} & -\frac{6D}{L^2} & 0 & \frac{12D}{L^3} & -\frac{6D}{L^2} \\
0 & \frac{6D}{L^2} & \frac{2D}{L} & 0 & -\frac{6D}{L^2} & \frac{4D}{L}
\end{bmatrix}
\begin{bmatrix} u_1 \\ v_1 \\ \theta_1 \\ u_2 \\ v_2 \\ \theta_2 \end{bmatrix}
\tag{5.2}
$$

where L describes the length between cross-links, and is thus variable depending on ionization. In effect, each node represents a charged functional group (either NH_3^+ of COO^-, for PAH and PAA respectively).

For the cross-links, we introduce ideal springs (Figure 5-3) with a derived electrostatic stiffness (see next section). The general stiffness equation for a single spring element:
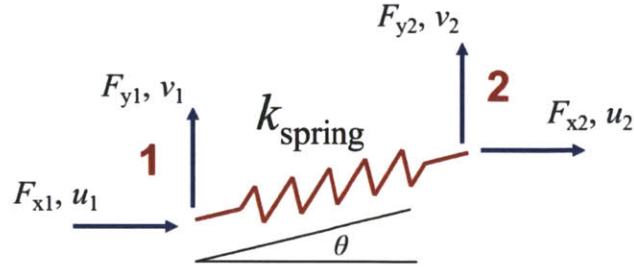
Figure 5-3: Local 2D spring element, defined by spring stiffness (k_{spring}) and orientation (θ). Element consists of two nodes with two degrees of freedom (deformation, u_i, v_i) resulting in a 4×4 stiffness matrix, corresponding to the four components of the load vector, as described by Equation 5.3.

$$
\begin{bmatrix} F_{x1} \\ F_{y1} \\ F_{x2} \\ F_{y2} \end{bmatrix} = k_{\text{spring}} \begin{bmatrix} \cos^2\theta & \sin\theta\cos\theta & -\cos^2\theta & -\sin\theta\cos\theta \\ \sin\theta\cos\theta & \sin^2\theta & -\sin\theta\cos\theta & -\sin^2\theta \\ -\cos^2\theta & -\sin\theta\cos\theta & \cos^2\theta & \sin\theta\cos\theta \\ -\sin\theta\cos\theta & -\sin^2\theta & \sin\theta\cos\theta & \sin^2\theta \end{bmatrix} \begin{bmatrix} u_1 \\ v_1 \\ u_2 \\ v_2 \end{bmatrix}
$$

where $\theta = 0°$, such that $\cos\theta = 1$ and $\sin\theta = 0$, then:

$$
\begin{bmatrix} F_{x1} \\ F_{y1} \\ F_{x2} \\ F_{y2} \end{bmatrix} = k_{\text{spring}} \begin{bmatrix} 1 & 0 & -1 & 0 \\ 0 & 0 & 0 & 0 \\ -1 & 0 & 1 & 0 \\ 0 & 0 & 0 & 0 \end{bmatrix} \begin{bmatrix} u_1 \\ v_1 \\ u_2 \\ v_2 \end{bmatrix} \tag{5.3}
$$

The element stiffness matrices can then be easily assembled to a global stiffness matrix, **K**, representing a polyelectrolyte of arbitrary length and cross-link density, depicted schematically in Figure 5-4. For a structure with n cross-links, this results in a global matrix on the order of $(3n+6) \times (3n+6)$ (*e.g.*, $n+2$ nodes per beam with three degrees of freedom per node). The computational cost is therefore a function of cross-links, and even large represented chains are computationally tractable. Note that coupling between the rigid backbones is achieved only through the defined cross links. The end result is an model that is similar in construction to an elastic network
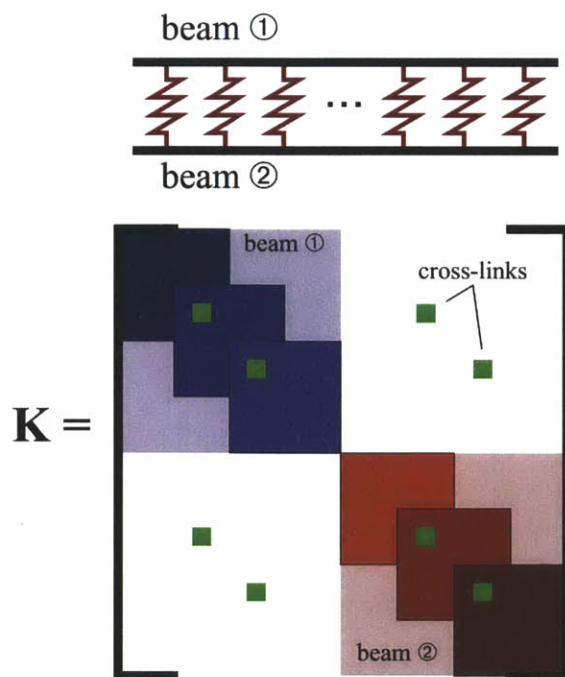
Figure 5-4: Representative global stiffness matrix, **K**, after assembly of beam elements and spring cross-links. Here, assembly of two cross-link system, with three beam elements per backbone, labeled beam ① (**blue**) and beam ② (**red**)). Total size of the matrix is $(3n + 6) \times (3n + 6)$, where n is the number of cross-links. While each beam element is coupled along the rigid backbone, coupling between backbones is achieved only through the defined cross-link springs (**green**).

model (albeit with beam members), developed specifically to capture the flexural deformation of two polyelectrolytes.

To parameterize the rigidities, the persistence lengths theoretically determined in **Chapter 3: Variation of Molecular Rigidity** were converted to rigidities based on the simple relation $EI = D = P \times k_B T$, assuming a finite temperature of 300K. To encompass ionization levels from approximately 0% to 100% for both PAA and PAH, pH from 4.0 to 11.0 was represented. The parameters for rigidity are summarized in Figure 5-5. Beam element length, L, is a function of number of cross-links, n. For the current model, a chain of fifty functional groups is represented ($N = 50$), with a unit distance monomer-to-monomer distance of $l \approx 2.8$Å. Thus, the beam length calculated simply as $L = lN/(n + 1)$.

The parameter T refers to the axial stiffness of a repeating carbon backbone

pH	PAA			PAH		
	%ion	persist Å	rigidity (kcal/mol)-Å	%ion	persist Å	rigidity (kcal/mol)-Å
4.00	0.32%	4.59	2.740	100.00%	14.18	8.457
4.25	0.56%	4.61	2.748	99.99%	14.18	8.457
4.50	0.99%	4.63	2.761	99.99%	14.18	8.457
4.75	1.75%	4.67	2.785	99.98%	14.18	8.457
5.00	3.07%	4.74	2.827	99.97%	14.18	8.456
5.25	5.32%	4.86	2.899	99.94%	14.18	8.455
5.50	9.09%	5.06	3.018	99.90%	14.17	8.453
5.75	15.10%	5.38	3.208	99.82%	14.17	8.450
6.00	24.03%	5.85	3.491	99.68%	14.16	8.445
6.25	35.99%	6.49	3.870	99.44%	14.14	8.436
6.50	50.00%	7.23	4.313	99.01%	14.12	8.419
6.75	64.01%	7.98	4.757	98.25%	14.07	8.389
7.00	75.97%	8.61	5.136	96.93%	13.98	8.338
7.25	84.90%	9.09	5.419	94.68%	13.83	8.250
7.50	90.91%	9.40	5.609	90.91%	13.59	8.103
7.75	94.68%	9.60	5.728	84.90%	13.19	7.869
8.00	96.93%	9.72	5.800	75.97%	12.61	7.521
8.25	98.25%	9.79	5.842	64.01%	11.83	7.055
8.50	99.01%	9.83	5.866	50.00%	10.91	6.510
8.75	99.44%	9.86	5.879	35.99%	10.00	5.964
9.00	99.68%	9.87	5.887	24.03%	9.22	5.498
9.25	99.82%	9.88	5.891	15.10%	8.63	5.150
9.50	99.90%	9.88	5.894	9.09%	8.24	4.916
9.75	99.94%	9.88	5.895	5.32%	8.00	4.769
10.00	99.97%	9.89	5.896	3.07%	7.85	4.681
10.25	99.98%	9.89	5.896	1.75%	7.76	4.630
10.50	99.99%	9.89	5.897	0.99%	7.71	4.601
10.75	99.99%	9.89	5.897	0.56%	7.69	4.584
11.00	100.00%	9.89	5.897	0.32%	7.67	4.574

Figure 5-5: Table of polyelectrolyte rigidities, pH 4.0 to 11.0, determined by the electrostatic contour adjustment to electrostatic persistence length as described in **Chapter 3: Variation of Molecular Rigidity**.

chain. To maintain independence of element length, L, we note that the axial spring stiffness of a beam (or truss) of finite length can be written as $k = EA/L$ such that $T = EA = kL$. For our parameterization, we use the effective molecular stiffness of a carbon backbone implemented by the MARTINI force field [208, 230], where $k = 1250$ kJ mol^{-1} nm^{-2} at an equilibrium distance of $r_0 = 0.35$ nm, such that $T \cong 438$ kJ mol^{-1} nm^{-1}. It is also recognized that, opposite to bending rigidity, the hydrophobic and charged functional groups can decrease the effective axial stiffness

174

by repulsive interactions. However, the effect of the functional groups are neglected as compared to the backbone the interactions are much weaker, and the flexural behavior is dominant. Indeed, as the axial stiffness is not critical to the desired flexural modes, this approximate value is deemed sufficient.

5.3.2 Stiffness of Electrostatic Cross-links

For clarity we repeat from **Chapter 2: Computational Methods** that, at the atomistic scale in the simplest form, an ENM is a coarse-grain model defined by a single potential for all atoms (or defined groups), where the elastic potential between network points (*e.g.*, nodes), can be expressed as:

$$\phi(\Delta) = \frac{1}{2}k_{\text{spring}}(r - r_0)^2 = \frac{1}{2}k_{\text{spring}}\Delta^2 \tag{5.4}$$

where $\Delta = r - r_0$ is simple the displacement of the point from the equilibrium position (in the direction defined by the spring). Here, each pair of atoms is assigned a harmonic spring bond potential with stiffness k_{spring} about an initial equilibrium spacing r_0. Converting to a force-displacement relationship, we find:

$$F(\Delta) = \frac{\partial \phi(\Delta)}{\partial \Delta} = k_{\text{spring}}\Delta \tag{5.5}$$

conducive with our formulation given by Equation 5.1. To account with possible variation of k_{spring} with respect to Δ, we can define the effective (or local) stiffness as:

$$Y(\Delta) = \frac{\partial^2 \phi(\Delta)}{\partial \Delta^2} = k_{\text{spring}} + 2k'_{\text{spring}}\Delta + \frac{1}{2}k''_{\text{spring}}\Delta^2 \tag{5.6}$$

where k'_{spring} and k''_{spring} are the first and second derivatives of k_{spring} with respect to Δ. It is apparent that, for near-linear stiffness and small deformation ($\Delta \ll 1.0$) that $Y(\Delta) \to k_{\text{spring}}$. Rather than a presumed spring potential (such as harmonic), it is at this point mechanical knowledge of the system is introduced into the elastic network. Indeed, since the desired interaction is known, a more accurate potential is

introduced for stiffness: the screened Debye-Hückel potential. Again, we define the interaction between two charges, q, at a distance r, as a screened Coulomb interaction, i.e., $\phi_{electrostatic}$:

$$\phi_{electrostatic} = \phi\left(r\right) = \frac{q_i q_j}{r} \exp\left(-\kappa r\right) \tag{5.7}$$

dependent on κ, the inverse screening length (or Debye length, κ^{-1}), related to the ionic strength of the electrolyte solution (note that here, for clarity, q incorporates the energy and dielectric constants of the solution). From this effective potential, the cross-link force can be derived where:

$$\begin{aligned} F\left(r\right) &= \frac{\partial \phi}{\partial r} = -\frac{q_i q_j}{r^2} \exp\left(-\kappa r\right) - \kappa \frac{q_i q_j}{r} \exp\left(-\kappa r\right) \\ &= -\frac{\phi\left(r\right)}{r} - \kappa \phi\left(r\right) \end{aligned}$$

$$\tag{5.8}$$

From which the local effective stiffness can be derived:

$$\begin{aligned} Y\left(r\right) &= \frac{\partial F}{\partial r} = \frac{\partial}{\partial r}\left[-\frac{\phi\left(r\right)}{r} - \kappa \phi\left(r\right)\right] \\ &= \frac{1}{r^2}\phi\left(r\right) - \frac{1}{r}\frac{\partial \phi}{\partial r} - \kappa \frac{\partial \phi}{\partial r} \\ &= \phi\left(r\right)\left[\frac{2}{r^2} + \frac{2\kappa}{r} + \kappa^2\right] \end{aligned}$$

$$\tag{5.9}$$

The effective elastic stiffness is a function of distance, screening, and potential energy, or $k_{\text{spring}} = Y\left(r\right) = f(r, \kappa^{-}1, \phi(r))$. As a simplification, we combine the effect of separation and screening to a single parameter, β_κ (units: m^{-2}), such that $k_{\text{spring}} = \beta_\kappa \phi(r)$.

To parameterize this potential, we rely on full atomistic studies of PAA and PAH as described in **Chapter 4: Rate Dependence and Ionization Effects on Ad-**
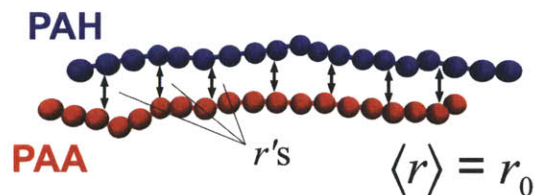
Figure 5-6: Equilibrium separation, full atomistic charged polyelectrolytes, PAA (red) + PAH (blue). To determine a representative separation to parameterize the cross-link stiffness, $Y(r)$, from the adhered polyelectrolytes, the backbone-to-backbone separation, r, is measured along chain length (at equilibrium at 300K) with an average inter-polymer distance of $r_0 = \langle r \rangle = 5.89 \pm 0.48$Å.

hesion. First, the geometric separation is determined. From the adhered polyelectrolytes, the backbone separation is measured along chain length (at equilibrium at 300K) with an average inter-polymer distance of $\langle r_0 \rangle = 5.89 \pm 0.48$Å (see Figure 5-6). Second, the effective electrostatic potential energy at this separation is required. We assume a constant energy per crosslink of $\phi_{electrostatic} = 9$ kcal/mol (the energy barrier as reported in **Chapter 4**). Note that, assuming an Debye screening length on the order of 5 to 10 Å, the energy of a pure electrostatic cross-link would be on the order of 0.2 to 0.4 kcal/mol at the measured distance of ≈ 5.9Å (according to Equation 5.7, assuming an the relative permittivity of water to be $\simeq 80\epsilon_0$, where ϵ_0 is vacuum permittivity). The effective energy barrier accounts for the combined contribution of hydrophobic interactions, steric effects, weak non-electrostatic interactions (*e.g.*, van der Waals and H-bonding) and entropic effects (*e.g.*, chain straightening). Moreover, geometrically, the ionic pairing is closer than the average backbone separation used here. Finally, the screening length, κ^{-1}, is calculated assuming a finite volume and charge neutrality (similar to the method reported in **Chapter 3: Variation of Molecular Rigidity**). It is noted that the screening length can be considered a free parameter based on the salt concentration of solution, and potentially varied to manipulate the effective stiffness (see Figure 5-7(a)-(c)).

It behooves us to note that we derive the linearized stiffness of an electrostatic interaction about a presumed equilibrium state. Without this assumption, it is true that the tangent modulus is nonlinear with respect to separation, r. However, this
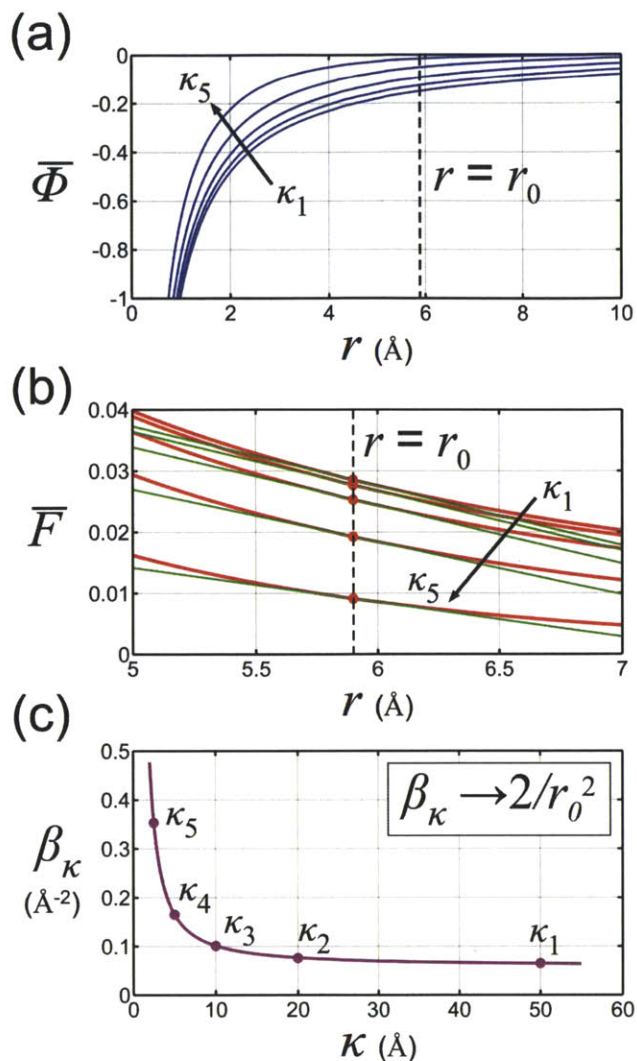
Figure 5-7: Linearization of electrostatic cross-links. (a) Screened Debye-Hückel potential, indicating decay of potential as a function of r with a decrease in screening ($\kappa_1 > \kappa_5$), resulting in variation of electrostatic energy at a given separation, r_0. (b) Tangent stiffness at prescribed separation ($r = r_0$) indicates close fit to nonlinear force behavior, as well as little variation as a function of κ. (c) Stiffness parameter, β_κ (units: m^{-2}), as a function of separation, r. Note that only very small screening lengths (*e.g.*, $\kappa^{-1} < 10$Å), is there a large variation in value, and thus a strong increases in stiffness.

effect is not critical to the free vibrational analysis (small deformation by definition). In effect, the electrostatic cross-links are "sufficiently" stiff to induce flexural modes. Consider the energy required to stretch our electrostatic spring:

$$dU_{\text{spring}} = \frac{1}{2}k_{\text{spring}}d\Delta^2 \tag{5.10}$$

178

where $k_{\text{spring}} = \beta_\kappa \phi(r)$. For a unit displacement ($d\Delta = 1\text{Å}$), and $\phi = 9$ kcal/mol, then dU would range from approximately 0.5 to 3.2 kcal/mol (depending on the screening length, see Figure 5-7). In contrast, consider the energy required to bend a flexural member (assuming three-point bending, where $F = 48D\Delta/L^3$), where:

$$dU_{\text{flexure}} = \frac{24D}{L^3} d\Delta^2 \qquad (5.11)$$

For a unit displacement ($d\Delta = 1\text{Å}$), the smallest beam length for three-point flexure ($L = 2l = 2 \times 2.8\text{Å}$), and the largest rigidity ($D = 8.457$ kcal mol^{-1} Å for PAA at pH 4.0), dU is ≈ 1.2 kcal/mol. This is the maximum energetic expense of flexure, and it is roughly the same order of magnitude as the electrostatic spring stiffness. As there is an inverse-cubic relation with beam length (*e.g*, $dU \propto L^{-3}$), at lower cross-link densities, the electrostatic cross-links become rigid in comparison to flexure (*e.g.*, $L = 4l$, then $dU_{\text{flexure}} \approx 0.1$ kcal/mol; $L = 6l$, then $dU_{\text{flexure}} \approx 0.04$ kcal/mol). As a direct result, small variation in stiffness (as a function of screening length, κ^{-1}, for example) does not change the discussed results. Of no surprise, the flexibility of polyelectrolytes (or, equivalently, the relatively small rigidity) is complementary to the strength of electrostatic cross-linking, wherein the ionic interactions able to induce coupled modes of deformation. More rigid molecules would therefore require stiffer cross-links.

5.3.3   Consistent Mass Matrix

To undertake dynamic and vibrational mode analysis, a mass matrix, $\mathbf{M}$, is required to pair with the stiffness matrix, $\mathbf{K}$. Here, mass is lumped to the corresponding node based on the atomistic mass of the polyelectrolyte chain. The local mass matrix for each beam element is given by:

$$[\mathbf{M}] = \frac{m_i}{420} \begin{bmatrix} 140 & 0 & 0 & 70 & 0 & 0 \\ 0 & 156 & 22L & 0 & 54 & -13L \\ 0 & 22L & 4L^2 & 0 & 13L & -2L^2 \\ 70 & 0 & 0 & 140 & 0 & 0 \\ 0 & 54 & 13L & 0 & 156 & -22L \\ 0 & -13L & -3L^2 & 0 & -22L & 4L^2 \end{bmatrix} \tag{5.12}$$

The masses, m_i, are calculated per monomer repeat ($m_{PAA} = 72$ amu per monomer; $m_{PAH} = 55$ amu per monomer), and assigned depending on the spacing of cross-links (*e.g.*, beam element length).

5.4 Eigenvalue Problem and Normal Modes

As described in **Chapter 2: Computational Methods**, the vibration of structures (macroscale of nanoscale alike) can be described by the equations of motion through eigenmode analysis - a classical eigenvalue problem. The governing matrices described above are arranged in the general equation such that [24, 213]:

$$[\mathbf{K} - \lambda\mathbf{M}]\bar{\eta} = [\mathbf{K} - \omega^2\mathbf{M}]\bar{\eta} = 0 \tag{5.13}$$

where $\mathbf{K}$ is the previously described global stiffness matrix, $\mathbf{M}$ the consistent mass matrix, λ the set of eigenvalues, and $\bar{\eta}$ the corresponding eigenvectors. The eigenvalues give the frequencies of corresponding modes, where $\lambda_i = \omega_i^2$ and the corresponding eigenvectors, $\bar{\eta}_i$, represent the mode shapes. From **Chapter 2: Computational Methods**, for a pure *flexural member*, the vibrational frequency for simplest transverse bending motion (under free vibration) of the Euler-Bernoulli beam model can be written as:

$$\omega_1 = (\frac{\pi}{L})^2 \sqrt{\frac{EI^*}{\rho_L}} \tag{5.14}$$

where EI^* denotes the effective rigidity of a flexural member, L is the total length of

the member, ρ_L the linear density (atomistic mass per length), and ω_1 indicates the solved eigenvalue corresponding to the desired flexural mode [341]. It is noted again that the expression given above does not take into account any rotational and shear contribution. To include such effects, more sophisticated models such as Timoshenko beam theory could be used [341].

The corresponding eigenvectors represent the mode shapes required to correlate to a mechanical response. Modes are ranked by eigenvalues from low to high, with low frequencies are collective modes, typically corresponding to elastic deformations such as twisting, bending and stretching. Here, we are looking for the first flexural mode, denoted by ω_1, and thus must inspect the shape of the first few eigenvectors (see Figure 5-8).

5.4.1 Effective Rigidity of the Complex

As depicted in Figure 5-8, solving the constructed eigenvalue problem returns the free vibrational frequencies of the lowest *flexural* modes of the polyelectrolyte complex (other modes not depicted), subject to 2D constraints. By construction, cooperative flexural deformation is a resulting eigenmode of the idealized beam-spring system (see first panels, ω_1, Figure 5-8(a) and (b)). From the associated frequency (*e.g.*, eigenvalue, ω_1) we assume equivalency of deformation between the complex and a classical flexural member (*i.e.*, a Euler-Bernoulli beam; as described by Equation 5.14), from which we attain an effective rigidity (EI^*) as a proxy. This is not to say the *rigidity* of the complex is equivalent to the attained value, but rather the necessary *frequency* of vibration is equivalent for the coupled *deformation*.

Since the flexural mode is a byproduct of the 2D formulation and elastic model construction, it is not necessarily a natural modal shape of two cross-linked polyelectrolytes. Indeed, subject to thermal fluctuations, it is unlikely the polymers would align and deform together. However, by comparing the effective rigidity with a simple summation of the rigidities of PAA and PAH, it is possible to compare which mode of deformation is preferable (*e.g.*, assuming entropic fluctuations drive conformational changes, low energy modes would be favored). Thus, if the effective rigidity

181
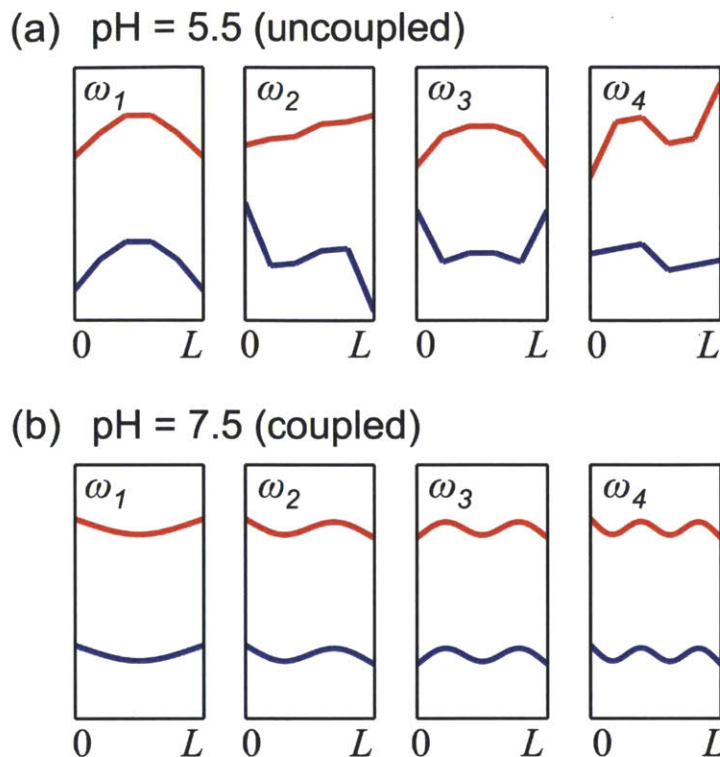
Figure 5-8: Representative flexural modal shapes, variation in cross-links; PAA (**red**) and PAH (**blue**). (a) Uncoupled mode shapes for pH of 5.5 (5 cross-links per 50 functional groups). Beyond the lowest mode (simple flexure, unavoidable due to 2D formulation and elastic model), there is no cooperative deformation for higher vibrational frequencies. (b) Couple (or cooperative) mode shapes for pH of 7.5 (46 cross-links per 50 functional groups). All mode shapes (ω_1 to ω_4) are indicative of cooperative deformation - each polyelectrolyte is driven by the other reciprocally. The lowest eigenvalue (ω_1) is used to solve for the effective rigidity of a representative beam, as described by Equation 5.14.

(by means of required vibrational frequency) is higher than the sum of the individual backbones, each polyelectrolyte will deform/bend independently (effectively "pinned" by the cross-links, which can be considered an energetic penalty for non-symmetric displacements). In contrast, if the effective rigidity is lower than the sum, cooperative deformation is the preferred vibrational mode. The rigidity of free vibration is less than the sum of the individual polymers, as each can be considered driven by the other reciprocally. This provides a mechanistic definition of complexation.

We thus step-through representative pH conditions, determining ionization of each backbone (*via* assumed pK_a values as done in **Chapters 3** and **4**) to parameterize a set of elastic models. The number of cross-links is assumed to be the minimum of

ionized functional groups (*e.g.*, at a pH of 6.0, PAA is approximately 25% ionized, whereas PAH is approximately 100% ionized; since the free COO^- groups of PAA determine the maximum number of cross-links, we assume 25% cross-link density, or $\simeq 13$ cross-links for 50 functional groups). The eigenvectors are then solved, and approximately the first ten modes inspected to isolate the lowest flexural response. In all cases, the first three modes are rigid body motions (two translational and on rotational) while the forth mode is simple shear (as the ionic cross-links provide no rotational resistance). Thus, the lowest flexural mode (denoted here by the frequency ω_1) is not the *absolute* lowest eigenvalue solution. We then take the frequency associated with the flexural mode, and solve for the effective rigidity, EI^*, according to Equation 5.14. The results are plotted in Figure 5-8(a).

As a comparison, we plot the effective rigidities of both PAA and PAH along with the their summation (denoted by "$\sum$" in Figure 5-9(a).) Again, we stress that the effective rigidity, EI^*, does not imply the complex is as stiff as plotted. Indeed, two cross-links at a pH of 5.0 does not result in a complex with a rigidity an order of magnitude greater than the sum of PAA and PAH at the same pH. What is indicated is that much higher vibrational frequencies are required to induce cooperative deformation. Consider at a pH of 5.0, the rigidity of PAA is ≈ 2.8 kcal mol^{-1} Å while the rigidity of PAA is ≈ 8.5 kcal mol^{-1} Å (see Figure 5-5). In terms of lowest flexural frequencies (Equation 5.14), the ratio of $\omega_1^{PAH}/\omega_1^{PAA}$ is approximately two - *i.e.*, the natural frequency of PAH is twice that of PAA. To accommodate this mismatch, the complex induces even higher vibrational frequencies, resulting in an apparent effective stiffness EI^* that is much larger, due to the constraints of the model. Changes in pH result in a convergence of polyelectrolyte rigidities.

As the number of cross-links increases (or, equivalently, an increase in cross-link density), there is a consistent drop in the resulting effective rigidity, EI^*. The links, acting as elastic constraints, induce cooperative deformation between the backbones, as the segments of free deformation are reduced. This is apparent in Figure 5-8(b), wherein all flexural modes are reflected by each polyelectrolyte. At a critical level of cross-links (a pH range of approximately 7.0 to 8.0), the effective rigidity of the

183
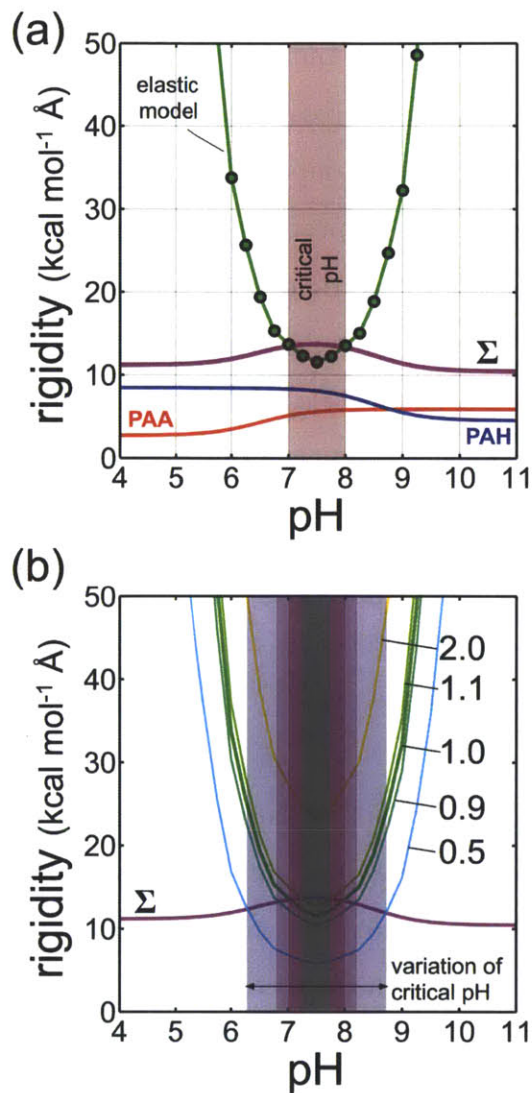
Figure 5-9: Effective rigidity of elastic model and polyelectrolytes. (a) Plot of effective rigidity, EI^*, of elastic model, determined by lowest flexural frequency, ω_1, according to Equation 5.14, and of the rigidities of both PAA and PAH, along with the their summation ($\sum$), as a function of pH. When the effective rigidity is less than the summation, cooperative deformation is preferred, providing a mechanical definition of complexation and delineating a critical pH range (here, approximately 7.0 to 8.0). (b) Variation in monomer spacing, l, and thus potential cross-link density, results in variation of critical pH range. Here, a factor of 2.0 results in no mechanical coupling (e.g., independent deformation always preferential), whereas a factor of 0.5 results in a broadening of the critical regime (6.25 to 8.75). Small variation ($\pm 10\%$) results in small variation in pH range (± 0.25).

complex is less then the summation of the rigidities of PAA and PAH. At this point, cooperative deformation is energetically preferred to individual chain bending. It is noted that this does not occur when the rigidities of PAA and PAH are closest (and

thus the individual vibrational frequencies the closest), but rather the highest density of cross-links, providing an energetic penalty for uncoupled deformation.

To explore the effect of cross-link density on the critical range of ionization (*i.e.*, pH), the monomer-to-monomer distance, l, was manipulated, assuming all other conditions remain constant. Significant increase ($2.0l$) results in no critical regime of pH - at all times, bending deformation of individual polymers is preferred to cooperative motion. Conversely, significant decrease ($0.5l$) results in a substantial increase in the critical pH range (between 6.25 to 8.75). Since the monomer-to-monomer distance is an approximate value based on the idealized polyelectrolyte structure, small variations ($\pm10\%$) indicate changes in the critical pH range (7.0 ± 0.25 to 8.0 ± 0.25). This change in critical pH range is reflected in Figure 5-9(b). Thus, it is not the absolute number of cross-links, but rather the number per length of polyelectrolyte that provides cooperative deformation. This effect can be further understood by the relation to polymer persistence length.

5.4.2   Cross-Links and Persistence Length

Systematic variation of cross-link stiffness (*i.e.*, $Y_{electrostatic}$) does not substantially effect the resulting modal shapes of vibrational frequencies. Indeed, as this is a first-order elastic analysis, the electrostatic cross-links are effectively reduced to "pins" which constrain the backbones to defined flexural shapes (increasing or decreasing the backbone separation induces a penalty that counters free vibration). It is partially for this reason that weak electrostatic interactions are successful in multilayer systems. We can extend this thought in consideration of persistence length, whereby if the "pins" are spaced significantly far apart (*e.g.*, beyond the persistence length), deformation between cross-links is free to act independently. There is no intrinsic coupling. Similarly, if the "pins" are spaced less than the persistence length, the deformation of one cross-link (node) is reciprocally affected by its neighbors. As the cross-link spacing is a prescribed model parameter (*i.e.*, beam element length), it can be directly compared to the persistence lengths of the constitutive polymers (see Figure 5-10(a)).
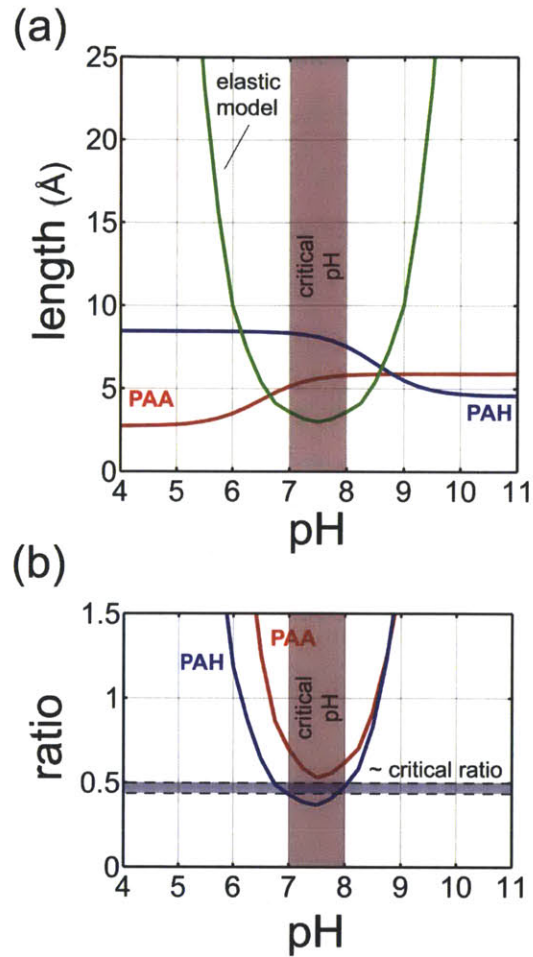
Figure 5-10: Critical cross-link spacing and persistence lengths. (a) Plot of prescribed cross-link spacing (*i.e.*, beam element length) and polyelectrolyte persistence length as a function of pH. The critical pH range for complexation is highlighted, and it is apparent that the critical cross-link spacing is less than *both* the persistence lengths. (b) Plot of the ratio of cross-link spacing to persistence length with critical pH range indicated. The critical cross-link spacing is estimated to be $\approx 0.5 P_{max}$, where P_{max} is the largest persistence length of the constitutive backbones (in this case PAH).

We indeed find that the critical cross-link spacing (or density) can be related to the persistence lengths of the constitutive polyelectrolytes. Plotting both indicates that the critical ionization and pH range occurs when the cross-link spacing is less than both the persistence length of PAA and PAH, as anticipated. However, plotting the ratio of cross-link spacing to persistence length is more revealing (Figure 5-10(b)). We find that the cooperative deformation and mechanical complexation occurs when the cross-link spacing is less than approximately $0.5 P_{max}$, where P_{max} is the largest

persistence length of the constitutive backbones (in this case PAH). This can be reconciled qualitatively considering that inducing a flexural mode requires *two* cross-link spacings at the minimum (*e.g.*, two beam elements), and thus the "bent" shape spans twice the element length. Cross-links spaced greater than $0.5P_{max}$ would allow local flexure that is not transferred node to node (*e.g.*, no correlation).

5.4.3 Extension to Critical Coupling of Molecules with Finite Rigidity

From the results presented in Figure 5-10, we note a correlation between critical cross-link spacing and persistence length of the associated molecules. Consider the critical cross-link spacing, c^*, such that $c^* = 0.5P = 0.5D/k_BT$, where, again, D indicates the bending rigidity of a macromolecule (k_BT representing the thermal energy). We further define the linear cross-link density simply as $\rho_c = 1/c$, such that the relation from bending rigidity, D, to critical density, ρ_c^*, can be written as:

$$D = \frac{2k_BT}{\rho_c^*} \tag{5.15}$$

or, for mechanical complexation to be achieved for a given cross-link density, ρ_c:

$$D > \frac{2k_BT}{\rho_c} \tag{5.16}$$

noting specifically that $D \propto \rho_c^{-1}$. The cross-link spacing, however, presumes the cross-links are sufficiently stiff. *E.g.*, compliant cross-links would not induce cooperative deformation (the springs would stretch, rather than flexure). As such, we further consider the critical spring stiffness, where $dU_{spring} = dU_{flexure}$ and attain a critical stiffness $k^* = 48D/L^3$, *e.g.*, the effective stiffness of a simply supported beam. Noting that, $L = 2c$, then $L = 2/\rho_c$, then:

$$D = \frac{k^*}{6\rho_c^3} \tag{5.17}$$

where, for mechanical complexation for a given cross-link stiffness, k:
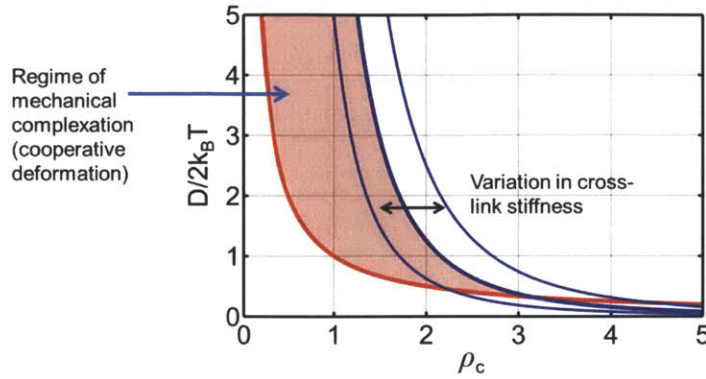
Figure 5-11: General upper and lower limits for range of mechanical complexation (*e.g.*, cooperative deformation). Red line presents lower limit for bending rigidity (for a given cross-link density). *E.g.*, for a given rigidity, the cross-link density must exceed a critical value (such that the spacing is less than one-half the persistence; see Figure 5-10). Blue lines represent the limits given a finite cross-link stiffness. Increasing the stiffness extends the accessible regime, whereas lowering the stiffness decreases it, as the energy to induce flexure is nonlinear with respect to cross-link spacing ($dU_{\text{flexure}} \propto L^{-3}$).

$$D < \frac{k}{6\rho_c^3} \tag{5.18}$$

where here, $D \propto \rho_c^{-3}$. Note that also, by substitution, the critical stiffness can be defined as $k^* = 12k_BT(\rho_c^*)^2$. The two inequalities provide the upper and lower bounds for mechanical complexation given molecular rigidity (D) and cross-link density (ρ_c). The relation is plotted in Figure 5-11.

Here, we note that, stiffer molecules require less cross-links (smaller cross link density) than flexible molecules. Decreasing cross-link strength (or stiffness, k) results in a smaller acceptable range of cross-link density - spaced too close together, it is more energetically favorable to stretch multiple cross-links that induce flexure, due to the L^{-3} dependence. Finally, for a given molecule, there is an upper-limit to cross-link density that must be considered (*e.g.*, the monomer-to-monomer spacing of PAA and PAH is on the order of 2.8 Å, such that $\rho_{max} \approx 0.4$. The presented relations can be used to determine the potential regime of mechanical cross-links for a variety of flexible molecules (*e.g.*, proteins, flexible nanoribbons, etc.) and chemical interactions (*e.g.*, hydrogen bonds, disulfide bonds, π-stacking, etc.).

5.5 Summary

The definition of mechanical complexation presented here is intended to be complementary to the electrostatically driven complexation process - it is not considered an isolated mechanism. Rather, whereas entropy and thermodynamics can explain why the process occurs (in terms of fluctuation of free energy), mechanical analysis can reconcile why the resulting composites are mechanically stable, *via* a quantifiable approach. Our results, albeit based on a simple model and ideal analytical solution quantitatively agree with observed experimental systems, providing physical insight into the underlying molecular mechanisms of PE complexation in addition to the commonly attributed ion pairing and electrostatic equilibration [287]. As first discussed in **Chapter 1: Introduction**, for example, experimental LbL assembly of 6.5/6.5 PAH/PAA (where n/m indicates the PAH was deposited at pH $= n$ and PAA at pH $= m$) indicates that both polymers are highly charged and form thin layers (*e.g.*, mechanically complexed as predicted here) [303]. In contrast, in a 7.5/3.5 PAH/PAA system the resultant films are thick (*e.g.*, mechanically decoupled; loops and tails) [303].

The normal-mode-based approach makes it possible to analyze the intrinsic mechanical properties of a system without the need for applied loads, boundary conditions and removes the constraint of accessible timescales in direct MD simulations. In contrast to applying force or strain loads, the normal mode decomposition of macromolecular motions provides a specific frequency and stiffness for each mode, and thus offers direct information on the elastic constants of an equivalent continuum model. However, normal-mode analysis is also limited by the simplicity of the representative elastic network model and the predicted mechanical properties are restricted to elastic response, with no indication of potential failure mechanisms.

Being said, recent work has suggested that nanoconfinement of hydrogen bonds induce cooperative deformation and thus serve to increase strength in beta-like protein structures [173, 172, 176], and a similar, general elastic model framework was used to extend such behavior to large beta-sheet assemblies [264]. In a similar manner,

ionization results in an increase in electrostatic cross-link density (*e.g.*, density can be considered a natural "confinement"). Subject to bending (rather than tension), the ionic cross-links induce cooperative flexural deformation as a preferred vibrational mode, and a means to mechanically define complexation. Due to the general nature of the elastic model, the parameters used in this study could be modified to other molecular systems, which imply applications in understanding the onset of cooperative deformation in highly flexible yet cross-linked systems.

Chapter 6

Beyond Full Atomistic Characterization

In this chapter, mechanical analysis is extended beyond the molecular scale to implement a novel coarse-grain model of PEM microtubes. The pH-dependent friction of layer-by-layer assemblies of PAH and PAA are quantified for microtube array structures *via* simulated lateral force microscopy (LFM) and directly compared to complementary experimental results. The coarse-grain tube model utilizes the same molecular dynamics framework described in previous chapters, modified by an elastic Hertzian contact potential (where $F \propto \delta^{3/2}$) to allow the efficient dynamic simulation of arrays consisting of hundreds of tubes at micrometer (μm) length scales with limited required parameters. By quantitatively comparing experimental and computational results, the coupling between geometry (*e.g.*, tube spacing and swelling) and material properties (*e.g.*, intrinsic stiffness) results in a transition from bending dominated deformation to bending combined with inter-tube contact, thereby modulating lateral resistance. Variation of tube spacing (and thus control of contact) can be used to exploit the normal and lateral resistance of the tube arrays as a function of pH, beyond the effect of areal tube density, with increased resistances (potential mutability) up to a factor of $\simeq$60. The results indicate that micro-geometry (*e.g.*, array spacing) can be used alongside stimulus-responsive material changes (*e.g.*, swelling, stiffness) to amplify and systematically tune *mutability*.

6.1   Stimuli Responsive Interfaces

Knowledge of the nanomechanical behavior of polyelectrolyte complex, as characterized in previous chapters, is only valuable as the potential material systems and composites it can compose. Indeed, it is akin to intimately knowing the mechanical characteristics of a steel beam - completely useless unless that beam is used to *build* something[1]. As such, here we focus on a microscale system composed of networked polyelectrolyte complexes, more commonly referred to as polyelectrolyte multilayers (PEMs). There is a growing interest on stimulus-responsive materials and structures beyond the molecular or nanoscale, that undergo actuation, swelling, variable permeability and wettability, and aggregation in the presence of external stimulus such as changes in pH, temperature, pressure, or light [280, 304, 124, 312, 80]. As demonstrated throughout this thesis, polyelectrolyte composes a subclass of these materials which exhibit a controlled mechanical responses - so-called "mechanomutable" materials - which attain a range of mechanical properties in response to external stimuli [191, 243, 219, 291, 59, 156, 292]. We have seen that both molecular rigidity (**Chapter 3**) and adhesion (**Chapter 4**) can be varied and exploited as a function of ionization - but do these effects extend beyond the scale of the molecular complex (**Chapter 5**)?

One possibility is that, unlike chemical changes that are bound to the molecular scale as done in conventional materials design (*i.e.*, intrinsic material mutability; *e.g.*, changes in molecular cross-link density), mechanical responses can be coupled with hierarchical effects at a larger-scale to amplify or manipulate the material response (*i.e.*, extrinsic system mutability; *e.g.*, changes in system geometry due to swelling). Indeed, the combination of cross-links combined with molecular rigidity achieve mechanical properties beyond simple additive laws - intrinsic coupling between mechanisms results in an amplification of mechanical properties (and a broader range of tunability). *Can structural hierarchies be exploited to attain even further amplification across scales?*

---

[1] *vice versa*, a structure should not be built with steel members without thorough knowledge of the beam, but that is why AISC building codes exist.

The stimuli-responsiveness of surface-bound nano- and microarrays has seldom been explored, mostly because of the inertness of many of the materials typically utilized to create them (such as carbon nanotubes [189, 227, 251], metallic nanopillars [132, 318], and/or nanobristles [258]). Of particular interest would be the ability to reversibly alter the physical and mechanical properties of nanoarrays through the use of simple triggers such as a change in solution pH or temperature. The collective behavior of the tubes could lead to phenomena such as an increase in compressive strength as a result of nanogranular friction and percolation effects. Additionally, a template approach allows precise control over the orientation and spacing of the resultant tubes during synthesis [59]. It has been recently shown theoretically that the mechanical response of an array is can be controlled through tube areal density, tube geometry (*e.g.*, diameter, height), and material properties (*e.g.*, modulus) [263, 337].

Recent studies investigated the coupling between the inherent material properties and deformation mechanisms (such as bending, buckling, and twisting) of PEM tube arrays, through experimental indentation and finite element modeling [337, 142, 143]. It was demonstrated that mechanomutability can be controlled through the coupling between the "inherent" material properties and the anisotropic microscale geometry in a PEM tube array system. A transition occurrs due to lateral constraint of the tubes (induced by material swelling and initial spacing), inducing a continuous multi-axial stress field, affecting discrete tube compression, bending, and buckling with variation in tube cross-sectional area.

In this chapter, the concept is extended to a fully 3D configuration using a coarse-grain element approach. Material systems that require multiscale methods to model and investigate inherently have nanostructures and mechanical behavior at scales from nanometers to micrometers that fall precariously between atomistic (*e.g.*, MD) and continuum (*e.g.*, FE) techniques. As experiments go down in size, with increasing atomistic and nanoscale precision, and with the emergence of multiscale modeling schemes, computational investigations have become increasingly relevant empirical work. Here, a coarse-grain mesoscopic representation of a vertically aligned array of constituent PEM tubes is developed and implemented. A coarse-grain representation

of PEM tubes is beneficial due to the dynamically driven evolution of the micro-tube array under indentation where the prevalence of intertube contact and discrete tube geometry hinders a 3D finite element representation. Further, the coarse-grain particle-spring elements provide a computationally efficient means of describing mechanical behavior with a limited number of necessary parameters.

In concord, high resolution atomic force microscopy (AFM)-based lateral force spectroscopy (LFS) experiments[2] are utilized to compare the responsive mechanical behavior of cylindrical PEM tube arrays - specifically the variation in mechanical friction of the array surface. Whereas several vertical nanoindentations are necessary to acquire a statistical average of mechanical properties, lateral microscopy facilitates local averaging *via* a single experiment. The results are utilized to validate the response of the developed coarse-grain models, which can then efficiently probe systems of varying geometry and mechanical parameterization.

Again, the model material system investigated here is the well-studied ionically complexed polyelectrolyte multilayer system of PAH and PAA [215, 151, 353, 59, 142, 143, 81]. Again, this PEM system undergoes a reversibly pH-dependent transition that induces swelling and variation in inherent mechanical behavior originating from the molecular level [81]. For example, at low pH (2.0), the polyelectrolyte network is highly swollen [59], with a heightened fraction of percolated water, and thus more compliant. When the pH is increased from 2.0 to 5.5, an increase in ionic cross-linking results in a less-swollen, electrostatically bound network, and an associated increase in stiffness [59]. While these mechanisms have been fundamentally explicated from a molecular perspective, the scale of interest can disregard the pH/ionization/cross-linking phenomena, and simply focus on the two microscale effects - geometric swelling/contraction and variation in stiffness.

---

[2]Experimental results courtesy: L. Han, CMSE, Department of Materials Science and Engineering, MIT.

Table 6.1: Approximate experimental values of geometric and mechanical properties of PEM microtubes necessary to parameterize coarse-grain model.

Property	pH = 2	pH = 5
Tube height, μm	18	12
Outer diameter, nm	1800	1200
Inner diameter, nm	500	350
Inertia, μm^4	0.4831	0.0954
Array spacing, μm	1.8	1.8
Modulus, E_{PEM}, MPa	1.2	125

6.2 Computational Lateral Force Microscopy

As a basis of model comparison, AFM-based lateral force spectroscopy was employed to quantify the mechanical response of the tube arrays. It is noted that the physical template dictates the center-to-center spacing and maximum dimensions of the tubes within the experimental array (a restriction not present in computational models). The heights and diameters of the tube arrays were measured *via* fluorescence microscopy at pH 2.0 and pH 5.5, and reported in Table 6.1. An estimate of modulus was attained through the nanoindentation of PEM films [142].

Lateral force spectroscopy was conducted using micro-spherical tip (a radius $R \approx$ 22.5μm; used to parameterize the computational model). Results used as a basis of comparison are depicted in Figure 6-1.

All parameters for the PEM tube coarse-grain potentials are given in Table 6.2. Vertically aligned arrays of PEM tubes were generated, consisting of regular grids of tubes with heights of either 12 μm (pH of 5.5) or 18 μm (pH of 2.0), and a spacing of 1.8 μm to approximate the experimental geometry, with array dimensions of 36 μm $\times$ 63 μm (see Figure 6-2(a) and (c)).

Computational lateral indentation is then implemented to characterize the contact friction of the PEM tube arrays. The lateral indentation process itself is simple: a spherical indenter tip is pressed normally into the array to a prescribed penetration, and subsequently moved laterally to the array surface at a constant velocity and depth (see Figure 6-2(b)). Indentation is simulated by the introduction of an ideal indenter potential, where a harmonic spherical indenter exerts a force of magnitude:
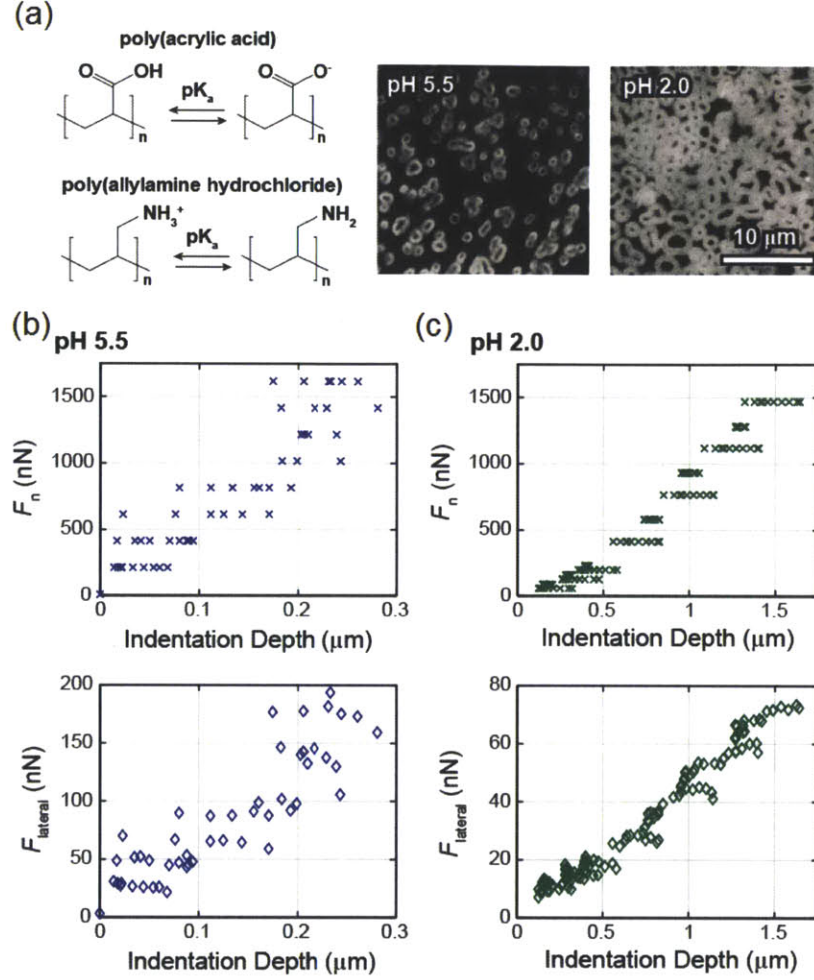
Figure 6-1: Experimental lateral force spectroscopy results. (a) Schematic of molecular-level interactions of PAA and PAH and corresponding top-view fluorescence microscopy images of the microtubes; (b, c) Normal and frictional force versus indentation depth measured *via* AFM-based lateral force microscopy at (b) pH 5.5 (0.01 M NaCl) and (c) pH 2.0, where each data point represents the measured value of one 6.25 μm lateral scan loop.

$$F_{\text{ind}}(r) = K_{\text{ind}}(r - R_{\text{ind}})^2 \qquad (6.1)$$

where K_{ind} is the specified force constant (approx. 1 N/μm), r is the distance of a coarse-grain particle to the (specified) center of the indenter, and R_{ind} is the radius of the indenter (22.5 μm). We note that K_{ind} was chosen as an extremely high stiffness to approximate a rigid body relative to the PEM system. Such an approach has been previously implemented for coarse-grain systems of carbon nanotube arrays [69], films [77], and similar soft plaques [247]. For all simulations, a constant speed of 10 m s^{-1}
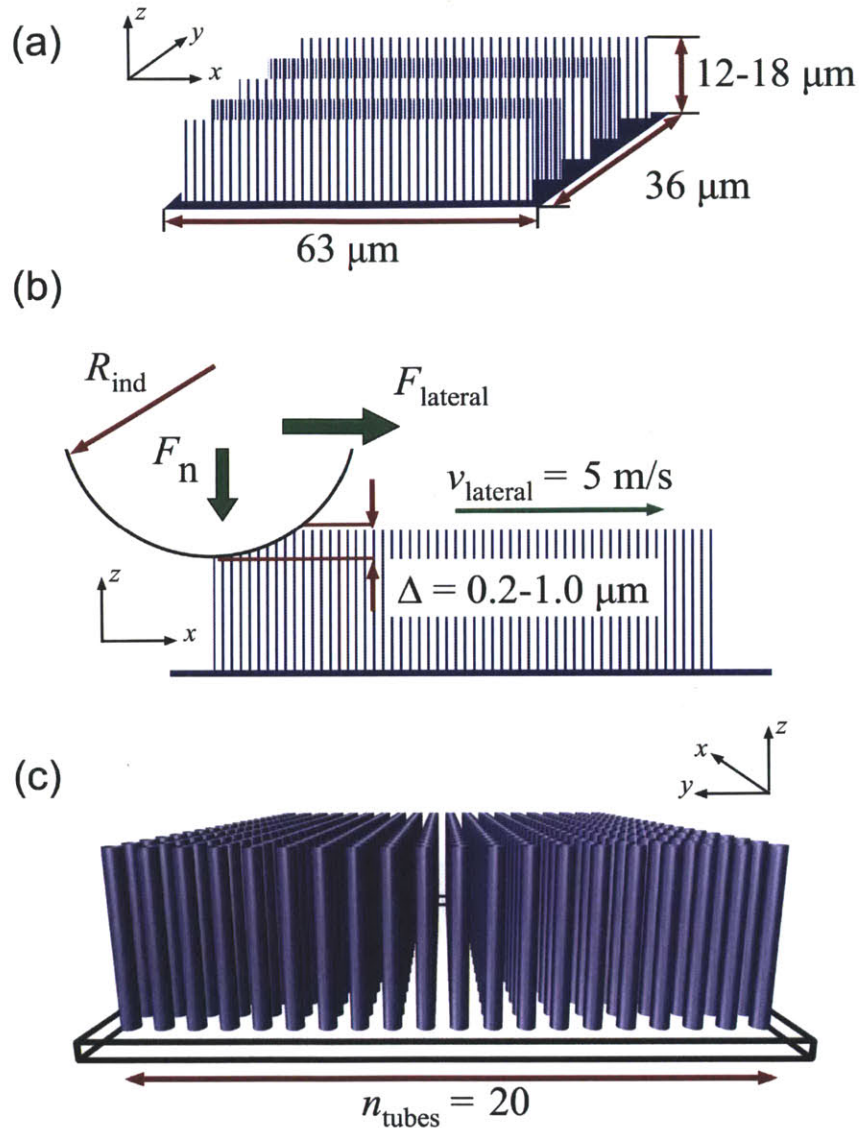
Figure 6-2: Schematic of array geometry and computational lateral force microscopy. (a) The PEM tube arrays consist of regular spacing of tubes, with heights reflecting representative pH (12 μm for pH of 5.5, 18 μm for pH of 2.0). Sufficient tubes were arranged to allow indentation within the interior of the array system without boundary effects, with subsequent array dimentions 36 μm × 63 μm representing hundreds of individual tubes. (b) Relevant parameters of lateral indentation, including radius of spherical indenter ($R_{\text{ind}} = 22.5\mu$m), constant lateral velocity ($v = 10 \text{ m s}^{-1}$), indentation depth (Δ), and recorded normal (F_{n}) and lateral (F_{lateral}) forces. (c) Visualization of computational model, indicating relative size and aspect ratio (here, pH of 5.5 with a tube height of 12 μm, diameter of 1.2 μm, and center-to-center spacing of 1.8 μm).

Table 6.2: Derived PEM tube coarse-grain model parameters (model description in **Chapter 2: Computational Methods**.

Parameter	Units	pH = 2	pH = 5
Equilibrium bead distance, r_0	nm	100	100
Tensile stiffness parameter, k_t	kcal/mol/Å^2	20.1	930.6
Equilibrium angle, θ_0	rad	π	π
Bending stiffness parameter, k_θ	kcal/mol/rad^2	$1.33(10^9)$	$27.31(10^9)$
Hertz contact radius, d_0	μm	1.8	1.2
Hertz contact parameter, $\alpha_{contact}$	kcal/mol/Å^3	0.012	1.070

was used. Both the normal and lateral forces (F_n and $F_{lateral}$ respectively), as well as the prescribed depth (Δ) of the indenter tip are recorded during the simulation.

Figure 6-3 depicts the characteristic results of the indentation simulations (for pH = 5.5, $\Delta = 0.8\mu$m). The indenter is initially pressed into the periphery of the array through a constant normal velocity. At the desired depth, the indenter is then held for a short equilibration period, followed by the onset of lateral motion at constant penetration depth. Contact with a higher region of the array (*e.g.*, movement from the periphery to the array interior) results in a relatively constant increase in normal force as more tubes resist the penetration. The number of tubes resisting lateral motion (at the forefront of the indenter motion) is relatively constant, and the magnitude of lateral force is relatively unchanged. After sufficient lateral motion ($\Delta t \approx 100$ ns, or a lateral displacement of approximately 10 μm), the indenter is sufficiently within the array interior - further lateral penetration does not significantly alter the loading conditions. At this point, the force-time relationship evolves into a repeating, oscillatory pattern, corresponding to the contact and slippage of subsequent rows of tubes. Lateral indentation is undertaken until approximately the midpoint of the array ($t = 500$ ns). Normal and lateral forces per each depth are calculated as the average over the final 300 ns of simulation (a mean of the oscillatory regime).

6.2.1 Model Validation

We note that experimentally, the indentation depth at a pH of 5.5 was limited to $\approx 0.3\mu$m, due to the limitation of the maximum applied force ($\approx 2\mu$N) in the cur-

(a)

(b)

$t \approx 100\ \mu s$

$t \approx 150\ \mu s$

$t \approx 200\ \mu s$
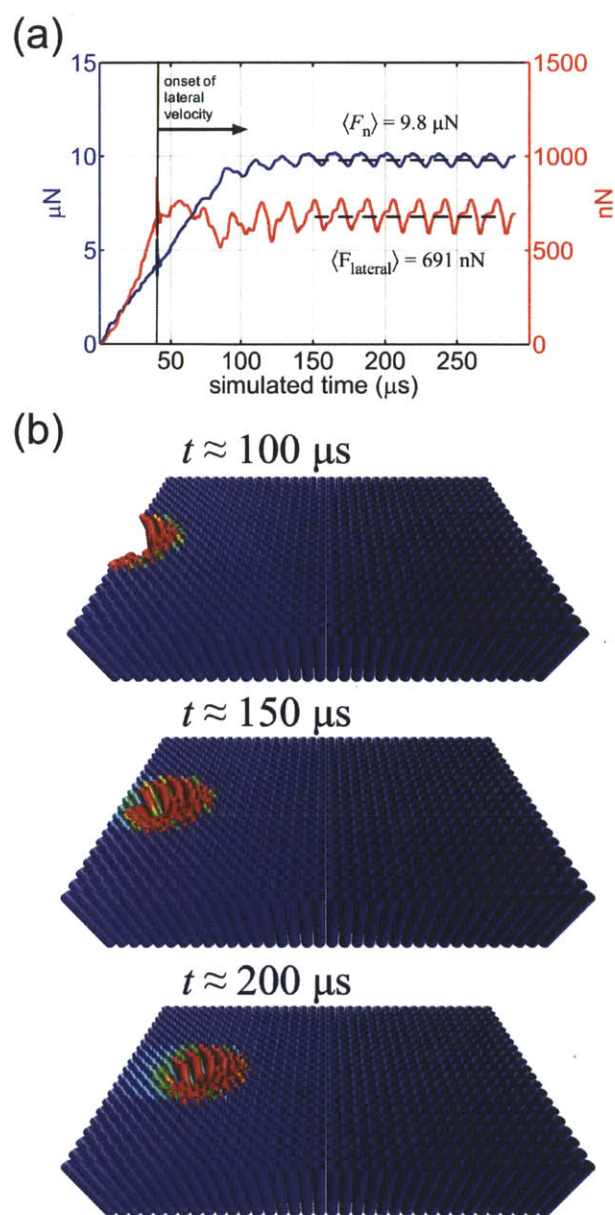
Figure 6-3: Characteristic force-time results of an indentation simulation (pH = 5.5, $\Delta = 0.8\ \mu m$). (a) Force-time history for both normal (F_n) and lateral ($F_{lateral}$) forces. The indenter is lowered into the periphery until the desired depth is attained, held for a short equilibration period, followed by the onset of constant lateral velocity ($10\ m\ s^{-1}$) at constant penetration depth. After sufficient lateral motion ($\Delta t \approx 100\ ns$), the indenter is sufficiently within the array interior. At this point, the force-time relationship evolves into a repeating, oscillatory pattern, corresponding to the contact with subsequent rows of tubes. Normal and lateral forces per each depth are calculated as the average over the final 300 ns of simulation (shorter sample depicted here for illustrative purposes). (b) Snapshots of deformation during lateral indentation simulation.

199

rent experimental arrangement (*e.g.*, the employed spectroscopy cantilever/probe). Such a limitation does not exist for the computational model. To facilitate direct comparison between models at pH 5.5 and pH 2.0, both model arrays were subject to the same range of computational indentation depths (up to 1.0 μm). A summary of force-indentation ($F - \Delta$) results are depicted in Figure 6-4 for simulation and experimentation at both pH levels. For a pH of 5.5 (Figure 6-4(a)), we note that the model overestimates the normal forces due to lateral spectroscopy (Figure 6-4(b)). This is likely due to the elastic assumption of the model, whereas the physical tubes would be subject to slight softening under bending load (*e.g.*, local buckling, plasticity due to molecular migration, etc.). For example, at an indentation depth of 0.2 μm, the simulation overestimates the normal force by approximately 35% (see Figure 6-4(b) inset). The opposite trend occurs for the lateral force, whereby the model underestimates the force levels (Figure 6-4(c)). Lack of friction between the indenter (modeled as an ideal harmonic surface) and tube reduces the contribution of frictional resistance (*e.g.*, probe tip-surface adhesion through non-specific, non-covalent interactions and/or adhesion-induced stretching of adsorbed polymer chains at the tip-sample interface [131]), and the lateral force is due to the bending and axial resistance only.

For a pH of 2.0 (Figure 6-4(d)), there is a change in observed correlation between simulation and experiment. For normal forces, the model underestimates the magnitudes (Figure 6-4(e)). While the model tubes are likely stiffer beyond small deformation due to the elastic assumption (similar to pH 5.5), it has been previously shown that the reduced intertube spacing (due to swelling of the PEM) results the increase of axial deformation (versus bending dominated modes), and induces a more homogeneous stress field mediated by intertube contact. This effect is enhanced at higher levels of indentation, with the experimental results depicting increased stiffening not present in the current model implementation. Again, comparing the lateral forces, the model underestimates the magnitude, contributed to the lack of indenter-tube interaction (Figure 6-4(f)). However, the trend is in agreement, whereby the increase in lateral resistance can be associated with contributions of bending/buckling and
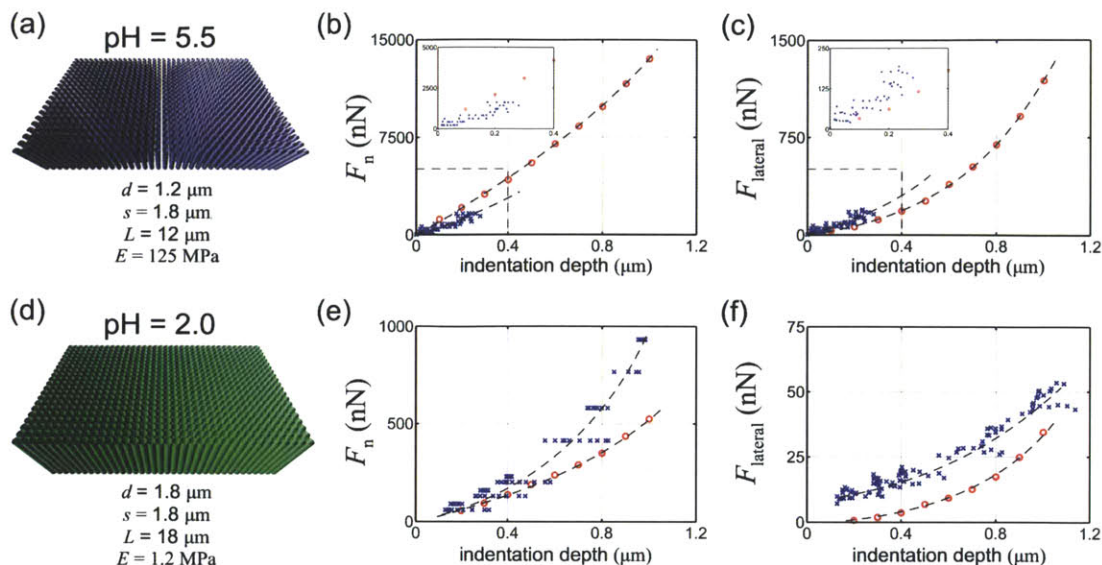
Figure 6-4: Force-indentation for simulation (red circles) and experimentation (blue x's) at (a)-(c) pH = 5.5 and (d)-(f) pH = 2.0. (a) Model schematic and relevant parameters for a pH of 5.5. (b) Normal force versus indentation depth. Simulations were undertaken at greater indentation depths for one-to-one comparison with pH 2.0 conditions. Computational results overestimate the normal forces recorded by experimental lateral spectroscopy. This is likely due to the elastic assumption of the model, whereas the physical tubes would be subject to slight softening under bending load. (c) Lateral force versus indentation depth. Computational results underestimates the force levels, due to lack of prescribed friction between the indenter and tube (lateral force due to bending and axial deformation only). (d) Model schematic and relevant parameters for a pH of 5.0. (e) Normal force versus indentation depth. For pH 2.0, the model underestimates the magnitudes - reduced inter-tube spacing (due to swelling of the PEM) results the increase of axial deformation (versus bending dominated modes), and induces a more homogeneous stress field mediated by inter-tube contact. This effect is enhanced at higher levels of indentation, with the experimental results depicting increased stiffening not present in the current model implementation. (f) Lateral force versus indentation. Computational results again underestimate the magnitude, contributed to the lack of indenter-tube interaction. For both cases, the general trend of force magnitudes is in agreement, whereby the increase in normal and lateral resistance can be associated with contributions of bending/buckling and inter-tube contact, captured by the coarse-grain model.

inter-tube contact, captured by the coarse-grain model.

The discrepancy between the computational and experimental results can potentially be associated with observed rate- and time-dependent mechanisms [142, 143], such as the breaking and reforming of ionic cross-links, charge migration, intrinsic viscoelasticity of the solid macromolecular components, and fluid flow-governed plasticity poroelasticity [33], unable to be captured by the elastic coarse-grain model

formulated. While there are deviations between simulated and experimental results, the models accurately capture the relative force magnitudes of each pH level. Considering the homogeneity of the model arrays, and relatively few fitted parameters, the current coarse-grain formulation provides a suitable modeling template to parametrically explore the potential mutable mechanical behavior of pH-responsive PEM tube arrays.

6.3 Lateral Linearity

Systems such as the current PEM tube arrays are promising for the ability to induce stimulus-responsive surface friction. The frictional surface behavior is commonly quantified by the friction coefficient, μ, or *lateral linearity*, defined as the slope of the lateral force versus applied normal force curve, as plotted in Figure 6-5.

6.3.1 Variation of pH

For pH 5.5, the bending dominated deformation results in near-linear behavior, regardless of indentation depth. Fitting the data results in $\mu_{exp} = 0.106$ and $\mu_{sim} = 0.092$. Again, we note that, for a given normal force (or, equivalently, indentation depth) the lateral load is underestimated by the model due to the lack of adhesion between indenter and tube surface. For pH 2.0, the deviation of recorded normal forces with an increase in depth (see Figure 6-4(e)) limits the comparison to a small deformation regime ($\Delta \leq 0.5\mu m$), and the curves deviate with increasing normal forces. Limited to the small deformation regime results in $\mu_{exp} = 0.043$ and $\mu_{sim} = 0.048$, portraying close agreement.

In terms of magnitude of change (or *mutability*), we define a pH-dependent frictional responsiveness ratio as $\mu_{pH5.5}/\mu_{pH2.0}$. This results in a ratio of approximately 2.47 for the experimental results and 1.92 for the simulated results (small deformation). For the PEM arrays, complementary experimental studies report linearties ranging from 0.100 to 0.116 for pH 5.5, and 0.025 to 0.045 for pH 2.0, increasing as a function of lateral displacement rate [143]. Experimentally, the rate is on the order
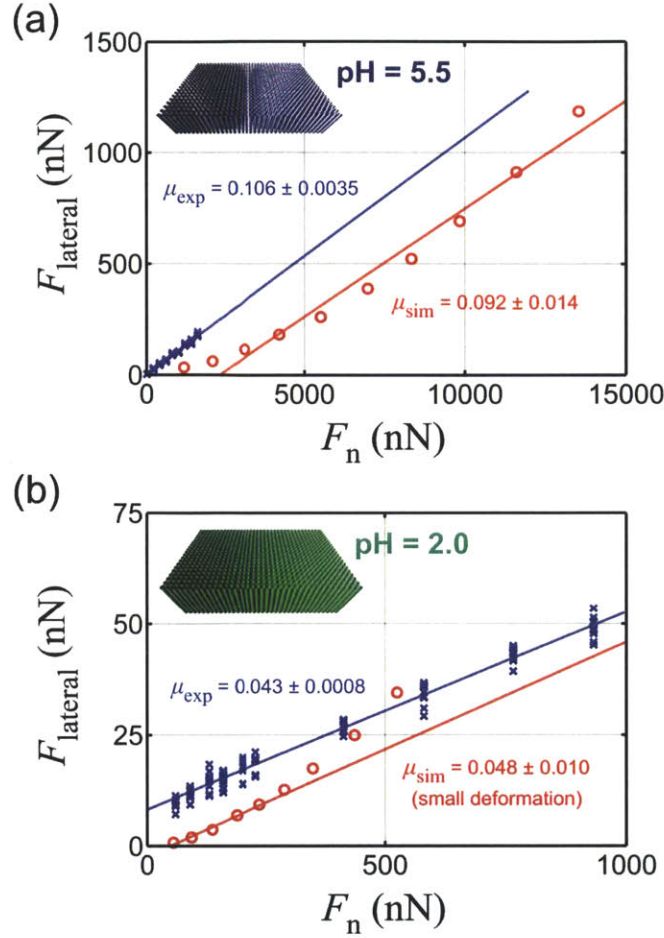
Figure 6-5: Lateral force ($F_{lateral}$) versus applied normal force (F_n) curves, experimental and simulation results; determination of lateral linearity, μ. (a) Results for pH = 5.5. The elastic bending dominated behavior of the tubes at pH 5.5 results in consistent behavior beyond the experimentally achieved indentation depths in terms of force magnitudes. Computational results underestimate lateral resistance at a given normal force due to lack of indenter-tube adhesion. Calculated slopes results in $\mu_{exp} = 0.106 \pm 0.0035$ and $\mu_{sim} = 0.092 \pm 0.014$. (b) Results for pH = 2.0. Intertube contact, and a transition from bending dominated to axial compression tube-tube interactions limits comparison beyond a small deformation regime ($\Delta \leq 0.5\mu m$). Calculated slopes results in $\mu_{exp} = 0.043 \pm 0.0008$ and $\mu_{sim} = 0.048 \pm 0.010$.

of 10^{-6} m s^{-1}, and thus the relatively high rate of simulation can be seen as an upper bound, negating proposed time-dependent visco/poroelastic effects. The simulation result of 1.92 (small deformation), approaches and is in closer agreement with the highest-rate experimental result (2.39 at $v = 100$ μm s^{-1}; *data not shown*).

Again, we note that the developed model is a pure elastic formulation, and thus deviates from the experimental results beyond small deformation and time-dependent

effects. For a pH of 5.5, the deformation mechanisms is dominated by discrete tube bending (see Figure 6-6), and there is closer agreement between the modeled arrays and experimental results in terms of force magnitudes, even extrapolated to higher indentation depths. As such, the determined lateral linearity at pH 5.5 is consistent. For a pH of 2.0, bending, axial compression and intertube contact contribute to the normal and lateral resistance. Beyond small deformation (an indentation depth of approximately 0.5 μm), the model behavior deviates from experimental results. Experimentally, the tube contact facilitates near film-like stress distributions due to the stress transfer between adjacent tubes, as well as possible ionic cross-links formed between the PAH/PAA of adjacent tubes. In contrast, the elastic model introduced here only transfers stress *via* direct compression - the tubes are free to slip along each other in the absence of friction. As a result, at higher indentation depths there is mainly a contribution due to bending (rather than the characteristic axial compression of near-homogeneous tubes akin to films). This is supported by the deviation in normal force versus indentation depth in Figure 6-4(e), where the experimental arrays show stiffening in excess of the model arrays. Thus, beyond small deformation, the ratio of lateral-to-normal resistance increases, resulting in deviation from linearity, as depicted in Figure 6-5(b).

The deviation of calculated lateral linearities limit direct experimental and model comparisons to relatively small deformation conditions in the absence of indenter-tube and tube-tube friction. However, the agreement between force magnitudes suggest the model can be used to quantify both the normal and lateral resistance as a function of pH as well as array density (through the variation of intertube spacing, s) to probe the effect of intertube contact on potential array mutability. The pH-dependent frictional responsiveness of approximately 2.47 for the experimental results and 1.92 for the simulated results suggest a mutability of about twofold, whereas films composed of the same PEM express fivefold changes [142, 143]. Moreover, other systems, such as end-grafted polymer brushes [239, 90, 141, 140, 357], polymer nanoparticles [21] and cross-linked hydrogels [55] have been shown to undergo changes in the friction coefficient, μ, up to an order of magnitude upon the application of stimuli such
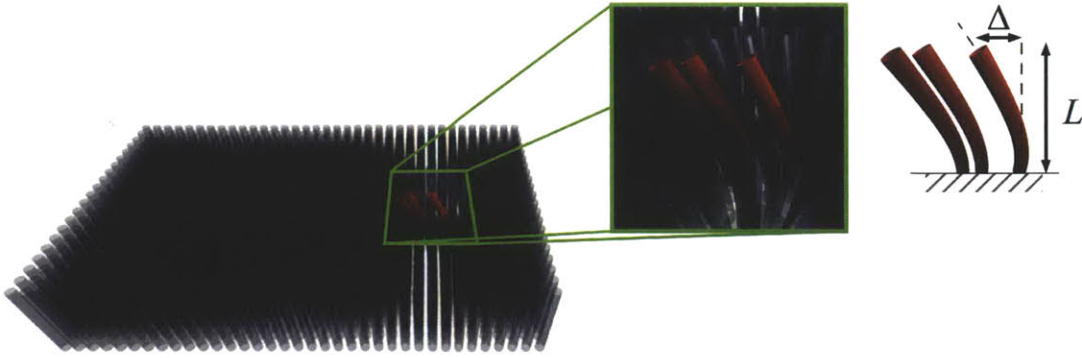
Figure 6-6: Subject to lateral force spectroscopy, at pH = 5.5, the deformation mechanism of the PEM microtube array is dominated by discrete tube bending, rather than tube contact (*e.g.*, each tube can be considered a cantilever of length, L). The deformation (*e.g.*, deflection of the tip, Δ) is not sufficient to induce significant contact. As a direct result, lateral resistance is a proportional to the number of tube contacts. For a pH of 2.0, bending, axial compression and intertube contact contribute to the normal and lateral resistance.

as temperature [239, 90, 55], pH [239], ionic strength [141, 140] and solvent [357]. The question arises, beyond small-scale intrinsic material changes, can larger-scale architectural or geometrical (*e.g.*, extrinsic) system parameters *amplify* the potential mutability? Here, we investigate the effect of initial tube spacing.

6.3.2   Variation of array spacing

To explore the effect of spacing (and, indirectly, induced tube contact) on the potential mutability of normal, lateral, and friction resistance, tube arrays were constructed with variation in intertube spacing, s, ranging from 1.2 μm to 3.6 μm (see Figure 6-7). Each array is then subject to the same lateral spectroscopy procedure as previously described, with indentation depths up to 1.0 μm. Results of the force-indentation curves for both normal and lateral forces are plotted in Figure 6-8. As anticipated, as the areal density of the tubes decreases (from a spacing of 1.2 μm to 3.6 μm; tube areal density ratio of $(s_2/s_2)^2$) there is a substantial decrease in force magnitude. For pH 5.5 at an indentation depth of 1.0 μm, for example, $F_n \approx 13.5\mu$N at a spacing of 1.8 μm and $F_n \approx 3.7\mu$N at a spacing of 3.6 μm. Free from intertube contact, the resistance would be in direct proportion to the areal density of tubes [263,
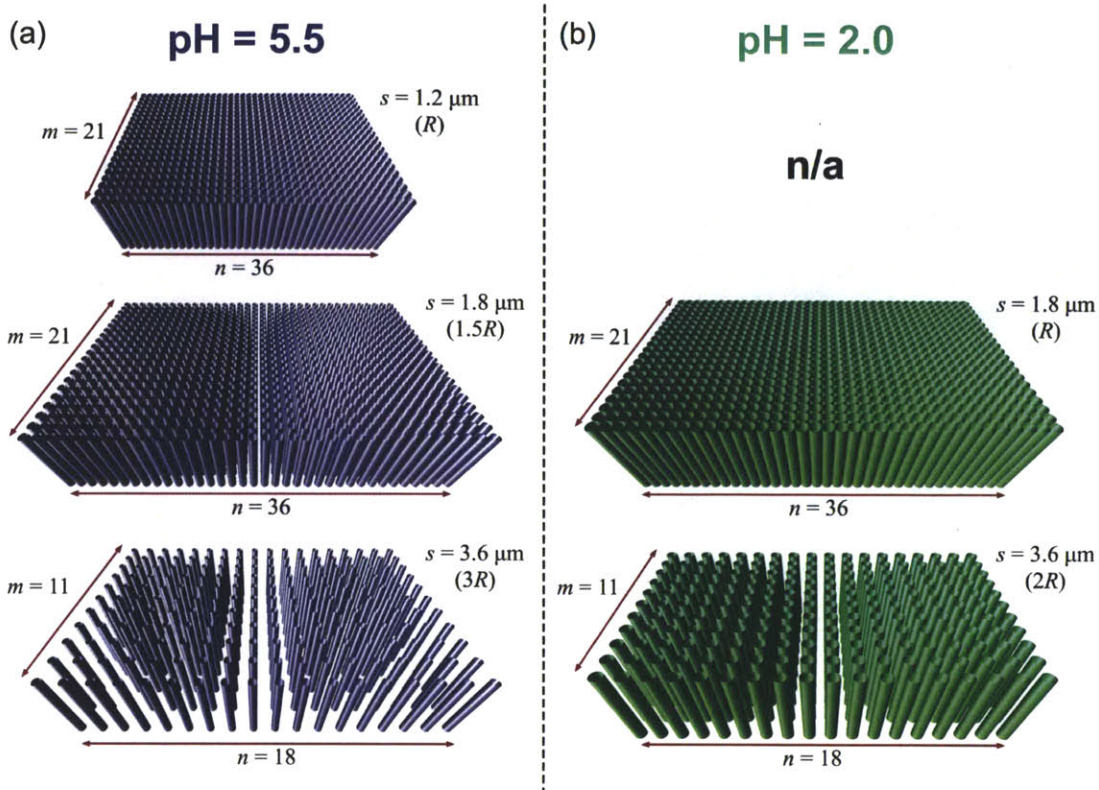
Figure 6-7: Variation in tube spacing. (a) Three model configurations for pH of 5.5, with intertube spacings (s) of 1.2 μm (initial contact), 1.8 μm, and 3.6 μm, or tube radius (R), 1.5R, and 3R, respectively. At $s = 1.2$ μm, the size of the array was lowered (to 24 μm × 42μm) to reduce the required number of tubes and computational time. (b) Two model configurations for pH of 2.0, with $s = 1.8$ μm (initial contact) and $s = 3.6$ μm, or R and 2R, respectively. For both cases, $s_{min} = R$.

337]. We see here that $F_n(1.8\mu m)/F_n(3.6\mu m) \approx 3.6$, whereas there is an increase in density of 4.0 ($= (3.6/1.8)^2 = 2.0^2$). This spacing dependence of F_n can be attributed to increase in tube contact at $s = 1.8$ μm with the introduction of an additional deformation mechanism providing increased resistance. In contrast, at a pH of 2.0 at an indentation depth of 1.0 μm, $F_n \approx 525$ nN at a spacing of 1.8 μm and $F_n \approx 65$ nN at a spacing of 3.6 μm, such that $F_n(1.8\mu m)/F_n(3.6\mu m) \approx 8.0$, indicating a change of mechanism between the two systems induced by spacing. To confirm, there is a similar transition at pH 5.5 at an indentation depth of 1.0 μm from $s = 1.2$ μm to $s = 1.8$ μm, where $F_n(1.2\mu m)/F_n(1.8\mu m) \approx 5.0$ whereas the areal density ratio is only 2.25 ($= (1.8/1.2)^2 = 1.5^2$).

To further quantify the effective resistances, we fit the force-indentation data to

206

a Hertzian relationship, where, repeated here from **Chapter 2: Computational Methods**:

$$F\left(\delta\right) = \frac{4}{3}KR^{1/2}\delta^{3/2} \tag{6.2}$$

such that $F \propto \delta^{3/2}$, for both normal and lateral forces. We note that this does *not* imply the calculation of the contact stiffness of the arrays, as the normal force is merely the force incurred at a constant indentation depth *subject to lateral motion*. However, similar to the derivation of Hertzian contact, the $F \propto \delta^{3/2}$ relation provides a quantitative metric to define and compare the effective normal and lateral resistances of the arrays subject to lateral force microscopy, defined here as N and L respectively (to avoid misuse as contact stiffness). We also note that using $F \propto \delta^{3/2}$ is consistent with our application of lateral linearity, μ. We can then define the potential mutability, η, calculated as the ratios $N_{\text{pH5.5}}/N_{\text{pH2.0}}$ and $L_{\text{pH5.5}}/L_{\text{pH2.0}}$, or $\eta(N)$ and $\eta(L)$ respectively (similarly, using this notation, the previous pH-dependent frictional responsiveness ratio can be simply expressed as $\eta(\mu)$). The results are summarized in Table 6.3.

At higher spacing ($s = 3.6\ \mu\text{m}$), reducing the chance of inter-tube contact, we find that the deformation mode is dominated by the bending of the tubes, and the mutability attributed to the change in bending resistance (*e.g.*, see Figure 6-6), similar to the discrete tube, bending-dominated behavior of carbon nanotube arrays [263, 251, 337]. If we consider the tubes as isolated cantilevers with an effective stiffness of $K \propto EI/L^3$, it follows that $\eta(K) = 69.5$. Indeed, we find that $\eta(N) \approx 60$ at $s = 3.6\ \mu\text{m}$, indicating a strong dependence on the cantilever deformation mode. Thus, the change in bending rigidity provides a close, first-order approximation (as *some* tube contact is incurred upon deformation, there is not one-to-one agreement). The dependence on bending rigidity is decreased as further tube-tube contact is introduced, with a substantial decrease in the change in normal resistance ($\eta(N) \approx 25$ at $s = 1.8\ \mu\text{m}$).

The mutability in lateral resistance, L, however, is near-constant for the two spacings considered ($\eta(L) \approx 32$ at $s = 3.6\ \mu\text{m}$ and $\eta(L) \approx 33$ at $s = 1.8\ \mu\text{m}$) indicating

(a)

F_n (mN)

x 10^4

indentation depth (μm)

(b)

$F_{lateral}$ (nN)

indentation depth (μm)

(c)

F_n (nN)

indentation depth (μm)

(d)

$F_{lateral}$ (nN)

indentation depth (μm)
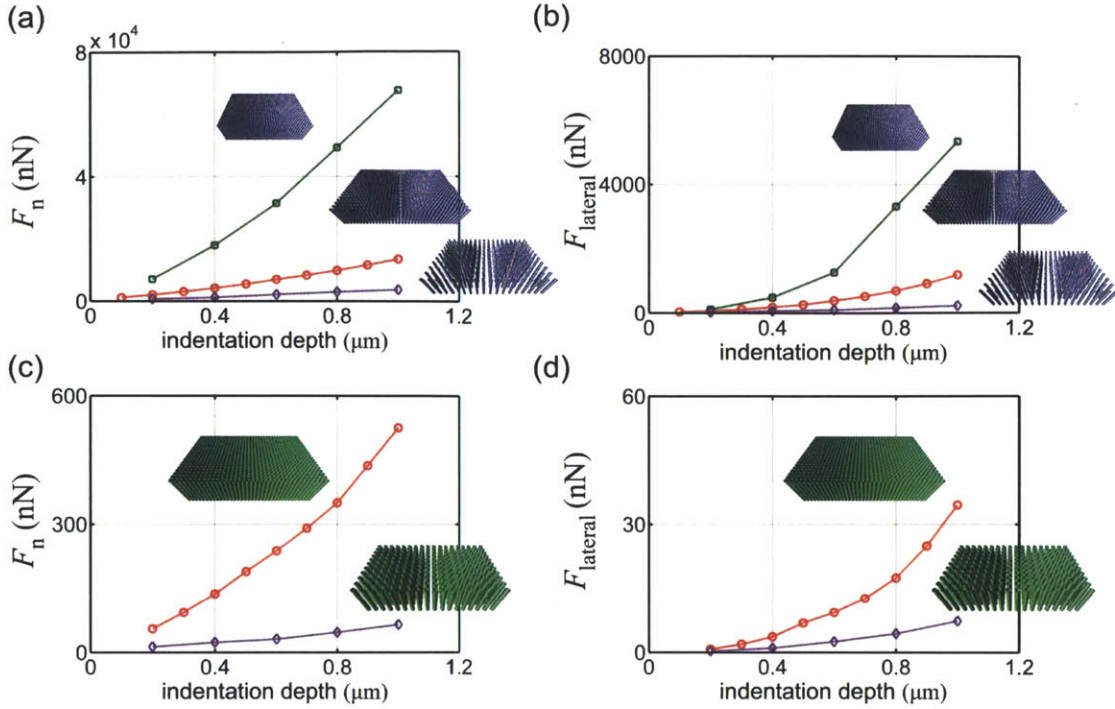
Figure 6-8: Computational force-indentation plots for arrays of variable intertube spacing, s. (a) Normal forces, F_n at pH = 5.5, s = 1.2, 1.8, and 3.6 μm (insets). (b) Lateral forces, $F_{lateral}$ at pH = 5.5, s = 1.2, 1.8, and 3.6 μm (insets). (c) Normal forces, F_n at pH = 2.0, s = 1.8 and 3.6 μm (insets). (d) Lateral forces, $F_{lateral}$ at pH = 2.0, s = 1.8 and 3.6 μm (insets). As anticipated, as the areal density of the tubes decreases (from a spacing of 1.2 μm to 3.6 μm) there is a substantial decrease in force magnitude. Upon intertube contact, the differences in resistances are not directly proportional to areal density (density ratio = $(s_2/s_1)^2$). Lateral resistances depicts less dependence on intertube contact. Fitted resistances and mutabilities (η) given in Table 6.3.

a frictional contribution with less dependence on tube interactions. This can also be understood in terms of the cantilever nature of the tube and the applied indenter load (normal to an idealized spherical surface) - the force components required to deflect individual tubes will result in a higher growth of lateral rather than normal loads due to a constant radius of the indenter, and thus *less* dependence on additional mechanisms such as contact deformation. Moreover, it was previously observed that swelling combined with a decrease in tube spacing results in a convergence to film-like behavior, as close-packed tubes result in a more continuous and stiffer mechanical behavior and stress field and the system behaves similar to a bulk volume, rather than the bending/buckling of discrete tubes [142, 143]. Previous experimental and finite

Table 6.3: Variation of intertube spacing (s) on normal (N) and lateral (L) resistance, and mutability (η).

s	N, MPa			L, MPa		
μm	pH 5.5	pH 2.0	$\eta(N)$	pH 5.5	pH 2.0	$\eta(L)$
1.2	19.24	n/a	n/a	1.707	n/a	n/a
1.8	3.61	0.144	25.1	0.333	0.010	33.3
3.6	0.96	0.016	60.0	0.064	0.002	32.0

element-based computational investigations [142, 143] indicate that there is a transition from bending-dominated to compression-dominated (*e.g.*, buckling) supported by the results here: compressive forces further contribute to the normal resistance rather than lateral resistance, leading to a purely mechanical decrease in a lateral linearity (as opposed to solvent or time-dependent porous effects).

Under lateral spectroscopy, the primary deformation mode is bending, as opposed to buckling modes associated with purely vertical indentation [337, 142]. Normal resistance (N) was found to vary by a factor of 25 to 60 times for the tube arrays at different pH levels, which depends greatly on tube density. Lateral resistance (L) varied by a factor of approximately 30 regardless of intertube spacing, indicating that lateral modes are less sensitive to tube-tube interactions, which trigger compressive deformation modes.

6.4 Summary

Investigation by lateral force spectroscopy has demonstrated that mechanomutability can be controlled through the coupling between the "inherent" molecular-level material properties of polyelectrolytes and the "acquired" anisotropic microscale geometry[3] in a PEM microtube model system. It is clear that the changes in this system behavior cannot be accounted for by polyelectrolyte properties alone. Geometric dependence due to external signals can be coupled with smaller-scale material property changes that *amplify* mechanomutability due to a transition in deformation

---

[3]we lable the geometry "acquired" as it is a function of the chosen (*e.g.*, designed) template, and not the polymers in themselves

mechanism. For example, in general, high friction is obtained from soft materials, which achieve intimate contact with the opposing surface due to their compliance. Fibrillar surfaces achieve a similar compliance due to the ability of each individual fiber to deform freely upon contact - the resistance from each contact adds up to induce friction. Previously reported studies on non-responsive surfaces have utilized surface texturing, roughness, patterning and fibrillar microstructures to control friction, which is primarily a contact area splitting effect [187, 204, 231, 214, 356, 164]. Here, material changes (induced swelling and compliance) effectively transition a fibrillar system (discrete rigid tubes at pH 5.5) to a more homogeneous, bulk system (compliant tubes in contact at pH 2.0) - coupling distinct responses into the *same* material system.

The microtube arrays demonstrate that induced intertube contact results in the amplification of normal and lateral resistance, suggesting a range of mechanical responses can be engineered by tailoring different geometrical parameters (*e.g.*, tube height, cross-section, spacing, etc.). Indeed, the associated deformation mechanisms and mechanical responsiveness vary markedly with larger-scale geometry (*i.e.*, extrinsic structural mutability) in collusion with smaller-scale material properties (*i.e.*, intrinsic material mutability) illustrating the potential of hierarchical material design in which mechanisms synergistically interact at multiple scales [142]. While the tubes here a pH-responsive and driven by change in ionization (*e.g.*, electrostatic cross-linking) the functional effect is reflected in a change of volume (*e.g.*, reversible geometric swelling) and material stiffness. As such, any material component (*i.e.*, "functional building block") with similar characteristics could be exploited in the same manner (assuming vertically aligned fibrillar architecture is feasible). It is *precisely* for this reason that the nanomechanics of the polyelectrolyte complex was explicitly characterized in previous chapters - to attain an abstract separation of mechanical *function* from material *properties*. In this way, a range of material "parts" can (in theory) be selected to satisfy and optimize material design problems - similar to the choice of steel or reinforced concrete in macroscale structural design.

One important observation emerging from this study is that the friction coefficient

(μ), normal resistance (N), lateral resistance (L), and governing deformation mechanisms of the polyelectrolyte system can be altered by both the solution pH (material stimulus) and the micro-scale geometry (*e.g.*, intertube spacing). The implications of coupling intrinsic responses with extrinsic morphologies at multiple hierarchical levels are neither material specific, nor scale dependent, suggesting the combination of stimuli-responsive materials with engineered hierarchical structures can be designed and employed for a multitude of functions, with additional mutable phases, triggers, and complex geometries. For example, it is known that the elasticity of a tissue scaffold can determine stem cell differentiation, from neurogenic cells (soft) to osteogenic cells (stiff) [95, 108] - a mutable scaffold, however, could be introduced and tuned for multiple cell types (and combined with secondary factors, such as porosity for nutrient transport). Such mechanomutable systems hold great potential for use as dynamic substrates for fundamental studies of cell behavior, control of particle or fluid transport, and tunable tissue engineering scaffolds [124, 80].

Chapter 7

Conclusion

While the previous chapters have characterized a single molecular system - specifically a molecular complex of PAA and PAH - the emergent properties and behaviors have implications beyond that of these two electrolyte species. To conclude, a summary of findings is presented, as well as an reiteration of the interpretation of the findings (*e.g.*, multiscale *nano-to-macro-to-nano*). Criticisms of the methods used are briefly discussed in recognition that, by definition, one approach is insufficient to completely characterize such complex systems. Potential future application of responsive polymer systems within the realm of biomaterials is discussed.

7.1 Summary

The layer-by-layer, or multilayer, method of thin film growth has evolved into a widely-used enabling technology. The physical assembly - alternating layers of positively and negatively charged polyelectrolytes - is, upon first glance, simple in concept. Being said, the fundamental science and understanding of multilayers have advanced substantially but still lack in key areas [287]. In actuality, PEMs offer a highly complex system wherein even the most fundamental interactions - the complexation and coupled nanomechanical behavior of a single polyanion and polycation - remain unknown and unpredictive quantitatively. As such, they cannot be precisely engineered as a functional material. The aim of this dissertation was to uncover and charac-

terize the emerging effects of complexation - the resulting mechanical properties of an electrostatically cross-linked polyelectrolytes beyond the simple summation of the constituent polymers - due to cooperativity at the molecular scale. As complexation serves as the basis of mutability for larger scale composite systems (*e.g.*, ionization changes polymer interaction, not the molecular structure of PAA or PAH), this fundamental "building block" may serve benchmark larger-scale performance.

The previous chapters primarily investigated the mechanical properties of a simple polyelectrolyte complex consisting of poly(acrylic acid), PAA, and poly(allylamine hydrochloride), PAH - two weak polyelectrolytes that have been successful in the synthesis of a layer-by-layer composite with tunable (and mutable) properties by precise control and manipulation of pH. Initial characterization focused on the behavior of individual molecules, specifically the potential range of rigidity due to ionization. In **Chapter 3: Variation of Molecular Rigidity**, it was determined:

- For flexible polyelectrolytes, the classical Odijk-Skolnick-Fixman (OSF) formulation of electrostatic persistence can be applicable through the consideration of an electrostatic contour length (defined as the spatial path connecting adjacent charges). Only simple energetic arguments (balancing electrostatic and equivalent elastic bending energy) are necessary.

- The modified OSF formula for electrostatic persistence converges to the classical form (κ^{-2} dependence) as intrinsic persistence increases, and collapses to linear screening length dependence (κ^{-1}) as intrinsic persistence decreases.

- The nominal intercharge spacing (A) is limited by the screening length (κ^{-1}) for highly flexible polymers.

- Electrostatic persistence length (and thus range of mutability) can be maximized by the ratio of intrinsic to electrostatic contour lengths ($P_e \propto a/A$) as well as the known effect of salt concentration (*e.g.*, screening).

- The derived expression for electrostatic persistence length (Eq. 3.30), is inherently *coupled* to the intrinsic persistence length through the the charge-to-charge

214

spacing along the electrostatic contour. This distance can only be quantified *ex post* - either through experimental or computational means. Thus the theory provides descriptive characterization, but is predictive only insofar as attained results.

- Both the persistence lengths (and associated rigidities) of PAA and PAH are shown to increase by approximately a factor of two with ionization. Rigidity values are directly correlated with ionization density and representative pH.

Upon characterization of the individual complex constituents, is is necessary to define the interaction between the two chemical species - namely, the electrostatic cross-linking behavior of PAA and PAH. In **Chapter 4: Rate Dependence and Ionization Effects on Adhesion**, it was determined:

- The functional groups of PAA ($COOH/COO^-$) and PAH (NH_2/NH_3^+) undergo a balance of electrostatics and hydrogen bonding that result in adhesion and complexation that varies in strength as a function of pH and ionic strength; the complex nature of pH dependence on protonation/deprotonation is simplified and short poleyelectrolyte chains are modeled to isolate the effects.

- Explicit solvation is necessary to capture the accurate adhesion and structure of a short polyelectrolyte complex; counterions have negligible effects at the time and length scales accessible to full atomistic MD.

- To reconcile the time restrictions of MD simulation, a systematic investigation of rate dependence was fit to an "extended" Bell Model, commonly associated with more complex protein structures. By extrapolation of the simulation results, the adhesion strengths are in good agreement with previous experimental results of the polyelectrolyte functional groups at lower (empirical) loading rates.

- Characteristic force-displacement response indicate (i) an elastic regime of polymer stretching and cross-link alignment followed by (ii) sequential cross-link rupture and reformation; maximum adhesion force increases approximately fivefold across the represented pH range.

215

- At zero percent ionization, there is minimum adhesion strength on the order of 10 nN, reflecting a propensity for attraction regardless of electrostatic interactions *via* hydrogen bonding and van der Waals interactions.

- An energy barrier of approximately 9 kcal/mol was found as representative as a single "electrostatic cross-link"; while higher than a single charge-to-charge interaction, the energy accounts for the combined interactions induced, including hydrogen bonding, hydrophobic and/or steric effects.

Completing the mechanical perspective involved combing the behavior of the components (*e.g.*, known rigidity of each polyelectrolyte as a function of ionization) with their interaction (*e.g.*, known cross-link density as a function of ionization) in a cohesive structure. *Via* a general elastic "truss" model, developed to isolate mechanical response (*e.g.*, eigenmodes), in **Chapter 5: Critical Ionization to Couple Polyelectrolytes**, it was shown:

- *In lieu* of entropic conformations (*e.g.*, statistical approaches), free vibrational modes can be used as a mechanical metric to compare induced flexural deformation with additive response, assuming near-elastic behavior about equilibrium. Similar to elastic network models for proteins which extract preferred motions, elastic mechanical behavior is *not* presumed, but merely used as a heuristic for comparative analysis (in this case cooperative deformation).

- The flexibility of polyelectrolytes (or, equivalently, the relatively small rigidity) is complementary to the strength of electrostatic cross-linking, wherein the ionic interactions are "sufficiently stiff" to induce coupled modes of deformation. More rigid molecules would require stiffer cross-links.

- Simple flexure of complexes with few cross-links result in relatively high vibrational modes (due to the mismatch of the natural frequencies of each individual polyelectrolyte). As such, the effective rigidity is much higher than the sum of each backbone chain, and uncoupled motions are preferred. Entropically driven thermal fluctuations would act independently for PAA and PAH.

216

- Increased cross-link density results in cooperativity between backbones. The cross-links effectively impose an energetic penalty for non-symmetric deformations. The effective rigidity is lower than the sum of the backbones, and cooperative motion is preferred. This regime is used to define mechanical complexation.

- Critical cross-link density is linked to a critical pH range, approximately 7.0 to 8.0 for the basis model, which agrees with experimental results observing complexation.

- Monomer-to-monomer spacing (and thus range of cross-link density) can be exploited to extend/contract the critical pH range. *E.g.*, 10% variation in length results in a critical range of 7.0±0.25 to 8.0±0.25.

- The critical cross-link spacing (or density) is related to the persistence length of the polyelectrolytes; cooperative deformation and complexation occurs when the cross-links are within $0.5P_{max}$, such that the flexural mode between adjacent cross-links is correlated.

Finally, the polyelectrolyte complex forms the basis of large-scale PEM systems. To demonstrate how mutability at the atomistic scale (*e.g.*, complexation and variation in stiffness due to ionization) can be exploited (and amplified) at larger scales, the behavior of an aligned array of PEM tubes were investigated (**Chapter 6: Beyond Full Atomistic Characterization**). Relying on MD procedures, a coarse-grain model was developed to account for microscale interactions (*e.g.*, Hertzian contact). Probing the effect of changing stiffness and geometry at the microscale on the mechanical response (specifically, lateral resistance), it was demonstrated that:

- Friction of a PEM microtube array structure is also pH-dependent, determined *via* complementary simulated lateral force microscopy (LFM) and experimental results.

- While chemical changes are bound to the molecular scale (*i.e.*, intrinsic material mutability; *e.g.*, changes in molecular cross-link density), mechanical responses

can be coupled with hierarchical effects at a larger-scale to amplify or manipulate the material response (*i.e.*, extrinsic system mutability; *e.g.*, changes in system geometry due to swelling).

- For rigid/unswollen tubes (pH 5.5), the deformation mechanisms is dominated by discrete tube bending, whereas for more compliant/swollen tubes (ph 2.0) bending, axial compression and intertube contact contribute to the normal and lateral resistance.

- Exploiting the effect of tube contact and dominant deformation mode, intertube spacing can be used to manipulate the mechanical variation *via* pH switching (*e.g.*, 2.0 ⇔ 5.5); for example high spacing results in a change in lateral resistance directly proportional to tube bending stiffness, as tube contact is avoided.

- The microtube arrays demonstrate that induced intertube contact results in the amplification of normal and lateral resistance, suggesting a range of mechanical responses can be engineered by tailoring different geometrical parameters (*e.g.*, tube height, cross-section, spacing, etc.). The friction coefficient (μ), normal resistance (N), lateral resistance (L), and governing deformation mechanisms of the polyelectrolyte system can be altered by both the solution pH (material stimulus) and the micro-scale geometry (*e.g.*, intertube spacing).

7.1.1 Caveats and Critiques

Undoubtedly, molecular simulation has developed as an indispensable tool for the investigation of material systems at the atomistic level, yet there is very few "standardized methods" for the determination of mechanical properties. Throughout this dissertation - to stress the atomistic basis and primary hierarchical scale of PEMs - a polyelectrolyte complex was considered the "fundamental building block" for the entire system. This, however, is not the *definitive* perspective. Many successful theories have been developed to describe the properties of polymer systems, including classical Flory-Huggins solution theory [117, 118] and more recent developments such as

group interaction modeling [259]. Typically, the importance and details of one-to-one molecular interaction is homogenized to a statistical description of the bulk. In practice, this is more than sufficient (and quite ingenious), but it need not be conclusive. Complementary to such approaches are relatively "narrow" molecular investigations, which are ever-increasing scope and applicability. Indeed, from a reductionist perspective, a focused study of the behavior of PAA and PAH can be associated with other molecular systems beyond the realm of "polymer theory" - it is specifically for this reason that simple energetic arguments, mechanical formulations, and elastic models were developed throughout this dissertation. While lacking sophistication in the face of the extended field of polymer science, value is found in atomistic *fidelity* and *transferability* to other molecular systems. In can be said colloquially that molecular models do not care if the carbon is associated with PAA, DNA, or graphene - the analytical approach is universal.

Being said, a standardized procedure for extracting mechanical properties from molecular simulation unfortunately does not exist. The challenge is to construct a suitable procedure and extract useful mechanical measures comparable to macroscale metrics (stiffness, strength, fracture toughness, etc.). As a result, there have been many methods developed to exploit the capabilities of atomistic simulation (such as the discussed temperature assisted sampling, SMD, free energy minimization, etc.), and various analytical tools and models to interpret such results (*e.g.*, the classical Bell model for rate dependence, worm-like chain models for end-to-end distance, etc.). Recognition and admittance of the limitations and constraints is a responsibility for any computational investigation. Four aspects of the current investigation that warrant immediate discussion are:

1. **Complexation of only two molecules**. Here, as a simplifying measure, we only consider two polyelectrolyte chains in isolation. This has two immediate implications. Primarily we are making an assumption of the structure of PEMs. Two models are commonly adopted to describe structures of LbL system: (i) ladder-like structures, wherein the ionic complexation are is considered chain-to-chain in an aligned configuration and (ii) scrambled structures, where

219

a large number of polyelectrolyte chains are agglomerated, highly entangled and penetrated through each other, with shared interactions. The definition of "complex" employed here most resembles the ladder-like configuration. Being said, be restricting the length of the chains, it is expected that short segments of polymer would align, in accordance with our model (see Fig. 4-1, for example). In such a structure, the results and behavior of the model can be interpreted as representing the local properties of a more entangled structure. Secondarily, it has been shown experimentally that polyelectrolyte interaction is dependent on the environmental conditions (layer confinement, salt concentration, etc.). This is why the pK_a values used here should be considered approximations only (as discussed in **Chapter 2**). In light of such effects, the results reported for one (in the case of **Chapter 3**) or two (**Chapters 4** and **5**) molecules in relative isolation can be considered benchmark conditions for future investigations.

2. **Static ionization** Here, protonation/deprotonation of functional groups was manually prescribed (either in a random or uniform manner) and held constant throughout each simulation, including the partial charges associated with all other atoms (*e.g.*, polarization of water molecules) and introduced counterions. Even more sophisticated atomistic potentials (such as the EAM [84] or ReaxFF [332] potentials) account for ionization and charge transfer by homogenizing the effects (*i.e.*, local charge density). Indeed, charge migration (*i.e.*, electron hopping) has been observed in LbL systems [190, 161], and salt condensation affects local ionization and screening, such affects cannot be represented in the current atomistic arrangement.

3. **Relatively short polyelectrolytes**. Again, similar to the restriction to two molecules, relatively short lengths (*e.g.*, less than 50 functional groups) are modeled, primarily to reduce the number of water molecules required for solvation. The relatively short chains restrict any statistical variation in terms of localized cross-links, distribution of charges, counterion condensation, long-range electrostatics, etc. Moreover, any length dependencies (typically associated with

average molecular weight) cannot be captured. There is no length dependence associated with the elastic model of **Chapter 5**, for example, and the end-to-end behavior in **Chapter 3** is also assumed independent of length. However, other investigations have demonstrated second order, long range effects [134]. Moreover, the chain length of constituent polymers has shown effects on the LbL assembly [157].

4. **Elastic assumption**. While an elastic (or small deformation) is suitable for characterization close about equilibrium, dynamic effects (*e.g.*, properties and conformational changes while pH is actively changing) cannot be demonstrated. Moreover, at larger scales, the breaking and reforming of ionic cross-links, charge migration, intrinsic viscoelasticity of the solid macromolecular components, or fluid flow-governed plasticity poroelasticity [33] are unable to be captured.

It is stressed that the results and characterizations reported herein are intended to complement and support additional computational and experimental assays across scales. Regressing to our structural analogy, while knowledge of structural rebar is necessary to understand a reinforced concrete member, it is not sufficient.

7.1.2 Nano-to-Macro-to-Nano

The analysis of material properties at multiple scales is a crucial issue in understanding complex materials, as their structure changes with hierarchical level (and thus length-scale), and therefore most material properties are strongly dependent on the scale of observation. For coupled polyelectrolytes, we see that ionization initiates mechanical effects beyond the simple cross-linking of two molecules - the emergent complex is both mechanically stable and highly cooperative. At the scale of PEM microtubes, we see a similar result where the system behavior can be amplified beyond the variation attributed to "known" mechanisms (in this case, variation in stiffness and controlled swelling). The introduction of material *hierarchics* - that is, structural order at distinct scales - serves to increase the accessible design space beyond "intrinsic" materials properties (*e.g.*, small-scale, chemistry dependent interactions).

Understanding the limits of such interactions (as well as how they propogate/emerge across scales) is critical if we are to design high performance, multi-functional materials from a few select (*e.g.*, low energy, widely available) building blocks.

Indeed, just as Nature relies on a mere twenty amino acids to form a wide selection of proteins, materials design could potential rely on hierarchical assembly rather than one-off "designer" components. Like a children's set of Legos©, creative efforts can be extended beyond the intended instructions. Discovery lies in the "rules of assembly", rather than the invention of "new" building blocks. Being said, the definition of "fundamental building blocks" is a (subjective) matter of perspective. Can they be traced to atoms? amino acids or functional groups? simple molecular structures? Perhaps even quarks or bosons? The critical scale for one system may differ from that of another. Here, a polyelectrolyte complex is labeled the necessary building block, as it is the root of mutable mechanical behavior of the corresponding PEM system, for example:

1. The functional groups can be considered a chemical structure, but mechanical properties only arise at the secondary (molecular) scale. *E.g.*, a building is not made of "steel", it is made of steel beams, columns, etc.

2. Variation in pH (and associated variation in ionization) drives the mechanical changes (*e.g.*, mechanomutability), but results in only superficial changes in the molecular structure of PAA or PAH alone (*e.g.*, protonation or deprotonation; no change in bonded polymer sequence). The main effect emerges in the associated interaction between PAA and PAH, enabling sequential adsorption.

3. It is presumed that this scale is similar in all LbL systems, thus a suitable basis of cross-system comparison. *I.e.*, the polymer complex defines a polyelectrolyte multilayer. While PAA and PAH can be substituted (by PDMA, PMAA, or PSS, for examples), the LbL system relies on the complexation of oppositely charged species. Thus, the behavior of the complex is essential.

In such a context, the complex can be considered the "building block" insofar as it is mutable, yet it is only a single aspect of the material system. We must recognize how behavior at one scale (*e.g.*, nano) drives behavior at another (*e.g.*, macro) in a reciprocal manner, and integrate such understanding across scales simultaneously.
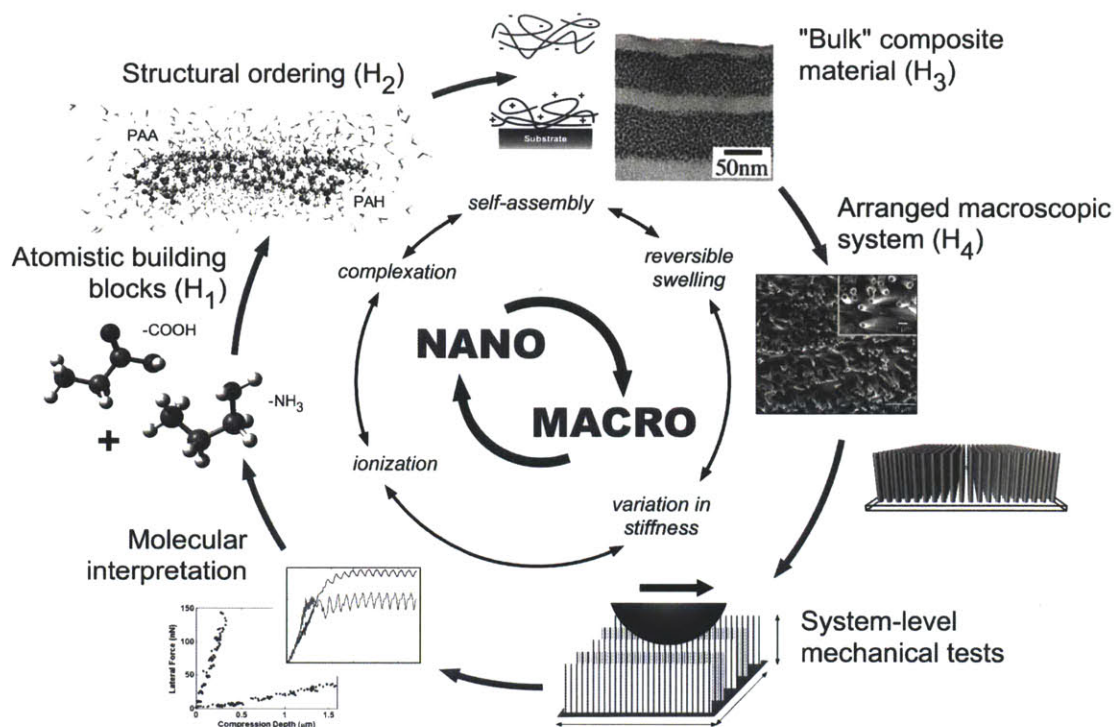
Figure 7-1: Holistic nano-to-macro-to-nano perspective of polyelectrolyte multilayer (PEM) composite, composed of PAA and PAH. Hierarchies indicated by H_i, from lowest atomistic (H_1) to PEM tube array (H_4).

Multi-scale experimental and simulation analyses are the key to improve our systematic understanding of how structure and properties are linked. Typically this is achieved from a *bottom-up* approach, linking more sophisticated lower length-scale parameters, which form the building blocks of the system at that level, to coarser, larger length-scales. Purely "bottom-up" approaches, however, are incomplete if they lack the interpretation of large-scale behavior to small-scale phenomena, an iterative "nano-to-macro-to-nano" paradigm. Full stratification of different levels of hierarchy using such analysis develops a powerful feedback loop where the bottom-up modeling approach catalyzes the insights we gain at each layer of the material ladder, with the possibility of controlling properties at multiple scales simultaneously, and to examine their effect on system function. Such a "nano-to-macro-to-nano" perspective is depicted schematically in Figure 7-1.

Such a perspective is not new - micromechanical models and "molecularly informed" constitutive laws have been developed extensively in the past inform mechanical theories (for example, the Arruda−Boyce hyperelastic model describes the mechanical behavior of rubbers and other polymeric substances, explicitly accounting for molecular chain length and density [11]). We have reached a critical junction, however, where bottom-up and top-down descriptions are no longer required to be antithesized - they can be used simultaneously for the same material system, providing mutual feedback. We note that the properties discussed in this dissertation emphasize the *mechanistic* function of the polyelectrolyte system. Undoubtedly, mechanical performance provides a means to characterize behaviors and properties analogous to engineering practices - we may want to mimic silk to attain a high-performance synthetic fiber, for example, and not a web-like meshwork to capture flies. Ultimately, the understanding of the complete materiome must encompass all potential functionalities, ranging from mechanistic to electrical or optical.

In addition, basic functions can manifest over and over - across scales - and appear universal between differing material systems. This fundamental viewpoint could revolutionize the engineering approach to use and create materials, by incorporating the atomistic to macroscopic scales into materials analysis and synthesis based on universal and cooperative functionalities.

7.2 Future Outlook

Polyelectrolyte multilayers have been thoroughly investigated for their potential in a diverse array of applications, including biosensing and bioelectronics [161], nanofiltration and fuel cell technology [358], drug delivery agents [85, 86], and cell and tissue engineering [133, 80]. Again, such applications tend to focus on the emergent system level characteristics, without consideration of smaller-scale properties that may influence performance. The studies presented throughout this dissertation were some of the first to explicitly quantify polyelectrolyte interaction with chemical specificity (*e.g.*, chemically accurate full atomistic models of PAA and PAH instead

of generalized polymer models). Indeed, for many common, well-understood and "everyday" systems, the details and behavior are adequately homogenized with an increase in scale, and bulk constitutive laws are sufficient. More commonly, however, the knowledge of macroscale behaviour is proven *insufficient* in practice. To illustrate the reason, we turn to another engineering analogy: the foundations of constructed structures [80]. Consider the field of biomaterials and tissue engineering - at the interface of "living" and "non-living" materials - what the tissue "sees" is dependent on the relevant scale; material interactions are inextricably linked across scales [73].

The complex hierarchical structure and interactions of biological materials presents fundamental challenges in the development and prediction of successful biomaterials [73]. Mimicking the target systems, a possible solution is to make the properties of the substrate dynamic and controllable *via* external stimuli or internal feedback, a concept known as *mutability*. Mutable materials are found widely in biology, characterized by a material's capacity to change its properties under external cues based on directed structural changes at specific material levels. Mutable materials are also inherently hierarchical, where property changes are often driving by interactions and processes at the molecular level. Through monitoring of self-assembly and growth or by internal feedback (*e.g.*, mechanical or geometric cues) mutable materials could potentially optimize according to the needs of the system. Potential candidates for such mutable materials are stimuli-responsive polymers, such as the pH-responsive PEM system investigated herein. Responsive polymer systems exhibit similar features as biological materials, and are capable of conformational and chemical changes on receiving an external signal. Such materials can adapt to surrounding environments, regulate transport of ions and molecules, change wettability and adhesion of different species on external stimuli, or convert chemical and biochemical signals into optical, electrical, thermal and mechanical signals, and vice versa [312].

The concept of mutability provides a paradigm shift and exciting opportunity in the area of active materials. Synthetic polymer systems with desired characteristics are currently being developed for a multitude of biological applications, such as responsive biointerfaces that are functionally similar to natural surfaces [298], coat-

ings that are capable of interacting with and responding to their environment [217], and composite materials that actuate and mimic the action of muscles [195]. The effect of mechanical cues on the stimulation of cellular signal expression can exploit materials such as photo-crosslinking polymer composites [180, 115] or the discussed pH-responsive systems [59, 81]. Thorough characterization of the system material and driven mechanisms across scales is required to predictably design such systems.

One important aspect of responsive material systems demonstrated here is the coupling that exists between the chemical, molecular and even microscopic scales (*e.g.*, polyelectrolyte complexation, PEM tube array response). The challenge is to understand at each molecular species with as much atomistic and chemical detail as possible, leading to the rational design of mutable and hierarchical materials. Prediction and understanding of thermodynamic, chemical, and structural properties is crucial, incorporating many of the different interactions (such hydrogen bonding [273] and chemical reactions [317]) present in these systems. However, practical technological application has so far been severely hindered due to lack of understanding of how to link the atomistic scale with material structure and device properties and function. The exploitation of hierarchical interactions provides a novel paradigm to make progress and unpredictability can be eliminated. Such an objective can be attained by the combination of bottom-up, multiscale investigations and top-down synthetic approaches.

As demonstrated, full understanding of a relatively simple two component system - *e.g.* PAA and PAH assembled within PEM films and tubes - is still being assimilated piece by piece. One proven route is to study and investigate the details of a material system across hierarchies (such as the current PEM system). A more daunting challenge is to solve the *inverse* problem - that is to say, given a necessary function, to be able to *engineer* such complexity and to create the necessary material from a library of universal and functional building blocks. The holistic study of materials systems - linking structure, properties, and (most importantly) functionality across scales *in lieu* of specific chemical components - embodies the emerging field of materiomics [71]. Necessitated by the complexity of *de novo* materials, and understanding the

relationships between material structure and function (defined as the *materiome*). No longer is it adequate to assemble material systems without engineered intent. If we can customize materials from the "molecules up", every effort should be made to answer Feynman's query posed in the opening chapter. The potential is limitless.

Appendix A

Sample LAMMPS Scripts

Sample LAMMPS input scripts for full atomistic molecular dynamics simulations implementing the CVFF potential as described in **Chapter 2: Computational Methods**. Not shown due to length are the geometry (coordinate files) that were initially constructed with Materials Studio, and converted to LAMMPS format *via* scripts packaged with LAMMPS. The geometry file explicitly defines all atoms positions, bond pairs, angle triplets, dihedrals and impropers for both PAA and PAH, as well as the partial charge (ionization) associated with each atom.

A.1 Sample LAMMPS Input Script: Temperature Assisted Sampling

LAMMPS input scripts for temperature assisted sampling (TAS) study, as described in **Chapter 2: Computational Methods** and implemented in **Chapter 3: Variation of Molecular Rigidity**. Four cycles shown here for illustrative purposes.

```
# -----------------------------------------------------------
#
# PAA/PAH Atomistic Model with Explicit Waterbox
# Prepared by: S. Cranford
# Laboratory of Atomistic and Molecular Mechanics
# Revised:  November, 2011
#
# Current Model: Single PAH oligomer (50 monomers)
#                100% ionization
#                Explicit solvent
#
# -----------------------------------------------------------
```

```
# Initialization/Neighbor Settings

units           real
neigh_modify    delay 2 every 1
atom_style      full

# Define Force Fields and Interactions (CVFF)

bond_style      harmonic
angle_style     harmonic
dihedral_style  harmonic
improper_style  cvff

pair_style      lj/cut/coul/cut 10.0
pair_modify     mix arithmetic

# Atom Definition (indicate input geometry file)

read_data       pah100.data

# ------------------------------------------------------------

# Water and Polymer Groups

group hold id 266

group backbone id 1 5 13 16 24 27 35 38 46 49 57 60 68
                   71 79 82 90 93 101 104 112 115 123 126 134
                   137 145 148 156 159 167 170 178 181 189 192
                   200 203 211 214 222 225 233 236 244 247 255
                   258 266 269 277 280 288 291 299 302 310 313
                   321 324 332 335 343 346 354 357 365 368 376
                   379 387 390 398 401 409 412 420 423 431 434
                   442 445 453 456 464 467 475 478 486 489 497
                   500 508 511 519 522 530 533 541 544 547

group charges id 11 22 33 44 55 66 77 88 99 110 121 132 143
                   154 165 176 187 198 209 220 231 242 253 264
                   275 286 297 308 319 330 341 352 363 374 385
                   396 407 418 429 440 451 462 473 484 495 506
                   517 528 539 550

# ------------------------------------------------------------
```

```
# Output files

dump          1 all xyz 2000 pah100_wb.xyz
dump          2 backbone xyz 2000 pah100_bb.xyz

dump          3 backbone dcd 2000 pah100_bb.dcd
dump_modify 3 unwrap yes

dump          4 charges dcd 2000 pah100_qq.dcd
dump_modify 4 unwrap yes


# ------------------------------------------------------------
# END OF BASIC SET-UP
# ------------------------------------------------------------

# Optimization/minimization

min_style       cg
minimize        0.0 1.0e-8 10000 1000000
min_modify      dmax 0.2

min_style       sd
minimize        0.0 1.0e-8 10000 1000000

fix        en1 all nvt temp 300. 300. 100.
velocity   all create 300.0 997854

fix        pinbb hold setforce 0.0 0.0 0.0
velocity   hold set 0.0 0.0 0.0 units box

thermo   1000

timestep        0.5

run             200000
min_style       cg
minimize        0.0 1.0e-8 10000 1000000

# ------------------------------------------------------------
# Temperature Cycles for TAS
# ------------------------------------------------------------

#RAMP TEMP 1 ---------------------------------

velocity    all create 300.0 324458
```

```
fix         pinbb hold setforce 0.0 0.0 0.0
velocity    hold set 0.0 0.0 0.0 units box


unfix en1
fix en2 all nvt temp 300. 1500. 100.
run 25000


unfix en2
fix en3 all nvt temp 1500. 300. 100.
run 25000


unfix en3
fix en4 all nvt temp 300. 300. 100.
run 320000


min_style   cg
minimize    0.0 1.0e-8 10000 1000000

#RAMP TEMP 2 -------------------------------

velocity all create 300.0 9989987
fix  pinbb hold setforce 0.0 0.0 0.0
velocity  hold set 0.0 0.0 0.0 units box


unfix en4
fix en5 all nvt temp 300. 1500. 100.
run 25000


unfix en5
fix en6 all nvt temp 1500. 300. 100.
run 25000


unfix en6
fix en7 all nvt temp 300. 300. 200.
run 260000


min_style   cg
minimize    0.0 1.0e-8 10000 1000000

#RAMP TEMP 3 -------------------------------

velocity all create 300.0 9519153
fix  pinbb hold setforce 0.0 0.0 0.0
velocity  hold set 0.0 0.0 0.0 units box
```

```
unfix en7
fix en8 all nvt temp 300. 1500. 100.
run 25000


unfix en8
fix en9 all nvt temp 1500. 300. 100.
run 25000


unfix en9
fix en10 all nvt temp 300. 300. 100.
run 280000


min_style   cg
minimize    0.0 1.0e-8 10000 1000000


#RAMP TEMP 4 ----------------------------------


velocity all create 300.0 79879
fix   pinbb hold setforce 0.0 0.0 0.0
velocity  hold set 0.0 0.0 0.0 units box


unfix en10
fix en11 all nvt temp 300. 1500. 100.
run 25000


unfix en11
fix en12 all nvt temp 1500. 300. 100.
run 25000


unfix   en12
fix en13 all nvt temp 300. 300. 50.
run 320000


min_style   cg
minimize    0.0 1.0e-8 10000 1000000


# ------------------------------------------------------
# END OF SIMULATION
# ------------------------------------------------------
```

A.2 Sample LAMMPS Input Script: Steered Molecular Dynamics

Sample LAMMPS input script for steered molecular dynamics (SMD) study undertaken in **Chapter 4: Rate Dependence and Ionization Effects on Adhesion**. Here, a pulling rate of 10 m s^{-1} is implemented.

```
# ------------------------------------------------------------
#
# PAA/PAH Atomistic Model with Explicit Waterbox
# Prepared by:  S. Cranford
# Laboratory of Atomistic and Molecular Mechanics
# Revised:  April 20th, 2009
#
# Current Model: Fixed PAA oligomer (20 monomers)
# Pulled PAH oligomer (20 monomers)
# Waterbox (~2,000 water molecules)
#
# ------------------------------------------------------------

# Initialization/Neighbor Settings

units           real
atom_style      full
neigh_modify    delay 2 every 1
timestep        0.5

# Define Force Fields and Interactions (CVFF)

bond_style      harmonic
angle_style     harmonic
dihedral_style  harmonic
improper_style  cvff

pair_style      lj/cut/coul/cut 5.0

# Atom Definition (indicate input geometry file)

read_data       polymer_pH43.data
pair_modify     mix arithmetic

# ------------------------------------------------------------
```

```
# Water and Polymer Groups

group waterbox type 1 2
group polymers subtract all waterbox

# Boundary Conditions

group           PAAend1 id 179
group           PAHend1 id 183

fix             PAA1 PAAend1 setforce 0.00 0.00 0.00

velocity        all create 300.00 376847

velocity        PAAend1 set  0.0 0.0 0.0  units box
velocity        PAHend1 set  0.0 0.0 0.0  units box

# ------------------------------------------------------------

# Optimization/minimization

thermo          1000
thermo_style    custom step etotal temp ke pe

min_style       cg
minimize        0.0 1.0e-8 10000 1000000

# ------------------------------------------------------------

# Output

fix             1 all nvt 300. 300. 100.

dump            1 all xyz 2500 all.xyz
dump            2 polymers xyz 2500 polymers.xyz
dump            3 waterbox xyz 2500 waterbox.xyz

# ------------------------------------------------------------
# END OF BASIC SET-UP
# ------------------------------------------------------------

# Short equilibration

fix  visfix all viscous 0.2
```

```
fix          PAH1 PAHend1 setforce 0.00 0.00 0.00

run          5000

# Steered molecular dynamics (SMD)

unfix PAH1

compute disp PAHend1 reduce max x
compute endf PAAend1 reduce sum fx

fix tether PAHend1 smd cvel -2.0 0.001 tether 140 NULL NULL 0

fix force1 PAHend1 ave/time 10 50 500 f_tether[1] f_tether[2]
             f_tether[3] f_tether[4] f_tether[5] f_tether[6]
             c_disp file pahforce.data
fix force2 PAHend1 ave/time 10 50 500 f_tether[1]
             c_disp c_endf file pahforce2.data

run 200000


# ------------------------------------------------------------
# END OF SIMULATION
# ------------------------------------------------------------
```

References

For further details, refer documentation on the LAMMPS website:

- LAMMPS Molecular Dynamics Simulator, http://lammps.sandia.gov/ [257].

Appendix B

Elastic Model Scripts for

Eigenvalue Problem

Matlab script(s) for solution of eigenvalue problem as described by **Chapter 5: Critical Ionization to Couple Polyelectrolytes**.

B.1   Master script

Matlab function to return the desired free vibration frequency with nominal input (polyelectrolyte and cross-link stiffness, mass, number of nodes, and a scaling factor for monomer-to-monomer spacing). Executed in Matlab, returns all eigenvectors (V) and eigenvalues (D).

```
function [V, D] = eigenproblem(d1, d2, y, lf, m1, m2, num)

D1 = d1;    % PAA rigidity
D2 = d2;    % PAH rigidity
T = 1.05;   % Polymer axial stiffness
Y = y;      % Electrostatic stiffness

length_factor = lf; % Monomer spacing factor

M1 = m1;    % Linear mass, PAA
M2 = m2;    % Linear mass, PAH

n = num;    % Number of nodes PER CHAIN (crosslinks + 2)

[KFULL] = beam_elastic_matrix(D1, D2, T, Y, n, length_factor);
K = KFULL;
```

```
[MFULL] = beam_mass_matrix(M1, M2, n, length_factor);
M = MFULL;

[V,D] = eig(K,M);    % Solving the eigenvalue problem;
max(D(:, 5))         % Extract eigenvalue for desired mode
```

B.2 Global Stiffness Matrix Construction, Beam and Spring Elements

Function called to construct global stiffness matrix of elastic model, **K**, including two polyelectrolytes and coupling cross-links.

```
function [KFULL] = beam_elastic_matrix(D1, D2, T, Y, n, s)

length = 51*2.8*s;
kspr = Y;

L = length/(n-1);
elements = 2*(n-1);

beam_elements = n-1;
BK1 = zeros(3*n, 3*n);
BK2 = zeros(3*n, 3*n);

k_single1 = K_2D_single(D1, T, L);

j = 1;
for i=1:beam_elements
    BK1(j:j+5, j:j+5) = BK1(j:j+5, j:j+5) + k_single1;
    j = j+3;
end

k_single2 = K_2D_single(D2, T, L);

j = 1;
for i=1:beam_elements
    BK2(j:j+5, j:j+5) = BK2(j:j+5, j:j+5) + k_single2;
    j = j+3;
end

% Assemble total stiffness

K = zeros(2*3*n, 2*3*n);
```

```
K(1:3*n, 1:3*n) = BK1;
K(1+3*n:2*3*n, 1+3*n:2*3*n) = BK2;

% Add cross-links

kspring = kspr;

s1 = zeros(6,6);
s1(2,2) = kspring;
s1_add = zeros(3*n, 3*n);

s2 = zeros(6,6);
s2(2,2) = -kspring;
s2_add = zeros(3*n, 3*n);

j = 4;
for i=2:beam_elements
    s1_add(j:j+5, j:j+5) = s1_add(j:j+5, j:j+5) + s1;
    s2_add(j:j+5, j:j+5) = s2_add(j:j+5, j:j+5) + s2;
    j = j+3;
end

SK = zeros(2*3*n, 2*3*n);
SK(1:3*n, 1:3*n) = s1_add;
SK(1+3*n:2*3*n, 1+3*n:2*3*n) = s1_add;
SK(1+3*n:2*3*n, 1:3*n) = s2_add;
SK(1:3*n, 1+3*n:2*3*n) = s2_add;

KFULL = K+SK;
```

B.2.1   Beam element, local stiffness matrix

Function called to construct local stiffness matrix (6×6) of each beam element; assumes Euler-Bernoulli beam behavior.

```
function [k_single] = K_2D_single(D, T, L)

% Define components of beam single element

k_single = zeros(6, 6);

kA = T;
kEI = D;

k_single(1,1) = kA/L;
```

```
k_single(1,2) = 0;
k_single(1,3) = 0;
k_single(1,4) = -kA/L;
k_single(1,5) = 0;
k_single(1,6) = 0;
k_single(2,1) = 0;
k_single(2,2) = 12*kEI/(L*L*L);
k_single(2,3) = 6*kEI/(L*L);
k_single(2,4) = 0;
k_single(2,5) = -12*kEI/(L*L*L);
k_single(2,6) = 6*kEI/(L*L);
k_single(3,1) = 0;
k_single(3,2) = 6*kEI/(L*L);
k_single(3,3) = 4*kEI/L;
k_single(3,4) = 0;
k_single(3,5) = -6*kEI/(L*L);
k_single(3,6) = 2*kEI/L;
k_single(4,1) = -kA/L;
k_single(4,2) = 0;
k_single(4,3) = 0;
k_single(4,4) = kA/L;
k_single(4,5) = 0;
k_single(4,6) = 0;
k_single(5,1) = 0;
k_single(5,2) = -12*kEI/(L*L*L);
k_single(5,3) = -6*kEI/(L*L);
k_single(5,4) = 0;
k_single(5,5) = 12*kEI/(L*L*L);
k_single(5,6) = -6*kEI/(L*L);
k_single(6,1) = 0;
k_single(6,2) = 6*kEI/(L*L);
k_single(6,3) = 2*kEI/L;
k_single(6,4) = 0;
k_single(6,5) = -6*kEI/(L*L);
k_single(6,6) = 4*kEI/L;

end
```

B.3   Global Consistent Mass Matrix Construction

Function called to construct consistent mass matrix of elastic model, **M**, including two polyelectrolytes and coupling cross-links. Mass lumped to nodes, accounting for both linear and rotational inertia.

```
function [MFULL] = beam_mass_matrix(M1, M2, n, s)
```

```
length = 51*2.8*s;

L = length/(n-1);

elements = 2*(n-1);

beam_elements = n-1;

BM1 = zeros(3*n, 3*n);
BM2 = zeros(3*n, 3*n);

m_single1 = M_2D_single(M1, L);

j = 1;
for i=1:beam_elements
    BM1(j:j+5, j:j+5) = BM1(j:j+5, j:j+5) + m_single1;
    j = j+3;
end

m_single2 = M_2D_single(M2, L);

j = 1;
for i=1:beam_elements
    BM2(j:j+5, j:j+5) = BM2(j:j+5, j:j+5) + m_single2;
    j = j+3;
end

% Assemble total stiffness

M = zeros(2*3*n, 2*3*n);
M(1:3*n, 1:3*n) = BM1;
M(1+3*n:2*3*n, 1+3*n:2*3*n) = BM2;

MFULL = M;
```

B.3.1   Beam element, consistent mass matrix

Function called to construct local consistent mass matrix (6×6) of each beam element; assumes Euler-Bernoulli beam behavior.

```
function [m_single] = M_2D_single(M, L)

% Define components of beam single element
```

```
m_single = zeros(6, 6);

factor = M/420;

m_single(1,1) = 140;
m_single(1,2) = 0;
m_single(1,3) = 0;
m_single(1,4) = 70;
m_single(1,5) = 0;
m_single(1,6) = 0;
m_single(2,1) = 0;
m_single(2,2) = 156;
m_single(2,3) = 22*L;
m_single(2,4) = 0;
m_single(2,5) = 54;
m_single(2,6) = -13*L;
m_single(3,1) = 0;
m_single(3,2) = 22*L;
m_single(3,3) = 4*L*L;
m_single(3,4) = 0;
m_single(3,5) = 13*L;
m_single(3,6) = -3*L*L;
m_single(4,1) = 70;
m_single(4,2) = 0;
m_single(4,3) = 0;
m_single(4,4) = 40;
m_single(4,5) = 0;
m_single(4,6) = 0;
m_single(5,1) = 0;
m_single(5,2) = 54;
m_single(5,3) = 13*L;
m_single(5,4) = 0;
m_single(5,5) = 156;
m_single(5,6) = -22*L;
m_single(6,1) = 0;
m_single(6,2) = -13*L;
m_single(6,3) = -3*L*L;
m_single(6,4) = 0;
m_single(6,5) = -22*L;
m_single(6,6) = 4*L*L;

end
```

References

For further details, refer to the following texts:

- *Dynamics of structures: Theory and applications to earthquake engineering* [63].

- *Matrix structural analysis* [213].

- *Finite element procedures* [24].

Appendix C

Coarse-Grain Scripts

Scripts for coarse-grain PEM microtube study, including geometry creation, modified Hertz potential, and lateral indentation *via* LAMMPS, as described in **Chapter 2: Computational Methods** and **Chapter 6: Beyond Full Atomistic Characterization**.

C.1 Microtube model generation

Python script used to construct a LAMMPS geometry file for a vertically aligned array of microtubes. Required parameters include tube height, particle spacing, tube spacing, and array dimensions $(n \times m)$. Generated data file includes all information for connectivity, including bond pairs and angle triples.

```
import os,sys,string
import time

from math import *
from Numeric import *

# Declare some variables

total = []
intro = []
masses = []
atoms = []
bonds = []
angles = []

cf=0
```

```
#  Define the masses of all types
mass = [2000]

# Define the unit cell

NL=121

cxx=1.
czz=18000.
cyy=18000.

cellx=cxx
celly=cyy
cellz=czz

nx=1
ny=21
nz=36

################ UNIT CELL definition

natypes = 1
nbondtypes = 1
nangletypes = 1
ndihtypes = 0
nimprtypes = 0


# First coordinates
uc_x = arange(0., NL*1000., 1000.0)
uc_y = zeros(NL)
uc_z = zeros(NL)
print uc_x
print uc_y
print uc_z

uc_typ=zeros(NL)
uc_bonds=zeros ( (NL-1)*2)
uc_btyp=zeros ( (NL-1)*2)
uc_angles=zeros( (NL-2)*3)
uc_antyp=zeros( (NL-2)*3 )

for ii in range (NL):
    uc_typ[ii]=ii%natypes+1
```

```python
uc_mol= ones (NL)
print uc_mol
for ii in range(len(uc_x)):

uc_y[ii]=uc_y[ii]+celly
uc_z[ii]=uc_z[ii]+cellz

molsperuc =2

for ii in range ( (NL-1)):
    uc_bonds[2*ii]=ii+1+1
    uc_bonds[2*ii+1]=ii+1
    uc_btyp[2*ii+1]=1
    uc_btyp[2*ii]=1

for ii in range ( (NL-2)):
    uc_angles[3*ii]=ii+2+1
    uc_angles[3*ii+1]=ii+1+1
    uc_angles[3*ii+2]=ii+0+1
    uc_antyp[3*ii]=1
    uc_antyp[3*ii+1]=1
    uc_antyp[3*ii+2]=1

ndihedrals=0
natoms =0
nbonds =0
nangles =0
nimpropers =0

atoms.append ("Atoms\n\n")
bonds.append ("Bonds\n\n")
angles.append ("Angles\n\n")

tcount = 0

for ii in range(nx):
for jj in range(ny):

tube_type_y = math.pow(-1,jj)
if (tube_type_y < 0.0):
    tube_type_shift = 1
if (tube_type_y > 0.0):
    tube_type_shift = 0

for ll in range(nz):
```

```python
        tube_type = tube_type_shift+2+math.pow(-1,ll)


    # Add all atoms
      for kk in range (len(uc_x)):

         Xpos= uc_x[kk]
         atoms.append ("%d %d %d %f %f %f\n"
                         % (kk+tcount*(len(uc_x) )+1,
                         uc_mol[kk]+tcount*(molsperuc ),
                         tube_type, uc_x[kk]+cellx*ii,
                         (uc_y[kk]+celly*jj)-cyy ,
                         (uc_z[kk]+cellz*ll)-czz))
         natoms=natoms+1


    # Add all bonds
       for kk in range (len(uc_bonds)/2):

         iop9=  (tcount*(len(uc_x)))
         bonds.append ("%d %d %d %d \n"
                         % (kk+tcount*(len(uc_bonds)/2 )+1,
                         uc_btyp[kk],
                         uc_bonds [kk*2]+ iop9,
                         uc_bonds[kk*2+1]+iop9 ))
         nbonds=nbonds+1



    # Add all angles
       for kk in range (len(uc_angles)/3):

         iop9=  (tcount*(len(uc_x)))
         angles.append ("%d %d %d %d %d \n"
                         % (kk+tcount*(len(uc_angles)/3 )+1,
                         uc_antyp[kk],
                         uc_angles [kk*3]+ iop9,
                         uc_angles[kk*3+1]+ iop9,
                         uc_angles[kk*3+2]+ iop9))
         nangles=nangles+1

    tcount=tcount+1

atoms.append ("\n");
bonds.append ("\n");
angles.append ("\n");
```

```python
intro.append("LAMMPS data file\n\n")
intro.append("%d atoms\n" % natoms)
intro.append("%d bonds\n" % nbonds)
intro.append("%d angles\n" % nangles)
intro.append("%d dihedrals\n" % ndihedrals)
intro.append("%d impropers\n\n" % nimpropers)

intro.append("%d atom types\n" % natypes)
intro.append("%d bond types\n" % nbondtypes)
intro.append("%d angle types\n" % nangletypes)
intro.append("%d dihedral types\n" % ndihtypes )
intro.append("%d improper types\n\n" % nimprtypes )

intro.append("%f %f xlo xhi\n" % (-1000, 10.*NL*3))
intro.append("%f %f ylo yhi\n" % (-0, cyy*(ny+1)))
intro.append("%f %f zlo zhi\n\n" % (-0, czz*(nz+1)))

intro.append("Masses\n\n")

for ii in range(len( mass )):

intro.append("%d %f \n" % (ii+1, mass[ii]))

intro.append ("\n");

total = intro+atoms+bonds+angles

newfile ="pemarray.data"

f = open(newfile,'w')
f.writelines(total)
f.close()

print "DONE preparing PEM microtube input file for LAMMPS"
print "**************************************************"
```

C.2 Modified LAMMPS code for Hertz Potential

Modified LAMMPS source code to implement Hertz contact potential as described in **Chapter 2: Computational Methods.** Partial C++ file shown of "`pair_morse.cpp`", where the packaged Morse potential was edited. The Morse potential was used as it uses the same number of input parameters, and thus only the calculation of force was required to be modified.

```
/**********************************************************************

EDITED MORSE POTENTIAL CODE FOR IMPLEMENTATION OF "HERTZ CONTACT"
POTENTIAL FOR MESO-SCALE CONTACT SIMULATIONS

where F = B*sqrt(r0)*(r-ro)^(3/2)

Using the Morse potential inputs where:

D = 1 (not used)
alpha  = B*sqrt(r0) = Contact Parameter in (kcal/mol/)A^3
r0 = Equilibrium spacing in A
rcut = r0 (only contact considered)

NOTE:   NOT EDITED TO RETURN PAIR POTENTIAL ENERGY

**********************************************************************/


void PairMorse::compute(int eflag, int vflag)
{
int i,j,ii,jj,inum,jnum,itype,jtype;
double xtmp,ytmp,ztmp,delx,dely,delz,evdwl,fpair;
double rsq,r,dr,dexp,factor_lj;
int *ilist,*jlist,*numneigh,**firstneigh;

/**********************************************************************/

// NEW VARIABLE(S)

double dr_pow; // dr_pow = (r-ro)^(3/2)

/**********************************************************************/

evdwl = 0.0;
if (eflag || vflag) ev_setup(eflag,vflag);
else evflag = vflag_fdotr = 0;

double **x = atom->x;
double **f = atom->f;
int *type = atom->type;
int nlocal = atom->nlocal;
int nall = nlocal + atom->nghost;
double *special_lj = force->special_lj;
```

250

```
int newton_pair = force->newton_pair;

inum = list->inum;
ilist = list->ilist;
numneigh = list->numneigh;
firstneigh = list->firstneigh;

// loop over neighbors of my atoms

for (ii = 0; ii < inum; ii++) {
    i = ilist[ii];
    xtmp = x[i][0];
    ytmp = x[i][1];
    ztmp = x[i][2];
    itype = type[i];
    jlist = firstneigh[i];
    jnum = numneigh[i];

    for (jj = 0; jj < jnum; jj++) {
        j = jlist[jj];

    if (j < nall) factor_lj = 1.0;
    else {
   factor_lj = special_lj[j/nall];
   j %= nall;
    }

    delx = xtmp - x[j][0];
    dely = ytmp - x[j][1];
    delz = ztmp - x[j][2];
    rsq = delx*delx + dely*dely + delz*delz;
    jtype = type[j];

/*****************************************************************/

// START OF EDITS

    if (rsq < cutsq[itype][jtype]) {

        r = sqrt(rsq);
        dr = fabs(r - r0[itype][jtype]);
        dr_pow = sqrt(dr*dr*dr);

        fpair = factor_lj*morse1[itype][jtype] * dr_pow / r;
```

```
f[i][0] += delx*fpair;
f[i][1] += dely*fpair;
f[i][2] += delz*fpair;
if (newton_pair || j < nlocal) {
    f[j][0] -= delx*fpair;
    f[j][1] -= dely*fpair;
    f[j][2] -= delz*fpair;
}

// END OF EDITS


/***********************************************************************/
```

C.3 Sample LAMMPS Input Script: Lateral Indentation

Sample LAMMPS input script for lateral indentation (simulated lateral force spectroscopy) study undertaken in **Chapter 6: Beyond Full Atomistic Characterization**. Here, indentation was to a depth of 0.3 μm.

```
# ------------------------------------------------------------
#
# PEM Array Mesoscale Model
# Prepared by: S. Cranford
# Laboratorty of Atomistic and Molecular Mechanics
# Date: Feb. 16, 2011
#
# Current Model: Simulate lateral spectroscopy PEMNT
#
# ------------------------------------------------------------

# Initialization

units real
atom_style angle
timestep 50.0

boundary  f p f

# Atom Definition (indicate input geometry file)

read_data pemarray.data
```

```
# Neighbor Settings

neighbor 1000 bin
neigh_modify every 100 delay 100

# Force Fields and Interactions

bond_style   harmonic
bond_coeff   1 76.28 1000.00

angle_style harmonic
angle_coeff 1 2576000000. 180.0

pair_style hybrid morse 11900. lj/cut 1000.

pair_coeff  1 1 lj/cut 0.0 890.9
pair_coeff  2 2 lj/cut 0.0 890.9
pair_coeff  3 3 lj/cut 0.0 890.9
pair_coeff  4 4 lj/cut 0.0 890.9
pair_coeff 1 2*4 morse 0.0 0.107 11900.  11900.
pair_coeff 2 3*4 morse 0.0 0.107 11900.  11900.
pair_coeff 3 4*4 morse 0.0 0.107 11900.  11900.

special_bonds  lj 0.0 0.0 0.0

# Basic Output

dump xyzDump all xyz 10000 pemarray_lat3_r.xyz

thermo       1000

# Set Ensemble

fix      1 all nvt 300. 300. 100.

region   1 block INF 5500. INF  INF INF INF  units box

group    fixx region 1
group    mobile subtract all fixx

# Initial Conditions

velocity         all create 300.00 376847

velocity         fixx set  0.0000  0.0 0.0  units box
```

```
fix             2 fixx setforce 0.00 0.00 0.00

# --------------------------------------------------------
# END OF BASIC SET-UP
# --------------------------------------------------------

# Equilibrium/Minimization

fix damp mobile viscous 10000.0
run 10000

# Lateral Indentation

fix ind1 mobile indent 1000.0 sphere 345000. 180000. -10000.
            225000. vel -0.0002 0.0 0.0 units box
fix      forceout1 mobile ave/time 1 100 1000 f_ind1 f_ind1[1]
            f_ind1[2] f_ind1[3] file forces1_lat3_r.indent
run 300000

unfix    ind1
unfix    forceout1
fix      ind2 mobile indent 1000.0 sphere 342000. 180000. -10000.
            225000. vel 0.0 0.0 0.0 units box
fix      forceout2 mobile ave/time 1 100 1000 f_ind2 f_ind2[1]
            f_ind2[2] f_ind2[3] file forces2_lat3_r.indent
run 25000

unfix ind2
unfix forceout2
fix ind3 mobile indent 100000.0 sphere 342000. 180000. -10000.
            225000. vel 0.0 0.0 0.0010 units box
fix  forceout3 mobile ave/time 1 100 1000 f_ind3 f_ind3[1]
            f_ind3[2] f_ind3[3] file forces3_lat3_r.indent
run 10000000

# --------------------------------------------------------
# END OF SIMULATION
# --------------------------------------------------------
```

References

For further details, refer documentation on the LAMMPS website:

- LAMMPS Molecular Dynamics Simulator, http://lammps.sandia.gov/ [257].

Bibliography

[1] T. Ackbarow and M. J. Buehler. Alpha-helical protein domains unify strength and robustness through hierarchical nanostructures. *Nanotechnology*, 20(7), 2009.

[2] T. Ackbarow, X. Chen, S. Keten, and M. Buehler. Hierarchies, multiple energy barriers, and robustness govern the fracture mechanics of alpha-helical and beta-sheet protein domains. *Proceedings of the National Academy of Sciences of the United States of America*, 104(42):16410–16415, 2007.

[3] T. Ackbarow, S. Keten, and M. Buehler. A multi-timescale strength model of alpha helical protein domains. *Journal of Physics: Condensed Matter*, 21:035111, 2009.

[4] J. Aizenberg and P. Fratzl. Biological and biomimetic materials. *Advanced Materials*, 21(4):387–388, 2009.

[5] B. J. Alder and T. E. Wainwright. Phase transition for a hard sphere system. *Journal of Chemical Physics*, 27(5):1208–1209, 1957.

[6] B. J. Alder and T. E. Wainwright. Studies in molecular dynamics .1. general method. *Journal of Chemical Physics*, 31(2):459–466, 1959.

[7] B. J. Alder and T. E. Wainwright. Studies in molecular dynamics .2. behavior of a small number of elastic spheres. *Journal of Chemical Physics*, 33(5):1439–1451, 1960.

[8] U. Alon. Simplicity in biology. *Nature*, 446(7135):497–497, 2007.

[9] G. Ariel and D. Andelman. Persistence length of a strongly charged rodlike polyelectrolyte in the presence of salt. *Physical Review E*, 67(1), 2003.

[10] G. Armstrong and M. Buggy. Hydrogen-bonded supramolecular polymers: A literature review. *Journal of Materials Science*, 40(3):547–559, 2005.

[11] E. M. Arruda and M. C. Boyce. A 3-dimensional constitutive model for the large stretch behavior of rubber elastic-materials. *Journal of the Mechanics and Physics of Solids*, 41(2):389–412, 1993.

[12] M. Ashby. *Materials Selection in Mechanical Design, 4th Edition*. Butterworth-Heinemann, Oxford, 2011.

[13] A. Atilgan, S. Durell, R. Jernigan, M. Demirel, O. Keskin, and I. Bahar. Anisotropy of fluctuation dynamics of proteins with an elastic network model. *Biophysical Journal*, 80:505–515, 2001.

[14] S. A. Baeurle, M. Charlot, and E. A. Nogovitsin. Grand canonical investigations of prototypical polyelectrolyte models beyond the mean field level of approximation. *Physical Review E*, 75(1), 2007.

[15] S. A. Baeurle and E. A. Nogovitsin. Challenging scaling laws of flexible polyelectrolyte solutions with effective renormalization concepts. *Polymer*, 48(16):4883–4899, 2007.

[16] S. A. Baeurle, T. Usami, and A. A. Gusev. A new multiscale modeling approach for the prediction of mechanical properties of polymer-based nanomaterials. *Polymer*, 47(26):8604–8617, 2006.

[17] F. Baftizadeh, X. Biarnes, F. Pietrucci, F. Affinito, and A. Laio. Multidimensional view of amyloid fibril nucleation in atomistic detail. *Journal of the American Chemical Society*, 134(8):3886–3894, 2012.

[18] I. Bahar, A. Atilgan, and B. Erman. Direct evaluation of thermal fluctuations in proteins using a single-parameter harmonic potential. *Folding and Design*, 2:173–181, 1997.

[19] I. Bahar and R. Jernigan. Inter-residue potentials in globular proteins and the dominance of highly specific hydrophilic interactions at close separation. *Journal of Molecular Biology*, 266(1):195–214, 1997.

[20] I. Bahar and A. Rader. Coarse-grain normal model analysis in structural biology. *Current Opinion in Structural Biology*, 15:586–592, 2005.

[21] X. Banquy, E. Charrault, and S. Giasson. Normal and lateral interactions between thermosensitive nanoparticle monolayers in water. *Journal of Physical Chemistry B*, 114(30):9721–9728, 2010.

[22] N. Barkai and S. Leibler. Robustness in simple biochemical networks. *Nature*, 387(6636):913–917, 1997.

[23] J. L. Barrat and J. F. Joanny. Persistence length of polyelectrolyte chains. *Europhysics Letters*, 24(5):333–338, 1993.

[24] K.-J. Bathe. *Finite element procedures*. Prentice Hall, Englewood Cliffs, N.J., 1996.

[25] M. Bathe. A finite element framework for computation of protein normal modes and mechanical response. *Proteins: Structure, Functions, and Bioinformatics*, 70(4):1595–1609, 2007.

[26] M. Bathe, G. C. Rutledge, A. J. Grodzinsky, and B. Tidor. A coarse-grained molecular model for glycosaminoglycans: Application to chondroitin, chondroitin sulfate, and hyaluronic acid. *Biophysical Journal*, 88(6):3870–3887, 2005.

[27] M. Beer, M. Schmidt, and M. Muthukumar. The electrostatic expansion of linear polyelectrolytes: Effects of gegenions, co-ions, and hydrophobicity. *Macromolecules*, 30(26):8375–8385, 1997.

[28] G. Bell. Models for the specific adhesion of cells to cells. *Science*, 200(4342):618–627, 1978.

[29] M. C. Berg, L. Zhai, R. E. Cohen, and M. F. Rubner. Controlled drug release from porous polyelectrolyte multilayers. *Biomacromolecules*, 7(1):357–364, 2006.

[30] R. B. Best, Y. G. Chen, and G. Hummer. Slow protein conformational dynamics from multiple experimental structures: The helix/sheet transition of arc repressor. *Structure*, 13(12):1755–1763, 2005.

[31] R. Bhowmik, K. Katti, and D. Katti. Molecular dynamics simulation of hydroxyapatite-polyacrylic acid interfaces. *Polymer*, 48:664–674, 2007.

[32] W. H. Binder and R. Sachsenhofer. 'click' chemistry in polymer and materials science. *Macromolecular Rapid Communications*, 28(1):15–54, 2007.

[33] M. A. Biot. Theory of propagation of elastic waves in a fluid-saturated porous solid .1. low-frequency range. *Journal of the Acoustical Society of America*, 28(2):168–178, 1956.

[34] A. Bobet, A. Fakhimi, S. Johnson, J. Morris, F. Tonon, and M. R. Yeung. Numerical models in discontinuous media: Review of advances for rock mechanics applications. *Journal of Geotechnical and Geoenvironmental Engineering*, 135(11):1547–1561, 2009.

[35] J. Boisvert, A. Malgat, I. Pochard, and C. Daneault. Influence of the counterion on the effective charge of polyacrylic acid in dilute condition. *Polymer*, 43:141–148, 2002.

[36] M. Bonomi and M. Parrinello. Enhanced sampling in the well-tempered ensemble. *Physical Review Letters*, 104(19):190601, 2010.

[37] V. Y. Borue and I. Y. Erukhimovich. A statistical-theory of globular polyelectrolyte complexes. *Macromolecules*, 23(15):3625–3632, 1990.

[38] C. Boura, S. Muller, D. Vautier, D. Dumas, P. Schaaf, J. Voegel, J. Stoltz, and P. Menu. Endothelial cell - interactions with polyelectrolyte multilayer films. *Biomaterials*, 26(22):4568–4575, 2005.

[39] G. H. Bratzel, S. W. Cranford, H. Espinosa, and M. J. Buehler. Bioinspired non-covalently crosslinked "fuzzy" carbon nanotube bundles with superior toughness and strength. *Journal of Materials Chemistry*, 20(46):10465–10474, 2010.

[40] D. W. Brenner. The art and science of an analytic potential. *Physica Status Solidi B-Basic Research*, 217(1):23–40, 2000.

[41] L. Bromberg, M. Temchenko, and T. Hatton. Smart microgel studies. polelectrolyte and drug-absorbing properties of microgels from polyether-modified poly(acrylic acid). *Langmuir*, 19(21):8675–8684, 2003.

[42] B. Brooks, R. Bruccoleri, B. Olafson, D. States, S. Swaminathan, and M. Karplus. Charmm: A program for macromolecular energy, minimization, and dynamics calculations. *Journal of Computational Chemistry*, 4(2):187–217, 1983.

[43] C. B. Bucur, Z. Sui, and J. B. Schlenoff. Ideal mixing in polyelectrolyte complexes and multilayers: Entropy driven assembly. *Journal of the American Chemical Society*, 128(42):13690–13691, 2006.

[44] M. Buehler. Mesoscale modeling of mechanics of carbon nanotubes: self-assembly, self-folding, and fracture. *Journal of Materials Research*, 21(11):2855–2869, 2006.

[45] M. Buehler. Strength in numbers. *Nature Nanotechnology*, 5(3):172–174, 2010.

[46] M. Buehler and Y. Yung. Deformation and failure of protein materials in physiologically extreme conditions and disease. *Nature Materials*, 8(3):175–188, 2009.

[47] M. J. Buehler. Tu(r)ning weakness to strength. *Nano Today*, 5(5):379–383, 2010.

[48] S. Burke and C. Barrett. Acid-base equilibria of weak polyelectrolytes in multilayer thin films. *Langmuir*, 19(8):3297–3303, 2003.

[49] K. Buscher, K. Graf, H. Ahrens, and C. Helm. Influence of adsorption conditions on the structure of polyelectrolyte multilayers. *Macromolecules*, 18(9):3585–3591, 2002.

[50] C. Calderon, L. Janosi, and I. Kosztin. Using stochastic models calibrated from nanosecond nonequilibrium simulations to approximate mesoscale information. *Journal of Chemical Physics*, 130:144908, 2009.

[51] J. M. Y. Carrillo and A. V. Dobrynin. Polyelectrolytes in salt solutions: Molecular dynamics simulations. *Macromolecules*, 44(14):5798–5816, 2011.

[52] M. Castelnovo and J. F. Joanny. Formation of polyelectrolyte multilayers. *Langmuir*, 16(19):7524–7532, 2000.

[53] M. Castelnovo and J. F. Joanny. Complexation between oppositely charged polyelectrolytes: Beyond the random phase approximation. *European Physical Journal E*, 6(5):377–386, 2001.

[54] W. Chan, D. Elmore, E. Farkas, A. Higton, B. Penke, I. Sovago, G. Toth, and G. Varadi. *Amino Acids, Peptides and Proteins*, volume 35. The Royal Society of Chemistry, Cambridge, UK, 2006.

[55] D. P. Chang, J. E. Dolbow, and S. Zauscher. Switchable friction of stimulus-responsive hydrogels. *Langmuir*, 23(1):250–257, 2007.

[56] J. Che, J. Dzubiella, B. Li, and J. A. McCammon. Electrostatic free energy and its variations in implicit solvent models. *Journal of Physical Chemistry B*, 112(10):3058–3069, 2008.

[57] J. H. Chen, C. L. Brooks, and J. Khandogin. Recent advances in implicit solvent-based methods for biomolecular simulations. *Current Opinion in Structural Biology*, 18(2):140–148, 2008.

[58] X. X. Chen, M. A. Dam, K. Ono, A. Mal, H. B. Shen, S. R. Nutt, K. Sheran, and F. Wudl. A thermally re-mendable cross-linked polymeric material. *Science*, 295(5560):1698–1702, 2002.

[59] K.-K. Chia, M. Rubner, and R. Cohen. ph-responsive reversibly swellable nanotube arrays. *Langmuir*, 24(25):1404414052, 2009.

[60] P. A. Chiarelli, M. S. Johal, D. J. Holmes, J. L. Casson, J. M. Robinson, and H. L. Wang. Polyelectrolyte spin-assembly. *Langmuir*, 18(1):168–173, 2002.

[61] J. Choi and M. Rubner. Selective adsorption of amphiphilic block copolymers on weak polyelectrolyte multilayers. *Journal of Macromolecular Science, Part A*, 38(12):1191–1206, 2001.

[62] J. Choi and M. Rubner. Influence of the degree of ionization on weak polyelectrolyte multilayer assembly. *Macromolecules*, 38:116–124, 2005.

[63] A. K. Chopra. *Dynamics of structures : theory and applications to earthquake engineering*. Prentice Hall, Upper Saddle River, N.J., 4th edition, 2012.

[64] P. Y. Chou and G. D. Fasman. Prediction of protein conformation. *Biochemistry*, 13(2):222–245, 1974.

[65] A. Chung and M. Rubner. Methods of loading and releasing low molecular weight cationic molecules in weak polyelectrolyte multilayer films. *Langmuir*, 18:1176–1183, 2002.

[66] S. Clark and P. Hammond. The role of secondary interactions in selective electrostatic multilayer deposition. *Langmuir*, 16:10206–10214, 2000.

[67] O. C. Compton, S. W. Cranford, K. W. Putz, Z. An, L. C. Brinson, M. J. Buehler, and S. T. Nguyen. Tuning the mechanical properties of graphene oxide paper and its associated polymer nanocomposites by controlling cooperative intersheet hydrogen bonding. *ACS Nano*, 6(3):2008–2019, 2011.

[68] W. Cornell, P. Cieplak, C. Bayly, and I. Gould. A second generation force field for the simulation of proteins, nucleic acids, and organic molecules. *Journal of the American Chemical Society*, 117:5179–5197, 1995.

[69] S. Cranford and M. Buehler. Mechanomutable carbon nanotube arrays. *International Journal of Materials and Structural Integrity*, 3(2/3):161–178, 2009.

[70] S. Cranford and M. Buehler. Materiomics: biological protein materials, from nano to macro. *Nanotechnology, Science and Applications*, 3(1):127–148, 2010.

[71] S. Cranford and M. Buehler. *Biomateriomics*. Springer, London, England, 2012.

[72] S. Cranford and M. J. Buehler. Twisted and coiled ultralong multilayer graphene ribbons. *Modelling and Simulation in Materials Science and Engineering*, 19(5), 2011.

[73] S. Cranford, J. de Boer, C. van Blitterswijk, and M. Buehler. Materiomics: an -omics approach to biomaterials research. *Advanced Materials*, in submission, 2012.

[74] S. Cranford, L. Han, C. Ortiz, and M. Buehler. Mutable polyelectrolyte tube arrays: Mesoscale modeling and lateral force microscopy. *in submission*, 2012.

[75] S. Cranford, D. Sen, and M. J. Buehler. Meso-origami: Folding multilayer graphene sheets. *Applied Physics Letters*, 95(12), 2009.

[76] S. Cranford, H. M. Yao, C. Ortiz, and M. J. Buehler. A single degree of freedom 'lollipop' model for carbon nanotube bundle formation. *Journal of the Mechanics and Physics of Solids*, 58(3):409–427, 2010.

[77] S. W. Cranford and M. J. Buehler. In silico assembly and nanomechanical characterization of carbon nanotube buckypaper. *Nanotechnology*, 21(26), 2010.

[78] S. W. Cranford and M. J. Buehler. *Multiscale Modeling: From Atoms to Devices*, chapter 2. Coarse-graining parameterization and multi-scale simulation of hierarchical systems part I: theory and model formulation. Taylor and Francis, 2010.

[79] S. W. Cranford and M. J. Buehler. *Multiscale Modeling: From Atoms to Devices*, chapter 3. Coarse-graining parameterization and multi-scale simulation of hierarchical systems part II: case studies. Taylor and Francis, 2010.

[80] S. W. Cranford and M. J. Buehler. Shaky foundations of hierarchical biological materials. *Nano Today*, 6(4):332–338, 2011.

[81] S. W. Cranford, C. Ortiz, and M. J. Buehler. Mechanomutable properties of a paa/pah polyelectrolyte complex: rate dependence and ionization effects on tunable adhesion strength. *Soft Matter*, 6(17):4175–4188, 2010.

[82] M. E. Csete and J. C. Doyle. Reverse engineering of biological complexity. *Science*, 295(5560):1664–1669, 2002.

[83] P. A. Cundall and O. D. L. Strack. Discrete numerical-model for granular assemblies. *Geotechnique*, 29(1):47–65, 1979.

[84] M. S. Daw and M. I. Baskes. Embedded-atom method - derivation and application to impurities, surfaces, and other defects in metals. *Physical Review B*, 29(12):6443–6453, 1984.

[85] S. De Koker, L. J. De Cock, P. Rivera-Gil, W. J. Parak, R. A. Velty, C. Vervaet, J. P. Remon, J. Grooten, and B. G. De Geest. Polymeric multilayer capsules delivering biotherapeutics. *Advanced Drug Delivery Reviews*, 63(9):748–761, 2011.

[86] M. L. De Temmerman, J. Demeester, S. De Smedt, and I. Rejman. Tailoring layer-by-layer capsules for biomedical applications. *Nanomedicine*, 7(5):771–788, 2012.

[87] G. Decher. Fuzzy nanoassemblies: Toward layered polymeric multicomposites. *Science*, 277:1232–1237, 1997.

[88] G. Decher, J. D. Hong, and J. Schmitt. Buildup of ultrathin multilayer films by a self-assembly process. 3. consecutively alternating adsorption of anionic and cationic polyelectrolytes on charged surfaces. *Thin Solid Films*, 210(1-2):831–835, 1992.

[89] G. Decher and J. Schlenoff. *Multilayer thin films: sequential assembly of nanocomposite materials*. Wiley-VCH, Weinheim, Germany, 2003.

[90] A. Dedinaite, E. Thormann, G. Olanya, P. M. Claesson, B. Nystrom, A. L. Kjoniksen, and K. Z. Zhu. Friction in aqueous media tuned by temperature-responsive polymer layers. *Soft Matter*, 6(11):2489–2498, 2010.

[91] M. Delarue and Y. H. Sanejouand. Simplified normal mode analysis of conformational transitions in dna-dependent polymerases: the elastic network model. *Journal of Molecular Biology*, 320(5):1011–1024, 2002.

[92] H. Dietz and M. Rief. Elastic bond network model for protein unfolding mechanics. *Physical Review Letters*, 100:098101, 2008.

261

[93] E. Dintwa, E. Tijskens, and H. Ramon. On the accuracy of the hertz model to describe the normal contact of soft elastic spheres. *Granular Matter*, 10(3):209–221, 2008.

[94] K. M. Dipple, J. K. Phelan, and E. R. B. McCabe. Consequences of complexity within biological networks: Robustness and health, or vulnerability and disease. *Molecular Genetics and Metabolism*, 74(1-2):45–50, 2001.

[95] D. E. Discher, P. Janmey, and Y. L. Wang. Tissue cells feel and respond to the stiffness of their substrate. *Science*, 310(5751):1139–1143, 2005.

[96] S. E. Dobbins, V. I. Lesk, and M. J. E. Sternberg. Insights into protein flexibility: The relationship between normal modes and conformational change upon protein-protein docking. *Proceedings Of The National Academy Of Sciences Of The United States Of America*, 105(30):10390–10395, 2008.

[97] A. V. Dobrynin. Electrostatic persistence length of semiflexible and flexible polyelectrolytes. *Macromolecules*, 38(22):9304–9314, 2005.

[98] E. Donath, G. B. Sukhorukov, F. Caruso, S. A. Davis, and H. Mohwald. Novel hollow polymer shells by colloid-templated assembly of polyelectrolytes. *Angewandte Chemie-International Edition*, 37(16):2202–2205, 1998.

[99] P. Doruker, R. Jernigan, and I. Bahar. Dynamics of large proteins through hierarchical levels of coarse-grained structures. *Journal of Computational Chemistry*, 23(1):119–127, 2002.

[100] K. Drexler. *Nanosystems: Molecular Machinery, Manufacturing, and Computation*. Wiley, 1992.

[101] N. Du, X. Y. Liu, J. Narayanan, L. A. Li, M. L. M. Lim, and D. Q. Li. Design of superior spider silk: From nanostructure to mechanical properties. *Biophysical Journal*, 91(12):4528–4535, 2006.

[102] S. Dubas and J. Schlenoff. Factors controlling the growth of polyelectrolyte multilayers. *Macromolecules*, 32(24):8153–8160, 1999.

[103] S. T. Dubas and J. B. Schlenoff. Swelling and smoothing of polyelectrolyte multilayers by salt. *Langmuir*, 17(25):7725–7727, 2001.

[104] O. Dudko, G. Hummer, and A. Szabo. Theory, analysis, and interpretation of single-molecule force spectroscopy experiments. *Proceedings of the National Academy of Sciences of the United States of America*, 105(41):15755–15760, 2008.

[105] P. Durand, G. Trinquier, and Y. H. Sanejouand. New approach for determining low-frequency normal-modes in macromolecules. *Biopolymers*, 34(6):759–771, 1994.

[106] J. Dzubiella, J. M. J. Swanson, and J. A. McCammon. Coupling hydrophobicity, dispersion, and electrostatics in continuum solvent models. *Physical Review Letters*, 96(8):087802, 2006.

[107] J. Dzubiella, J. M. J. Swanson, and J. A. McCammon. Coupling nonpolar and polar solvation free energies in implicit solvent models. *Journal of Chemical Physics*, 124(8), 2006.

[108] A. J. Engler, S. Sen, H. L. Sweeney, and D. E. Discher. Matrix elasticity directs stem cell lineage specification. *Cell*, 126(4):677–689, 2006.

[109] E. Evans. Probing the relation between force, lifetime, and chemistry in single molecular bonds. *Annual Reviews in Biophysics and Biomolecular Structure*, 30(1):105–128, 2001.

[110] E. Evans and K. Ritchie. Dynamic strength of molecular adhesion bonds. *Biophysical Journal*, 72:1541–1555, 1997.

[111] R. Everaers, A. Milchev, and V. Yamakov. The electrostatic persistence length of polymers beyond the osf limit. *European Physical Journal E*, 8(1):3–14, 2002.

[112] E. Fadrna, K. Hladeckova, and J. Koca. Long-range electrostatic interactions in molecular dynamics: An endothelin-1 case study. *Journal of Biomolecular Structure and Dynamics*, 23(2):151–162, 2005.

[113] T. R. Farhat and J. B. Schlenoff. Ion transport and equilibria in polyelectrolyte multilayers. *Langmuir*, 17(4):1184–1192, 2001.

[114] R. Feynman. There's plenty of room at the bottom. *Caltech Engineering and Science*, 23:22–36, 1960.

[115] J. P. Fisher, D. Dean, and A. G. Mikos. Photocrosslinking characteristics and mechanical properties of diethyl fumarate/poly(propylene fumarate) biomaterials. *Biomaterials*, 23(22):4333–4343, 2002.

[116] M. Fixman and J. Skolnick. Polyelectrolyte excluded volume paradox. *Macromolecules*, 11(5):863–867, 1978.

[117] P. J. Flory. Thermodynamics of high polymer solutions. *Journal of Chemical Physics*, 9(8):660–661, 1941.

[118] P. J. Flory. *Principles of polymer chemistry*. The George Fisher Baker non-resident lectureship in chemistry at Cornell University. Cornell University Press, Ithaca, 1953.

[119] P. J. Flory. Statistical thermodynamics of random networks. *Proceedings of the Royal Society of London Series a-Mathematical Physical and Engineering Sciences*, 351(1666):351–380, 1976.

[120] M. Forney, L. Janosi, and I. Kosztin. Calculating free-energy profiles in biomolecular systems from fast nonequilibrium processes. *Physical Review E - Statistical, Nonlinear, and Soft Matter Physics*, 78(5):051913, 2008.

[121] P. Fratzl. Biomimetic materials research: what can we really learn from natures structural materials. *Journal of the Royal Society Interface*, 4:637–642, 2007.

[122] P. Fratzl and R. Weinkamer. Nature's hierarchical materials. *Progress in Materials Science*, 52:1263–1344, 2007.

[123] G. H. Fredrickson, V. Ganesan, and F. Drolet. Field-theoretic computer simulation methods for polymers and complex fluids. *Macromolecules*, 35(1):16–39, 2002.

[124] M. T. Frey and Y. L. Wang. A photo-modulatable material for probing cellular responses to substrate rigidity. *Soft Matter*, 5(9):1918–1924, 2009.

[125] L. A. Galin. *Contact problems in the theory of elasticity*. Dept. of Mathematics, School of Physical Sciences and Applied Mathematics, Raleigh, 1961. 62062676 (Lev Aleksandrovich) Translated from the Russian by Mrs. H. Moss. Editor: I. N. Sneddon. illus. 28 cm. Includes bibliography.

[126] H. Gao, B. Ji, I. Jager, E. Arzt, and P. Fratzl. Materials become insensitive to flaws at nanoscale: Lessons from nature. *Proceedings of the National Academy of Sciences of the United States of America*, 100(10):5597–5600, 2003.

[127] B. R. Gelin and M. Karplus. Sidechain torsional potentials and motion of amino-acids in proteins - bovine pancreatic trypsin-inhibitor. *Proceedings Of The National Academy Of Sciences Of The United States Of America*, 72(6):2002–2006, 1975.

[128] K. Ghosh, G. A. Carri, and M. Muthukumar. Configurational properties of a single semiflexible polyelectrolyte. *Journal of Chemical Physics*, 115(9):4367–4375, 2001.

[129] T. Giesa, D. Spivak, and M. Buehler. Reoccurring patterns in hierarchical protein materials and music: The power of analogies. *BioNanoScience*, 1(4):153–161, 2011.

[130] H. Gohlke and M. F. Thorpey. A natural coarse graining for simulating large biomolecular motion. *Biophysical Journal*, 91(6):2115–2120, 2006.

[131] J. Gong and Y. Osada. Gel friction: A model based on surface repulsion and adsorption. *Journal of Chemical Physics*, 109(18):8062–8068, 1998.

[132] L. E. Greene, M. Law, J. Goldberger, F. Kim, J. C. Johnson, Y. F. Zhang, R. J. Saykally, and P. D. Yang. Low-temperature wafer-scale production of zno nanowire arrays. *Angewandte Chemie-International Edition*, 42(26):3031–3034, 2003.

[133] V. Gribova, R. Auzely-Velty, and C. Picart. Polyelectrolyte multilayer assemblies on materials surfaces: From cell adhesion to tissue engineering. *Chemistry of Materials*, 24(5):854–869, 2012.

[134] A. Gubarev, J. M. Y. Carrillo, and A. V. Dobrynin. Scale-dependent electrostatic stiffening in biopolymers. *Macromolecules*, 42(15):5851–5860, 2009.

[135] Y. M. Guo, W. Geng, and J. Q. Sun. Layer-by-layer deposition of polyelectrolyte-polyelectrolyte complexes for multilayer film fabrication. *Langmuir*, 25(2):1004–1010, 2009.

[136] B. Y. Ha and D. Thirumalai. Electrostatic persistence length of a polyelectrolyte chain. *Macromolecules*, 28(2):577–581, 1995.

[137] C. S. Hajicharalambous, J. Lichter, W. T. Hix, M. Swierczewska, M. F. Rubner, and P. Rajagopalan. Nano- and sub-micron porous polyelectrolyte multilayer assemblies: Biomimetic surfaces for human corneal epithelial cells. *Biomaterials*, 30(23-24):4029–4036, 2009.

[138] T. Haliloglu, I. Bahar, and B. Erman. Gaussian dynamics of folded proteins. *Physical Review Letters*, 79(16):3090–3093, 1997.

[139] D. R. Han, S. Pal, J. Nangreave, Z. T. Deng, Y. Liu, and H. Yan. Dna origami with complex curvatures in three-dimensional space. *Science*, 332(6027):342–346, 2011.

[140] L. Han, D. Dean, P. Mao, C. Ortiz, and A. J. Grodzinsky. Nanoscale shear deformation mechanisms of opposing cartilage aggrecan macromolecules. *Biophysical Journal*, 93(5):L23–L25, 2007.

[141] L. Han, D. Dean, C. Ortiz, and A. J. Grodzinsky. Lateral nanomechanics of cartilage aggrecan macromolecules. *Biophysical Journal*, 92(4):1384–1398, 2007.

[142] L. Han, L. F. Wang, K. K. Chia, R. E. Cohen, M. F. Rubner, M. C. Boyce, and C. Ortiz. Geometrically controlled mechanically responsive polyelectrolyte tube arrays. *Advanced Materials*, 23(40):46674673, 2011.

[143] L. Han, J. Yin, L. Wang, K.-K. Chia, R. Cohen, M. Rubner, C. Ortiz, and M. Boyce. Geometrically controlled stimulus-responsive surface friction. *Soft Matter, in submission*, 2012.

[144] G. Hannig and S. C. Makrides. Strategies for optimizing heterologous protein expression in escherichia coli. *Trends in Biotechnology*, 16(2):54–60, 1998.

[145] J. Hansen, R. Skalak, S. Chien, and A. Hoger. An elastic network model based on the structure of the red blood cell membrane skeleton. *Biophysical Journal*, 70:146–166, 1996.

[146] M. Hara. *Polyelectrolytes : science and technology.* Marcel Dekker, New York, 1993.

[147] L. Hartwell. Theoretical biology: A robust view of biochemical pathways. *Nature*, 387(6636):855, 1997.

[148] L. H. Hartwell, J. J. Hopfield, S. Leibler, and A. W. Murray. From molecular to modular cell biology. *Nature*, 402(6761):C47–C52, 1999.

[149] S. Hayward and N. Go. Collective variable description of native protein dynamics. *Annual Review of Physical Chemistry*, 46:223–250, 1995.

[150] D. Heyes and H. Okumura. Equation of state and structural properties of the weeks-chandler-anderson fluid. *Journal of Chemical Physics*, 124:164597, 2006.

[151] J. Hiller, J. Mendelsohn, and M. Rubner. Reversibly erasable nanoporous anti-reflection coatings from polyelectrolyte multilayers. *Nature Materials*, 1:59–63, 2002.

[152] J. Hiller and M. Rubner. Reversible molecular memory and ph-switchable swelling transitions in polyelectrolyte multilayers. *Macromolecules*, 36(11):4078–4083, 2003.

[153] K. Hinsen. Analysis of domain motions by approximate normal mode calculations. *Proteins: Structure, Functions, and Genetics*, 33:417–429, 1998.

[154] K. Hinsen, A. Thomas, and M. Field. Analysis of domain motions in large proteins. *Proteins: Structure, Functions, and Genetics*, 34:369–382, 1999.

[155] R. W. Hockney and J. W. Eastwood. *Computer simulation using particles.* A. Hilger, Bristol England ; Philadelphia, special student edition, 1988.

[156] N. Holten-Andersen, M. J. Harrington, H. Birkedal, B. P. Lee, P. B. Messersmith, K. Y. C. Lee, and J. H. Waite. ph-induced metal-ligand cross-links inspired by mussel yield self-healing polymer networks with near-covalent elastic moduli. *Proceedings of the National Academy of Sciences of the United States of America*, 108(7):2651–2655, 2011.

[157] M. Houska, E. Brynda, and K. Bohata. The effect of polyelectrolyte chain length on layer-by-layer protein/polyelectrolyte assembly-an experimental study. *Journal of Colloid and Interface Science*, 273(1):140–147, 2004.

[158] P. Y. Hsiao. Chain morphology, swelling exponent, persistence length, like-charge attraction, and charge distribution around a chain in polyelectrolyte solutions: Effects of salt concentration and ion size studied by molecular dynamics simulations. *Macromolecules*, 39(20):7125–7137, 2006.

[159] G. Hummer and A. Szabo. Kinetics from nonequilibrium single-molecule pulling experiments. *Biophysical Journal*, 85(1):5–15, 2003.

[160] C. Hyeon and D. Thirumalai. Measuring the energy landscape roughness and the transition state location of biomolecules using single molecule mechanical unfolding experiments. *Journal of Physics: Condensed Matter*, 19(11):113101, 2007.

[161] R. M. Iost and F. N. Crespilho. Layer-by-layer self-assembly and electrochemistry: Applications in biosensing and bioelectronics. *Biosensors and Bioelectronics*, 31(1):1–10, 2012.

[162] K. Itano, J. Choi, and M. Rubner. Mechanism of the ph-induced discontinuous swelling/deswelling transitions of poly(allylamine hydrochloride)-containing polyelectrolyte multilayer films. *Macromolecules*, 38:3450–3460, 2005.

[163] J. A. Jaber and J. B. Schlenoff. Mechanical properties of reversibly cross-linked ultrathin polyelectrolyte complexes. *Journal of the American Chemical Society*, 128(9):2940–2947, 2006.

[164] A. Jagota and C. Y. Hui. Adhesion, friction, and compliance of bio-mimetic and bio-inspired structured interfaces. *Materials Science and Engineering R-Reports*, 72(12):253–292, 2011.

[165] J. Jeon, V. Panchagnula, J. Pan, and A. V. Dobrynin. Molecular dynamics simulations of mutilayer films of polyelectrolytes and nanoparticles. *Langmuir*, 22(10):4629–4637, 2006.

[166] X. Jiang, C. Ortiz, and P. T. Hammond. Exploring the rules for selective desposition: Interactions of model polyamines on acid and oligoethylene oxide surfaces. *Langmuir*, 18:1131–1143, 2002.

[167] K. Johnson. *Contact Mechanics*. Cambridge University Press, Cambridge, 1985.

[168] B. Jonsson, C. Peterson, and B. Soderberg. Variational approach to the structure and thermodynamics of linear polyelectrolytes with coulomb and screened coulomb interactions. *Journal of Physical Chemistry*, 99(4):1251–1266, 1995.

[169] W. Jorgensen, J. Chandrasekhar, and J. Madura. Comparison of simple potential functions for simulating liquid water. *Journal of Chemical Physics*, 79(21):926, 1983.

[170] W. L. Jorgensen, D. S. Maxwell, and J. TiradoRives. Development and testing of the opls all-atom force field on conformational energetics and properties of organic liquids. *Journal of the American Chemical Society*, 118(45):11225–11236, 1996.

[171] S. Keten, J. F. R. Alvarado, S. Muftu, and M. J. Buehler. Nanomechanical characterization of the triple beta-helix domain in the cell puncture needle of bacteriophage T4 virus. *Cellular and Molecular Bioengineering*, 2(1):66–74, 2009.

[172] S. Keten and M. J. Buehler. Asymptotic strength limit of hydrogen-bond assemblies in proteins at vanishing pulling rates. *Physical Review Letters*, 100(19):198301, 2008.

[173] S. Keten and M. J. Buehler. Strength limit of entropic elasticity in beta-sheet protein domains. *Physical Review E*, 78(6), 2008.

[174] S. Keten and M. J. Buehler. Nanostructure and molecular mechanics of spider dragline silk protein assemblies. *Journal of the Royal Society Interface*, 7(53):1709–1721, 2010.

[175] S. Keten, C. C. Chou, A. C. T. van Duin, and M. J. Buehler. Tunable nanomechanics of protein disulfide bonds in redox microenvironments. *Journal of the Mechanical Behavior of Biomedical Materials*, 5(1):32–40, 2012.

[176] S. Keten, Z. P. Xu, B. Ihle, and M. J. Buehler. Nanoconfinement controls stiffness, strength and mechanical toughness of beta-sheet crystals in silk. *Nature Materials*, 9(4):359–367, 2010.

[177] E. Kharlampieva, V. Kozlovskaya, and S. A. Sukhishvili. Layer-by-layer hydrogen-bonded polymer films: From fundamentals to applications. *Advanced Materials*, 21(30):3053–3065, 2009.

[178] E. Kharlampieva and S. Sukhishvili. Ionization and ph stability of multilayers formed by self-assembly of weak polyelectrolytes. *Langmuir*, 19(4):1235–1243, 2003.

[179] A. R. Khokhlov and K. A. Khachaturian. On the theory of weakly charged poly-electrolytes. *Polymer*, 23(12):1742–1750, 1982.

[180] K. Kim, D. Dean, J. Wallace, R. Breithaupt, A. G. Mikos, and J. P. Fisher. The influence of stereolithographic scaffold architecture and composition on osteogenic signal expression with rat bone marrow stromal cells. *Biomaterials*, 32(15):3750–3763, 2011.

[181] T. P. Knowles, A. W. Fitzpatrick, S. Meehan, H. R. Mott, M. Vendruscolo, C. M. Dobson, and M. E. Welland. Role of intermolecular forces in defining material properties of protein nanofibrils. *Science*, 318(5858):1900–1903, 2007.

[182] T. P. J. Knowles, T. W. Oppenheim, A. K. Buell, D. Y. Chirgadze, and M. E. Welland. Nanostructured films from hierarchical self-assembly of amyloidogenic proteins. *Nature Nanotechnology*, 5(3):204–207, 2010.

[183] H. C. Kolb, M. G. Finn, and K. B. Sharpless. Click chemistry: Diverse chemical function from a few good reactions. *Angewandte Chemie-International Edition*, 40(11):2004–2021, 2001.

[184] J. Kotz, S. Kosmella, and A. Ebert. Polyanion-polycation interactions in concentrated aqueous systems 1th comm.: interactions between poly(ethylene imine) and poly(acylic acid) in dependence on polymer concentration. *Acta Polymerica*, 43(6):313–319, 1992.

[185] O. Kratky and G. Porod. Diffuse small-angle scattering of x-rays in colloid systems. *Journal of Colloid Science*, 4(1):35–70, 1949.

[186] R. Kugler, J. Schmitt, and W. Knoll. The swelling behavior of polyelectrolyte multilayers in air of different relative humidity and in water. *Macromolecular Chemistry and Physics*, 203:413–419, 2002.

[187] J. Kwon, E. Cheung, S. Park, and M. Sitti. Friction enhancement via micropatterned wet elastomer adhesives on small intestinal surfaces. *Biomedical Materials*, 1(4):216–220, 2006.

[188] L. D. Landau and E. M. Lifshits. *Theory of elasticity*. Pergamon Press, London, 1959.

[189] K. K. S. Lau, J. Bico, K. B. K. Teo, M. Chhowalla, G. A. J. Amaratunga, W. I. Milne, G. H. McKinley, and K. K. Gleason. Superhydrophobic carbon nanotube forests. *Nano Letters*, 3(12):1701–1705, 2003.

[190] D. Laurent and J. B. Schlenoff. Multilayer assemblies of redox polyelectrolytes. *Langmuir*, 13(6):1552–1557, 1997.

[191] M. Lemieux, D. Usov, S. Minko, M. Stamm, H. Shulha, and V. V. Tsukruk. Reorganization of binary polymer brushes: Reversible switching of surface microstructures and nanomechanical properties. *Macromolecules*, 36(19):7244–7255, 2003.

[192] M. Levitt and A. Warshel. Computer-simulation of protein folding. *Nature*, 253(5494):694–698, 1975.

[193] H. Li, B. Liu, X. Zhang, C. Gao, J. Shen, and G. Zou. Single-molecule force spectroscopy on poly(acrylic acid) by afm. *Langmuir*, 15:2120–2124, 1999.

[194] H. Li and T. A. Witten. Fluctuations and persistence length of charged flexible polymers. *Macromolecules*, 28(17):5921–5927, 1995.

[195] Z. S. Liu and P. Calvert. Multilayer hydrogels as muscle-like actuators. *Advanced Materials*, 12(4):288–291, 2000.

[196] H. Lu, B. Isralewitz, A. Krammer, V. Vogel, and K. Schulten. Unfolding of titin immunoglobulin domains by steered molecular dynamics simulation. *Biophysical Journal*, 75(2):662–671, 1998.

[197] W. B. Luo, T. Q. Yang, and Q. L. An. Time-temperature-stress equivalence and its application to nonlinear viscoelastic materials. *Acta Mechanica Solida Sinica*, 14(3):195–199, 2001.

[198] B. A. Luty, M. E. Davis, I. G. Tironi, and W. F. Vangunsteren. A comparison of particle-particle, particle-mesh and ewald methods for calculating electrostatic interactions in periodic molecular-systems. *Molecular Simulation*, 14(1):11–20, 1994.

[199] S. P. Lyu, J. Schley, B. Loy, D. Lind, C. Hobot, R. Sparer, and D. Untereker. Kinetics and time-temperature equivalence of polymer degradation. *Biomacromolecules*, 8(7):2301–2310, 2007.

[200] A. MacKerell, D. Bashford, M. Bellott, and R. Dunbrack. All-atom empirical potential for molecular modeling and dynamics studies of proteins. *Journal of Physical Chemistry B*, 102:3586–3616, 1998.

[201] A. D. Mackerell. Empirical force fields for biological macromolecules: Overview and issues. *Journal of Computational Chemistry*, 25(13):1584–1604, 2004.

[202] M. W. Mahoney and W. L. Jorgensen. A five-site model for liquid water and the reproduction of the density anomaly by rigid, nonpolarizable potential functions. *Journal of Chemical Physics*, 112(20):8910–8922, 2000.

[203] A. Maitra and G. Arya. Model accounting for the effects of pulling-device stiffness in the analyses of single-molecule force measurements. *Physical Review Letters*, 104(10):108301, 2010.

[204] C. Majidi, R. E. Groff, Y. Maeno, B. Schubert, S. Baek, B. Bush, R. Maboudian, N. Gravish, M. Wilkinson, K. Autumn, and R. S. Fearing. High friction from a stiff polymer using microfiber arrays. *Physical Review Letters*, 97(7):076103, 2006.

[205] F. Mallwitz and A. Laschewsky. Direct access to stable, freestanding polymer membranes by layer-by-layer assembly of polyelectrolytes. *Advanced Materials*, 17:1296–1299, 2005.

[206] M. Mandel. The potentiometric titration of weak polyacids. *European Polymer Journal*, 6(6):807–822, 1970.

[207] J. E. Mark and B. Erman. *Science and technology of rubber*. Elsevier Academic Press, Amsterdam ; Boston, 3rd edition, 2005.

[208] S. Marrink, H. Risselada, S. Yefimov, D. Tieleman, and A. de Vries. The martini force filed: Coarse grained model for biomolecular structures. *Journal of Physical Chemistry B*, 111:7812–7824, 2007.

[209] M. W. Matsen. The standard gaussian model for block copolymer melts. *Journal of Physics-Condensed Matter*, 14(2):R21–R47, 2002.

[210] S. L. Mayo, B. D. Olafson, and W. A. Goddard. Dreiding - a generic force-field for molecular simulations. *Journal of Physical Chemistry*, 94(26):8897–8909, 1990.

[211] K. Mayya, D. Gittins, A. Dibaj, and F. Caruso. Nanotubes prepared by templating sacrificial nickel nanorods. *Nano Letters*, 1(12):727–730, 2001.

[212] J. A. McCammon, B. R. Gelin, and M. Karplus. Dynamics of folded proteins. *Nature*, 267(5612):585–590, 1977.

[213] W. McGuire, R. H. Gallagher, and R. D. Ziemian. *Matrix structural analysis*. John Wiley, New York, 2nd edition, 2000.

[214] R. M. McMeeking, L. F. Ma, and E. Arzt. Mechanism maps for frictional attachment between fibrillar surfaces. *Journal of Applied Mechanics-Transactions of the ASME*, 76(3), 2009.

[215] J. Mendelsohn, C. Barrett, V. Chan, A. Pal, A. Mayes, and M. Rubner. Fabrication of microporous thin films from polyelectrolyte multilayers. *Langmuir*, 16(11):5017–5023, 2000.

[216] J. Mendelsohn, S. Yang, J. Hiller, A. Hochbaum, and M. Rubner. Rational design of cytophilic and cytophobic polyelectrolyte multilayer thin films. *Biomacromolecules*, 4:96–106, 2003.

[217] P. M. Mendes. Stimuli-responsive surfaces for bio-applications. *Chemical Society Reviews*, 37(11):2512–2529, 2008.

[218] D. Mertz, J. Hemmerle, F. Boulmedais, J. C. Voegel, P. Lavalle, and P. Schaaf. Polyelectrolyte multilayer films under mechanical stretch. *Soft Matter*, 3(11):1413–1420, 2007.

[219] D. Mertz, C. Vogt, J. Hemmerle, J. Mutterer, V. Ball, J. C. Voegel, P. Schaaf, and P. Lavalle. Mechanotransductive surfaces for reversible biocatalysis activation. *Nature Materials*, 8(9):731–735, 2009.

[220] R. Messina. Polyelectrolyte multilayering on a charged planar surface. *Macromolecules*, 37(2):621–629, 2004.

[221] N. Metropolis, A. W. Rosenbluth, M. N. Rosenbluth, A. H. Teller, and E. Teller. Equation of state calculations by fast computing machines. *Journal of Chemical Physics*, 21(6):1087–1092, 1953.

[222] N. Metropolis and S. Ulam. The monte carlo method. *Journal of the American Statistical Association*, 44(247):335–341, 1949.

[223] S. Metzger, M. Muller, K. Binder, and J. Baschnagel. Adsorption transition of a polymer chain at a weakly attractive surface: Monte carlo simulation of off-lattice models. *Macromolecular Theory and Simulations*, 11:985–995, 2002.

[224] A. Michaels and R. Miekka. Polycation-polyanion complexes: preparation and properties of poly-(vinylbenzyltrimethylammonium) poly-(styrenesulfonate). *Journal of Physical Chemistry*, 65:1765–1773, 1961.

[225] U. Micka and K. Kremer. Persistence length of the debye-huckel model of weakly charged flexible polyelectrolyte chains. *Physical Review E*, 54(3):2653–2662, 1996.

[226] N. Miyashita, J. E. Straub, D. Thirumalai, and Y. Sugita. Transmembrane structures of amyloid precursor protein dimer predicted by replica-exchange molecular dynamics simulations. *Journal of the American Chemical Society*, 131(10):34383439, 2009.

[227] K. Mizuno, J. Ishii, H. Kishida, Y. Hayamizu, S. Yasuda, D. N. Futaba, M. Yu-mura, and K. Hata. A black body absorber from vertically aligned single-walled carbon nanotubes. *Proceedings of the National Academy of Sciences of the United States of America*, 106(15):6044–6047, 2009.

[228] F. Mohn, L. Gross, N. Moll, and G. Meyer. Imaging the charge distribution within a single molecule. *Nature Nanotechnology*, page doi:10.1038/nnano.2012.20, 2012.

[229] F. Molnar and J. Rieger. "like-charge attraction" between anionic polyelec-trolytes: molecular dynamics simulations. *Langmuir*, 21(2):786–789, 2005.

[230] L. Monticelli, S. Kandasamy, X. Periole, R. Larson, D. Tieleman, and S. Mar-rink. The martini coarse-grained force field: Extension to proteins. *Journal of Chemical Theory and Computation*, 4:819–834, 2008.

[231] M. P. Murphy, B. Aksak, and M. Sitti. Adhesion and anisotropic friction en-hancements of angled heterogeneous micro-fiber arrays with spherical and spat-ula tips. *Journal of Adhesion Science and Technology*, 21(12-13):1281–1296, 2007.

[232] M. Muthukumar. Double screening in polyelectrolyte solutions: Limiting laws and crossover formulas. *Journal of Chemical Physics*, 105(12):5183–5199, 1996.

[233] I. Navizet, R. Lavery, and R. Jernigan. Myosin flexibility: structural domains and collective vibrations. *Proteins: Structure, Functions, and Bioinformatics*, 54:384–393, 2004.

[234] R. R. Netz and H. Orland. Variational theory for a single polyelectrolyte chain. *European Physical Journal B*, 8(1):81–98, 1999.

[235] H. Nguyen and C. Hall. Molecular dynamics simulations of spontaneous fibril formation by random-coil peptides. *Proceedings of the National Academy of Sciences of the United States of America*, 101(46):16180–16185, 2004.

[236] H. Nguyen and C. Hall. Spontaneous fibril formation by polyalanines; dis-continuous molecular dynamic simulations. *Journal of the American Chemical Society*, 128(6):1890–1901, 2006.

[237] L. E. Nielsen and R. F. Landel. *Mechanical properties of polymers and composites*. Mechanical engineering. M. Dekker, New York, 2nd edition, 1994.

[238] A. J. Nolte, R. E. Cohen, and M. F. Rubner. A two-plate buckling technique for thin film modulus measurements: Applications to polyelectrolyte multilayers. *Macromolecules*, 39(14):4841–4847, 2006.

[239] N. Nordgren and M. W. Rutland. Tunable nanolubrication between dual-responsive polyionic grafts. *Nano Letters*, 9(8):2984–2990, 2009.

[240] A. Noy, C. Frisbie, L. Rozsnyai, M. Wrighton, and C. Lieber. Chemical force microscopy: exploiting chemically-modified tips to quantify adhesion, friction, and functional group distributions in molecular assemblies. *Journal of the American Chemical Society*, 117(30):7943–7951, 1995.

[241] T. Odijk. Polyelectrolytes near rod limit. *Journal of Polymer Science Part B: Polymer Physics*, 15(3):477–483, 1977.

[242] T. Odijk and A. C. Houwaart. Theory of excluded-volume effect of a polyelectrolyte in a 1-1 electrolyte solution. *Journal of Polymer Science Part B-Polymer Physics*, 16(4):627–639, 1978.

[243] B. Ozbas, J. Kretsinger, K. Rajagopal, J. P. Schneider, and D. J. Pochan. Salt-triggered peptide folding and consequent self-assembly into hydrogels with tunable modulus. *Macromolecules*, 37(19):7331–7337, 2004.

[244] V. Panchagnula, J. Jeon, and A. V. Dobrynin. Molecular dynamics simulations of electrostatic layer-by-layer self-assembly. *Physical Review Letters*, 93(3):037801, 2004.

[245] R. Paparcone and M. J. Buehler. Microscale structural model of alzheimer a beta(1-40) amyloid fibril. *Applied Physics Letters*, 94(24), 2009.

[246] R. Paparcone, S. Cranford, and M. J. Buehler. Compressive deformation of ultralong amyloid fibrils. *Acta Mechanica Sinica*, 26(6):977–986, 2010.

[247] R. Paparcone, S. W. Cranford, and M. J. Buehler. Self-folding and aggregation of amyloid nanofibrils. *Nanoscale*, 3(4):1748–1755, 2011.

[248] S. Park, C. Barrett, M. Rubner, and A. Mayes. Anomalous adsorption of polyelectrolyte layers. *Macromolecules*, 34:3384–3388, 2001.

[249] P. A. Patel, A. V. Dobrynin, and P. T. Mather. Combined effect of spin speed and ionic strength on polyelectrolyte spin assembly. *Langmuir*, 23(25):12589–12597, 2007.

[250] P. A. Patel, J. Jeon, P. T. Mather, and A. V. Dobrynin. Molecular dynamics simulations of layer-by-layer assembly of polyelectrolytes at charged surfaces: Effects of chain degree of polymerization and fraction of charged monomers. *Langmuir*, 21(13):6113–6122, 2005.

[251] S. Pathak, Z. G. Cambaz, S. R. Kalidindi, J. G. Swadener, and Y. Gogotsi. Viscoelasticity and high buckling stress of dense carbon nanotube brushes. *Carbon*, 47(8):1969–1976, 2009.

[252] P. V. Pavoor, A. Bellare, A. Strom, D. H. Yang, and R. E. Cohen. Mechanical characterization of polyelectrolyte multilayers using quasi-static nanoindentation. *Macromolecules*, 37(13):4865–4871, 2004.

[253] D. Pearlman, D. Case, J. Caldwell, W. Ross, I. Cheatham, T.E., S. DeBolt, D. Ferguson, G. Seibel, and P. Kollman. Amber, a package of computer programs for applying molecular mechanics, normal mode analysis, molecular dynamics and free energy calculations to simulate the structural and energetic properties of molecules. *Computer Physics Communications*, 91(1):1–41, 1995.

[254] A. I. Petrov, A. A. Antipov, and G. B. Sukhorukov. Base-acid equilibria in polyelectrolyte systems: From weak polvelectrolytes to interpolyelectrolyte complexes and multilayered polyelectrolyte shells. *Macromolecules*, 36(26):10079–10086, 2003.

[255] B. Philipp, H. Dautzenberg, K.-J. Linow, J. Kotz, and W. Dawydoff. Polyelectrolyte complexes - recent developments and open problems. *Progress in Polymer Science*, 14:91–172, 1989.

[256] T. A. Plaisted and S. Nemat-Nasser. Quantitative evaluation of fracture, healing and re-healing of a reversibly cross-linked polymer. *Acta Materialia*, 55(17):5684–5696, 2007.

[257] S. Plimpton. Fast parallel algorithms for short-range molecular dynamics. *Journal of Computational Physics*, 117:1–19, 1995.

[258] B. Pokroy, S. H. Kang, L. Mahadevan, and J. Aizenberg. Self-organization of a mesoscale bristle into ordered, hierarchical helical assemblies. *Science*, 323(5911):237–240, 2009.

[259] D. Porter. *Group interaction modelling of polymer properties*. Dekker, New York, 1995.

[260] N. V. Prabhu, M. Panda, Q. Y. Yang, and K. A. Sharp. Explicit ion, implicit water solvation for molecular dynamics of nucleic acids and highly charged molecules. *Journal of Computational Chemistry*, 29(7):1113–1130, 2008.

[261] N. M. Pugno. On the strength of the carbon nanotube-based space elevator cable: from nanomechanics to megamechanics. *Journal of Physics-Condensed Matter*, 18(33):S1971–S1990, 2006.

[262] N. M. Pugno. The role of defects in the design of space elevator cable: From nanotube to megatube. *Acta Materialia*, 55(15):5269–5279, 2007.

[263] H. J. Qi, K. B. K. Teo, K. K. S. Lau, M. C. Boyce, W. I. Milne, J. Robertson, and K. K. Gleason. Determination of mechanical properties of carbon nanotubes and vertically aligned carbon nanotube forests using nanoindentation. *Journal of the Mechanics and Physics of Solids*, 51(11-12):2213–2237, 2003.

[264] Z. Qin and M. J. Buehler. Cooperative deformation of hydrogen bonds in beta-strands and beta-sheet nanocrystals. *Physical Review E*, 82(6), 2010.

[265] Z. Qin, S. Cranford, T. Ackbarow, and M. J. Buehler. Robustness-strength performance of hierarchical alpha-helical protein filaments. *International Journal of Applied Mechanics*, 1(1):85–112, 2009.

[266] D. Qiu, P. S. Shenkin, F. P. Hollinger, and W. C. Still. The GB/SA continuum model for solvation. a fast analytical method for the calculation of approximate Born radii. *Journal of Physical Chemistry A*, 101(16):3005–3014, 1997.

[267] A. Rahman. Correlations in the motion of atoms in liquid argon. *Physical Review*, 136:A405–A411, 1964.

[268] A. Rahman and Stilling.Fh. Molecular dynamics study of liquid water. *Journal of Chemical Physics*, 55(7):3336, 1971.

[269] F. Rao and A. Caflisch. Replica exchange molecular dynamics simulations of reversible folding. *Journal of Chemical Physics*, 119(7):4035–4042, 2003.

[270] A. K. Rappe, C. J. Casewit, K. S. Colwell, W. A. Goddard, and W. M. Skiff. Uff, a full periodic-table force-field for molecular mechanics and molecular-dynamics simulations. *Journal of the American Chemical Society*, 114(25):10024–10035, 1992.

[271] C. E. Reed and W. F. Reed. Monte-carlo electrostatic persistence lengths compared with experiment and theory. *Journal of Chemical Physics*, 94(12):8479–8486, 1991.

[272] W. F. Reed, S. Ghosh, G. Medjahdi, and J. Francois. Dependence of polyelectrolyte apparent persistence lengths, viscosity, and diffusion on ionic-strength and linear charge-density. *Macromolecules*, 24(23):6189–6198, 1991.

[273] C. L. Ren, R. J. Nap, and I. Szleifer. The role of hydrogen bonding in tethered polymer layers. *Journal of Physical Chemistry B*, 112(50):16238–16248, 2008.

[274] Y. M. Rhee and V. S. Pande. Multiplexed-replica exchange molecular dynamics method for protein folding simulation. *Biophysical Journal*, 84(2):775–786, 2003.

[275] L. Richert, A. J. Engler, D. E. Discher, and C. Picart. Elasticity of native and cross-linked polyelectrolyte multilayer films. *Biomacromolecules*, 5(5):1908–1916, 2004.

[276] L. Richert, P. Lavalle, D. Vautier, B. Senger, J. F. Stoltz, P. Schaaf, J. C. Voegel, and C. Picart. Cell interactions with polyelectrolyte multilayer films. *Biomacromolecules*, 3(6):1170–1178, 2002.

[277] H. Rmaile and J. Schlenoff. "Internal pK_a's" in polyelectrolyte multilayers: coupling protons and salt. *Langmuir*, 18(22):8263–8264, 2002.

[278] P. W. K. Rothemund. Folding dna to create nanoscale shapes and patterns. *Nature*, 440(7082):297–302, 2006.

[279] B. Roux and T. Simonson. Implicit solvent models. *Biophysical Chemistry*, 78(1-2):1–20, 1999.

[280] T. P. Russell. Surface-responsive materials. *Science*, 297(5583):964–967, 2002.

[281] H. Saether, H. Holme, G. Maurstad, O. Smidsrod, and B. Stokke. Polyelectrolyte complex formation using alginate and chitosan. *Carbohydrate Polymers*, 74:813–821, 2008.

[282] D. S. Salloum, S. G. Olenych, T. C. S. Keller, and J. B. Schlenoff. Vascular smooth muscle cells on polyelectrolyte multilayers: Hydrophobicity-directed adhesion and growth. *Biomacromolecules*, 6(1):161–167, 2005.

[283] K. Y. Sanbonmatsu and A. E. Garcia. Structure of met-enkephalin in explicit aqueous solution using replica exchange molecular dynamics. *Proteins-Structure Function and Genetics*, 46(2):225–234, 2002.

[284] A. Sassi, S. Beltran, H. Hooper, H. Blanch, J. Prausnitz, and R. Siegel. Monte carlo simulations of hydrophobic weak polyelectrolytes: Titration properties and ph-induced structural transistions for polymers containing weak electrolytes. *Journal of Chemical Physics*, 97(11):8767–8774, 1992.

[285] M. Schaefer and M. Karplus. A comprehensive analytical treatment of continuum electrostatics. *Journal of Physical Chemistry*, 100(5):1578–1599, 1996.

[286] T. Scheibel, R. Parthasarathy, G. Sawicki, X. M. Lin, H. Jaeger, and S. L. Lindquist. Conducting nanowires built by controlled self-assembly of amyloid fibers and selective metal deposition. *Proceedings of the National Academy of Sciences of the United States of America*, 100(8):4527–4532, 2003.

[287] J. B. Schlenoff. Retrospective on the future of polyelectrolyte multilayers. *Langmuir*, 25(24):14007–14010, 2009.

[288] J. B. Schlenoff and S. T. Dubas. Mechanism of polyelectrolyte multilayer growth: Charge overcompensation and distribution. *Macromolecules*, 34(3):592–598, 2001.

[289] J. B. Schlenoff, H. Ly, and M. Li. Charge and mass balance in polyelectrolyte multilayers. *Journal of the American Chemical Society*, 120(30):7626–7634, 1998.

[290] F. Schmid. Self-consistent-field theories for complex fluids. *Journal of Physics-Condensed Matter*, 10(37):8105–8138, 1998.

[291] D. J. Schmidt, F. C. Cebeci, Z. I. Kalcioglu, S. G. Wyman, C. Ortiz, K. J. Van Vliet, and P. T. Hammond. Electrochemically controlled swelling and mechanical properties of a polymer nanocomposite. *ACS Nano*, 3(8):2207–2216, 2009.

[292] D. J. Schmidt, Y. Min, and P. T. Hammond. Mechanomutable and reversibly swellable polyelectrolyte multilayer thin films controlled by electrochemically induced ph gradients. *Soft Matter*, 7(14):6637–6647, 2011.

[293] J. Schmitt, T. Grunewald, G. Decher, P. Pershan, K. Kjaer, and M. Losche. Internal structure of layer-by-layer adsorbed polyelectrolyte films: a neutron and x-ray reflectivity study. *Macromolecules*, 26:7058–7063, 1993.

[294] A. Schneider, G. Francius, R. Obeid, P. Schwinte, J. Hemmerle, B. Frisch, P. Schaaf, J. Voegel, B. Senger, and C. Picart. Polyelectrolyte multilayers with a tunable young's modulus: influence of film stiffness on cell adhesion. *Langmuir*, 22:1193–1200, 2006.

[295] D. T. Seaton, S. J. Mitchell, and D. P. Landau. Monte carlo simulations of a semi-flexible polymer chain: A first glance. *Brazilian Journal of Physics*, 36(3A):623–626, 2006.

[296] U. Seifert. Rupture of multiple parallel molecular bonds under dynamic loading. *Physical Review Letters*, 84(12):2750–2753, 2000.

[297] U. Seifert. Dynamic strength of adhesion molecules: role of rebinding and self-consistent rates. *Europhysics Letters*, 58(5):792–798, 2002.

[298] W. Senaratne, L. Andruzzi, and C. K. Ober. Self-assembled monolayers and polymer brushes in biotechnology: Current applications and future perspectives. *Biomacromolecules*, 6(5):2427–2448, 2005.

[299] J. Shelley, M. Shelley, R. Reeder, S. Bandyopadhyay, and M. Klein. A coarse grain model for phospholipid simulations. *Journal of Physical Chemistry B*, 105:4464–4470, 2001.

[300] J. Shelley, M. Shelley, R. Reeder, S. Bandyopadhyay, P. Moore, and M. Klein. Simulations of phospholipids using a coarse-grain model. *Journal of Physical Chemistry B*, 105(9785-9792), 2001.

[301] P. Sherwood, B. Brooks, and M. Sansom. Multiscale methods for macromolecular simulations. *Current Opinion in Structural Biology*, 18:630–640, 2008.

[302] S.-Y. Sheu, D.-Y. Yang, H. Selze, and E. Schlag. Energetics of hydrogen bonds in peptides. *Proceedings of the National Academy of Sciences of the United States of America*, 100(22):12683–12687, 2003.

[303] S. Shiratori and M. Rubner. ph-dependent thickness behavior of sequentially adsorbed layers of weak polyelectrolytes. *Macromolecules*, 33:4213–4219, 2000.

[304] A. Sidorenko, T. Krupenkin, A. Taylor, P. Fratzl, and J. Aizenberg. Reversible switching of hydrogel-actuated nanostructures into complex micropatterns. *Science*, 315(5811):487–490, 2007.

[305] T. G. Sitharam. Numerical simulation of particulate materials using discrete element modelling. *Current Science*, 78(7):876–886, 2000.

[306] J. Skolnick and M. Fixman. Electrostatic persistence length of a wormlike polyelectrolyte. *Macromolecules*, 10(5):944–948, 1977.

[307] H. P. Sorensen and K. K. Mortensen. Advanced genetic strategies for recombinant protein expression in escherichia coli. *Journal of Biotechnology*, 115(2):113–128, 2005.

[308] M. Sotomayer and K. Schulten. Single-molecule experiments in vitro and in silico. *Science*, 316:1144–1148, 2007.

[309] D. I. Spivak, T. Giesa, E. Wood, and M. J. Buehler. Category theoretic analysis of hierarchical protein materials and social networks. *PloS One*, 6(9), 2011.

[310] V. Spiwok, P. Hobza, and J. Rezac. Free-energy simulations of hydrogen bonding versus stacking of nucleobases on a graphene surface. *Journal of Physical Chemistry C*, 115(40):19455–19462, 2011.

[311] W. C. Still, A. Tempczyk, R. C. Hawley, and T. Hendrickson. Semianalytical treatment of solvation for molecular mechanics and dynamics. *Journal of the American Chemical Society*, 112(16):6127–6129, 1990.

[312] M. A. C. Stuart, W. T. S. Huck, J. Genzer, M. Muller, C. Ober, M. Stamm, G. B. Sukhorukov, I. Szleifer, V. V. Tsukruk, M. Urban, F. Winnik, S. Zauscher, I. Luzinov, and S. Minko. Emerging applications of stimuli-responsive polymer materials. *Nature Materials*, 9(2):101–113, 2010.

[313] G. K. Such, A. P. R. Johnston, and F. Caruso. Engineered hydrogen-bonded polymer multilayers: from assembly to biomedical applications. *Chemical Society Reviews*, 40(1):19–29, 2011.

[314] Y. Sugita and Y. Okamoto. Replica-exchange molecular dynamics method for protein folding. *Chemical Physics Letters*, 314(1-2):141–151, 1999.

[315] Z. Sui and J. Schlenoff. Phase separations in ph-responsive polyelectrolyte multilayers: charge extrusion versus charge explusion. *Langmuir*, 20(14):6026–6031, 2004.

[316] M. Surin, P. G. A. Janssen, R. Lazzaroni, P. Leclere, E. W. Meijer, and A. P. H. J. Schenning. Supramolecular organization of ssdna-templated pi-conjugated oligomers via hydrogen bonding. *Advanced Materials*, 21(10-11):1126–1130, 2009.

[317] M. Tagliazucchi, E. J. Calvo, and I. Szleifer. Redox and acid base coupling in, ultrathin polyelectrolyte films. *Langmuir*, 24(6):2869–2877, 2008.

[318] Y. Tak and K. J. Yong. Controlled growth of well-aligned zno nanorod array using a novel solution method. *Journal of Physical Chemistry B*, 109(41):19263–19269, 2005.

[319] F. Tama. Normal mode analysis with simplified models to investigate the global dynamics of biological systems. *Protein and Peptide Letters*, 10(2):119–132, 2003.

[320] F. Tama, F. X. Gadea, O. Marques, and Y. H. Sanejouand. Building-block approach for determining low-frequency normal modes of macromolecules. *Proteins-Structure Function and Genetics*, 41(1):1–7, 2000.

[321] F. Tama and Y. H. Sanejouand. Conformational change of proteins arising from normal mode calculations. *Protein Engineering*, 14(1):1–6, 2001.

[322] C. H. Tan and R. Luo. Nonpolar implicit solvent models. *Biophysical Journal*, 88(1):514a–514a, 2005.

[323] D. Tanner, J. A. Fitzgerald, and B. R. Phillips. The kevlar story - an advanced materials case-study. *Angewandte Chemie-International Edition in English*, 28(5):649–654, 1989.

[324] P. A. Thompson, V. Munoz, G. S. Jas, E. R. Henry, W. A. Eaton, and J. Hofrichter. The helix-coil kinetics of a heteropeptide. *Journal of Physical Chemistry B*, 104(2):378–389, 2000.

[325] M. F. Thorpe. Comment on elastic network models and proteins. *Physical Biology*, 4(1):60–63, 2007.

[326] M. Tirion. Large amplitude elastic motions in proteins from a single-parameter, atomic analysis. *Physical Review Letters*, 77(9):1905–1908, 1996.

[327] V. Tozzini. Coarse-grained models for proteins. *Current Opinion in Structural Biology*, 15:144–150, 2005.

[328] G. A. Tribello, M. Ceriotti, and M. Parrinello. A self-learning algorithm for biased molecular dynamics. *Proceedings of the National Academy of Sciences of the United States of America*, 107(41):17509–17514, 2010.

[329] M. Ullner. Comments on the scaling behavior of flexible polyelectrolytes within the debye-huckel approximation. *Journal of Physical Chemistry B*, 107(32):8097–8110, 2003.

[330] M. Ullner, B. Jonsson, C. Peterson, O. Sommelius, and B. Soderberg. The electrostatic persistence length calculated from monte carlo, variational and perturbation methods. *Journal of Chemical Physics*, 107(4):1279–1287, 1997.

[331] M. Ullner and C. E. Woodward. Orientational correlation function and persistence lengths of flexible polyelectrolytes. *Macromolecules*, 35(4):1437–1445, 2002.

[332] A. C. T. van Duin, S. Dasgupta, F. Lorant, and W. A. Goddard. Reaxff: A reactive force field for hydrocarbons. *Journal of Physical Chemistry A*, 105(41):9396–9409, 2001.

[333] H. W. T. van Vlijmen and M. Karplus. Normal mode analysis of large systems with icosahedral symmetry: Application to (dialanine)(60) in full and reduced basis set implementations. *Journal of Chemical Physics*, 115(2):691–698, 2001.

[334] J. F. V. Vincent, O. A. Bogatyreva, N. R. Bogatyrev, A. Bowyer, and A. K. Pahl. Biomimetics: its practice and theory. *Journal of the Royal Society Interface*, 3(9):471–482, 2006.

[335] O. I. Vinogradova, O. V. Lebedeva, K. Vasilev, H. F. Gong, J. Garcia-Turiel, and B. S. Kim. Multilayer dna/poly(allylamine hydrochloride) microcapsules: Assembly and mechanical properties. *Biomacromolecules*, 6(3):1495–1502, 2005.

[336] E. Walton, S. Lee, and K. Van Vliet. Extending bell's model: How force transducer stiffness alters measures unbinding forces and kinetics of molecular complexes. *Biophysical Journal*, 94:2621–2630, 2008.

[337] L. F. Wang, C. Ortiz, and M. C. Boyce. Mechanics of indentation into micro- and nanoscale forests of tubes, rods, or pillars. *Journal of Engineering Materials and Technology-Transactions of the Asme*, 133(1), 2011.

[338] T. Wang, M. Rubner, and R. Cohen. Polyelectrolyte multilayer nanoreactors for preparing silver nanoparticle composites: controlling metal concentration and nanoparticle size. *Langmuir*, 18(8):3370–3375, 2002.

[339] T. Wang, M. Rubner, and R. Cohen. Manipulating nanoparticle size within polyelectrolyte multilayers via electroless nickel deposition. *Chemistry of Materials*, 15(1):299–304, 2003.

[340] T. C. Wang, B. Chen, M. F. Rubner, and R. E. Cohen. Selective electroless nickel plating on polyelectrolyte multilayer platforms. *Langmuir*, 17(21):6610–6615, 2001.

[341] W. Weaver, S. Timoshenko, and D. Young. *Vibration Problems in Engineering*. Wiley-Interscience, Hoboken, NJ, 2001.

[342] J. Weeks, D. Chandler, and H. Anderson. Role of repulsive forces in determining the equilibrium structure of simple liquids. *Journal of Chemical Physics*, 54(12):5237–5247, 1971.

[343] D. West, D. Brockwell, P. Olmsted, S. Radford, and E. Paci. Mechancial resistance of proteins explained using simple molecular models. *Biophysical Journal*, 90(1):287–297, 2006.

[344] S. Williams, T. P. Causgrove, R. Gilmanshin, K. S. Fang, R. H. Callender, W. H. Woodruff, and R. B. Dyer. Fast events in protein folding: Helix melting and formation in a small peptide. *Biochemistry*, 35(3):691–697, 1996.

[345] E. L. Wilson. The static condensation algorithm. *International Journal for Numerical Methods in Engineering*, 8(1):198–203, 1974.

[346] A. Xie and S. Granick. Local electrostatics within a polyelectrolyte multilayer with embedded weak polyelectrolytes. *Macromolecules*, 35(5):1805–1813, 2002.

[347] Z. Xu, R. Paparcone, and M. J. Buehler. Alzheimer's a(1-40) amyloid fibrils feature size-dependent mechanical properties. *Biophysical Journal*, 98, 2010.

[348] L. Yang, G. Song, A. Carriquiry, and R. L. Jernigan. Close correspondence between the motions from principal component analysis of multiple hiv-1 protease structures and elastic network modes. *Structure*, 16(2):321–330, 2008.

[349] L. Yang, G. Song, and R. L. Jernigan. How well can we understand large-scale protein motions using normal modes of elastic network models? *Biophysical Journal*, 93(3):920–929, 2007.

[350] D. Yoo, S. S. Shiratori, and M. F. Rubner. Controlling bilayer composition and surface wettability of sequentially adsorbed multilayers of weak polyelectrolytes. *Macromolecules*, 31(13):4309–4318, 1998.

[351] Y. Yoshikawa, H. Matsuoka, and N. Ise. Ordered structure of polyallylamine hydrochloride in dilute-solutions as studied by small-angle x-ray-scattering. *British Polymer Journal*, 18(4):242–246, 1986.

[352] Y. Yu, F. Wang, W. Q. Shi, L. Y. Wang, W. B. Wang, and J. C. Shen. Conformations and adsorption behavior of poly(allylamine hydrochloride) studied by single molecule force spectroscopy. *Chinese Science Bulletin*, 53(1):22–26, 2008.

[353] L. Zhai, F. C. Cebeci, R. E. Cohen, and M. F. Rubner. Stable superhydrophobic coatings from polyelectrolyte multilayers. *Nano Letters*, 4(7):1349–1353, 2004.

[354] C. Zhang and D. E. Hirt. Layer-by-layer self-assembly of polyelectrolyte multilayers on cross-section surfaces of multilayer polymer films: A step toward nano-patterning flexible substrates. *Polymer*, 48:6748–6754, 2007.

[355] H. P. Zhang and H. A. Makse. Jamming transition in emulsions and granular materials. *Physical Review E*, 72(1):011301, 2005.

[356] X. H. Zhang and Q. W. Li. Enhancement of friction between carbon nanotubes: An efficient strategy to strengthen fibers. *ACS Nano*, 4(1):312–316, 2010.

[357] Z. Y. Zhang, A. J. Morse, S. P. Armes, A. L. Lewis, M. Geoghegan, and G. J. Leggett. Effect of brush thickness and solvent composition on the friction force response of poly(2-(methacryloyloxy)ethylphosphorylcholine) brushes. *Langmuir*, 27(6):2514–2521, 2011.

[358] Q. Zhao, Q. F. An, Y. Ji, J. Qian, and C. Gao. Polyelectrolyte complex membranes for pervaporation, nanofiltration and fuel cell applications. *Journal of Membrane Science*, 379(12):19–45, 2011.

[359] W. Zheng and S. Doniach. A comparative study of motor-protein motions by using a simple elastic-network model. *Proceedings of the National Academy of Sciences of the United States of America*, 100(23):13253–13258, 2003.

[360] W. J. Zheng. A unification of the elastic network model and the gaussian network model for optimal description of protein conformational motions and fluctuations. *Biophysical Journal*, 94(10):3853–3857, 2008.

[361] R. Zwanzig. Diffusion in a rough potential. *Proceedings of the National Academy of Sciences of the United States of America*, 85(7):2029–2090, 1988.